THE UNIVERSITY OF WARWICK

Development of Electrochemical Probe Microscopy and Related Techniques

Martin Andrew Edwards

A thesis submitted for the degree of Doctor of Philosophy

Molecular Organisation and Assembly in Cells (MOAC)

University of Warwick

September 2008

Table of Contents

List of Figures

List of Tables

Acknowledgements

I would like to offer my sincerest thanks to all the people who have helped me out through the duration of my PhD; those who have helped make it an academic success, but also a hugely enjoyable period of my life.

I would like to thank Professor Alison Rodger, director of the Molecular Organisation and Assembly in Cells (MOAC) Doctoral Training Centre, whose vision for an interdisciplinary science centre enticed me to undertake to become the interdisciplinary scientist I am today. Through the interactions with the great bunch of people she brought together I have learnt much and made many friends.

I owe a huge debt of gratitude to Professor Patrick Unwin for his endless enthusiasm and tireless work ethic that have made my project both enjoyable and successful. His guidance and willingness to allow me to explore made this experience so fruitful.

I thank Dr. Anna Whitworth and Professor Julie Macpherson for their help and guidance. Without their willingness to explain things to me, no matter how trivial, I would never have made it to the end.

To the wonderful group of friends and colleagues that are the Warwick Electrochemistry and Interfaces group, I give my thanks; for making it such a fun time, for welcoming me into the group, and for always being there and willing to lend a hand and help me out. From these people I learnt so much. These were the people that were there through the high and the lows, the people who put a smile on my face when things didn't go to plan. To the many collaborators with whom I have worked, I offer my warmest gratitude; your hard work and dedication did not go unnoticed.

I offer my thanks to my friends outside “the bubble”, who were always there when I needed them and who were always there to keep my feet firmly on the ground.

Declaration

The work contained within this thesis is my own except where outlined below. I confirm that this thesis has not been submitted for any degree at another university. Parts of the introduction (chapter 1) have been included in the review article:

Edwards, M., S. Martin, et al. (2006). "Scanning electrochemical microscopy: principles and applications to biophysical systems." Physiol. Meas. **27**: R63-108.

Collaborative Works

Chapter 3

The data for the SICM and AFM images (Figures 3-9 and 3-10) were kindly provided by Cara G. Williams.

Chapter 4

The experimental data within this chapter are the results of the tireless work of Dr. Fei Li.

Chapter 6

Experimental data were provided by Cara G. Williams, who was ably assisted by Dr. Anna Colley, for the work on Al alloys. Figure 6-9, an AFM image of HOPG, was obtained by Dr. Manon Guille.

Chapter 7

All experimental data were kindly provided by Dr. Paolo Bertoncello

Summary

This thesis presents work on the development of a number of scanned electrochemical probe microscopies. Such techniques have widespread applications, from materials science to the life sciences. Advances in flexible instrumentation, coupled with the theoretical description of electrochemical systems, are central themes which allowed for the fruitful investigation of a variety of experimental systems.

Theoretical descriptions of scanning ion conductance microscopy (SICM) were developed, particularly to investigate the effect of tip-geometry on imaging resolution. This technique has already found a number of applications in the life sciences, but image resolution has not previously been addressed adequately. Images were recorded showing tip-convolution that were in agreement with theoretical predictions.

The scanning microcapillary contact method (SMCM) was developed, as a method of assessing spatial heterogeneities in electrode activity on the sub-micron length-scale. An electrolyte filled microcapillary containing a reference/auxiliary electrode was approached to a substrate (working) electrode surface, via piezoelectric positioners. Contact of the electrolyte meniscus with the substrate electrode was sensed by a current flowing. Electrochemical measurements were performed before the microcapillary was retracted and another point on the sample was characterised. Spatial heterogeneities in electrode activity were imaged on a sub-micron length-scale and the activity of basal plane highly oriented pyrolytic graphite (HOPG) was demonstrated.

Tip position modulation scanning electrochemical microscopy (SECM-TPM), where an ultramicroelectrode (UME) is oscillated perpendicularly to a surface and an amperometric current is recorded, was investigated experimentally and theoretically. A model including convective mass-transport was developed that gave an accurate description of the experimental situation. It was demonstrated that SECM-TPM is a potentially powerful approach for the measurement of the permeability of a sample.

SECM experiments were performed investigating the growth of Ag particles at a liquid/liquid interface, which was caused through the electrodissolution of a Ag UME in an aqueous phase, and the reduction of the Ag^+ ion by an electron donor in the organic phase. A model was created that allowed for the interpretation of data.

Cyclic voltammetry investigations of HOPG covered with a Nafion film containing a redox mediator confirmed the activity of basal plane HOPG, as demonstrated by SMCM measurements. Nafion slowed diffusion sufficiently to allow the spatial-decoupling of surface sites with different activity.

Chapter 1: Introduction

This chapter introduces the fundamentals of the techniques used in subsequent chapters. Both instrumental techniques, i.e. scanning electrochemical microscopy (SECM), scanning ion conductance microscopy (SICM), and the numerical methods used to quantify and enable understanding of the systems subsequently investigated, specifically the finite element method (FEM), are covered. Also covered are basics of dynamic electrochemistry, which underpin the understanding of the systems investigated in this work.

1.1 Dynamic Electrochemistry

Dynamic electrochemistry refers to the field of study of charge transfer processes taking place at electrodes poised at a non-equilibrium potential. In amperometric methodologies the potential at the electrode is controlled and the current arising from the charge transfer is measured.[1] Alternatively, in a galvanostatic experimental setup, a constant current is maintained through varying the applied potential. The processes in a system under study can be split up into electrode processes, e.g. charge transfer processes, mass transport processes – the method by which species arrive to the electrode, and further physicochemical processes, which vary as widely as the systems one can investigate, but which include reactions, either in solution or at phase boundaries and growth and nucleation phenomena. We address the first two groups in the subsequent section, leaving the third group to be introduced with the system in the remaining chapters. A schematic of the processes involved is seen in Figure 1.1.

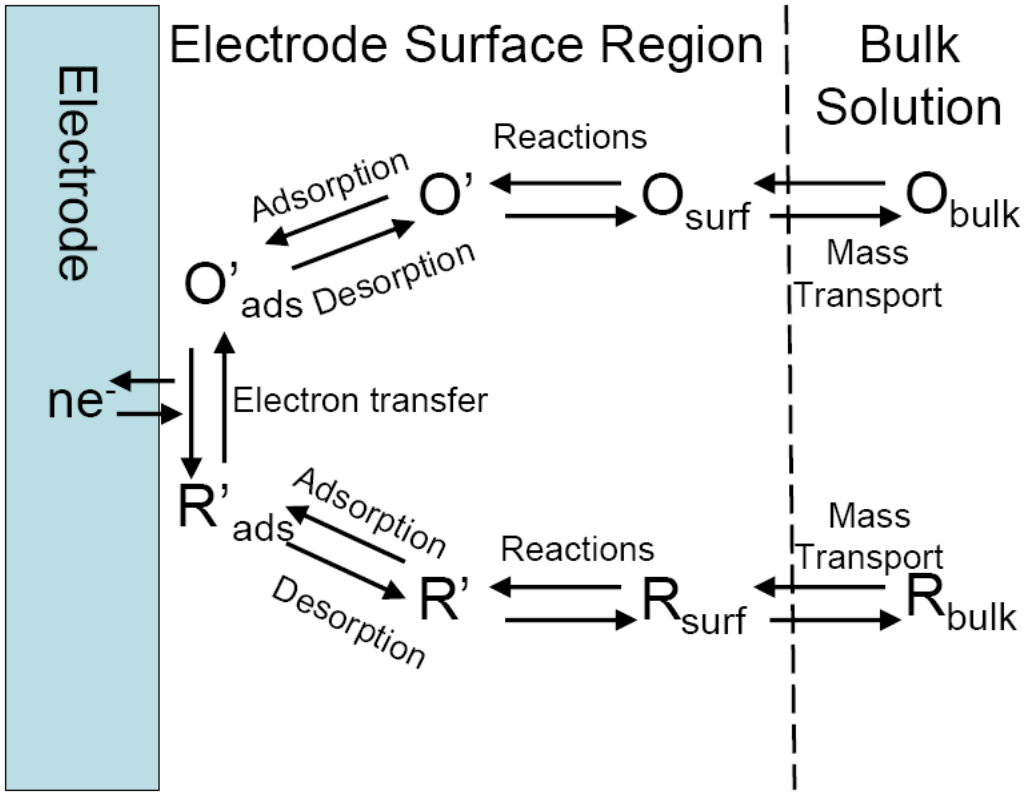

Figure 1.1: A schematic representation of processes involved in a basic dynamic electrochemistry experiment.

1.1.1 Electron transfer at the electrode Nernst/Butler-Volmer equations

Charge transfer may occur at the electrode-electrolyte interface if it is thermodynamically favourable. In a metallic electrode material (as most electrodes are) the energy level of the electrons occupies a continuum of states below the Fermi level. If this level is higher than the highest occupied molecular orbital (HOMO) or below the lowest unoccupied molecular orbital (LUMO) level of the molecules in the electrolyte then electron transfer becomes thermodynamically viable.[1] For an equilibrium system, such as described in equation 1.1, thermodynamic considerations give the relation of voltage and activity known as the Nernst equation (1.2).

$$O + ne^- \rightleftharpoons R \qquad (1.1)$$

$$E = E^0 + \frac{RT}{nF}\ln\frac{(\mathrm{O})}{(\mathrm{R})} \qquad (1.2)$$

Where E is the electrode potential, E^0 the standard electrode potential, R is the molar gas constant, F is Faraday's constant, n arises from the stoichiometry in equation 1.1, (O) and (R) take the standard meaning of activities of the oxidised and reduced forms of the species respectively.[2]

While none of the systems under study in dynamic electrochemistry are at equilibrium it is often the case that the kinetics of electron transfer are so fast in comparison to the mass transport processes involved that this can be considered the case. Such a system is said to display Nernstian or reversible kinetics, described by equation 1.3, a modification of equation 1.2 where $\mathrm{O}\big|_{elec}$ and $\mathrm{R}\big|_{elec}$ represent the concentration of the oxidised and reduced forms respectively at the surface of the electrode.

$$E = E^0 + \frac{RT}{nF}\ln\frac{\mathrm{O}\big|_{elec}}{\mathrm{R}\big|_{elec}} \qquad (1.3)$$

Where this is not the case the kinetics of the electrode reaction must be considered. In equilibrium these should necessarily agree with the thermodynamic equilibrium described in the Nernst Equation (1.2). The simplest of these was introduced by Butler and Volmer and is frequently referred to as Butler-Volmer kinetics. For the reaction in equation 1.4 the forward, k_f, and backward, k_b, rate constants are defined in equations 1.5 and 1.6.

$$\mathrm{O} + ne^- \underset{k_b}{\overset{k_f}{\rightleftharpoons}} \mathrm{R} \qquad (1.4)$$

$$k_f = k^0 \exp(-\alpha nF(E - E^{0'})/RT) \qquad (1.5)$$

$$k_b = k^0 \exp\left((1-\alpha)nF(E - E^{0'})/RT\right) \qquad (1.6)$$

Where k^0 is known as the standard rate constant, α is the electron transfer coefficient, $E^{0'}$ is the formal electrode potential, and all other variables are as

previously defined. The basis of the derivation of equations 1.5 and 1.6 lies in transition state theory. More complex models of electron transfer kinetics do exist, but are deemed outside the scope of this work.[2]

1.1.2 The electrode-solution interface (double layer)

The phase discontinuity at the electrode-solution interface, of indeed any other phase boundaries with the solution should be considered if one is to understand the processes that take place at it. Various successive models have been proposed which all describe how the charge density on the electrode is matched by the species in solution. A typically presented model is outlined in Figure 1.2 and is known as the Grahame model. The two labelled lines the inner Helmholtz plane (IHP) and the outer Helmholtz plane (OHP) represent respectively the plane at the centre of ions that have specifically absorbed onto the electrode and the plane of closest approach for solvated ions. The term double layer is often given to this region, this stems from a simplified model where the balancing charges were described as residing in single layers, either on the electrode surface or in solution.[1]

The description of two sets of charges in parallel planes is that of a parallel plate capacitor, therefore it should come of little surprise that the double layer is frequently represented in an equivalent circuit as a capacitor. The current flowing due to the changing of the composition of the double layer is usually termed the charging current. It can limit the sensitivity of electrochemical measurements, particularly in a temporal sense.[2]

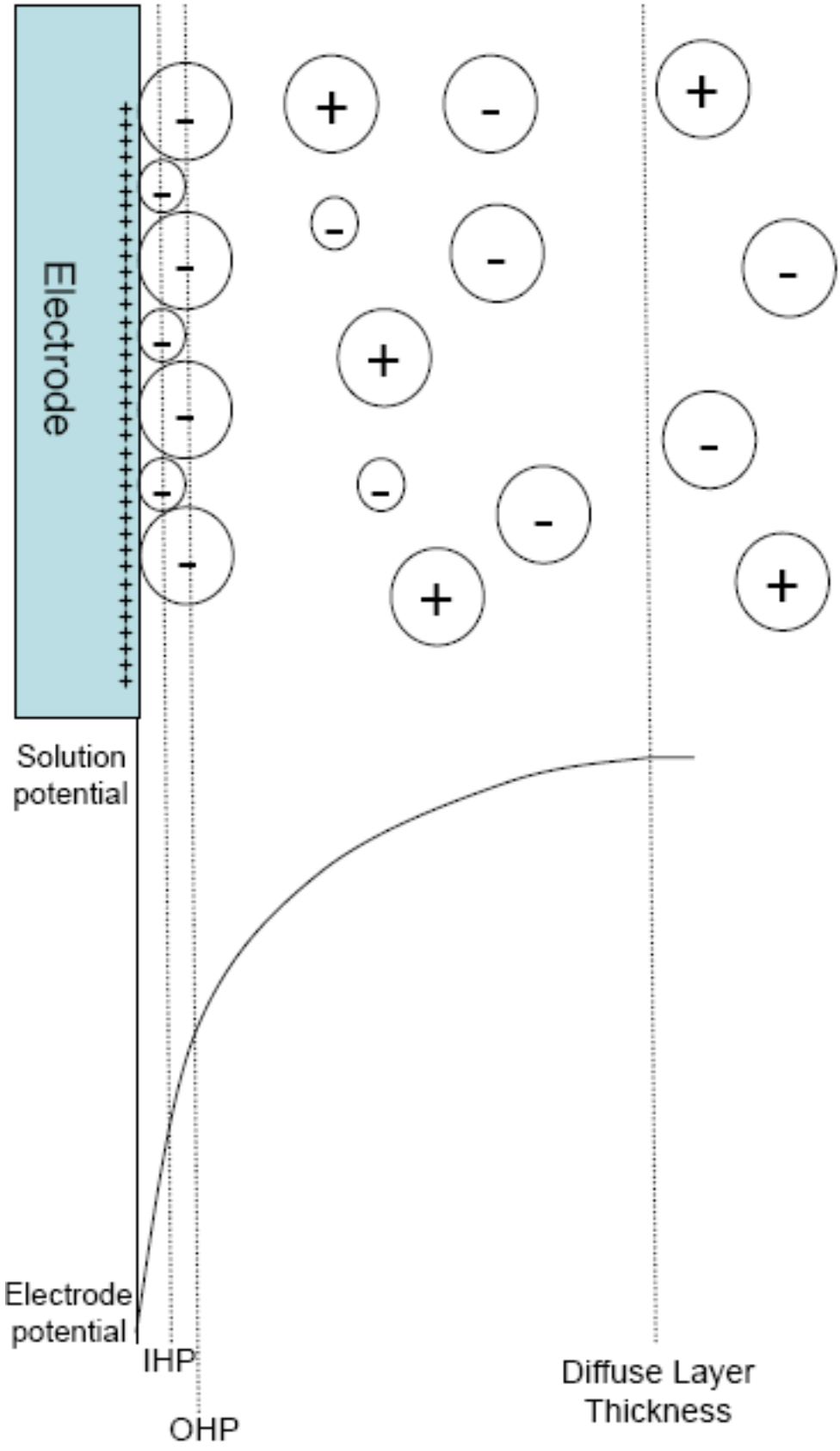

Figure 1.2: Representation of the Grahame model of the electrode-solution interface, showing how the potential returns to the solution potential. Key: IHP = Inner Helmholtz Plane; OHP = Outer Helmholtz Plane

1.1.3 Mass transport

Mass transport is the term used to describe the method with which material is transported in solution and can be split into diffusion, migration and convection. It is the sum of all of these different processes that dictates the overall mass transport. The overall partial differential equation we use to describe mass transport is the Nernst-Plank equation.[2]

$$\begin{aligned} J_i &= J_{i,d} + J_{i,m} + J_{i,c} \\ &= -D_i \nabla C_i - \frac{z_i F}{RT} D_i C_i \nabla \phi + C_i \underline{v} \end{aligned} \tag{1.7}$$

J_i, $J_{i,d}$, $J_{i,m}$ and $J_{i,c}$ represent the total/diffusive/migrative/convective elements of the flux of species *i*; D_i is the diffusion coefficient of species *i*; C_i represents the concentration of species *i*; z_i represents the charge on species *i*; ϕ represents an electric potential; $\underline{v}$ represents the velocity of the solution; T is the absolute temperature and all other terms are as previously defined. NB: many of the terms in equation 1.7 are, or may be, functions of both space and time. The following sections will introduce each of the components of mass transport in more detail.

1.1.3.1 Diffusion

Diffusion refers to the net flux that occurs due to a concentration (strictly activity) gradient. It arises from the Brownian motion of molecules. Equations describing diffusion were described by the physician Adolf Fick and to this day his name endures in Fick's first 1.8 and second 1.9 laws.[2]

$$J_{i,d} = -D_i \nabla C_i \tag{1.8}$$

$$\frac{\partial C_i}{\partial t} = D_i \nabla^2 C_i \tag{1.9}$$

Both laws are descriptions in terms of concentration and should be interpreted carefully when a single or a few molecules are being considered. The first law is derived from a discretised random walk model. The second is the result of combining Fick's first law with a continuity equation 1.10, which is merely a description of the conservation of matter.

$$\frac{\partial C_i}{\partial t} = -\nabla \cdot J_i \tag{1.10}$$

1.1.3.2 Migration

The term migration is used within the context of electrochemistry to refer to the movement of charged species due to an electric field, $\nabla\phi$, with ϕ being the potential for the field. Migrative flux is described by:

$$j_m = -\frac{z_i F}{RT} D_i C_i \nabla\phi \tag{1.11}$$

The absolute value of the coefficient $\frac{z_i F}{RT} D_i$ is frequently called the mobility of the ion and is denoted u_i. Equation 1.11 is arrived upon by balancing the force arising from the electric field with the drag on the ion by the solution.[2]

To arrive at the electric field it is generally necessary for one to solve Laplace's equation 1.12 with appropriate boundary conditions.

$$\nabla^2\phi = 0 \tag{1.12}$$

1.1.3.3 Convection

Convection refers to flux caused by the motion of the fluid. The convective component of flux is given by:

$$J_{i,c} = C_i \underline{v} \tag{1.13}$$

In the case where convection and diffusion are the only forms of mass transport that it is necessary to consider, which is the case in many systems where an excess of supporting electrolyte is added, once can arrive at the convective-diffusion equation 1.14.[2]

$$\frac{\partial C_i}{\partial t} = D_i \nabla^2 C_i - \underline{v} \cdot \nabla C_i \tag{1.14}$$

The obtaining of the velocity field $\underline{v}$ is the field of fluid dynamics, of which a comprehensive study is well beyond the scope of this work. Briefly, the

governing equations of fluid motion are the Navier-Stokes equations, which for an incompressible Newtonian (constant viscosity) fluid, a good approximation for aqueous solution at the velocity/pressures typically encountered in electrochemical experimentation, reduce to:

$$\nabla \cdot \underline{v} = 0 \tag{1.15}$$

$$\rho\left(\frac{\partial \underline{v}}{\partial t} + \underline{v} \cdot \nabla \underline{v}\right) = -\nabla P + \mu \nabla^2 \underline{v} + \underline{f} \tag{1.16}$$

ρ is the density of the solution, P the pressure, μ the viscosity, and $\underline{f}$ is the volume force, typically the force due to gravity, although if can also be used to compensate for forces due to for example a magnetically active fluid. Solution of these equations is usually performed by numerical methods although analytical solutions may be available for particular simple cases.[2] Occasionally it is possible to use experimental methods, e.g. particle tracer methods, to determine the fluid velocity profile.[3]

1.2 Scanning Electrochemical Microscopy (SECM)

Scanning electrochemical microscopy (SECM; the same acronym is used to describe the instrument) has developed into a powerful technique for quantitative investigations of interfacial physicochemical processes, in a wide variety of areas, as considered in several recent reviews.[4-13] In the simplest terms, SECM involves the use of a mobile ultramicroelectrode (UME) probe, either amperometric or potentiometric, to investigate the activity and/or topography of an interface on a localized scale, typically resolution is on a micron length scale.

Several modes of SECM have been developed to allow the local chemical properties of interfaces to be investigated. A comprehensive review of all of the techniques can be found in Bard and Mirkin.[14] Figure 1.3 demonstrates the wide ranging information that can be extracted from the current of an amperometric UME, used as the probe in SECM. The arrows represent the flux of a redox active species (or ion in the special case of a micro-ITIES (interface between two immiscible electrolyte solutions) probe).

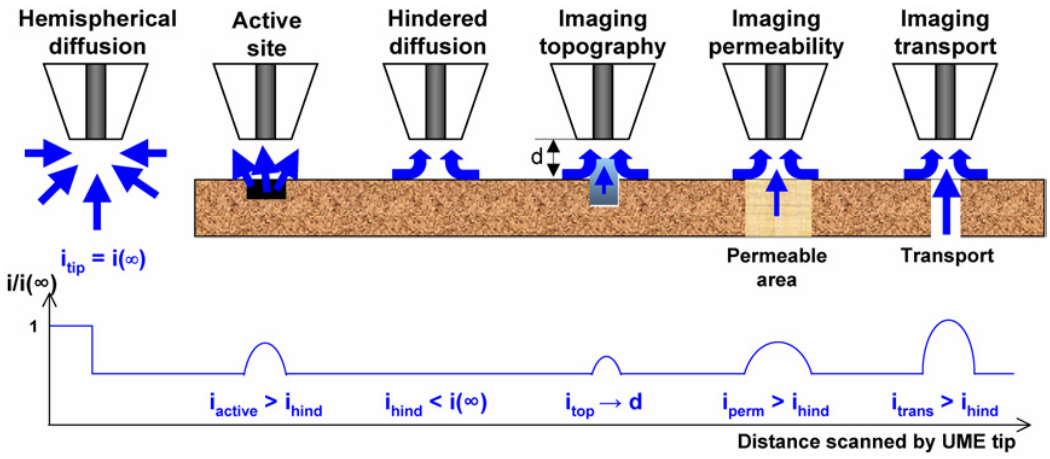

Figure 1.3: Schematic of the varied modes of application of SECM (top) and the current response observed in each (bottom), as normalised by the current far from the surface i(∞).

1.2.1 Instrumentation

The basic elements of a typical SECM setup are outlined in Figure 1.4 and will be introduced in more detail in the following sections.

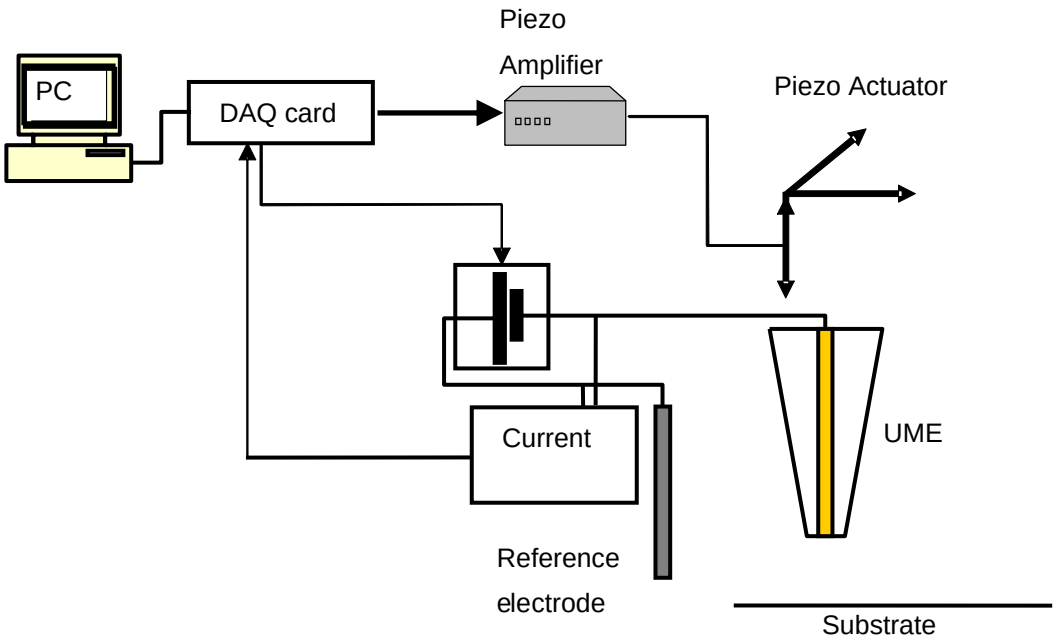

Figure 1.4 Schematic of a typical SECM rig

1.2.1.1 Ultra microelectrodes (UMEs)

The type of probe electrode used in SECM depends on the particular process under investigation. A diversity of probes is available for amperometry and

potentiometry. These are often have to be prepared in house the most common type and the one used throughout this work is the micron-sized disc-shaped electrodes sealed in glass, which is covered in detail below. In depth reviews of UME design, fabrication and characterization can be found in Zoski[15] and Forster[16].

Micron-sized disc-shaped electrodes sealed in glass

Typically, amperometry involves electrolysis at a solid UME, usually a disc-shaped electrode, with a diameter of 0.6 - 25 μm. This type of electrode is readily fabricated by sealing a wire of the material of interest, in a glass capillary, making an electrical connection and polishing the end flat; see Figure 1.5 for illustrations of such an electrode.[17-19] Pt, Au and C electrodes have been successfully fabricated in this way. For most SECM studies, the ratio of the diameter of the tip (electrode plus surrounding insulator, $2r_s$) to that of the electrode itself, 2a, RG = r_s/a is typically around 10. This minimizes effects from back diffusion (from behind the probe), making the electrode response more sensitive to the surface process.

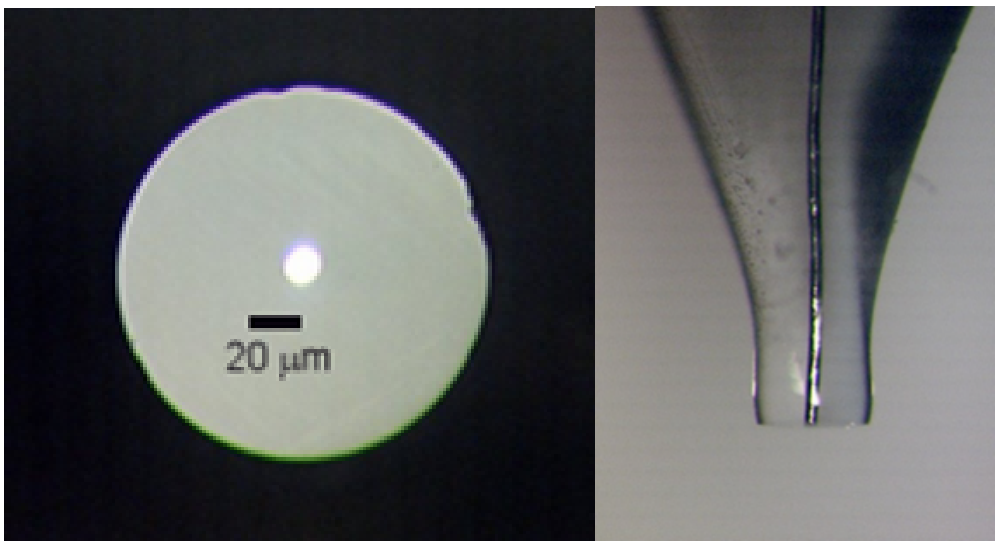

Figure 1.5: End on (left) and side on (right) views of a disk UME.

SECM images may be convoluted with both activity and topographical contributions. To resolve such effects, it may be possible to scan the sample twice, with the mediator of interest and then with a moiety that is inert with respect to the sample, so mapping the topography.[20, 21] Dual amperometric probes

with one channel serving as a topographic sensor and the other to determine activity have also been crafted.[22] Such probes have found application for dual potentiometric-amperometric/conductivity sensing.[23] Other solutions to the problem of deconvoluting topographic and activity components of an image can be found in section 1.2.3.

1.2.1.2 Positioning

The tip is attached to positioners, which allow it to be moved and positioned relative to the interface under investigation. A variety of positioners have been employed in SECM instruments, with the choice depending on the type of measurement and spatial resolution required. For the highest (nanometre) resolution, piezoelectric positioners similar to those used in scanning tunnelling microscopy (STM) are mandatory.[24] There has also been some use of stepper motors to control the position of the tip in the *x*-*y* plane,[25-27] parallel to the interface of interest.

In the application of SECM at solid/liquid interfaces, high resolution *x*, *y*, *z* positioning and scanning is usually required. However, many SECM measurements *e.g*. at air/liquid interfaces, simply involve the translation of a tip towards and/or away from a specific spot on an interface, in the perpendicular (*z*) direction. In this situation, it is only necessary to have high resolution *z*-control of the tip, typically using a piezoelectric positioner, while manual stages suffice for the other two axes.[28, 29] It has further been shown that SECM measurements can be made with manual stages on all axes, with the *z*-axes driven by a differential micrometer and the *x*-*y* stages controlled by fine adjustment screws. This simple cost-effective set-up allows tip approach measurements to be made with a spatial resolution of ±0.25 μm.[30, 31] The use of a video microscope, aligned such that the electrode may be observed from the side, has proved useful in facilitating the positioning of the UME probe relative to the interface of interest.[28, 29]

1.2.1.3 Current measuring equipment

For amperometric control of the tip, with externally unbiased interfaces, a simple two-electrode system suffices (Figure 1.4). A potential is applied to the tip, with

respect to a suitable reference electrode, to drive the process of interest at the tip and the corresponding current that flows is typically amplified by a current to voltage converter. If the sample is also to be biased externally, a bipotentiostat is required. For some studies of membrane transport, ion flow is driven from a donor to receptor compartment galvanostatically, and a potentiostatically controlled tip serves as a detector [32]. Potentiometric detection with UMEs of various types is readily accomplished [23, 33], typically using a voltage follower with an input impedance appropriate to the type of indicator electrode used.

1.2.2 Modes of operation

1.2.2.1 Negative Feedback

Many applications of SECM involve using the tip to locally perturb an interfacial process, by electrolysis or ion transfer, and determining the kinetic effect from the resulting tip current. In this situation, the tip is usually held at a potential to drive the detection of a target analyte (present in bulk solution) at a diffusion-limited rate (no electrode kinetic limitations to the current). The baseline response for these measurements, when the interface is inert with respect to the tip-detected species, is termed "negative feedback"[18, 34] and it is useful to consider this, by way of introduction to other modes, such as positive feedback (redox activity mapping) and SECM induced transfer (SECMIT)1.2.2.2. When the tip is positioned at a relatively long distance from the target interface, $d > 10\ a$, where d is the tip–interface distance and a is the electrode radius, it behaves as a conventional UME. In this situation, a steady-state current, $i(\infty)$, is rapidly established due to hemispherical diffusion of the target species (Red in Figure 1.6(a)). As the tip is brought close to an interface which is inert with respect to the species involved in the electrode process, diffusion to the UME becomes hindered (Figure 1.6 (b)) and the steady-state current, i, decreases compared to $i(\infty)$. In general, measurements of $i/i(\infty)$ as a function of d are termed "approach curves".

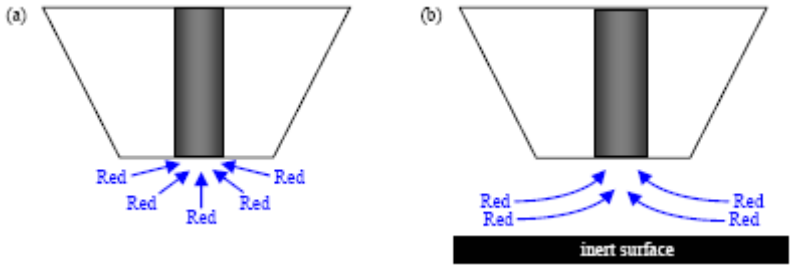

Figure 1.6 (a) Schematic of the hemispherical diffusion-field established for the steady-state diffusion-limited oxidation of a bulk solution species, Red, at a disc-shaped UME, giving rise to a current *i*(∞). (b) When the UME is positioned close to an inert target interface, diffusion of Red from the bulk solution to the UME is hindered and the current, *i*, decreases.

Since the dependence of the $i/i(\infty)$ ratio on d and the tip geometry can be calculated theoretically [34], using methodology such as that highlighted in section 1.4, simple current measurements with mediators which do not interact at the interface can be used to provide information on either the tip to sample separation or the topography of the sample of interest. For the latter application, an amperometric UME is typically scanned at a constant height above the target interface (*x*-*y* plane) and the diffusion-limited current for electrolysis of the target species is measured. This, in turn, can be related to the distance between the tip and the interface, from which topographical information is obtained.

When either the solution species of interest (Red in Figure 1.6), or tip electrode reaction product(s), interact with the target interface, the hindered mass transport picture of Figure 1.6 (b) is modified. The effect is manifested in a change in the tip current, which is the basis of using SECM to investigate interfacial reactivity. Under these conditions, independent methods for determining topography of the sample are often useful, see section 1.2.3 for details of such methods.

1.2.2.2 Concept of using an SECM tip to perturb and monitor an interfacial process

There are three main ways in which an amperometric electrode has been used to both induce and monitor interfacial processes. The basic mass transport pictures in Figure 1.7 serve to illustrate these methods, for the general cases where the liquid phase containing the UME is in contact with a second phase, which has

fluid-like transport properties (*e.g*. a second immiscible liquid, biomaterial or gas). Although a redox reaction is considered at the tip, similar experiments may be carried out with ion transfer voltammetric probes. Transport processes in phase 2 can usually be neglected when phase 2 is a solid or a gas (due to the rapidity of gas transport compared to diffusion in liquids).

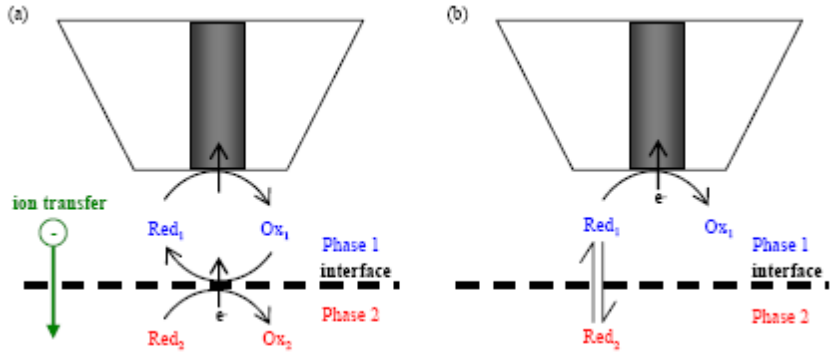

Figure 1.7 Methods for inducing and monitoring interfacial processes with SECM: (a) feedback mode and (b) induced transfer.

Positive feedback mode

The feedback mode, depicted in Figure 1.7 (a) is one of the most widely used SECM techniques, applicable mainly to the study of interfacial redox processes,[18] although feedback based on assisted ion transfer has also been reported.[35, 36] For redox processes, the basic idea is to generate a species at the tip in its oxidized or reduced state (generation of Ox_1 in Figure 1.7 (a)), typically at a diffusion-controlled rate, by electrolysis of the other half of a redox couple (Red_1). The tip-generated species diffuses from the UME to the target interface. If it undergoes a redox reaction at the interface, which converts it to the original form, the mediator diffuses back to the tip, thereby establishing a feedback cycle and enhancing the current at the UME. The redox reaction could occur at a fixed site on the interface, as in the case of immobilized oxidoreductase enzymes.[37-39] Alternatively, the reaction could require the diffusion of a partner species in phase 2 to the interface (Red_2 in Figure 1.7(a)), as in the case of electron transfer at immiscible liquid/liquid interfaces.

Permeability mapping - SECM induced transfer (SECMIT)

This technique, depicted schematically in Figure 1.7 (b), can be used to characterize reversible phase transfer processes at a wide variety of interfaces.[29] The basic idea is to perturb the process, initially at equilibrium, through local amperometry at the UME located in one of the phases, close to the interface with the second phase.[29, 40] A potential is applied to the tip, sufficient to deplete the species of interest in phase 1 (oxidation of Red_1 to Ox_1 in Figure 1.7 (b)), which drives the transfer of species Red from phase 2 to phase 1. This enhances the current, compared to the situation where there is no net transfer across the target interface and species Red reaches the tip only by hindered diffusion through phase 1. For a given tip–interface separation, the overall current response is governed by diffusion in the two phases and the interfacial kinetics.[29] This technique has mainly been used in conjunction with metal tips,[29] but ion transfer voltammetric probes can also be used.[40] SECMIT offers the advantage of non-invasive measurement of quantities in the second phase. It has proved particularly powerful in investigations of solute transfer across interfaces formed between biological tissues and a bathing solution[20, 21, 41] where contact of UME with the sample itself might otherwise damage the sample or lead to contamination of the electrode surface. When there are no kinetic limitations to the interfacial transfer process, SECMIT is also an effective analytical technique for determining the permeability, concentration and diffusive properties of a solute in a target phase.[29]

SECMIT has been used successfully to measure the diffusion coefficient of oxygen in pig laryngeal cartilage. Figure 1.8 shows a typical steady-state approach curve for the diffusion-limited reduction of oxygen at a 25 μm diameter Pt disk electrode approaching a thin slice of cartilage in aerated aqueous electrolyte. Close to the interface, the measured currents are higher than predicted for an inert surface, since the electrolysis process promotes the transfer of oxygen from the cartilage matrix to the aqueous solution, enhancing the flux at the UME. Through these measurements, the space-averaged diffusion coefficient of oxygen in cartilage was estimated to be ca. 50% of that in aqueous solution.[41] It has also been established that the interterritorial regions, i.e. the areas between cells in the surface of the cartilage presented to the UME, provided the most facile transport pathways.[41]

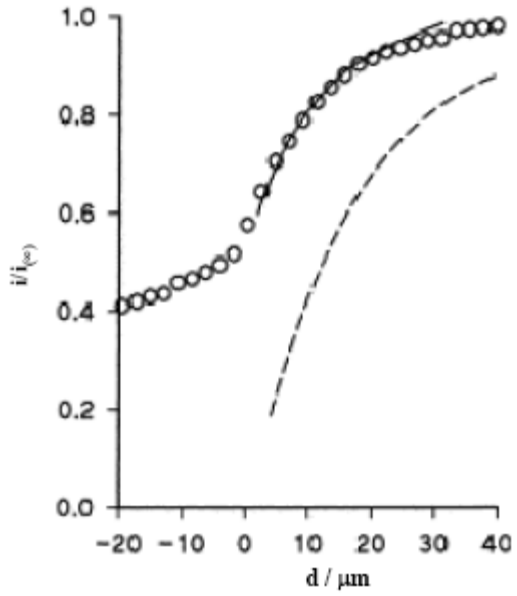

Figure 1.8 Approach curve of normalized steady-state current versus probe/interface separation for the diffusion-controlled reduction of oxygen at an UME scanned towards a sample of laryngeal cartilage (O). The dashed line shows the theoretical response for an inert interface (hindered diffusion only of oxygen in the aqueous phase containing the UME), while the solid line shows the behaviour for induced transfer with the oxygen diffusion coefficient having a value of 50 % of that in aqueous solution. The partition coefficient for oxygen between the aqueous and cartilage phases was considered to be unity. (Reproduced with permission from Barker *et al* (1999) Copyright 1999 Elsevier.)

1.2.3 Activity/Topography Deconvolution

As mentioned in section 1.2.1.2, in SECM the tip usually needs to be positioned close to an interface with high precision. Accurate positioning is achieved by attaching the tip to piezoelectric translators, but this still leaves the problem of determining the separation of the tip and the surface. Although one can use the amperometric response of the tip electrode in some instances (usually when the surface of interest is inert,[20, 21] for many systems it may be difficult to add a redox-active species to solution, without affecting the process of interest. Consequently, much effort has been given to the development of alternate procedures for tip positioning and distance determination, which are briefly considered in this section.

1.2.3.1 Shear force modulation

Control of the tip-substrate separation can be achieved by 'dithering' the electrode, via a small oscillation in the *x*-*y* plane. As the electrode is brought close to a surface the oscillation is damped, to a degree which depends on the tip-substrate separation.[42] Images are usually acquired at constant damping amplitude, which corresponds to a constant distance between the tip and substrate; thus the tip follows the surface contours. The oscillation amplitude is mainly monitored in one of two ways, either: (i) using a laser which is focused at the end of the tip electrode, with the signal detected by a split photodiode;[42, 43] or (ii) by monitoring the vibration amplitude of a tuning fork attached to the electrode.[44, 45] The method of feedback described was originally used in near-field scanning optical microscopy (NSOM).[46]

With this experimental arrangement, it is possible to replace conventional SECM probes with an open glass capillary, opening up the possibility of filling the capillary with a myriad of 'chemical cocktails'. For example, in one study[43] a glass capillary was filled with a biocatalyst, which could be released and detected at an underlying Pt electrode. Since the topographical resolution of this type of approach is determined by the diameter of the overall probe, the use of submicron, needle-like UMEs, is essential for high resolution electrochemical and topographical imaging,[47] where their low mass to allows sufficient amplitude of oscillation.

1.2.3.2 Tip position modulation

Tip position modulation SECM refers to an operation where an amperometric tip is oscillated in a sinusoidal motion perpendicular to the surface (typical amplitude 10% of the tip radius). The resulting current varies with the frequency of the driving oscillation.[48] The amplitude and phase of the oscillating current enable one to deconvolute the activity and topography of the surface.[49] The phase of the current is the same as the phase of the tip/surface separation when the probe is oscillated above an inert surface, whereas they are entirely out of phase above a conducting surface (in positive feedback mode). It is expected that the amplitude of the oscillating current, for small amplitudes of oscillation, should be proportional to the derivative of the steady-state current, measured while the tip

is held at the midpoint of its oscillation; equivalently, it is expected to be proportional to the derivative of the current-distance approach curve, again evaluated at the midpoint of the oscillation. This has been shown to be a good approximation for an active substrate (positive feedback mode), however, some deviations from this are seen when the UME is allowed to approach an insulating surface.[48] Furthermore, as the frequency of the current oscillation is known, low frequency background noise (e.g. drift) is filtered out, meaning the signal is robust. A lock-in amplifier is generally used to acquire the amplitude and phase of the oscillating current. TPM is the subject of chapter 5.

1.2.3.3 SECM-AFM

A recent development in scanning probe design has been the combination of atomic force microscopy (AFM) with SECM. AFM maps the topography of a substrate with nanometre vertical resolution, by monitoring the interaction force between the sample and a sharp tip, that is attached to the end of a force sensing cantilever.[50-52] By integrating an electrode into the AFM probe design it is possible to obtain both electrochemical and topographical information, thus enabling structure-activity related problems to be addressed at high spatial resolution. The size of the electrode is of paramount importance and this should be in the micron or sub-micron range (spatial resolution of the electrochemical response scales with electrode dimension). Alternatively, one can use the electrode component of an SECM-AFM probe to induce a topographical change, such as the dissolution or growth of a surface,[53-55] which can then be tracked through the AFM component of the instrument.

SECM-AFM has been used to image diffusion at microscale electrodes and transport through pores in membranes;[56] several further studies have shown the approach suitable for single microscale and nanoscale pores.[57, 58]

Figure 1.9 shows examples of SECM-AFM data. In (a) one can see the topography of an array of microelectrodes, while (b) shows the corresponding current map, which clearly indicates that one electrode is essentially inactive. These data were obtained with a microfabricated probe.[59] In (c) a simple hand-made probe was used to image a synthetic membrane and (d) shows the corresponding current map. The combination of AFM and SECM in this case

allows one to accurately characterize the topography of the pores and thus present a more thorough analysis of the transport phenomena which can be deduced from the magnitude of the current response.[58] Thus far, SECM-AFM has only been applied to synthetic membranes, but there is no inherent reason for this restriction and biological applications should follow, with the more ready availability of probes.

SECM-AFM has also been used to simultaneously map enzyme activity, as seen in section 1.2.2.2, and topography. Glucose oxidase (GOD) activity has been mapped, both while supported in a soft polymer matrix, electrodeposited on a micropatterned substrate,[60] and through a synthetic membrane.[61] The technique has also been used to image immobilised horseradish peroxidase.[62]

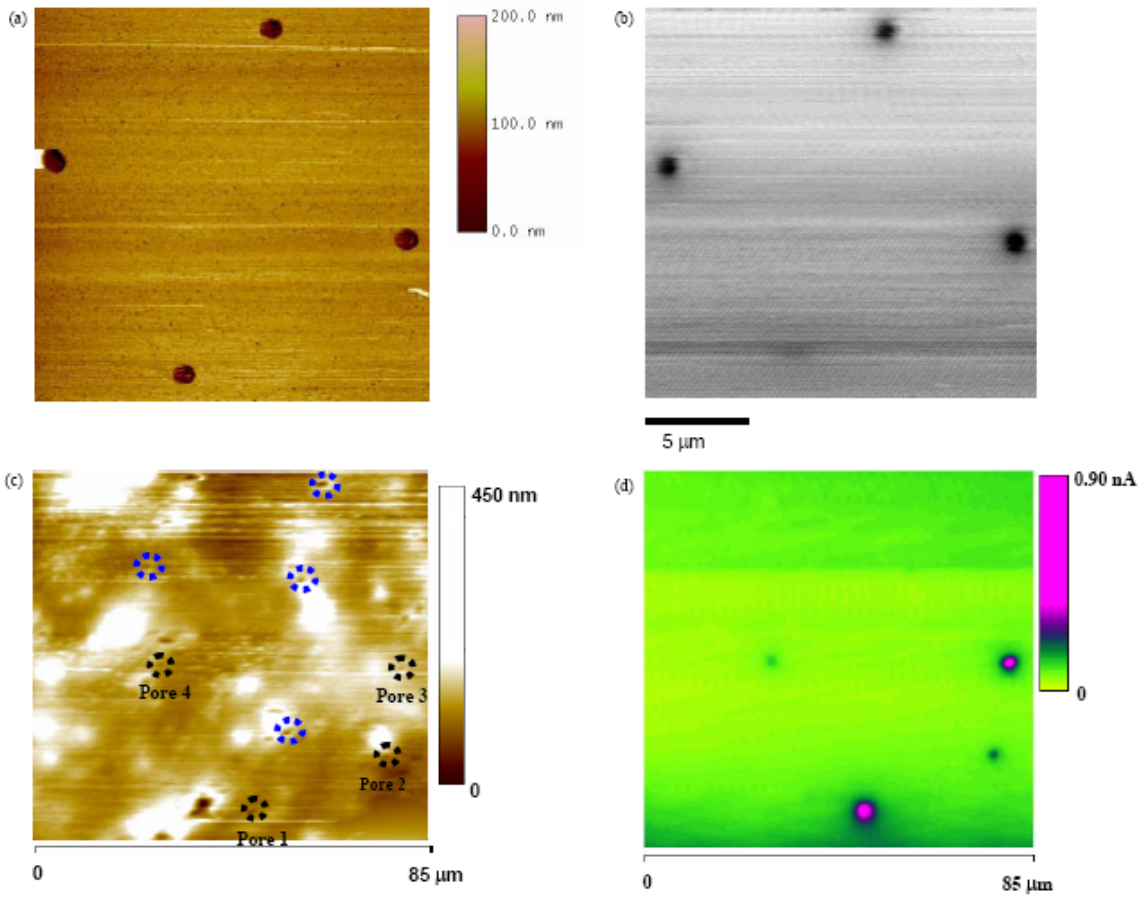

Figure 1.9 (a) Topography and (b) unfiltered fixed-height current maps for the diffusion-controlled tip detection of $Ru(NH_3)_6^{2+}$, generated from the diffusion-limited reduction of $Ru(NH_3)_6^{3+}$ at an array of 1-µm-diameter substrate electrodes. SECM–AFM topography (c) and fixed-height current images (d), illustrating the structure and transport activity of a synthetic membrane. The SECM–AFM probe, placed in the receptor phase, was biased at a potential sufficient to detect $Fe(CN)_6^{4-}$ at a transport-controlled rate. The blue circles in (c)

highlight some of the potential candidates for open pores (not all are ringed). The black circles show the pores which are active to transport. Reprinted with permission from Dobson *et* al (2005) (a & b) Copyright 2005 ACS, and Gardner *et al* (2005) (c & d) Copyright 2005 Elsevier.

SECM-AFM also has the potential to perturb interfacial systems through electrochemistry, while simultaneously imaging topography. This methodology has been applied to crystal dissolution studies.[54]

1.2.3.4 Dual Mediator

One can perform experiments with two mediators, one active, one inert, with respect to the activity being probed on the surface. This allows one to gain purely topographical information on an initial scan with the inert mediator. A subsequent scan uses the topography extracted from the first to keep the probe a constant distance from the surface. As the distance from the surface is known calculations of activity are possible. This approach has been used to probe permeability of methyl viologen and oxygen in cartilage.[21, 63]

1.2.3.5 Impedance

Alpuche-Aviles and Wipf demonstrated that one can determine the tip-surface separation through the measurement of electrical impedance.[64] Impedance is calculated through measuring the response to a low amplitude high frequency AC voltage superimposed upon a much large DC component. Through judicious design of circuitry the two components can be separated, allowing one to use the impedance component as a measure of tip-surface separation. A more complete investigation was performed by Gabrielli et al.[65] Feedback based upon impedance has been shown success in biological situations.[66, 67]

1.3 Scanning Ion Conductance Microscopy (SICM)

Scanning ion conductance microscopy (SICM),[68] like SECM, is a member of the scanned probe microscopy family of instruments. It is also operated through measuring the current flowing between two electrodes under solution. The difference between the two techniques lies in the form of the tip electrode, which

is contained within an electrolyte filled micro- or nanopipette in SICM compared to a UME in SECM. The nature of the current flowing in SICM is a migrative current limited by ion flow through the pipette aperture this compares to the typically diffusive, and sometimes convective, flux in SECM. As with SECM there is a dependence of current on tip-substrate separation, which has allowed SICM to be used successfully as an imaging tool. Typically the mediator of the ionic flux is electrochemically inert and the images produced are of a topographical nature only.

1.3.1 Instrumentation

As alluded to previously, there are great similarities between SICM and SECM, these similarities extend to the instrumentation used in experimentation. Positioning and measurement of current occur as in SECM and outlined in section 1.2.1.

1.3.1.1 Pipettes

Micro- or nanopipettes are fabricated by heating and pulling of glass or quartz capillaries. This is typically done in a controlled manner by using a programmable laser puller where the heating time, pull force and duration are amongst the adjustable parameters. A well designed program should allow for the reproducible pulling of matched pairs of pipettes.

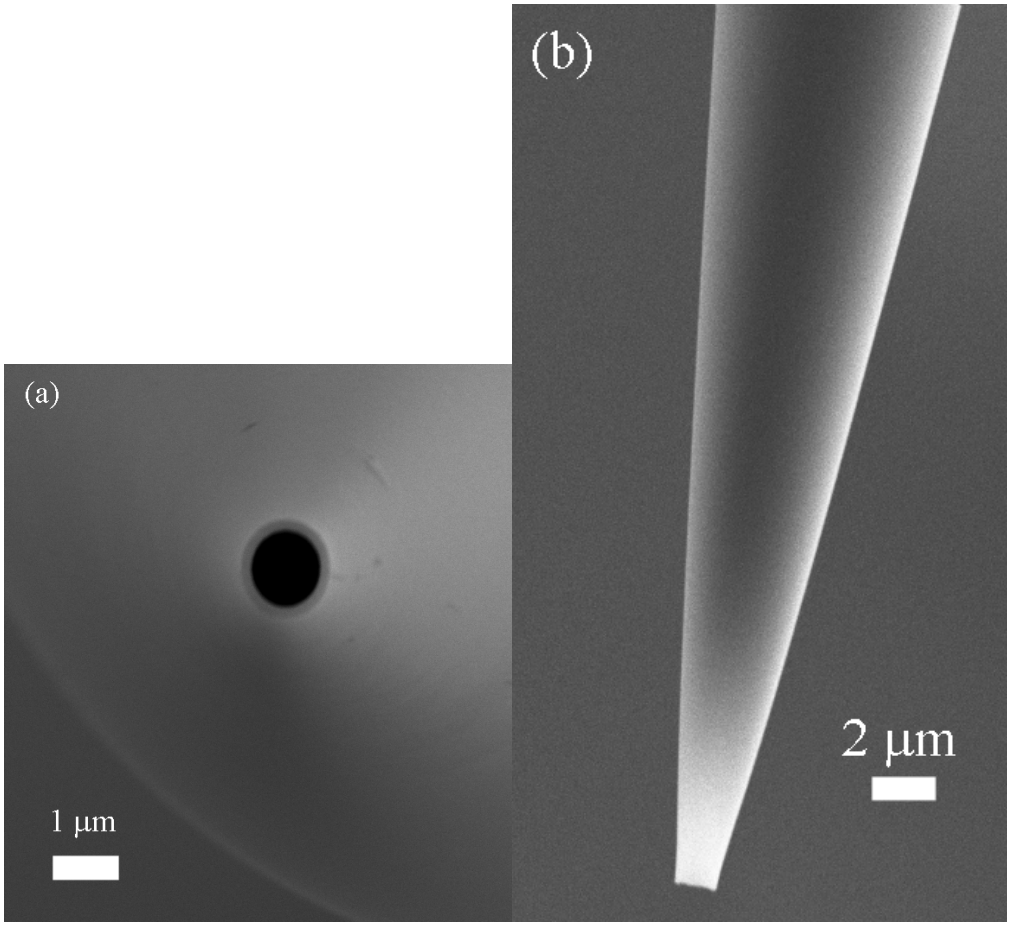

Figure 1.10: Electron micrographs of a typical pipette used for SICM imaging. a) end on view, b) side on view.

1.3.2 Previous systems studied

SICM is predominantly operated in a distance modulated mode,[69] whereby the tip is oscillated sinusoidally in a direction normal to the surface being imaged. The current, which is sensitive to the tip-sample separation, oscillates, also in a sinusoidal manner. The magnitude of these sinusoidal oscillations is highly sensitive to the tip-sample separation, increasing dramatically as the surface in approached; this is in contrast to the slight decrease in current one sees when the tip is approached to the surface. The distance modulated mode of operation has offered dramatic improvements both to stability - imaging has been demonstrated over a period of 24 hours[70] - and also to the responsiveness of the feedback, of which the most dramatic example is arguably the imaging of a beating cardiac myocyte.[69]

Most of the systems studied with SICM have been of a biological nature, this is due to the advantages the technique offers in this area over many of the other available techniques. SICM allows non-contact imaging under biologically relevant conditions, thus allowing the observation of dynamic processes without perturbing the soft samples. In addition, SICM offers resolution superior to optical microscopy,[69] the major other non-perturbative imaging technique.

SICM has also been combined with other techniques to the benefit of both techniques. Combining SICM with patch-clamp apparatus in so called "smart patch-clamp" methodology has allowed the measuring ion channel current.[71, 72] Improvements offered to patch-clamping are: improved success in clamping ion channels, and less variation between operators.[73] Additionally, the combined technique also offers superior spatial resolution of ion channel locations, allowing spatial heterogeneity of ion channels to be demonstrated.[71]

SICM has been combined with scanning near-field optical microscopy (SNOM), a method which allows light microscopy to get below the Rayleigh criterion by scanning a light source in very close constant proximity to the surface, typically a few 10 nm separation (for review of SNOM see Richards[74]). In the combined method the pipette has been used as a light source either through inclusion of an optic fibre into an aluminium coated pipette[75] or through the generation of a fluorescent complex at the tip through the reaction or the internal and external pipette solutions[76], the SICM feedback is used to maintain a constant distance of the light from the source from the substrate; the light is collected through optical microscopy usually of the confocal form.[77]

SICM has also been combined with confocal microscopy to look at virus-like particles of circa 100 nm diameter associating with a membrane. The SICM is used for high resolution imaging of the particles with the confocal offering complementary fluorescence imaging to confirm the identity of the particles imaged.[78]

SICM has also been demonstrated as a method of substrate patterning, where the pipette is used for the delivery of amongst other things biomolecules[79, 80] and metals.[81] The deposition is controlled by the applied potential.

SICM is the subject of chapter 3.

1.4 Modelling

The interpretation of electrochemical experimental results typically requires the formulation of a model of the process being investigated. The model is informed by knowledge of the physicochemical process of interest and experimental data. Experimentally, typically only current or potential is measured (as a function of probe position and sometimes time); from these measurements one seeks to determine transport phenomena, reaction kinetics, or some other physicochemical process taking place in the system under study. The careful design of experiments and formulation of underlying models is thus imperative. In this section we briefly highlight methods commonly used for modelling electrochemical systems.

While some simple setups are amenable to an analytical solution, frequently via Laplace transforms, many experiments with complex geometries and many coupled phenomena may only be addressed by numerical simulation. As the latter is the case within this work it is upon this that the following section concentrates.

Many of the recent numerical approaches for solving the differential equations describing mass transport in microelectrode problems mirror those used in engineering to treat fluid flow[82] and heat transfer[83], namely finite element methods (FEMs)[84, 85] or finite difference methods (FDMs)[86]. In the application of these approaches to electrochemical problems, the continuous diffusion field (concentration as a function of space and time) is described in terms of discrete values at prescribed locations, e.g. at the nodes of a grid dissecting the diffusion field.

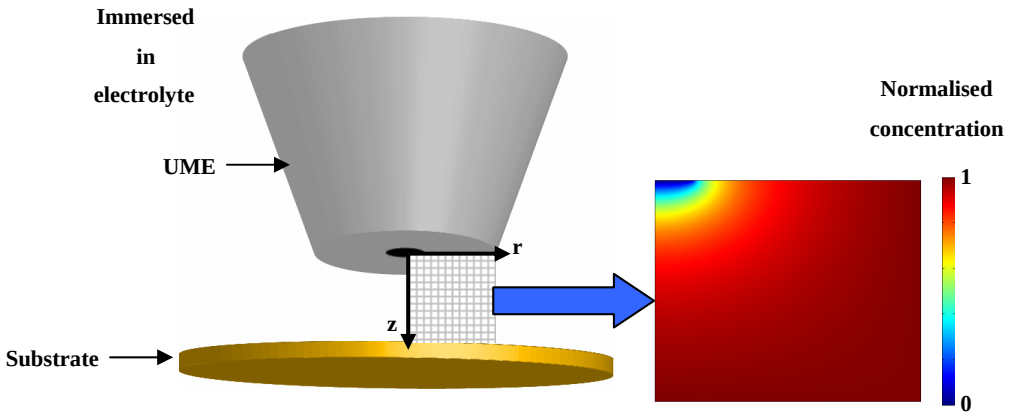

Figure 1.11: Two-dimensional reduction of a typical problem

The first treatment of mass transfer in the SECM geometry used the FEM to calculate the steady-state tip current response and concentration profile, for an UME operating in the SECM feedback mode positioned close to an infinite, planar, conducting or inert substrate.[34]

The alternating direction implicit finite-difference method, ADIFDM, has also been employed extensively as an efficient digital simulation technique for solving two-dimensional time-dependent problems (2-dimensional reduction of a problem is illustrated in Figure 1.11). This was first used to simulate the SECM feedback response for the case where the tip-generated species undergoes homogeneous chemical reaction in solution.[87] The method was subsequently employed to model the SECM feedback mode with heterogeneous kinetics for infinite and arbitrary-sized substrates.[88] Since these initial applications, ADIFDM has been used to model a variety of kinetic situations for several different SECM modes, incorporating heterogeneous[37, 55, 89-93] or homogeneous[94-96] kinetics.

The effect on the SECM chronoamperometric response of allowing the two redox forms of a couple to have arbitrary diffusion coefficients has been assessed through model calculations using the ADIFDM, for the positive feedback[30] and generation/collection[31] modes and for the reverse transient behaviour of SECM double potential step chronoamperometry (DPSC)) measurements in bulk solution.[97]

A comprehensive theoretical treatment of SECM induced transfer (SECMIT) occurring between two phases is offered in Barker *et al*.[29] The parameter space characterized by: the partition coefficient of the solute, K_e, the relative diffusion coefficients of the solute in the two phases, γ, and the interfacial transfer kinetics has been explored using the ADIFDM to simulate chronoamperometric responses of a UME.

The ADIFDM has also been used to treat lateral proton diffusion studied by either SECMIT[98] or a novel proton feedback method.[99, 100] These latter models take into account the potential-dependent association/dissociation constant of the interfacial acid groups, illustrating that SECM is sensitive to rather complex interfacial processes. A triple-potential step method has been used to study the diffusion of redox-active amphiphiles in Langmuir monolayers at the water/air interface, and this has also been simulated using the ADIFDM approach in Zhang *et al*.[101]

The recent trend in SECM modelling has been towards the use of proprietary software packages, such as Comsol Multiphysics (previously Femlab; Comsol Ab, Sweden). Packages of this type provide several advantages over the direct implementation of numerical algorithms. Primarily, one is able to develop a model more rapidly, taking advantage of complex algorithms, which have been efficiently programmed. Graphical user interfaces (GUIs) have facilitated the input and modelling of complicated experimental geometries with relative ease, e.g. SECM-AFM probes.[59, 102] Within the GUI, results of simulations are effectively visualized. Also useful is the coupling of several equation systems covering different physical phenomena,[103] e.g. hydrodynamics[104], kinetics[105] and lateral charge propagation.[106]

1.5 Outline

The chapters contained within this thesis are arranged as self-contained works; as such they introduce topics afresh. Following on from the introduction, chapter 2 introduces the principal components of the instrumentation built, which was used throughout the rest of the work. The following chapters each introduce experimental scenarios and theoretical techniques designed to interpret the data that arise. The first three of these represent major contributions to the

development or enhancement of important SEPMs. Chapter 3 concerns scanning ion conductance microscopy (SICM) and investigates the parameters which affect imaging resolution, an issue which has not been addressed appropriately before. Chapter 4 demonstrates the use of scanning electrochemical microscopy (SECM) for assessing the rate of growth of silver particles at a liquid/liquid interface. Chapter 5 looks at developing the tip position modulation (TPM) mode of SECM. A quantitative model is introduced, which incorporates convective mass-transport, and an experimental assessment of the technqiue is made. Chapters 6 and 7 introduce and develop two novel methodologies for assessing the electron transfer activity of heterogeneous electrodes, and focus particularly on highly oriented pyrolytic graphite (HOPG) as a substrate. Chapter 6 introduces a new scanned probe technique, the scanning microcapillary contact method (SMCM), which uses an electrolyte-containing capillary, only touching the substrate electrode with its meniscus, as the probe. In chapter 7 the methodology used involves applying a thin film on the electrode material that slows down diffusion. Variabilities that would be averaged out by diffusional overlap on typical voltammetric timescales in standard media are accessible. It is shown that recent high profile work which proposes that HOPG is inactive requires correction. Chapter 8 provides some conclusions of the work undertaken.

References

(1) Fisher, A. C. *Electrode Dynamics*; Oxford University Press, 1996.
(2) Bard, A. J.; Faulkner, L. R. *Electrochemical Methods: fundamentals and applications*, 1st ed.; Wiley, 1980.
(3) Taylor, J. A.; Yeung, E. S. *Anal. Chem.* **1993**, *65*, 2928--2932.
(4) Barker, A. L.; Gonsalves, M.; Macpherson, J. V.; Slevin, C. J.; Unwin, P. R. *Anal. Chim. Acta* **1999**, *385*, 223-240.
(5) Mirkin, M. V. *Mikrochimica Acta* **1999**, *130*, 127-153.
(6) Mirkin, M. V.; Horrocks, B. R. *Anal. Chim. Acta* **2000**, *406*, 119-146.
(7) Amemiya, S.; Ding, Z. F.; Zhou, J. F.; Bard., A. J. *J. Electroanal. Chem.* **2000**, *483*, 7.
(8) Yasukawa, T.; Kaya, T.; Matsue, T. *Electroanalysis* **2000**, *12*, 653-659.
(9) Gyurcsányia, R. E.; Jágerszkia, G.; Kiss, G.; Tóth, K. *Bioelectrochem.* **2004**, *63*, 207-215.
(10) Pu, G.; Longo, M. L.; Borden, M. A. *J. Am. Chem. Soc.* **2005**, *127*, 6524-6525.
(11) Barker, A. L.; Slevin, C. J.; Unwin, P. R.; Zhang, J. In *Liquid Interfaces in Chemical, Biological, Pharmaceutical Applications*; Volkov, A. G., Ed.; Marcel Dekker: New York, 2001, pp 325-354.
(12) Edwards, M. A.; Martin, S.; Whitworth, A. L.; Macpherson, J. V.; Unwin, P. R. *Physiological Measurement* **2006**, *27*, R63-R108.
(13) Wittstock, G.; Burchardt, M.; Pust, Sascha E.; Shen, Y.; Zhao, C. *Angewandte Chemie International Edition* **2007**, *46*, 1584-1617.
(14) In *Scanning Electrochemical Microscopy*; Bard, A. J., Mirkin, M. V., Eds.; Marcel Dekker: New York, 2001, pp 1-16.
(15) Zoski, C. G. *Electroanalysis* **2002**, *14*, 1041-1051.
(16) Forster, R. J. In *Encyclopedia of electrochemistry volume 3: Instrumentation and electroanalytical chemistry*; Bard, A. J., Stratmann, M., Unwin, P. R., Eds.; Wiley, 2003; Vol. 3, pp 160-195.
(17) Wightman, R. M.; Wipf, D. O. In *Electroanalytical Chemistry, Vol. 15*; Bard, A. J., Ed.; Marcel Dekker: New York, 1989, pp 267-353.
(18) Bard, A. J.; Fan, F.-R. F.; Kwak, J.; Lev, O. *Anal. Chem.* **1989**, *61*, 132-138.
(19) Bard, A. J.; Fan, F.-R. F.; Mirkin, M. V. In *Electroanalytical Chemistry, Vol. 18*; Bard, A. J., Ed.; Marcel Dekker: New York, 1993, pp 243-373.
(20) Gonsalves, M.; Barker, A. L.; Macpherson, J. V.; Unwin, P. R.; O'Hare, D.; Winlove, C. P. *Biophys. J.* **2000**, *78*, 1578-1588.
(21) Gonsalves, M.; Macpherson, J. V.; O'Hare, D.; Winlove, C. P.; Unwin, P. R. *Biochim. Biophys. Acta.* **2000**, *1524*, 66-74.
(22) Yasukawa, T.; Kaya, T.; Matsue, T. *Anal Chem* **1999**, *71*, 4637-4641.
(23) Wei, C.; Bard, A. J.; Nagy, G.; Toth, K. *Anal. Chem.* **1995**, *67*, 1346-1356.
(24) Liu, H. Y.; Fan, F.-R. F.; Lin, C. W.; Bard., A. J. *J. Am. Chem. Soc.* **1986**, *108*, 3838-3839.

(25) Kranz, C.; Ludwig, M.; Gaub, H. E.; Schuhmann, W. *Adv. Mater.* **1995**, *7*, 568-571.
(26) Kranz, C.; Ludwig, M.; Gaub, H. E.; Schuhmann, W. *Adv. Mater.* **1995**, *7*, 38-40.
(27) Hliva, P.; Kapui, I.; Nagy, G.; Czako, L. *Magyar Kemiai Folyoirat* **1998**, *104*, 224-231.
(28) Slevin, C. J.; Umbers, J. A.; Atherton, J. H.; Unwin., P. R. *J. Chem. Soc. Faraday Trans.* **1996**, *92*, 5177-5180.
(29) Barker, A. L.; Macpherson, J. V.; Slevin, C. J.; Unwin, P. R. *J. Phys. Chem. B* **1998**, *102*, 1586-1598.
(30) Martin, R. D.; Unwin, P. R. *J. Electroanal. Chem.* **1997**, *439*, 123-136.
(31) Martin, R. D.; Unwin, P. R. *Anal. Chem.* **1998**, *70*, 276-284.
(32) Bath, B. D.; White, H. S.; Scott, E. R. In *Scanning Electrochemical Microscopy*; Bard, A. J., Mirkin, M. V., Eds.; Marcel Dekker: New York, 2001, pp 343-395.
(33) Amman, D. *Ion-Selective Microelectrodes: Principles, Design, Application*; Springer: Berlin, 1986.
(34) Kwak, J.; Bard, A. J. *Anal. Chem.* **1989**, *61*, 1221-1227.
(35) Shao, Y.; Mirkin, M. V. *J. Electroanal. Chem.* **1997**, *439*, 137-143.
(36) Shao, Y.; Mirkin, M. V. *J. Phys. Chem. B* **1998**, *102*, 9915-9921.
(37) Pierce, D. T.; Unwin, P. R.; Bard, A. J. *Anal Chem* **1992**, *64*, 1795-1804.
(38) Pierce, D. T.; Bard, A. J. *Anal. Chem.* **1993**, *65*, 3598-3604.
(39) Kranz, C.; Wittstock, G.; Wohlschläger, H.; Schuhmann., W. *Electrochim. Acta* **1997**, *42*, 3105-3111.
(40) Evans, N. J.; Gonsalves, M.; Gray, N. J.; Barker, A. L.; Macpherson, J. V.; Unwin., P. R. *Electrochem. Commun.* **2000**, *2*, 201-206.
(41) Macpherson, J. V.; O'Hare, D.; Unwin, P. R.; Winlove, C. P. *Biophys. J.* **1997**, *73*, 2771-2781.
(42) Ludwig, M.; Kranz, C.; Schuhmann, W.; Gaub, H. E. *Rev. Sci. Instrum.* **1995**, *66*, 2857-2860.
(43) Hengstenberg, A.; Kranz, C.; Schuhmann, W. *Chem. Eur. J.* **2000**, *6*, 1547-1554.
(44) James, P.; Casillas, N.; Smyrl, W. H. *Proceedings - Electrochemical Society* **1996**, *95*, 425-434.
(45) Buchler, M.; Kelley, S. C.; Smyrl, W. H. *Electrochemical and Solid-State Letters* **2000**, *3*, 35-38.
(46) Betzig, E.; Finn, P. L.; Weiner, J. S. *Applied Physics Letters* **1992**, *60*, 2484.
(47) Ballesteros-Katemann, B.; Schuhmann, W. *Electroanalysis* **2002**, *14*, 22-28.
(48) Wipf, D. O.; Bard, A. J. *Anal. Chem.* **1992**, *64*, 1362-1367.
(49) Wipf, D. O.; Bard, A. J. *Anal. Chem.* **1993**, *65*, 1373-1377.
(50) Binnig, G.; Quate, C. F.; Gerber, C. *Phys. Rev. Lett.* **1986**, *56*, 930-933.
(51) Rugar, D.; Hansma, P. K. *Phys. Today* **1990**, *43*, 23-30.
(52) Wiesendanger, R. *Scanning Probe Microscopy, Spectroscopy*; Cambridge University Press: Cambridge, UK, 1994.
(53) Jones, C. E.; Macpherson, J. V.; Unwin, P. R. *J. Phys. Chem. B* **2000**, *104*, 2351-2359.
(54) Jones, C. E.; Unwin, P. R.; Macpherson, J. V. *ChemPhysChem* **2003**, *4*, 139-146.

(55) Macpherson, J. V.; Unwin, P. R. *J. Phys. Chem.* **1996**, *100*, 19475-19483.
(56) Macpherson, J. V.; Unwin, P. R. *Anal. Chem.* **2000**, *72*, 276-285.
(57) Macpherson, J. V.; Jones, C. E.; Barker, A. L.; Unwin, P. R. *Anal Chem* **2002**, *74*, 1841-1848.
(58) Gardner, C. E.; Unwin, P. R.; Macpherson, J. V. *Electrochemistry Communications* **2005**, *7*, 612-618.
(59) Dobson, P. S.; Weaver, J. M. R.; Holder, M. N.; Unwin, P. R.; Macpherson, J. V. *Anal Chem* **2005**, *77*, 424-434.
(60) Keung, A.; Kranz, C.; Lugstein, A.; Bertagnolli, E.; Mizaikoff, B. *Angew. Chem. Int. Ed.* **2003**, *42*, 3238-3240.
(61) Kueng, A.; Kranz, C.; Lugstein, A.; Bertagnolli, E.; Mizaikoff, B. *Angewandte Chemie International Edition* **2005**, *44*, 3419-3422.
(62) Kranz, C.; Kueng, A.; Lugstein, A.; Bertagnolli, E.; Mizaikoff, B. *Ultramicroscopy* **2004**, *100*, 127-134.
(63) Macpherson, J. V.; O'Hare, D.; Unwin, P. R.; Winlove, C. P. *Biophys. J.* **1997**, *73*, 2771.
(64) Alpuche-Aviles, M. A.; Wipf, D. O. *Anal Chem* **2001**, *73*, 4873-4881.
(65) Gabrielli, C.; Huet, F.; Keddam, M.; Rousseau, P.; Vivier, V. *J. Phys. Chem. B* **2004**, *108*, 11620-11626.
(66) Osbourn, D. M.; Sanger, R. H.; Smith, P. J. S. *Anal Chem* **2005**, *77*, 6999-7004.
(67) Kurulugama, R. T.; Wipf, D. O.; Takacs, S. A.; Pongmayteegul, S.; Garris, P. A.; Baur, J. E. *Anal Chem* **2005**, *77*, 1111-1117.
(68) Hansma, P. K.; Drake, B.; Marti, O.; Gould, S. A. C.; Prater, C. B. *Science* **1989**, *243*, 641-643.
(69) Shevchuk, A. I.; Gorelik, J.; Harding, S. E.; Lab, M. J.; Klenerman, D.; Korchev, Y. E. *Biophys. J.* **2001**, *81*, 1759-1764.
(70) Gorelik, J.; Zhang, Y.; Shevchuk, A. I.; Frolenkov, G. I.; Sánchez, D.; Lab, M. J.; Vodyanoy, I.; Edwards, C. R. W.; Klenerman, D.; Korchev, Y. E. *Molecular and Cellular Endocrinology* **2004**, *217*, 101-108.
(71) Korchev, Y. E.; Negulyaev, Y. A.; Edwards, C. R. W.; Vodyanoy, I.; Lab, M. J. *Nat Cell Biol* **2000**, *2*, 616-619.
(72) Gorelik, J.; Gu, Y.; Spohr, H. A.; Shevchuk, A. I.; Lab, M. J.; Harding, S. E.; Edwards, C. R. W.; Whitaker, M.; Moss, G. W. J.; Benton, D. C. H.; Sanchez, D.; Darszon, A.; Vodyanoy, I.; Klenerman, D.; Korchev, Y. E. *Biophys. J.* **2002**, *83*, 3296-3303.
(73) Gu, Y.; Gorelik, J.; Spohr, H. A.; Shevchuk, A.; Lab, M. J.; Harding, S. E.; Vodyanoy, I.; Klenerman, D.; Korchev, Y. E. *FASEB J.* **2002**, 01-1024fje.
(74) Richards, D. *Philosophical Transactions of the Royal Society of London, Series A: Mathematical, Physical and Engineering Sciences* **2003**, *361*, 2843-2857.
(75) Korchev, Y. E.; Raval, M.; Lab, M. J.; Gorelik, J.; Edwards, C. R. W.; Rayment, T.; Klenerman, D. *Biophys. J.* **2000**, *78*, 2675-2679.
(76) Rothery, A. M.; Gorelik, J.; Bruckbauer, A.; Yu, W.; Korchev, Y. E.; Klenerman, D. *Journal of Microscopy* **2003**, *209*, 94-101.
(77) Gorelik, J.; Shevchuk, A.; Ramalho, M.; Elliott, M.; Lei, C.; Higgins, C. F.; Lab, M. J.; Klenerman, D.; Krauzewicz, N.; Korchev, Y. *Proceedings of the National Academy of Sciences* **2002**, *99*, 16018-16023.

(78) Shevchuk, A. I.; Hobson, P.; Lab, M. J.; Klenerman, D.; Krauzewicz, N.; Korchev, Y. E. *Biophys. J.* **2008**, *94*, 4089-4094.
(79) Bruckbauer, A.; Zhou, D.; Ying, L.; Korchev, Y. E.; Abell, C.; Klenerman, D. *J. Am. Chem. Soc.* **2003**, *125*, 9834-9839.
(80) Bruckbauer, A.; Ying, L.; Rothery, A. M.; Zhou, D.; Shevchuk, A. I.; Abell, C.; Korchev, Y. E.; Klenerman, D. *J. Am. Chem. Soc.* **2002**, *124*, 8810-8811.
(81) Zhang, H.; Wu, L.; Huang, F. *Journal of Vacuum Science and Technology B* **1999**, *17*, 269-272.
(82) Johnson, R. W., Ed. *The Handbook of Fluid Dynamics*; CRC Press: Boca Raton, 1998.
(83) Hewitt, G. F.; Shires, G. L.; Polezhaev, Y. V., Eds. *International Encyclopedia of Heat and Mass Transfer*; CRC Press: Boca Raton, 1997.
(84) Huebner, K. J.; Thornton, E. A. *The Finite Element Method for Engineers, 2nd edn.*; Wiley-Interscience: New York, 1982.
(85) Rao, S. S. *The Finite Element Method in Engineering*; Pergamagon Press: New York, 1982.
(86) Feldberg, S. In *Electrochemistry*; Mathson, J. S., Jr, H. B. M., Jr, H. C. M., Eds.; Marcel Dekker: New York, 1972; Vol. 2, pp 185-215.
(87) Unwin, P. R.; Bard, A. J. *J. Phys. Chem.* **1991**, *95*, 7814-7824.
(88) Bard, A. J.; Mirkin, M. V.; Unwin, P. R.; Wipf, D. O. *J. Phys. Chem.* **1992**, *96*, 1861-1868.
(89) Unwin, P. R.; Bard, A. J. *J. Phys. Chem.* **1992**, *96*, 5035-5045.
(90) Macpherson, J. V.; Unwin, P. R. *J. Phys. Chem.* **1994**, *98*, 1704-1713.
(91) Macpherson, J. V.; Unwin, P. R. *J. Phys. Chem.* **1995**, *99*, 3338-3351.
(92) Macpherson, J. V.; Unwin, P. R. *J. Phys. Chem.* **1995**, *99*, 14824-14831.
(93) Slevin, C. J.; Macpherson, J. V.; Unwin, P. R. *J. Phys. Chem. B* **1997**, *101*, 10851-10859.
(94) Zhou, F.; Unwin, P. R.; Bard, A. J. *J. Phys. Chem.* **1992**, *96*, 4917-4924.
(95) Demaille, C.; Unwin, P. R.; Bard, A. J. *J. Phys. Chem.* **1996**, *100*, 14137-14143.
(96) Martin, R. D.; Unwin, P. R. *J. Chem. Faraday Trans.* **1998**, *94*, 753-759.
(97) Macpherson, J. V.; Unwin, P. R. *Anal. Chem.* **1997**, *69*, 2063-2069.
(98) Slevin, C. J.; Unwin., P. R. *J. Am. Chem. Soc.* **2000**, *122*, 2597-2602.
(99) Zhang, J.; Unwin, P. R. *Phys. Chem. Chem. Phys.* **2002**, *4*, 3814-3819.
(100) Zhang, J.; Unwin, P. R. *J. Am. Chem. Soc.* **2002**, *124*, 2379-2383.
(101) Zhang, J.; Slevin, C. J.; Morton, C.; Scott, P.; Walton, D. J.; Unwin, P. R. *J. Phys. Chem. B* **2001**, *105*, 11120-11130.
(102) Holder, M. N.; Gardner, C. E.; Macpherson, J. V.; Unwin, P. R. *Journal of Electroanalytical Chemistry* **2005**, *585*, 8-18.
(103) Liljeroth, P.; Johans, C.; Slevin, C. J.; Quinn, B. M.; Kontturi, K. *Anal Chem* **2002**, *74*, 1972-1978.
(104) Carlsson, S.; Liljeroth, P.; Kontturi, K. *Anal Chem* **2005**, *77*, 6895-6901.
(105) Burt, D. P.; Cervera, J.; Mandler, D.; Macpherson, J. V.; Manzanares, J. A.; Unwin, P. R. *Phys. Chem. Chem. Phys.* **2005**, *7*, 2955-2964.
(106) O'Mullane, A. P.; Macpherson, J. V.; Unwin, P. R.; Cervera-Montesinos, J.; Manzanares, J. A.; Frehill, F.; Vos, J. G. *J. Phys. Chem. B* **2004**, *108*, 7219-7227.

Chapter 2: Building the instrument

Several scanned probe microscopes have been built throughout the course of this PhD. They are built from similar basic components: An electrochemical probe and cell arrangement; hardware for current amplification and conversion to voltage; components for positioning the probe; and a computer with appropriate software and hardware to communicate with the electrochemical cell and positioners, and also to record and analyse the resulting signals. This chapter outlines each of these components and the options used for each of them. The instruments are essentially modular and most combinations of components are possible.

2.1 Hardware

2.1.1 Data Acquisition

Data acquisition hardware typically converts analogue signals to digital signals, which can be interpreted by the computer, to do so hardware called an analogue to digital converter (ADC) is used. To control an external system it is sometimes required to generate an analogue signal, this is done through a digital to analogue converter (DAC). These two functions may be combined in to one piece of hardware or may be separate. This sort of data acquisition (DAQ) card tends to be easy to interface with software via simple commands, where the typical parameters are which channels to use, which frequency to acquire/generate at, and how many points to acquire/what data to generate.

A common and important issue with data acquisition tasks is synchronisation and timing. It is often important that one knows the exact time that a particular stimulus was applied in order to appropriately analyse the resulting signal. Synchronisation of multiple tasks (e.g. generating a potential step and recording

the current) is possible, up to the resolution of clock on the DAQ card. This is achieved through first setting up all but one of the tasks as a triggered (slave) task, next the remaining (master) task is set up and the output of its clock wired as the trigger(s) of the other task(s). This wiring is sometimes a software task or may involve physical wiring of the hardware. As the master task is started its clock begins to deliver a digital wave consisting of pulses, this triggers the slave tasks to begin executing, thus achieving synchronisation.

The flexible data acquisition has been achieved through the use of field programmable gate array (FPGA) based DAQ cards. These cards consist of many logic gates that can, through the use of appropriate software, be connected up in numerous ways. They can execute logical operations as a computer equipped with software would, but at a far higher rate and with a guaranteed execution time per loop. Typical uses of such reconfigurable hardware include prototyping and fast feedback loops. The programs on the card have direct access to the ADCs and DACs. The FPGA DAQ card is essentially a separate small computer, to communicate with the main PC it is necessary to explicitly dictate which data gets passed to the main computer and use low level communication protocols to transfer it. Advantages of such hardware include the possibility to pre-process the acquired signal prior to passing it to the main computer, thus removing some of the load both in terms of data processing and also data transfer. One may also perform complex timing and synchronisation tasks. Disadvantages include increased complexity in programming; relatively long compile times, as the programs must be converted to a pattern of logic gates; a reduced command/feature set as compared to PC based programming.

2.1.2 Analogue Electronics

2.1.2.1 Current Measurement

Current measurement involves the amplification of the small, typically nano/picoamp, current flowing followed by the conversion of the current to a voltage. For a typical two electrode setup this has been achieved in two ways. Either via a home built current to voltage amplifier which is called a “current follower” or, for low current measurement, a commercial device Chem-Clamp

(Dagan Corp., MN), which achieves low current amplification through the inclusion a high resistance (100 MΩ) head-stage, positioned close to the electrochemical setup.

Where a three electrodes setup is to be used, or a substrate must be biased it is necessary to use a (bi)potentiostat. This uses circuitry to pass the current between a counter electrode (CE) and the working electrode(s) (WE) while maintaining a desired potential between the reference electrode (RE) and the WE(s). To this end a commercial (bi)potentiostat (C730C, CH Instruments, Texas) is used. The current is output by the instrument as a voltage and can be recorded via a DAQ device. This device does restrict one to constant potential techniques as it is not possible to externally decide the applied potential, however this is not an inherent weakness of potentiostats just a technology issue with this model.

2.1.2.2 Oscillation electronics

For techniques where the tip is to be oscillated sinusoidally, e.g. scanning ion conductance microscopy (SICM)(see chapter 3) and tip position modulation scanning electrochemical microscopy (TPM-SECM) (see chapter 5), two additional pieces of analogue hardware are used. The first is a sine wave generator, which generates a sine wave at a chosen frequency and amplitude. This was checked to make sure it was ‘pure’, i.e. contained no other harmonics. The second piece of hardware is termed a signal adder. This takes two analogue signals and sums them. In our case the signals would be the voltage relating to the piezo height and the oscillating (reference) signal. The sum response would thus be a sine wave with a specific offset. The signal adder was built with a bypass option, where only the signal relating to the piezo height was transmitted. This removed the need to switch cables when changing between oscillating/non-oscillating techniques. The frequency transmission of the adder was checked and found to only suffer drop-off with frequencies exceeding 1000 Hz, as can be seen in Figure 2-1, so we can assume no attenuation takes place in the range we work in.

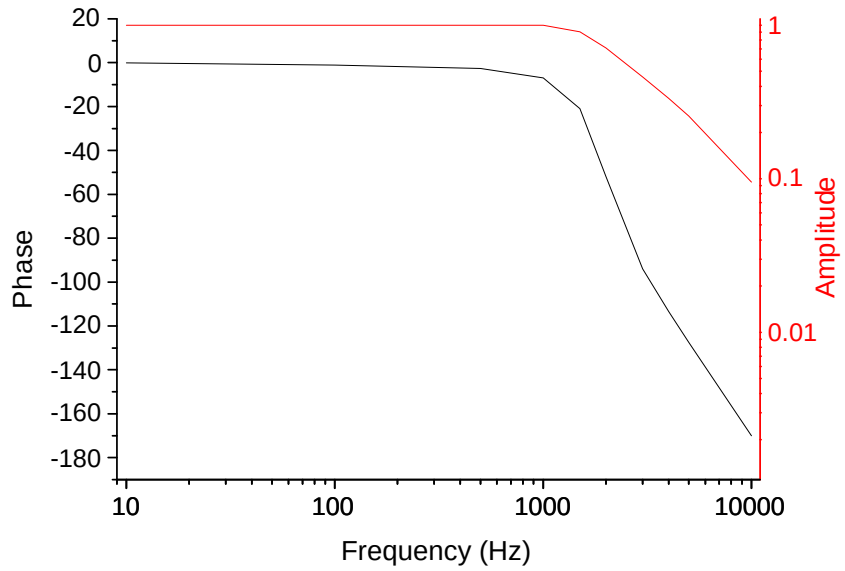

Figure 2-1. Plot demonstrating the amplitude and phase response of the signal adder as a function of frequency.

In principal all the above features may be implemented in software and would remove the need for any additional hardware.

2.1.2.3 Dual Solid State Switch

The instrument is equipped with a digitally controlled dual solid state switch. This allows the electrodes to be left at open circuit when desired. Additionally this allows the use of a choice of two separate reference electrodes. These were typically geometrically separated and thus differences in current measured indicated differences in the paths between the selected reference electrode and the working electrode.

2.1.3 Actuation

2.1.3.1 Piezos

As mentioned in section 1.2.1.2, piezoelectric actuators (piezos) are used for the finest positioning available. These are materials which change their expansion in a continuous manner with applied voltage. As applications require scanning the probe in a plane while adjusting the height the piezos were orthogonally mounted in groups of three. The ranges of the piezos in the rigs built are from 38 to 400

microns. Piezos tend to display some hysteresis, to account for this we use a sensor attached to the piezos to measure the actual displacement. The sensors used have been of two forms; a strain gauge sensor, where the resistance change measured from extending a strain gauge is converted to a distance based upon a calibration; or a capacitative sensor, where the capacitance of two plates is converted to a distance, again based upon calibration. In both cases the calibration is performed by the manufacturer and is based upon interferometry. The piezos may be operated in closed loop mode, where a feedback loop (see section 2.2.6.1) is used, which monitors the sensors and adjusts the applied voltage to maintain the requested position, or open loop mode, where no such loop is used and the voltage applied is directly related to the voltage commanded. The time-constant of the closed loop mode of operation means that for higher frequency work it is often necessary to use a piezo in open loop mode, however it is still possible to monitor the position information measured by the sensors.

An amplifier unit is used to generate the high voltage required to move the piezos. Two forms were used; an external unit, which receives signals via an external command voltage, returning the position information through voltage outputs, and an internal card in the PC where all communication is achieved via the computer interface and a set of supplied command modules.

It is necessary to be able to move the probe over a greater range than can be offered by the piezos. This may be in order to position the probe over an interesting point on a sample, or to move the probe away from the sample, in a controlled way, without damaging either the probe or the sample. Positioning over a greater range than possible with piezos, but with a lower resolution, can be achieved in a couple of ways.

2.1.3.2 Micropositioners

Micropositioners consist of a set of three orthogonally mounted linear stages equipped with differential micrometers. The micrometers are adjustable by hand. Reproducibility and accuracy are down to the Vernier scale, typically 0.5 μm.

2.1.3.3 DC motors

As an alternative to micrometers, systems have also been built where the long range movement is achieved through DC motors (Physik Instrumente M122). These are equipped with an optical encoder to provide a closed loop positioning system. These are controlled through a PC board which can be driven by commands. DC motors are considerably more expensive that micropositioners, but offer improved functionality, arising in part from the fact that they can be programmatically controlled.

2.1.4 Probes

There are two types of electrochemical probe that have been used in this work: ultramicroelectrodes (UMEs) of the disc in plane geometry, as introduced in section 1.2.1.1, were produced through sealing a thin metal wires in a pipette and polishing (a more detailed procedure has been reported elsewhere[1]). Micropipette tips were prepared through pulling a borosilicate glass capillary (1.2 mm outer diameter, 0.69 mm inner diameter) on a laser puller (Sutter, model P-2000, CA). Parameters that were varied to alter the geometry are: temperature, heating pattern, velocity at which to stop heating, delay between heating and pulling and pull force. Pipettes were then prepared through backfilling with electrolyte solution using either a micropipette equipped with either a microfil (World Precision Instruments, FL) or Microloader pipette tip (Eppendorf, U.K.) and then inserting a (quasi-)reference electrode.

2.1.5 Camera

A camera (PixeLink PL-B776U, Edmund Optics) equipped with high magnification lens (Infinistix, 44 mm WD2X, Edmund Optics) and light source attached to the computer allows accurate positioning of the tip when traditional electrochemical based positioning techniques (e.g. negative feedback, section 1.2.2.1) are not available, scanning microcapillary contact method (SMCM) (Chapter 6). .

2.1.6 Cells

A variety of cells were used throughout the work. The aim of all cells was to secure the sample perpendicularly to the tip while allowing it to be bathed in

electrolyte solution. When using a camera the cell was designed to facilitate imaging, through the inclusion of a planar glass viewing window.

2.2 Software

All software has been written in National Instruments LabVIEW (versions 7.1/8.0/8.2), this is a modular based system. The modules are called virtual instruments (VIs), this reflects the fact that the package is built with instrument control in mind. Every VI consists of a front panel, where the user can interact with the module, and a back panel where the underlying code is written in a graphical form. The interfaces on the front panel are designed to mirror the sort of controls one would find on an instrument, for example, dials, sliders, buttons, etc. for input and gauges, graphs, numerical displays, etc. for output. The major components of the system are introduced below. The lower level VIs are introduced first as they are used by those subsequently introduced.

2.2.1 Basic SubVIs

2.2.1.1 DAQ Input/Output VIs

As the software is to be used on a number of computers with slightly different DAQ hardware, it was prudent to package the DAQ components in self contained modules, with their content tailored to the particular hardware installed on the individual machine. In this way, changing hardware would only require a single change, rather than excessive changes in every location where DAQ takes occurs in the software. As well as being simpler, it is also a more robust method, as it is not possible to by accident forget to change one of the occasions when DAQ is performed. The basic DAQ modules are: output a single voltage, output a voltage waveform (number of voltage points at a set frequency), acquire samples (one or multiple channels) and synchronous acquisition/output functions (as outlined in 2.1.1).

2.2.1.2 Piezo move

As mentioned previously section 2.1.3.1, the movement of piezos was either controlled via a PC card or an external amplifier. In the former case the

manufacturer provided control VIs, this was then a case of embedding these in subVIs and calling the initiation protocols at the appropriate times. With externally controlled piezos, it was first necessary to encode the calibration curves for applied voltage/extension. In open loop mode the calibration curves were taken to be the average of the expansion and retraction curves reported by the manufacturers, no effort was made to compensate for hysteresis/memory effects. In closed loop mode the calibration curves are trivial linear functions. Upon being called the VI generated a linear ramp between the voltages equating to the starting and finishing extensions.

2.2.1.3 Lock-in

A lock-in amplifier is a piece of equipment able to obtain the periodic component of a measured signal at a particular frequency against a large background noise. The frequency of detection is given by a reference signal, a sinusoidal wave, which is the same signal used to generate the oscillation in the measured signal. This allows the lock-in amplifier to act as an exceptionally narrow bandpass filter and also offers robustness to frequency drift.

The mathematics underpinning the lock-in amplifier arise from a few trigonometric relations. The basic operation involves taking the product of the reference and measured signals and evaluating the long term average of this product. The orthogonality relations for sinusoidal functions dictate that the mean of the product of two sinusoidal waves of different frequencies will tend to zero; from this relation robustness to background noise is born.

We denote the reference signal as $v_{\text{ref}} = \sin(\omega T)$, where $\omega = 2\pi f$ is the angular frequency and its quarter phase shifted version as $v'_{\text{ref}} = \cos(\omega T)$. If the measured signal is denoted $v_{\text{meas}} = B\sin(\omega T + \phi)$ then we have the following products:

$$v_{\text{ref}} \cdot v_{\text{meas}} = \sin(\omega T) \times B\sin(\omega T + \phi) = \frac{1}{2} B\big(\cos(\phi) - \cos(\phi + 2\omega T)\big) \tag{2.1}$$

$$v'_{\text{ref}} \cdot v_{\text{meas}} = \cos(\omega T) \times B\sin(\omega T + \phi) = \frac{1}{2} B\big(\sin(2\omega T + \phi) - \sin(-\phi)\big) \tag{2.2}$$

From inspecting the right hand sides it is clear that one averages the product over a sufficiently long time the results will tend to:

$$\bar{x} = \tfrac{1}{2} B \cos(\phi) \tag{2.3}$$

and

$$\overline{x'} = \tfrac{1}{2} B \sin(\phi) \tag{2.4}$$

for (2.1) and (2.2) respectively. Using this it is possible to calculate the phase and amplitude of the measured signal.

For our application, the frequency (equivalently period) of the reference signal was known, thus the inputs to the lock-in amplifier VI were the period of the reference frequency, the signal (either current of piezo position), the sampling frequency of this signal and the order of the harmonic to find. Calculation of phase was implemented in two different ways, both involving phase shifting the reference frequency and gave similar results, knowing the reference period (or frequency) meant it was possible to regenerate the reference signal, or any higher harmonic of it, at any phase shift with minimum effort. In both methods of phase detection the signal was initially limited to the largest integer number of cycles in the sampling window to avoid any aliasing effects.

The first method for calculating phase and amplitude involved choosing the phase shift which maximised the mean of the product (2.1); maximising occurs when $\cos(\varphi)$ is 1, that is when φ is integer multiple of 2π, which is equivalent of the two signals being in phase.

The second method for calculating phase and amplitude involved solving the simultaneous equations (2.3) and (2.4). Doing so we arrive at:

$$\begin{aligned} B &= 2\sqrt{\bar{x}^2 + \overline{x'}^2} \\ \phi &= \arccos\left(\frac{\bar{x}}{\sqrt{\bar{x}^2 + \overline{x'}^2}} \right) \end{aligned} \tag{2.5}$$

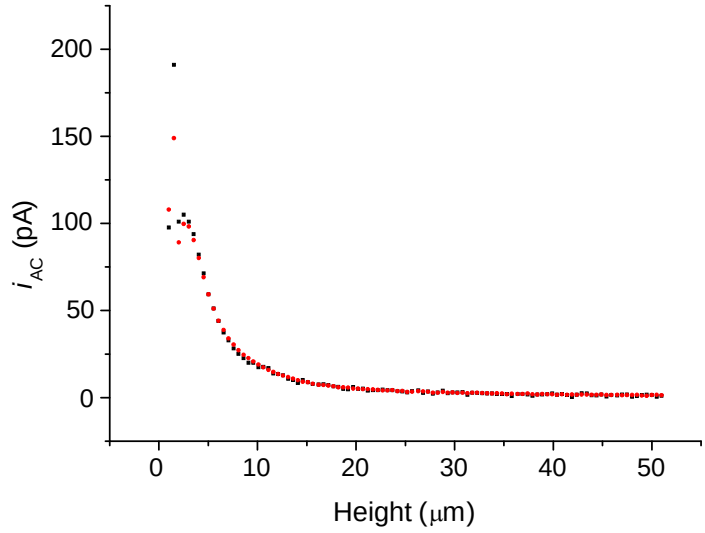

Figure 2-2. Oscillating component of the current, i_{AC}, as an ultramicroelectrode was approached towards an insulating surface while it was oscillated in a direction perpendicular to the surface. Red points, i_{AC} calculated using hardware lock-in amplifier (Stanford Research, SR810); black points, i_{AC} calculated using software lock-in amplifier.

As shown in Figure 2-2 the software lock-in gave an identical measure of amplitude to a hardware lock-in amplifier (Stanford Research, SR810).

2.2.2 Voltammetric Control Techniques

Voltammetry refers to electrochemical techniques where the current is recorded as the potential is varied. Two such techniques that have been implemented are detailed below. In these, and all subsequent techniques, the data acquisition settings, i.e. the frequency of acquisition; the amplifier gain; the channel to acquire data on, are all user-defined options and shall not be mentioned specifically. Additionally, an optional pause is available at the start of every technique to allow the system to equilibrate before the start of the measurements.

2.2.2.1 Cyclic/Linear Sweep Voltammetry (CV/LSV)

CV and LSV are basic electrochemical techniques used to characterise a system. The potential is changed as a linear function of time, the gradient (V/s) is known as the sweep rate. In LSV a single linear sweep between two points is performed. In CV, as the name suggests, the potential is cycled between limiting potentials

starting from an initial potential. The potential is generated as a waveform of potentials, each with a small change from the previous potential, with the generation frequency chosen to match the scan rate. This means that there is essentially a series of potential steps taking place. However, if the generation frequency is high and the step size small, relative to the acquisition frequency and the potential range, then the effect of this is negligible. The acquisition is typically over-sampled and then averaged to give better signal to noise ratio; the original signal is viewable on request which can help in diagnosis of noise sources. Through synchronisation of the data acquisition and potential generation it is possible to deduce the potential applied at any time.

2.2.3 Potential Step

A commonly used electrochemical technique is the potential step. The current response is recorded as the potential is stepped from one potential to another. On some occasions a number of potential steps are couple together in e.g. double potential step chronoamperometry (DPSC) or triple potential step chronoamperometry (TPSC). As a discrete, discontinuous voltage event occurs it is exceptionally important to coordinate the potential application with the data acquisition. The program allows an indefinite number of segments whose duration and potential are defined. Additionally the state of a computer controlled lamp may be defined, which allows the investigation of photo-electrochemical species (not included in this work).

2.2.4 Approach Techniques

In scanned probe techniques the measured quantity, current in our case, varies with the separation of the tip and the interface being approach, as well as being dependent on as several other factors. The following techniques make use of the piezo actuators to investigate this response or to adapt to it.

2.2.4.1 Z-approach (with stop)

The most commonly used technique for investigating the distance modulated signal is the z-approach, the probe is moved in the direction normal to the surface (z), while the current is monitored. This has been implemented in a step-wise fashion in the software. First a (linearly spaced) number of points between a start

and end height are chosen by the user. The piezo moves the probe to the first height, pauses for a user-defined amount of time, before recording the current. The probe is then moved to the second height, pauses then records, etc.. The function of the pause is to allow equilibration, both chemical and physical.

An additional function that has been defined in the z-approach software is the ability to stop/pause upon a pre-defined current condition, i.e. the (absolute) current being above/below a particular threshold level. The threshold is typically chosen as indicative of a close approach to the surface and can be used to avoid crashing the probe into the sample.

2.2.4.2 Oscillating probe (AC) approach

This technique has many similarities to the z-approach. The difference lies in the fact that the probe is being oscillated during the approach and analysis of the resulting oscillating current signal takes place at each height. The step-wise approach involves the same step-pause-record cycle as outlined above for the z-approach (section 2.2.4.1). The piezos must be operated in open loop in order to respond with suitable rapidity to the oscillating stimulus. The signals recorded are: the oscillating reference signal, the piezo position, and the current. Processing occurs as follows:

- The frequency and amplitude of the reference signal is found using standard LabVIEW module for extracting such information from sine waves
- The mean value of the piezo position and current are calculated
- Lock-in amplification is performed on the piezo signal to return the amplitude and phase of the piezo oscillation
- Lock-in amplification is performed on the current signal (1^{st} and 2^{nd} harmonics)
- The phase difference between the piezo and current signal is calculated

The frequency, amplitude and mean value of the stimulating signal; phase relative to the stimulating signal, amplitude and mean value of the piezo position; mean, phase, first/second harmonic amplitude of the current are all recorded at every point. In addition it is possible to record the individual waveforms for the reference signal, the piezo position, and the current at each individual height if further processing is desired to be performed.

2.2.4.3 Tip loading

This program allows one to safely move a probe towards a surface using a long-range positioning method, e.g. Micropositioners (section 2.1.3.2) or DC motors (section 2.1.3.3), without crashing the probe into the surface. This is particularly important in situations where the probe sample interaction occurs on a very short length scale, e.g. SICM (chapter 3) or small UMEs[2]. The approach is as follows:

With the probe a far distance from the surface the piezo is extended to full expansion. A potential is applied to the probe and a threshold current response set by the user, which is indicative of a surface response. The user then moves the probe towards the surface using the long-range positioning methodology while the current is monitored by the computer. Upon the threshold current being reached the piezo is automatically immediately retracted to minimum expansion and a warning sent to the user to stop approaching. The computer/piezo can respond far more quickly than humanly possible thus massively reducing risk of damage to the probe/sample and also allowing a more rapid approach to be performed. Following the retraction it is expected that the probe is at a distance from the surface approximately equal to the piezo expansion range (the exact value depends on both the distance from the surface that the threshold was defined at and also how quickly the user stopped winding upon retraction).

2.2.5 Scanning Techniques

To build up images with a scanned probe technique the probe must necessarily be scanned in a plane close to the sample. A quantity or quantities are measured at every point on a grid to build up an image. The positioning of the probe may be at a constant height or may be based upon feedback of some parameter. Both options have been implemented and are described below.

2.2.6 Scanning Electrochemical/Ion Conductance Microscope (SECM/SICM)

This software is designed to be as general as possible and therefore is able to record all the signals that the oscillating probe approach (section 2.2.4.2) program records as well as additional channels, from the DAQ card, of data if required.

Each scan commences with the tip being approached to the surface. Typically the approximate location of the surface is known from a z-approach type technique, in this case the user can suggest an initial height for the tip. Possibly following this, or instead of this, a feedback routine *vide infra* is used to place the tip at the desired distance from the surface. If a constant height scan is to be performed the second step will not take place and the initial height moved to will be precisely the scan height.

The probe will be moved in a raster pattern of discrete points; there is an optional pause upon each move to allow equilibration. Each line scanned in the forward and reverse direction before proceeding to the next line. In this way the sample is scanned twice. Discrepancies between the forward and reverse scans over a point may indicate several things, including: change in the sample structure/activity, damage to the tip, drift, or a discrepancy in the tip height due to ineffective feedback routines. Both images may be recorded for further analysis.

2.2.6.1 Feedback

When the user chooses to use feedback it is implemented through a simple discrete proportional-integral (PI) loop, a commonly used control loop methodology. A manipulated variable (MV), in our case the piezo expansion, is adjusted in order to maintain a constant value of the process variable (PV). Initially the user chooses the PV, e.g. average current, first harmonic amplitude; along with a set-point (SP) value at which to maintain this quantity. Next error bounds are set, within which the feedback loop is defined to have achieved its goal: PV≅SP. The two parameters used to tune the feedback loop are k_p for the proportional (P) term and k_i for the integral (I) term. The P term looks at the error e=SP-MV. The I term looks at the history of the error over a user defined number of steps, l. The value of the MV is updated based upon these two values as follows:

$$MV(t+1) = MV(t) + k_p e(t) + k_i \frac{1}{l} \sum_{j=\max(0,t-l)}^{t} e(j) \qquad (2.6)$$

where t=0 is taken to be the first point recorded at a particular xy position. As can be deduced, the choice of sign of the feedback parameters (k_i and k_p) depends

on whether the PV increases or decreases upon approach to the surface. The user should choose the feedback parameters so as to rapidly approach the SP value, but without drastic overshoots or instability, both of which could damage the probe/sample. For convenience the facility to save and load the feedback parameters has been included.

2.2.6.2 Training Mode

To allow the user to familiarise themselves with the system without possible damage to tips, samples or other equipment, a training mode has been implemented. Analytic functions were fitted to the response from an oscillating approach for a couple of different probes and a subVI written that would return a signal based upon these curves but with the addition of noise. Virtual test surfaces were generated such that the responses would be as if the sample was being scanned over a real substrate. While running in training mode none of the mechanical components of the system are moved, but all responses in the user interface match what would happen with a real system.

2.2.6.3 Dual Reference Electrode Scanning

The program has the additional functionality that a line may be scanned twice with two different reference electrodes through using the dual solid state switch (section 2.1.2.3). As mentioned previously this allows one to assess transport properties through a sample. Initially a line is scanned as outlined above; next the reference electrode is changed through a digital signal; an optional pause is executed; and the line is rescanned at the same height as in the previous scan over the line. If feedback was used then the height is the final height from the feedback loop. Using this methodology a total of four images are created (forward and reverse scan with first and second reference electrodes).

2.2.7 Scanning Micropipette Contact Method (SMCM)

The scanned micropipette method (SMCM) is discussed further in chapter 6. Briefly, a electrolyte filled micropipette in air is approached to a surface until the meniscus touches the surface, an electrochemical technique is performed and the pipette retracted and moved to another point, before repeating the cycle. Through

repeating this in a raster pattern a survey of the electrochemistry of the surface is performed.

The software for performing the SMCM combines several of the previously mentioned techniques. The approach to the surface is controlled by the z-approach program with the stopping threshold set by the user to be slightly above the level of background noise; the user-defined step size should be set small enough that the meniscus comes in contact without damaging the pipette. The electrochemical technique upon contact with the surface is selected from one of those mentioned above but in principle could be any technique of choosing.

The main VI for this program has the job of scanning the pipette in a raster, recording the data, and calling the VIs mentioned above. When calling the z-approach the first approach is for the full range requested by the user, subsequent approaches start a user-defined distance from where the surface was previously engaged. This distance is typically much less than the original start distance thus significantly increasing the speed of the scan while maintaining robustness and still allowing the meniscus to be detached from the surface.

References

(1) Bard, A. J.; Fan, F. R. F.; Kwak, J.; Lev, O. *Anal. Chem.* **1989**, *61*, 132-138.
(2) Katemann, B.; Schuhmann, W. *Electroanalysis* **2002**, *14*, 22.

Chapter 3: A realistic model for the current response in scanning ion conductance microscopy (SICM): implications for imaging

3.1 Introduction

Scanning electrochemical probe microscopies (SEPMs) have received much attention for the functional imaging of interfaces.[1-8] SEPMs work by moving a fine electrode probe in close proximity to an interface and, simultaneously, measuring and recording an electrochemical signal while the scan takes place. It is possible to build a 2-dimensional image from this signal, measured as a function of electrochemical probe position in a plane parallel to the interface. The probes for SEPMs may be either a solid ultramicroelectrode (UME) or a micro- or nano-pipette containing a an electrolyte solution and a wire electrode to provide a contact. Scanning electrochemical microscopy (SECM)[1-3, 6, 9] employs both types of probe and usually detects a species of interest via either diffusion-limited amperometry[9] or potentiometry.[10] In contrast, scanning ion conductance microscopy (SICM)[4, 5] measures the conductivity between an electrode inside a micro- or nano-pipette and an electrode placed in bulk solution. The conductivity may also be measured through impedance SECM measurements.[11-13] The measured quantity in SICM and many SECM imaging modes is the current; understanding how the current is affected by the probe geometry and physical situation is important for interpreting the signal in these microscopies. Considerable attention has been given to understanding the current response at the UME in SECM,[14-21] but there has been comparatively little work on

understanding the current response in SICM, even though the technique offers superior spatial resolution.[5, 22]

SICM employs a feedback loop, to maintain a constant distance between the pipette and the surface, so that the displacement of the scanning pipette normal to the sample represents the topography of the surface. The quantity used for feedback may be the (DC) current[4], or more successfully its derivative,[5] which is calculated by measuring the amplitude of the current oscillation (AC current) when the pipette position is modulated perpendicular to the surface. Clearly, understanding how the geometry of the pipette and the topography of the surface affect the current is important for the interpretation and analysis of images.

SICM-type pipettes have also been the basis of other techniques. In hybrid SICM- scanning near field optical microscopy (SNOM),[23] an optical fibre within the pipette is maintained at a constant distance from the surface, providing the light source for SNOM. A pipette filled with fluorescently labelled DNA has been used for nano-writing, using the electric field created near the tip of the pipette to control DNA deposition.[24] A double-barrelled micropipette, with an SICM-channel used as a distance sensor for an ion sensitive microelectrode employed in the second channel,[25] has facilitated scanning ion-selective potentiometric microscopy as a sub-technique of SECM.

Two models are available which describe the current at a micropipette electrode as a function of distance from a planar surface; both represent the physical situation by a number of resistors in series using an idealized pipette geometry.[25, 26] Additionally, Ying and co-workers[27] used the finite element method to investigate the electric field inside a nanopipette in bulk solution. The current at the pipette was not of interest, nor did they consider the effect of a surface in proximity to the tip, because their work concerned the trapping of DNA dielectrophoretically in a nanopipette.[27] The goal of this chapter is to assess the extent to which the models alluded to above are applicable in practice and to develop a more comprehensive model of SICM which lends itself to more realistic probe and substrate geometries.

The approximation of a resistance by a series of resistors, as used in the treatments above, remains true only if the splitting is applied along an equipotential line. The studies in this chapter demonstrate that this rule has not been followed in the previous two models,[25, 26] since the pipette aperture is not an equipotential line. This necessarily leads to inaccuracy in the previous models, and we quantify this. Furthermore, only the simple situation of a pipette above a planar surface has been considered, although Nitz et al. have used this to infer the response over a step.[26] In this chapter, full numerical simulations of the current to a micropipette, in geometries relevant to imaging, are performed. Comparison is made of our results with the currently available models and the result of varying the pipette geometry is explored. Experimental data are then presented to highlight features in that the simulated results that occur in practice.

3.2 Materials and Methods

3.2.1 Probe preparation and characterization

Pairs of near identical (as checked by scanning electron microscopy) micropipettes of internal diameter 1-4 μm were pulled from capillaries of 1.2 mm outer diameter, 0.69 mm inner diameter borosilicate glass (Harvard Apparatus, UK), using a laser puller (Model P-2000, Sutter Instrument Co., Novato, CA) following procedures outlined in the user manual. From each pair of pipettes pulled, one was used to approach a surface, while the other was characterized by a Supra55-VP field emission-scanning electron microscope (Zeiss). Pipettes for imaging were backfilled with a solution of 0.1 M KCl (Fisher Scientific, UK) prepared using Milli-Q reagent grade water (Millipore Corp.). Both internal and external electrodes were chloridised silver wires (Goodfellow Metals, Ltd., Cambridge, UK), of 125 μm diameter and 1 mm diameter, respectively.

3.2.2 Electrochemical measurements

The micropipette was mounted perpendicular to the surface of interest, with coarse positioning using micrometer-driven linear stages (Newport, 461-XYZ-M). Piezoelectric actuators, fitted with strain gauge sensors (Nanocube P-611.3S, Physik Instrumente, Germany), were used for fine positioning. These were controlled by an amplifier/servo (E-664 LVPZT, Physik Instrumente), operated

in open loop mode. This, in turn, was controlled by signals from a digital to analogue converter (DAC) card (Model no. NI-6731, National Instruments). Data was acquired using a data acquisition (DAQ) card (Model No. NI PCI-6143, National Instruments.). Both cards were installed in a PC running LabVIEW 7.1 software (National Instruments). All experimental measurements were made in a Faraday cage. Tip currents were converted to voltages using a home built current to follower prior to data acquisition. The data were acquired through self-written LabVIEW virtual instruments. The pipette was moved to discrete points in a raster pattern. At each step the micropipette was allowed to settle before the current was measured and the DC and AC components extracted. Feedback was implemented through a proportional-integral control loop.

3.2.3 Substrates

The calibration grid was silicon oxide with a "waffle" pattern of 5 μm pits with a 10 μm pitch and 180 nm pit depth, purchased from Digital Instruments. A substrate of 5 μm bands of 0.5 μm height with 20 μm pitch, was fabricated precisely using a mask aligner.

3.2.4 Finite element modelling

Modelling was performed on a Viglen Intel Core 2 Duo 2.4 GHz computer equipped with 4 GB of RAM running Windows XP 64 bit edition. The commercial finite element modelling package Comsol Multiphysics 3.3a (Comsol AB, Sweden), with the Matlab interface (Release 2006b) (The MathWorks, Cambridge, UK) was used for simulations. A minimum of 20000 triangular mesh elements (2D simulations) or 60000 tetrahedral mesh elements (3D simulations) were employed in the simulations. All elements were of the second-order Lagrangian type. Mesh resolution was defined to be greatest around the tip of the pipette, and also the edges of the pit/step (where modelled). Simulations with finer meshes and using an adaptive solver, which refined the mesh where the error was greatest, were completed (neither shown), to confirm the meshes used were fine enough to not adversely affect the accuracy of the solution.

3.3 Theory

Geometric quantities used in the models and throughout this paper are: r_{ie}, radius of the internal electrode; r_i ,internal radius of the pipette tip; r_o, outer radius of the pipette tip; h, pipette height; d, pipette to surface separation; θ, pipette semi-angle The additional geometric parameter, RG, is defined to be the ratio of the outer and inner radii, r_o/r_i. Additionally, we shall use U to represent the applied potential and κ the conductance of the electrolyte. Throughout, we shall also use i_{DC} to represent the current to the electrode and i_{AC} to represent the oscillating component of the current, which arises from oscillation of the tip position.

Nitz and co-workers[26] developed a fully analytical model using three resistors to represent the resistance of the inner pipette, R_p, a distance dependent resistance, R_z, and a resistance of the electrolyte solution outside the pipette radius, R_r. R_z was subsequently separated into three further resistors. The resistance of each resistor was calculated from a set of assumed electric fields. The resistance of the pipette, R_p, was given by:

$$R_p = \frac{1}{\kappa}\frac{h}{\pi \cdot r_{ie} \cdot r_i} \tag{3.1}$$

The final expression for the current, as a function of z, arrived at, after approximating one of the resistances further was:

$$I(z) \approx I_{sat}\left(1+\frac{\tfrac{3}{2}\ln\left(r_o / r_i\right)\cdot r_{ie}\cdot r_i}{h\cdot d}\right)^{-1} \tag{3.2}$$

where

$$I_{sat} = \frac{U}{R_p} \tag{3.3}$$

The semi-analytical model presented by Wei and co-workers [25] breaks the full resistance into two resistors; one for the resistance inside the pipette and the other for the solution outside. An analytical expression was obtained for the resistance inside the pipette, equivalent to equation 3.1, although formulated in terms of different geometric parameters. The external resistance was deduced

from the fit of an analytical function to numerical simulations.[16] The resulting equations, for the change in resistance, $\Delta R(L)$, equation 3.4 and equation 3.5, are:

$$\Delta R(L) = R_t(L) - R_{t,\infty} \tag{3.4}$$

$$\Delta R(L)/R_{sol,\infty} = -0.708 + 1.5151/L + 0.6553\exp(-2.4035/L) \tag{3.5}$$

where $R_{sol,\infty}$ is the bulk resistance (resistance with the probe in bulk solution) and $R_t(L)$ is the resistance as a function of normalized height, $L = d/a$. The solution resistance, $R_{sol,\infty}$, is set as $R_{sol,\infty} = 1/4\kappa a$, which was calculated by Newman[28] to be the resistance to a conducting disk of radius *a* situated in an infinite, insulating plane, surrounding by a medium of uniform conductivity, κ. Equations 3.4, 3.5 and a version of equation 3.1 are rearranged to give current as a function of normalized distance, $i(L)$:

$$i(L) = \frac{4\pi a r_0}{4L_p + \pi r_0(0.292 + 1.5151/L + 0.6553\exp(-2.4035/L)} \tag{3.6}$$

Dividing equation 3.6 by the limiting current as the distance tends to infinity, i_∞, results in:

$$i(L)/i_\infty = \frac{4L_p + 0.9473\pi r_0}{4L_p + \pi r_0(0.292 + 1.5151/L + 0.6553\exp(-2.4035/L)} \tag{3.7}$$

For our model we make a number of simplifying assumptions whose effects are negligible for the situations that concern us, but which generate caveats in the conclusions drawn. First, as both electrodes are large in surface area and the electrode reaction is rapid, we ignore the effects of electrode charging and charge transfer resistance. We also choose to ignore the effect of any charge, and the associated double layer, on the pipette wall. The reasons for this and the effects are discussed later. Additionally, the substrate above which the pipette is placed is modelled as a perfect insulator, passing no current and permitting no electric field across it.

A variety of geometries were simulated, as illustrated in Figure 3-1. These were chosen to be representative of some commonly found experimental geometries; while in no way exhaustive they can be used intuitively to highlight the effects of various parameters encountered in SICM experiments.

3.3.1 2-D Model

When the pipette is perpendicular to a planar surface, the geometry of the problem displays axial symmetry, thus the 2-D geometry depicted in Figure 3-1a can be used. The reference electrode in bulk solution is sufficiently large relative to the aperture that it will present no resistance. Consequently, the effect of the external electrode is distributed along edges 10 and 12. It is important to note that the current lines at long distance are a consequence of this idealization and should not be taken as representative of the real situation in this location; however, this does not affect the calculated resistance. Similarly, modelling the internal electrode as an arc of a circle (edge 11), does not influence the current. The full set of boundary conditions is defined in Table 3-1.

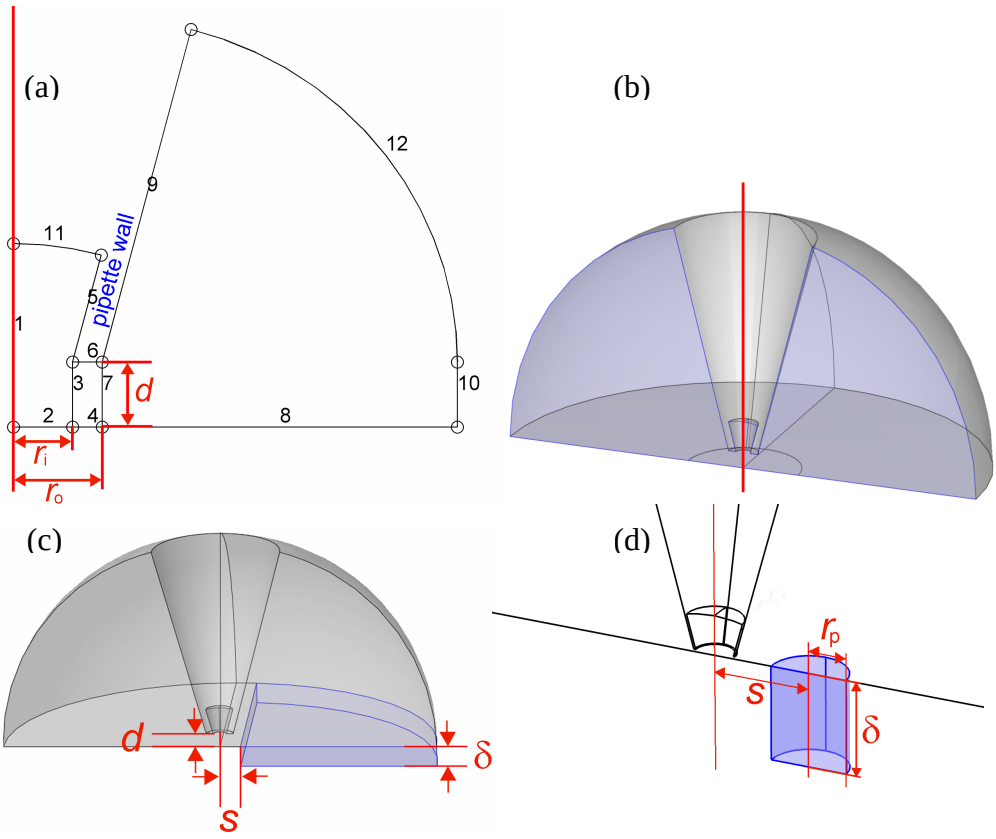

Figure 3-1. Geometries used for finite element simulations of: (a) two-dimensional, cylindrically symmetric approach to a planar surface; and three-dimensional simulation geometries to a planar surface (b), a step edge (c) and a cylindrical pit zoomed in to the region near pipette end (d).

Table 3-1: Boundary conditions for the simulations. The vector $\vec{n}$ is defined to be the unit normal to the boundary.

Edge number	Coordinates	Physical Representation	Boundary Condition
1	$r = 0;\ -d \le z \le h$	Centre-line of pipette	$\nabla\Phi \cdot \vec{n} = 0$
2	$z = 0;\ 0 < r < r_i$	Inert Surface	$\nabla\Phi \cdot \vec{n} = 0$
3	$r = r_i;\ -d < z < 0$	'Phantom' boundary*	-
4	$z = -d;\ r_i \le r \le r_o$	Inert Surface	$\nabla\Phi \cdot \vec{n} = 0$
5	$z = t\cos(\theta);\ r = r_i + t\sin(\theta);\ 0 \le t \le h$	Pipette Wall	$\nabla\Phi \cdot \vec{n} = 0$
6	$z = 0;\ r_i < r < r_o$	Pipette Wall	$\nabla\Phi \cdot \vec{n} = 0$
7	$r = r_o;\ -d < z < 0$	'Phantom' boundary*	-
8	$z = 0;\ r_o < r < r_o + r_e$	Inert Surface	$\nabla\Phi \cdot \vec{n} = 0$
9	$z = t\cos(\theta); r = r_o t\sin(\theta); 0 < \mathrm{t} < \mathrm{r_e}$	Pipette Wall	$\nabla\Phi \cdot \vec{n} = 0$
10	$r = r_o + r_e;\ -d \le z \le 0$	External electrode	$\Phi = U = 1$
11	$r = (h + r_i/\tan(\theta))\sin(\varphi)$ $z = (h + r_i/\tan(\theta))\cos(\varphi) - r_i/\tan(\theta)$ † $0 < \varphi < \theta$	Internal Electrode	$\Phi = 0$
12	$r = r_o + r_e\cos(\varphi)$ $z = r_e\sin(\varphi)$ $0 < \varphi < 90 - \theta$	External electrode	$\Phi = U = 1$

* 'Phantom' boundaries are introduced to aid in producing a high quality mesh, but do not enforce condition upon the solution.

† These coordinates represent the arc of the circle whose centre is the intersection of the extrapolation of the pipette centre-line and the pipette inner wall.

To calculate the current, Laplace's equation was first solved for the electrolyte solution. The axisymmetric cylindrical nature of the geometry of interest warrants the use of cylindrical polar coordinates, with the angular term omitted. Thus, choosing *r* and *z* to be the radial and axial coordinates, respectively, we have:

$$\nabla^2\Phi = \frac{\partial^2\Phi}{\partial r^2} + \frac{1}{r}\frac{\partial\Phi}{\partial r} + \frac{\partial^2\Phi}{\partial z^2} = 0 \tag{3.8}$$

Where Φ is the potential. The current, *i,* is calculated by the integration of flux on the boundary representing the electrode, Ω, which is boundary 11 in Figure 3-1a

$$i = 2\pi\kappa\int_{\Omega} r\nabla\Phi\cdot\vec{n} \tag{3.9}$$

where $\vec{n}$ is the unit normal to the edge.

As equation 3.8 is linear, it is possible to obtain a solution to it in normalized coordinates. The pipette inner radius, r_i,, is used to normalize the geometry. In addition, both the electrolyte conductivity, κ, and the potential, *U,* are taken to be unity, giving a general solution that may be scaled appropriately to match an experimental situation.

The length of the pipette is large compared to the pipette aperture; it is inefficient, although possible, to model the entire pipette. Greater efficiency in the simulations can be achieved by noting that the resistance, $R_{A,B,\gamma}$, between the conical segment of two concentric, spherical shells is

$$R_{A,B,\gamma} = \frac{B-A}{2\pi\kappa AB(1-\cos(\gamma))} \tag{3.10}$$

where A and B are the radii of the outer and inner spheres respectively, γ is the semi-angle of the conical section and the other variables are as defined previously. Equation 3.10 is arrived at by first finding the potential distribution between two concentric shells, radii $A<B$, separated by a uniform medium, of conductivity κ. The inner shell is poised at a potential of 0 V, while the outer shell is at 1 V. We describe the geometry of the system in spherical polar

coordinates: r,ϕ,ψ; where r is the radial coordinate, ϕ is the azimuthal coordinate and ψ is the polar coordinate. The symmetry of the system dictates that the solution will be independent of either angle, thus the equation solved is:

$$\begin{aligned} 0 &= \nabla^2\Phi \\ &= \frac{1}{r^2}\frac{\partial}{\partial r}\left(r^2\frac{\partial\Phi}{\partial r}\right)+\frac{1}{r^2\sin\theta}\frac{\partial}{\partial\theta}\left(\sin\theta\frac{\partial\Phi}{\partial\theta}\right)+\frac{1}{r^2\sin^2\theta}\frac{\partial^2\Phi}{\partial\theta^2} \\ &= \frac{1}{r^2}\frac{\partial}{\partial r}\left(r^2\frac{\partial\Phi}{\partial r}\right) \end{aligned} \tag{3.11}$$

The ansatz $\Phi(r,\phi,\theta)=\Phi(r)=\alpha+\beta/r$, with α, β constants to be determined, is made. Knowing the potential at the shells gives the simultaneous equations:

$$0=\alpha+\beta/A \tag{3.12}$$

$$1=\alpha+\beta/\mathrm{B} \tag{3.13}$$

Solving 3.12 and 3.13 gives:

$$\alpha=B/B-A \quad \text{and} \quad \beta=AB/A-B \tag{3.14}$$

Through inspection we see the ansatz to be correct.

The current is calculated by integrating the normal flux $-\kappa\beta r^{-2}$ over the portion of the inner shell lying within the bounds of the pipette ($\phi<\gamma$).

$$\begin{aligned} \text{Current} &= \int_0^{2\pi}\int_0^{\gamma} -\beta/A^2\,\kappa A^2\sin\phi\,d\phi d\theta \\ &= AB/(B-A)\,2\pi(1-\cos\gamma) \end{aligned} \tag{3.15}$$

The resistance is precisely the reciprocal of the current on application of a unit voltage, which is the relation of equation 3.15 to equation 3.10.

Equation 3.10 was used to calculate the resistance of the pipette from $2r_i$ upwards, which was found through simulation to offer an accurate solution.

3.3.2 3-D model

The starting geometry used in three dimensional simulations was initially generated as the volume of rotation through 180° of the geometry shown in Figure 3-1a and described in Table 3-1, giving the geometry shown in Figure 3-1b. Boundary conditions on the boundary surfaces were identical to those of the boundary lines of the 2-D model from which they arose. There is no longer a boundary condition applied on the axis of symmetry, which has been rotated about edge 1. The boundary shaded in blue in Figure 3-1b is the plane of symmetry for the simulation and, as such, has a 'no flux' boundary condition applied to it, i.e. $\nabla\Phi\cdot\vec{n}=0$, where the vector $\vec{n}$ is defined to be the unit normal to the boundary plane. The partial differential equation solved was Laplace's equation in 3D Cartesian coordinates (*x* ,*y*, *z*):

$$\nabla^2\Phi=\frac{\partial^2\Phi}{\partial x^2}+\frac{\partial^2\Phi}{\partial y^2}+\frac{\partial^2\Phi}{\partial z^2}=0 \qquad (3.16)$$

The current, *i*, was calculated from equation 3.17, the analogue to the flux integral described by equation 3.9, where Ω is now the boundary surface representative of one of the electrodes:

$$i=\kappa\int_{\Omega}\nabla\Phi\cdot\vec{n} \qquad (3.17)$$

All equations were solved using the finite element method [29] which discretizes the problem as a series of polynomials on connected polyhedra. Initially, test simulations, for comparison with the two dimensional formulation, were performed to confirm the validity of the mesh (not shown). Following this, two additional geometries, which cannot be represented in two dimensions, were considered: (i) the situation where the probe is scanned over a step (Figure 3-1c); (ii) where the probe is scanned over a cylindrical pit (Figure 3-1d). In each case the shaded area in Figure 3-1c and d represents these additional features. The boundary conditions were 'no flux' on all but the outer edge of the step domain, where the continuation of the outer hemisphere was given the condition $\Phi=U=1$. Additional geometric parameters were introduced as follows: r_p is the pit radius; *s* represents the offset from the centre-line of the pipette to the feature;

δ represents the depth of the feature, be it a pit or a step. In the case of the step geometry, positive *s* referred to the case where the pipette was above the higher part of the step as illustrated in Figure 3-1c. For the cylindrical pit case, there is a symmetry plane through the axis of the pit and we make the arbitrary decision to only consider the case where *s* is non-negative. The perpendicular distance from the bottom end of the pipette to the upper part of the surface, as illustrated in Figure 3-1c, is denoted as *d*.

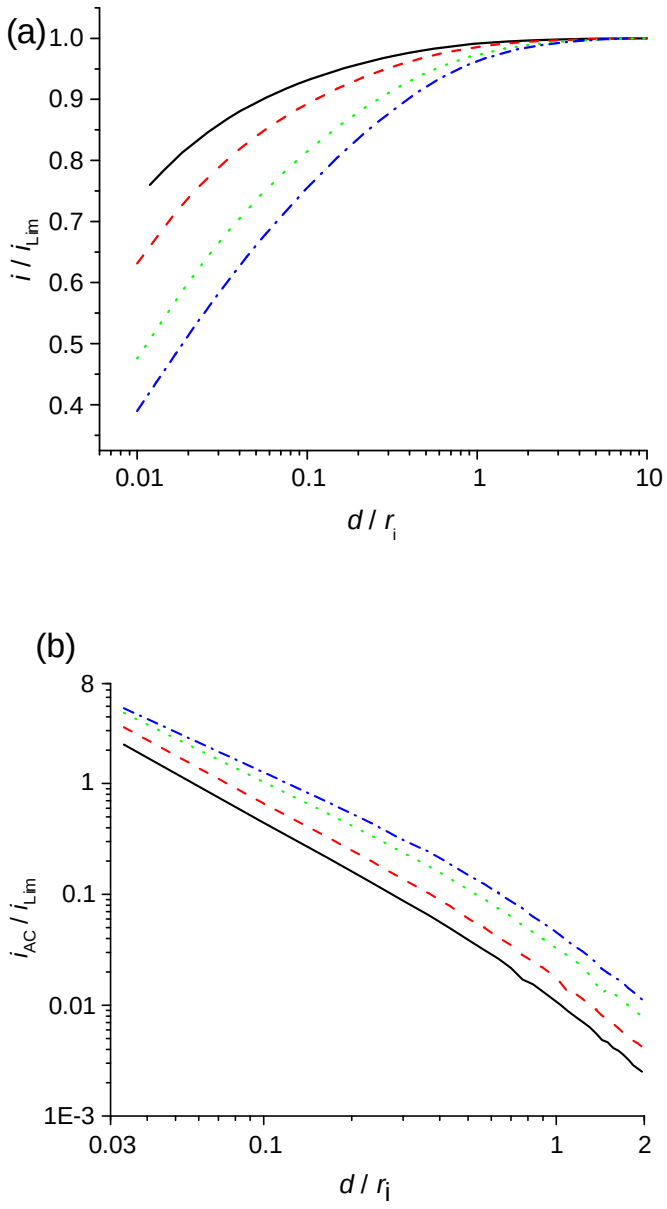

Figure 3-2. Simulated curves of the normalized current (a) and 1st harmonic (b), versus normalized distance, for the approach of *RG* = 1.1 micropipettes, of varying semi-angle, θ, to a planar inert surface. Solid black line, θ = 3°; dashed red line, θ = 5°; dotted green line, θ = 10°; dash-dotted blue line, θ = 15°.

3.4 Results and Discussion

3.4.1 2-D simulations: factors influencing SICM approach curves

Initially the effect of the micropipette semi-angle on the current-distance response is considered. Figure 3-2a shows a set of current-distance curves for a

micropipette of *RG*=1.1, for θ values of 3°, 5°, 10° and 15°. It can be seen that increasing the pipette angle, θ, results in a steeper drop of normalized current as the tip is approached close to the surface. Thus, a tip with a small semi-angle is, in essence, a less sensitive probe of tip-surface distance. The effect is easily understood in terms of the internal resistance of the pipettes. The resistance of the pipette represents a large constant resistance in series with the resistance outside the pipette. The larger the resistance of the pipette (smaller the semi-angle, see equation 3.10) the more dominant its contribution to the overall resistance, and the smaller the contribution from the remaining resistance (including distance-dependent resistance).

The effect of tip semi-angle is further evident in Figure 3-2b, where the 1st harmonic (equivalent to the derivative) is calculated by differentiation of the normalized current, which is achieved by fitting a second-order interpolation polynomial through the simulated data points and differentiating this function. Note, however, the first harmonic amplitude is zero far from the surface and increases more steeply with decreasing distance from the substrate (note the log scale on the graphs in Figure 3-2b). This contrasts with the DC signal (Figure 3-2a) where the current is large far from the surface and decreases only slowly initially with decreasing tip-substrate separation. The signal is largest with the larger θ value. Figure 3-2 shows clear evidence of the increased sensitivity afforded by using the 1^{st} harmonic as the feedback quantity, rather that the DC signal.

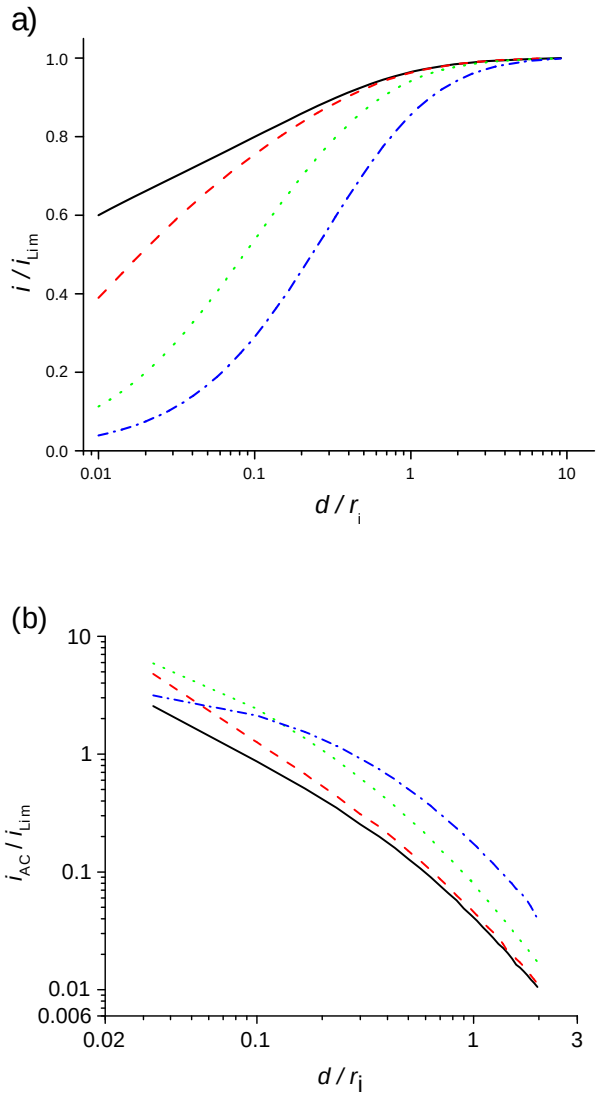

Figure 3-3. Simulation of the normalized current (a) and 1st harmonic (b), versus normalized distance, for the approach of 15° semi-angle micropipettes, of varying RG, to a planar inert surface. Solid black line, *RG* = 1.01; dashed red line, *RG* = 1.1; dotted green line, *RG* = 2; dash-dotted blue line, *RG* = 10.

Just as increasing the pipette semi-angle increased the sensitivity of the current response to distance, Figure 3-3a shows that increasing *RG* has the same effect, as evident in the simulated current-distance curves for θ = 15°, with *RG* = 1.01, 1.1, 2 and 10. It is important to note that although the distance-dependent currents shown in Figure 3-3a are normalized by the bulk current for each particular pipette, the latter quantity only varies slightly with the *RG* value, with a decrease of just 3.3% from *RG* = 1.01 to *RG* = 10. This change under-represents the change in external resistance due to the large series resistance of

the pipette interior, which contributes to the total resistance. It is clear that the increase in resistance with decreasing tip-substrate separation is much more significant with larger RG pipettes. This trend is also evident in the plots of 1st harmonic normalised current versus distance shown in Figure 3-3b. The origin of the effect can be seen by inspection of Figure 3-4, which is a plot of the potential of the electric field around a tip of *RG* = 5. A significant potential drop, indicative of a high resistance, occurs in the annulus below the tip, bounded by the tip inner and outer radii. An increase in the size of this annulus necessarily increases the resistance and, consequently, the sensitivity of the tip response to distance from the surface. Examination of the isopotential contours in Figure 3-4 highlights that the aperture of the pipette (dashed line in the figure) is not an isopotential line; rather, the potential varies along it as can be seen by the intersection with numerous isopotential contours. This means that splitting resistances along this line, as applied in previous treatments,[25, 26] is not strictly correct.

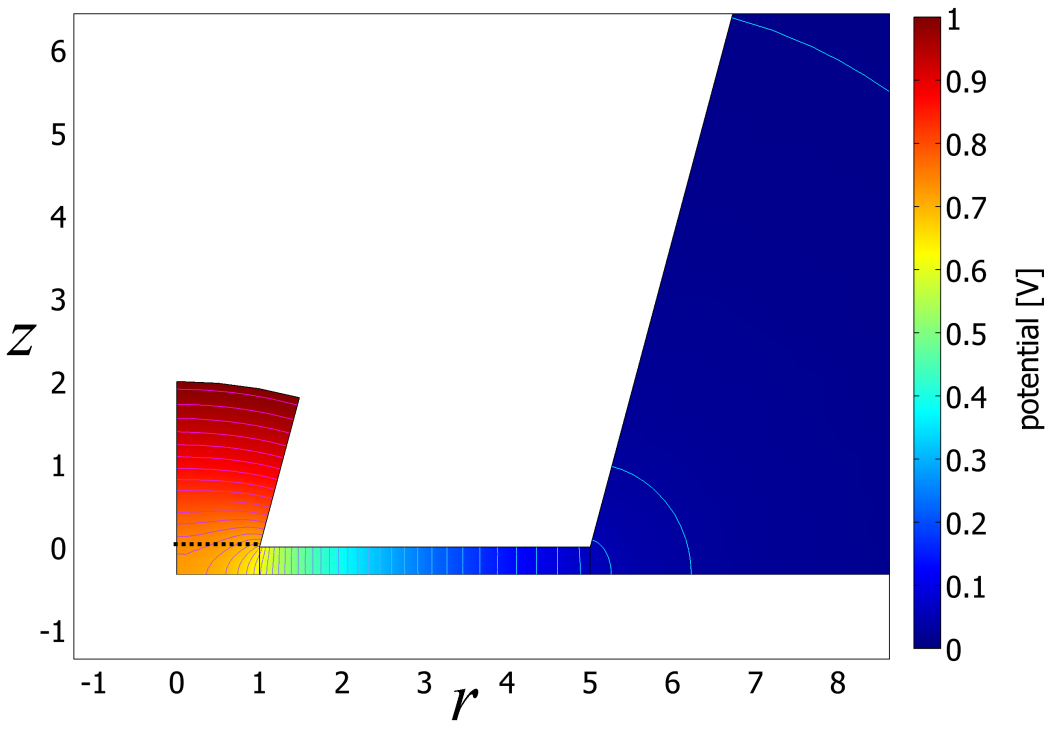

Figure 3-4: Plot of potential field of a large *RG* = 5 tip near to a planar inert surface. Contours are isopotential lines (20 mV separation). Exterior only partially shown. Dashed black line denotes the tip aperture where previous treatments have chosen to split the resistance.

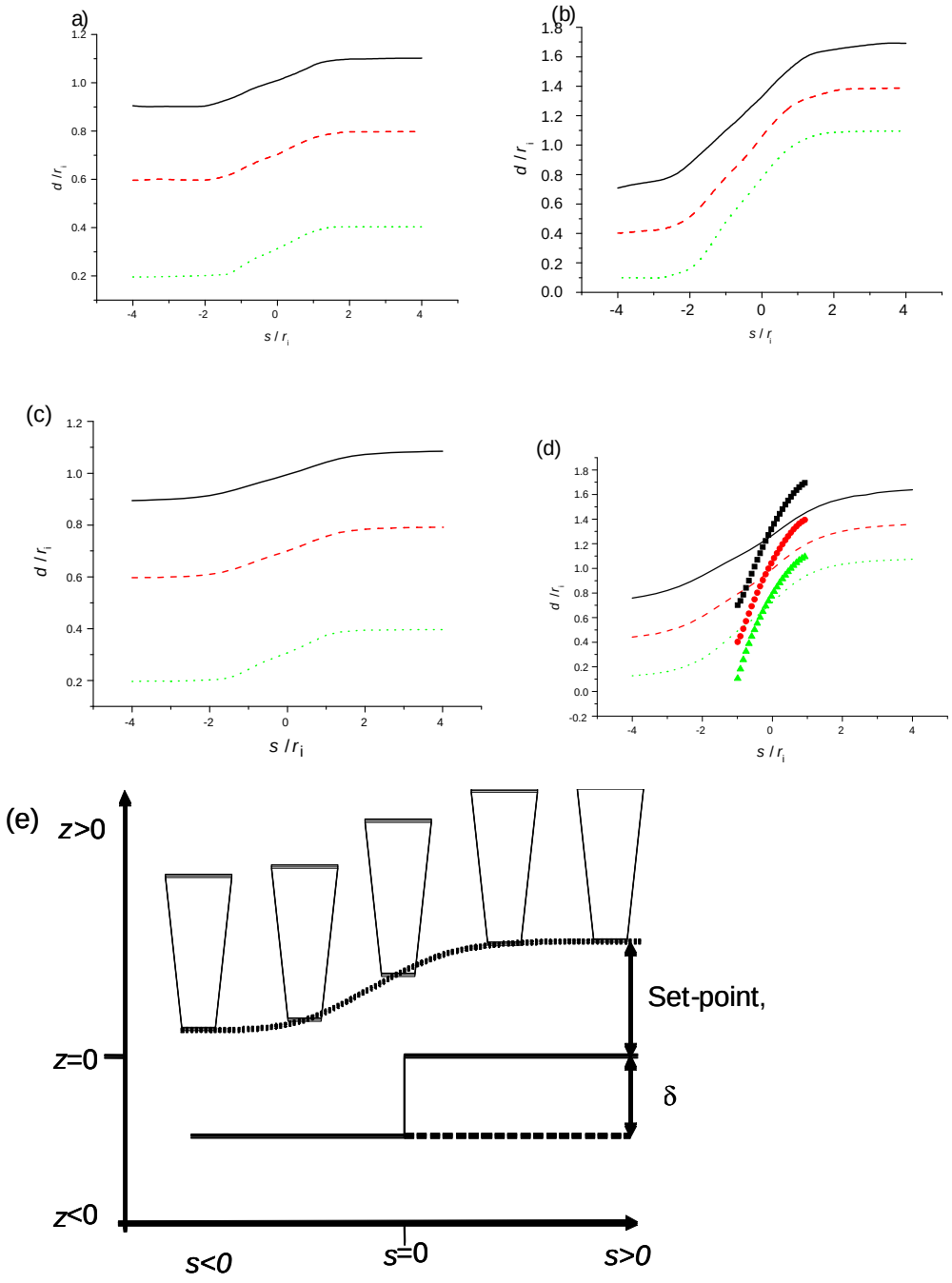

Figure 3-5: Profiles of tip height as a pipette (*RG* = 1.1, θ = 15°) is scanned over a step under feedback control. Lines in (a)-(d) are heights based on finite element simulations. The step height was: $\delta = 0.2r_i$ (a) and (c); and $1.0r_i$ (b) and (d). Feedback control considered: 1st harmonic (a) and (b); and the mean current (c) and (d). The different lines shown in each plot represent different set-points: for (a) and (c) the solid black lines are $d = 1.1\ r_i$, dashed red lines, $d = 0.\ r_i$, dotted green lines $d = 0.4\ r_i$. For (b) and (d) the solid black line is $d = 1.7r_i$, dashed red line, $d = 1.4r_i$, dotted green line $d = 1.1r_i$. In part (d), the points represent the height of a pipette as it is scanned over a step ($\delta = 1r_i$) using feedback based on the mean current as calculated in Nitz et al

[26] to maintain the tip height; set-point heights: black squares, $1.7r_i$; red circles, $1.4r_i$; green triangles $1.1r_i$. Part (e) summarises the problem solved, with a schematic of the tip, together with the geometric parameters labelled.

3.4.2 Effect of substrate topography

As discussed earlier, SICM imaging typically involves maintaining the 1st harmonic current signal of a perpendicularly oscillating probe to maintain a constant tip-substrate separation as the tip is scanned across the surface. Figure 3-5 shows simulations of the path tracked by a tip as it is scanned over a step. The simulations were for a pipette geometry of $RG = 1.1$, with $\theta = 15°$, scanned over a step of height $\delta = 0.2r_i$ (a) and (c), with feedback set-points of $d = 0.4r_i$, $d = 0.8r_i$ or $d = 1.1r_i$; or a step of height $\delta = r_i$ with feedback set-points of $d = 1.1r_i$, $d = 1.4r_i$ or $d = 1.7r_i$, (b) and (d). Feedback control was achieved by maintaining the feedback quantity of either i_{AC} (a) and (b), or i_{DC} (c) and (d). The height was solved for, to give a tip-substrate separation where the feedback quantity attained the set-point value.

A schematic illustrating the problem solved is given in Figure 3-5e, together with the various parameters defining the problem. It can be seen that a step influences the tip position normal to the surface over relatively long lateral distances and this effect becomes more extensive as the set-point is adjusted so as to move the imaging pipette further from the surface. Furthermore, it should be noted that the effect of the step does not result in a symmetric image profile. For example, in Figure 3-5b the tip begins to move perpendicularly to the surface at $s > 2r_i$ from the step, but reaches a plateau in less than $1.5r_i$ beyond the step. An important deduction from these results is that, the greater the height of the step and/or the tip set-point (distance from surface) the more blurred the feature will appear in an SICM image. For example, in Figure 3-5a, when the feedback set-point is at $d = 0.4r_i$ the pipette height traces out the step within a lateral distance of $\approx 2.9r_i$, whereas at a set-point of $d = 1.1r_i$ the response occurs over a greater lateral distance of $\approx 3.7r_i$. Comparing Figure 3-5a, with a step height of $\delta = 0.2r_i$, to Figure 3-5b where $\delta = r_i$, it can be seen that the large step is visible to the SICM probe, with equal ($d = 1.1r_i$) set-points, over a marginally greater distance, which results in a loss of lateral resolution.

Figure 3-5c illustrates the probe scanning over the same step as Figure 3-5a, but the feedback quantity is i_{DC} rather than i_{AC}. A dramatic deterioration of lateral resolution is evident upon this switch, illustrated by the broadening of the tip-height response to the step. In the experiments herein, and in present SICM practice, i_{AC} has been selected for as the quantity for feedback to increase stability, as the AC signal is relatively immune to noise and drift, but the simulations reported herein also clearly demonstrate that AC, feedback control yields better spatial resolution.

Figure 3-5d is the profile of a pipette scanning over a step $\delta = 1r_i$, while i_{DC} is maintained constant for feedback. The lines show tip heights for feedback set-points $d = 1.1r_i$, $d = 1.4r_i$, and $d = 1.7r_i$. The points on the plot represent the tip height for the same set-points, but using the current as calculated by Nitz et al[26] for a tip scanning over a step. A dramatic difference is clear and is an indication of the dangers of erroneous extrapolation of 2-dimensional results to 3 dimensions. The extrapolation method takes the fraction of the pipette aperture over either side of the step to determine the fraction of the total current corresponding to a pipette at the equivalent distance from a planar surface. e.g. a pipette r_i directly above a $\delta = 0.5r_i$ high step would be attributed a current $\frac{1}{2}\left(i_{DC}(r_i) + i_{DC}(1.5r_i)\right)$. This method, which only takes into account features directly below the pipette, concludes that a complete response to the step would occur in a lateral distance equal to the pipette diameter ($2r_i$), this is regardless of the set-point or of the height of the step. The inaccuracy is because the method does not take into account lateral effects on the resistance.

Figure 3-6 summarises the results examining the effect of a pit in the substrate (depths: $\delta = 0.73r_i$, $\delta = 1.35r_i$, $\delta = 5.74r_i$) on the current response. In the cases shown, the tip and pit cylindrical axes of symmetry were coincident, as schematised in Figure 3-6d.

Figure 3-6a considers the case of a pit that is slightly smaller than the pipette aperture ($r_p = 0.73r_i$). It is clear that the pit remains invisible to tips situated directly above them, as is indicated by the coincidence of all of the curves for the pits with the current-distance curve for a planar surface.

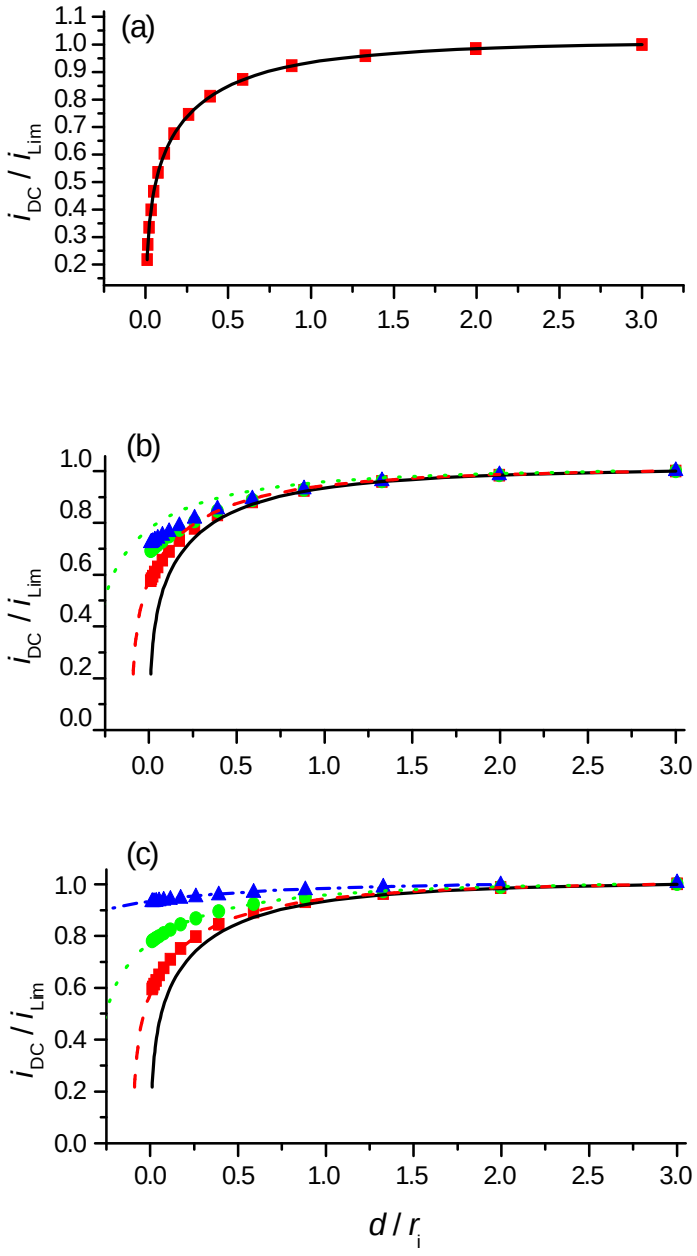
(a)
(b)
(c)
i_{DC} / i_{Lim}
d / r_i

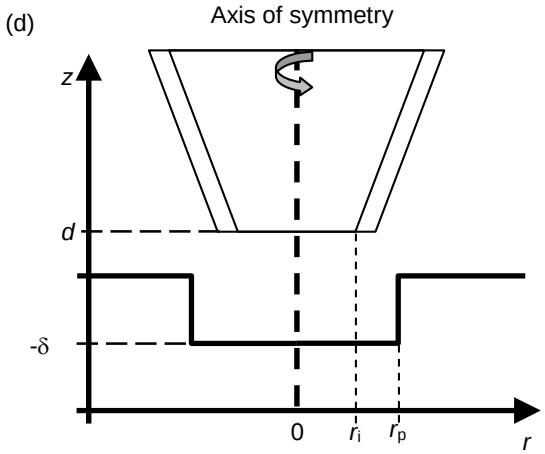
(d)
Axis of symmetry
z
d
-δ
0
r_i
r_p
r

Figure 3-6. Steady-state current-distance curves as a pipette (*RG* = 1.1, θ = 15°) is approached to cylindrical pits (points in each plot) compared to the behaviour for the same pipette approaching planar surfaces (curves). Pit radii: $r_p = 0.73r_i$ (a); $r_p = 1.35r_i$ (b); and $r_p = 5.74\ r_i$ (c). Pipette and pit centre-lines coincide ($s = 0$) i.e. an axisymmetric cylindrical geometry is considered. Pit depths: red squares, $\delta = 0.1\ r_i$; green circles $\delta = 0.31\ r_i$; blue triangles, $\delta = 1\ r_i$. Planar surfaces at heights: 0 r_i, solid black line; 0.1 r_i, dashed red line; 0.31 r_i, dotted green line; 1 r_i, dash-dotted blue line.

Figure 3-6b shows that when the pit is slightly larger than the pipette ($r_p = 1.35r_i$) it becomes visible to the tip, as is indicated by a positive current deviation from the current-distance curve for a planar surface. However, it is only for the shallowest of pits ($\delta = 0.1r_i$) where the depth of the pit is accurately assessed by SICM, i.e. where the current response is comparable to a pipette approaching a planar surface at δ = -0.1. The lack of coincidence of the equivalent curves for deeper pits indicates that caution must be exercised when using SICM to infer the depth of pits which are small in relation to the pipette.

Figure 3-6c demonstrates that for pits much larger than the pipette, e.g. $r_p = 5.74r_i$, there is coincidence between the current response of a pipette approaching a pit and a planar surfaces of the same depth; we conclude that for pits of this size SICM measurements in the pit centre are an accurate reflection of pit depth.

Figure 3-7 shows the simulated trajectory of a pipette as it is scanned over a cylindrical pit (width $r_p=1.1r_i$ (a) and $r_p=2r_i$ (b) (for the geometry see Figure 3-1(d) and Figure 3-7(c). The height was maintained using feedback on i_{AC} (feedback set-points $d = 0.35r_i$, $d = 0.45r_i$, $d = 0.6r_i$ (a); and $d = 0.8r_i$, $d = 1.1r_i$, $d = 1.4r_i$ (b)) as previously explained. The width of the tip response to the pit represents an exaggeration of the pit size, as seen from the height deviation, which extends far beyond the pit edge (indicated by the vertical lines in Figure 3-7 (a) and (b)). These responses are consistent with those seen above the step feature. Additionally, as found for a pipette scanning over a step, there is a loss of lateral resolution as the set-point distance from the surface increases, as can most readily by comparing the curves in Figure 3-7b with feedback at $d = 0.8r_i$ and $d = 1.4\ r_i$. The larger set-point distance results in an increase of ca. r_i in the width of the height response traced out over the half pit.

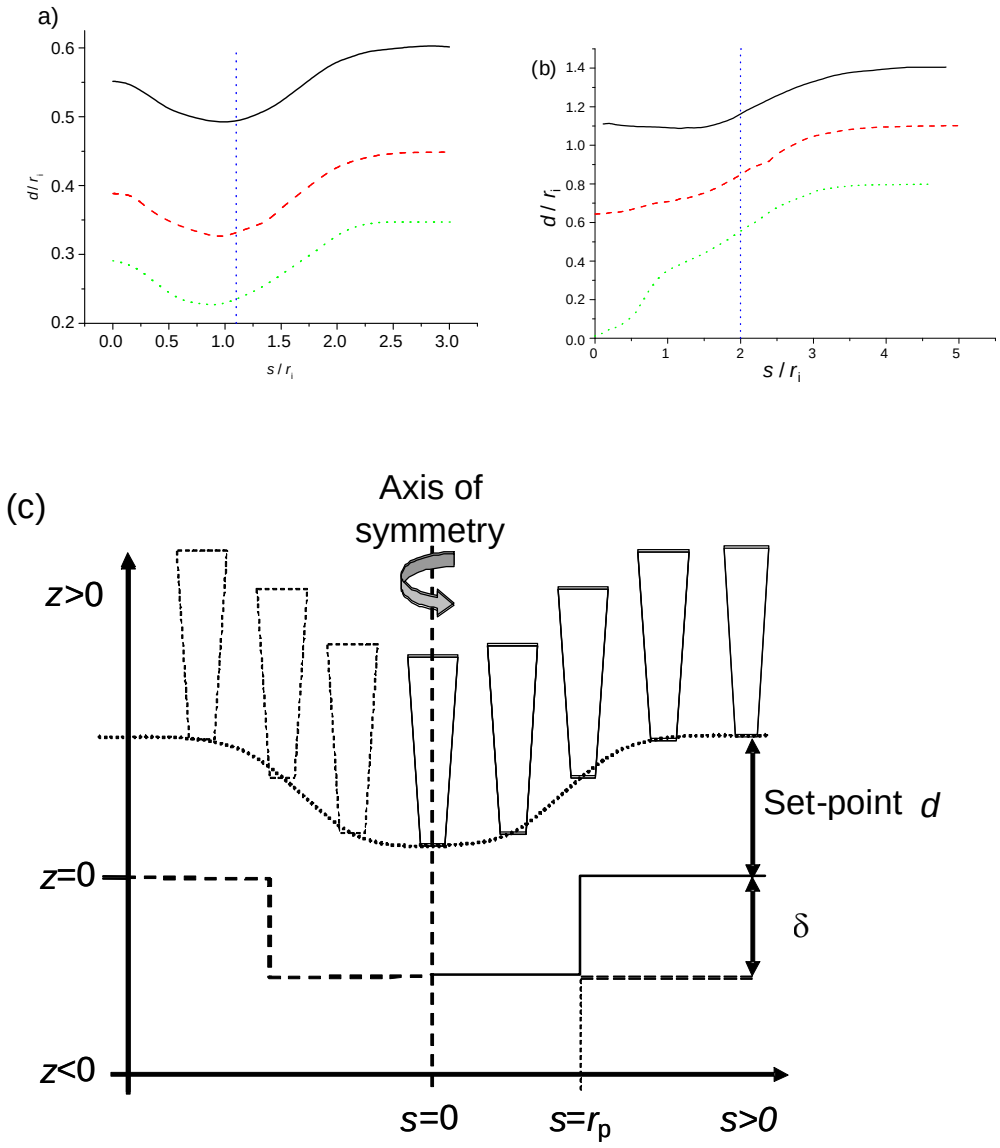

Figure 3-7. Profiles of tip height as a pipette (*RG* = 1.1, θ = 15°) is scanned over a cylindrical pit of depth δ = 5 r_i. Pit radii were: r_p = 1.1 r_i (a) and r_p = 2 r_i (b). Vertical lines indicate the horizontal coordinate of the edge of the pit. Feedback control utilized the 1st harmonic and the set-points were defined as distances from a planar surface as follows: solid black line *d* = 0.6 r_i, dashed red line, *d* = 0.45 r_i, dotted green line *d* = 0.35 r_i (a); and solid black line *d* = 1.4 r_i, dashed red line, *d* = 1.1 r_i, dotted green line *d* = 0.8 r_i (b). Part (c) is a schematic of the pit and tip with the geometric parameters labelled. This indicates that the scans in (a) and (b) start with the tip and pit co-axial and the tip is then moved radially outwards.

An interesting feature in Figure 3-7 is a 'halo' artefact, where there is a decrease in tip height around the perimeter of the pit followed by an increase as the probe

approaches the pit centre; this would be indicated by a halo in a 2-dimesional scan. Small halo features have been previously observed by when imaging small features with SICM. To understand the origin of the 'halo' artefact it is necessary to consider the ion paths in the vicinity of the tip, as are illustrated schematically in Figure 3-8. When the tip is centred directly over the pit the only route for ion flow involves the narrow path between the pipette and surface (Figure 3-8a); however, if the pipette is off-centre a second lower resistance path opens up, from the pipette via the pit to the exterior solution, as illustrated by the heavy arrow in Figure 3-8b. This artefact offers some explanation as to why a small pit remains invisible when it is coaxial with the pipette, as shown earlier in Figure 3-6a. It is clear that the artefact is no longer evident for the larger pit ($r_p = 2r_i$), i.e. for the case where the glass aperture of the micropipette no longer encloses the entire pit (Figure 3-7b). However, for the closest feedback set-point ($d = 1.1r_i$), there is a second inflection at $s \approx 0.75r_i$, which corresponds to the pipette sidewall being within the region of the pit. In this situation there is an additional ion path of the type mentioned above and illustrated by the heavy arrow in Figure 3-8c.

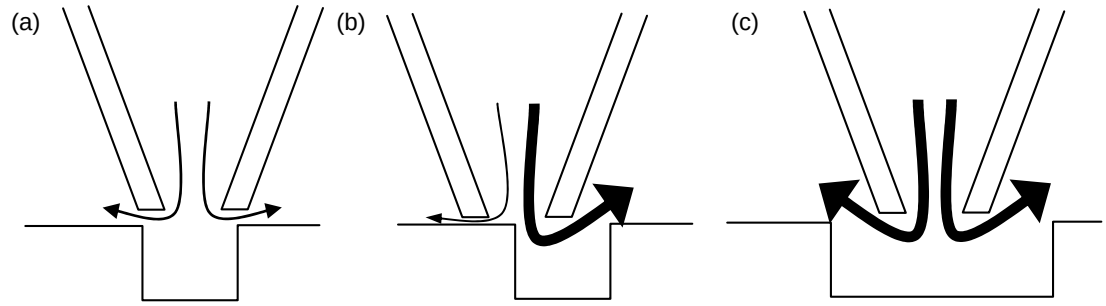

Figure 3-8. Schematic of the path of ion flow as a pipette is positioned above a pit, either coaxially (a) or offset (b) over a small pit, or coaxially over a larger pit (c). The weight of the arrow is indicative of the relative magnitude of the ion flux out of the pipette. NB: there will be a net flow equal and opposite to balance the charge (not shown).

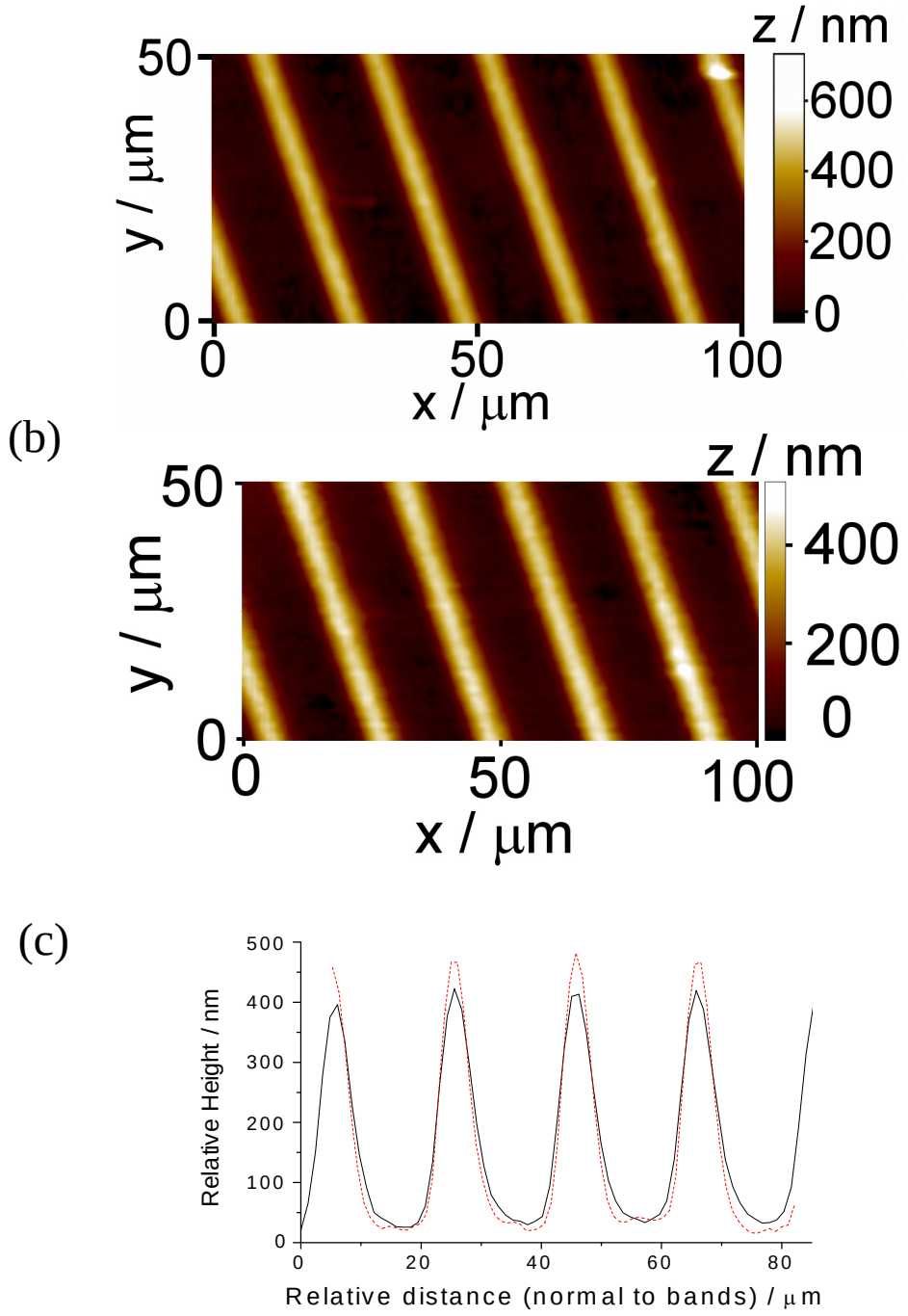

Figure 3-9. SICM image of raised band structure on silicon wafer, taken with 3.5 μm inner diameter pipette under feedback utilising the first harmonic, with two different set-points. Band width 5 μm, band height 0.5 μm , 20 μm repeating pattern. (a) and (b) are images over the same 100x50 μm area, with the set point of (a) ≈ 1.4 d / a, closer to the surface than the set-point for (b), ≈ 1.92 d / a. (c) shows the average cross section in the direction normal to the bands for (a) dashed and (b) solid. Lines have been shifted so that the flat areas between bands match approximately, so as to aid comparison.

To examine the extent to which the characteristic features of SICM, identified by simulation, were seen in practice, we carried out experiments on well-defined test samples. As an example, Figure 3-9 shows SICM images of a silicon sample comprising of an array of 5 μm wide, 0.5 μm high ridges, with 20 μm pitch. The pipette had an inner diameter of 3.5 μm and the tip-substrate separation was achieved by maintaining the value of i_{AC} equivalent to the tip being close to the surface (≈ 1.4 d / a) (a) or far from the surface (b) (≈ 1.92 d / a). Comparing the images obtained with the different set-points, in both the images and in the cross-section plot shown in (c), it is clear that neither set-point was able to access the full height of the ridges, but the topography response is a function of feedback set-point. The set-point closest to the surface (image (a)), yields a sharper image (dashed line in Figure 3-9c), than for the more distant set-point (solid line Figure 3-9(c)).In both cases, the ridge was insufficiently wide compared to the tip to allow the tip profile to plateau at a height equal to the ridge thickness, however, the maximum height difference measured with the close set-point was greatest.

All of the features observed in these experiments are consistent with the simulated results of a tip scanning over a step (Figure 3-5). The lack of a plateau in the tip height image over the centre of the band is also expected from the simulation results, which showed that three or more tip radii beyond a step was required for a stable response to be attained. This condition can clearly not be achieved for a band of width circa $3r_i$ as was employed in the experiments. This factor in resolution of SICM images is further evident when one examines the part of the images corresponding to the flat portions between the bands. In the image with the set-point closer to the surface the flat portion is eventually reproduced faithfully, but this is not the case with the set-point further from the surface. The response for the latter case indicates the tip detects the next step (band edge) before the effect of the previous one has passed and is thus unable to clearly see the base. The mid-point between the step edges is 7.5 μm, representing a lateral distance of ca. $4r_i$ from the edges of the bands. The simulated height profiles in Figure 3-5b show that when imaging close to the surface, $4r_i$ is beyond the distance where a height change would be expected in response to a step, but this is at the limit where such a response would be seen when imaging further from the surface.

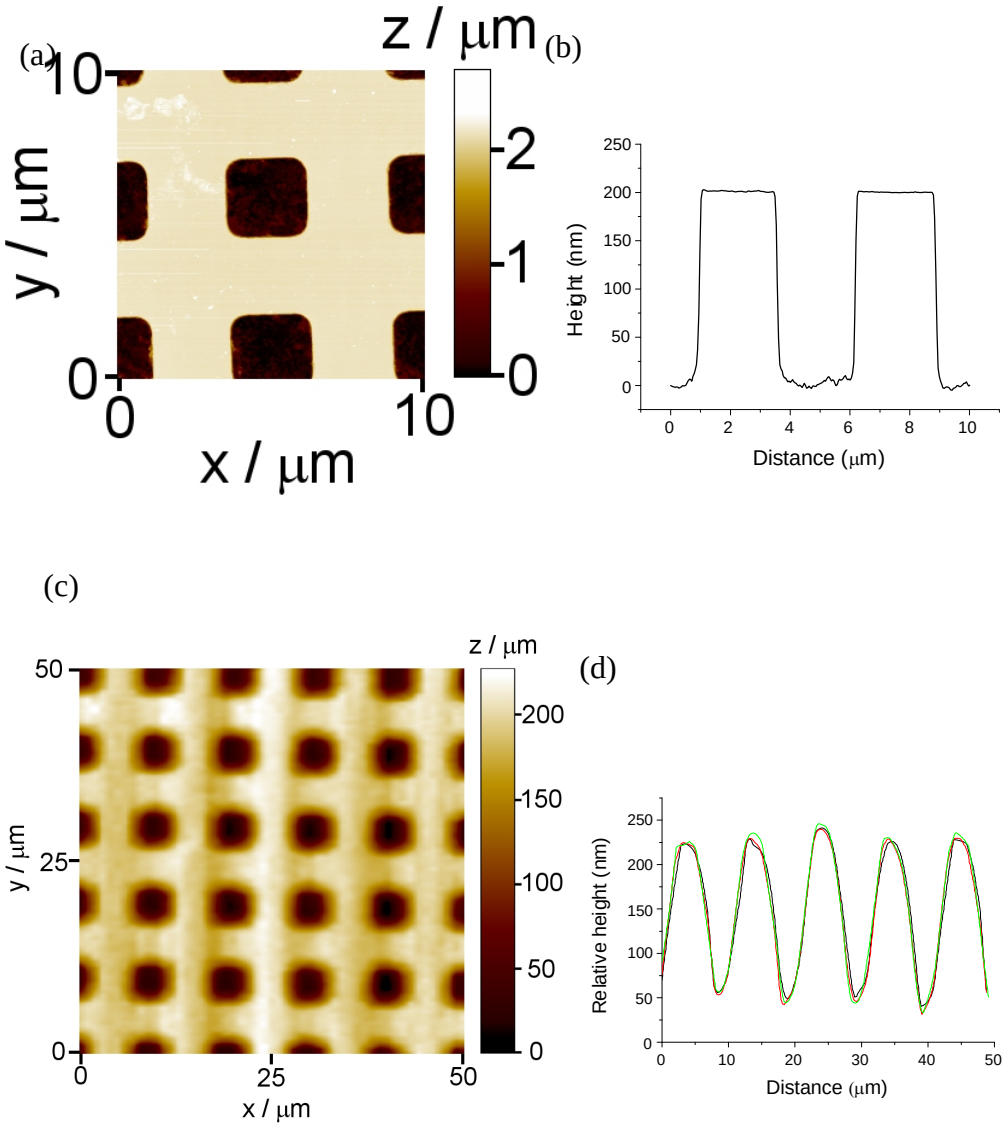

Figure 3-10. Images of a calibration grid, 10 μm pitch, 180 nm depth, taken with: an AFM (a) and (b); and SICM (1 μm diameter pipette, i_{AC} feedback, set-point ≈1.2*a*) (c) and (d). (b) and (d) are cross-sections of the 2-dimensional images in taken through the centre of the pits, in (a) and (c), respectively. Curves in (d) have been aligned horizontally and vertically to aid comparison.

Figure 3-10 contains images of a calibration grid taken with atomic force microscopy (AFM) (a) and SICM (c). For SICM imaging the internal diameter of the pipette was 1 μm and the tip-surface separation was achieved through maintaining the value of i_{AC} (set-point ≈1.2*a* from planar surface). While the planar surfaces between the pits are clearly visible in the cross-section of the AFM image (b), these surfaces are clearly convoluted in the cross section of the SICM image (d). The depth at the centre of the pits, when measured SICM (≈ 170 nm), is in good agreement with the actual depths as quoted by the

manufacturer (180 nm). The features in these experimental data are consistent with the simulated results of an approach to a shallow pit illustrated in Figure 3-6b.

3.5 Conclusions

Finite element modelling has enabled the current response of an electrolyte filled SICM micropipette approaching a planar surface as a function of the pipette geometry to be investigated. The model represents an improvement of previous attempts to study this problem [25, 26] which are shown to be invalid in this chapter. We have demonstrated that a larger pipette semi-angle and a larger ratio of glass to aperture radii make the SICM more sensitive to tip-sample separation.

To explore surface topography in SICM the current responses of a pipette scanned perpendicularly towards a pit, and laterally over a step and a cylindrical pit have been investigated. An instantaneous step in a surface is shown to be convoluted to a feature typically visible over approximately four tip radii with the response being dependent on the tip/surface separation; close tip/surface separation enhances the resolution. The lateral resolution of the technique itself has a strong dependence on the choice of feedback quantity, with the 1^{st} harmonic offering significantly better resolution when compared with the mean current. The ability to judge the depth of pits has shown to be dependent on the pit width, with only wide pits generally accessible.

The model treats the experimental situation as a homogenous, resistive medium, with pipette walls and inert substrate both infinitely resistive. The homogeneity condition will break down in the case that there is a concentration source, e.g. a surface reaction, in which case a Nernst-Planck model, which considers diffusion acting on concentration gradients as well as migration of charged particles, must be used. If the electrolyte concentration is very low, or the pipette very small then the size of the double layer on the glass will be significant as charge separation occurs; this case is not covered by the model presented. This would be seen through permselectivity of the pipette reflected in a non-linear current-voltage response, so called current rectification, a treatment of which is found in

Wei et al[30]. In such conditions or with very high electric fields it may become prudent to include electro-osmotic flow within the model.

The geometry of the pipette used in the modelling is a simplification of the experimental geometry, typically a pipette may have multiple tapers. However, it has been shown that the region where the resistance is concentrated is the tip of the pipette and its immediate exterior; thus in modelling this accurately we give a very accurate approximation to the response of a fully realistic pipette geometry. Although the pipette is oscillated with a small amplitude perpendicular to the surface to obtain the 1st harmonic, no attempt is made to model the fluid flow associated or the transient effects as the electric field is developed. These simplifications are supported by experiments showing excellent agreement between the derivative of the current upon approach to a surface and the 1st harmonic on approach of the same pipette to the same surface, as has been shown previously [5]. The assumption of no charge transfer resistance is sound assuming care is taken to produce good reference electrodes.

Experimentally, the 1st harmonic is obtained through lock-in amplification; the mathematical equivalent of this operation being:

$$2f\int_0^{1/f} i(d+\tfrac{\delta}{2}\sin(2\pi ft))\sin(2\pi ft)\mathrm{d}t \qquad (3.18)$$

where $i(-)$ is the current as a function of height. The quantity measured is thus a function of oscillation amplitude. However, as δ diminishes this tends to $\delta\left.\frac{\partial i(h)}{\partial h}\right|_{h=d}$ which upon normalization leaves us with the definition we have used throughout. With large amplitude oscillation some difference may be seen.

References

(1) **Edwards, M. A.; Martin, S.; Whitworth, A. L.; Macpherson, J. V.; Unwin, P. R.** ***Physiological Measurement*** **2006,** ***27,*** **R63-R108.**

(2) **Wittstock, G.; Burchardt, M.; Pust, Sascha E.; Shen, Y.; Zhao, C.** ***Angewandte Chemie International Edition*** **2007,** ***46,*** **1584-1617.**

(3) **Bard, A. J.; Mirkin, M. V.** ***Scanning Electrochemical Microscopy*****; Marcel Dekker: New York, 2001.**

(4) **Hansma, P. K.; Drake, B.; Marti, O.; Gould, S. A.; Prater, C. B.** ***Science*** **1989,** ***243,*** **641--643.**

(5) **Shevchuk, A. I.; Gorelik, J.; Harding, S. E.; Lab, M. J.; Klenerman, D.; Korchev, Y. E.** ***Biophys. J.*** **2001,** ***81,*** **1759-1764.**

(6) **Amemiya, S.; Bard, A. J.; Fan, F.-R. F.; Mirkin, M. V.; Unwin, P. R.** ***Annual Review of Analytical Chemistry*** **2008,** ***1,*** **95-131.**

(7) **Kranz, C.; Friedbacher, G.; Mizaikoff, B.** ***Anal. Chem.*** **2001,** ***73,*** **2491.**

(8) **Macpherson, J.; Unwin, P.** ***Anal. Chem.*** **2000,** ***72,*** **276.**

(9) **Bard, A. J.; Fan, F. R. F.; Kwak, J.; Lev, O.** ***Anal. Chem.*** **1989,** ***61,*** **132-138.**

(10) **Horrocks, B. R.; Mirkin, M. V.; Pierce, D. T.; Bard, A. J.; Nagy, G.; Toth, K.** ***Anal. Chem.*** **1993,** ***65,*** **1213-1224.**

(11) **Ervin, E. N.; White, H. S.; Baker, L. A.; Martin, C. R.** ***Anal. Chem.*** **2006,** ***78,*** **6535-6541.**

(12) **Alpuche-Aviles, M. A.; Wipf, D. O.** ***Anal. Chem.*** **2001,** ***73,*** **4873-4881.**

(13) **Ervin, E. N.; White, H. S.; Baker, L. A.** ***Anal. Chem.*** **2005,** ***77,*** **5564-5569.**

(14) **Fulian, Q.; Fisher, A. C.; Denuault, G.** ***J. Phys. Chem. B*** **1999,** ***103,*** **4387-4392.**

(15) **Fulian, Q.; Fisher, A. C.; Denuault, G.** ***J. Phys. Chem. B*** **1999,** ***103,*** **4393-4398.**

(16) **Kwak, J.; Bard, A. J.** ***Anal. Chem.*** **1989,** ***61,*** **1221-1227.**

(17) **Ciani, I.; Burt, D. P.; Daniele, S.; Unwin, P. R.** ***J. Phys. Chem. B*** **2004,** ***108,*** **3801-3809.**

(18) **Dobson, P. S.; Weaver, J. M. R.; Holder, M. N.; Unwin, P. R.; Macpherson, J. V.** ***Anal. Chem.*** **2005,** ***77,*** **424-434.**

(19) **Amphlett, J. L.; Denuault, G.** ***J. Phys. Chem. B*** **1998,** ***102,*** **9946-9951.**

(20) **Pierce, D. T.; Unwin, P. R.; Bard, A. J.** ***Anal. Chem.*** **1992,** ***64,*** **1795-1804.**

(21) **Zoski, C. G.; Mirkin, M. V.** ***Anal. Chem.*** **2002,** ***74,*** **1986-1992.**

(22) **Shevchuk, A. I.; Frolenkov, G. I.; Sánchez, D.; James, P. S.; Freedman, N.; Lab, M. J.; Jones, R.; Klenerman, D.; Korchev, Y. E.** ***Angewandte Chemie International Edition*** **2006,** ***45,*** **2212-2216.**

(23) **Korchev, Y. E.; Raval, M.; Lab, M. J.; Gorelik, J.; Edwards, C. R. W.; Rayment, T.; Klenerman, D.** ***Biophys. J.*** **2000,** ***78,*** **2675-2679.**

(24) **Bruckbauer, A.; Ying, L.; Rothery, A. M.; Zhou, D.; Shevchuk, A. I.; Abell, C.; Korchev, Y. E.; Klenerman, D.** ***J. Am. Chem. Soc.*** **2002,** ***124,*** **8810-8811.**

(25) **Wei, C.; Bard, A. J.; Nagy, G.; Toth, K.** ***Anal. Chem.*** **1995,** ***67,*** **1346-1356.**

(26) **Nitz, H.; Kamp, J.; Fuchs, H.** ***Probe Microscopy*** **1998,** ***1,*** **187--200.**

(27) **Ying, L.; White, S. S.; Bruckbauer, A.; Meadows, L.; Korchev, Y. E.; Klenerman, D.** ***Biophys. J.*** **2004,** ***86,*** **1018-1027.**

(28) **Newman, J.** ***Journal of The Electrochemical Society*** **1966,** ***113,*** **501-502.**

(29) **Burnett, D. S.** ***Finite Element Analysis*****; Addison-Wesley: Reading, MA, 1987.**

(30) **Wei, C.; Bard, A. J.; Feldberg, S. W.** ***Anal. Chem.*** **1997,** ***69,*** **4627-4633.**

Chapter 4: Silver Particle Nucleation and Growth at Liquid/Liquid Interfaces: A Scanning Electrochemical Microscopy (SECM) Approach

4.1 Introduction

The unique properties of liquid/liquid (L/L) interfaces, such as freedom from defect sites and the fact that the interfacial potential can be altered, make it an interesting environment for metal deposition via assembly of pre-formed particles or interfacial growth.[1-14] The basic processes of nucleation and growth at L/L interfaces are similar to solid electrodes, i.e., formation of a nucleus, which grows after reaching a critical size[15] to form a particle,[5-9] film[11,14] or cluster.[12] However, for metal nucleation at L/L interfaces, the metal ion precursor and reducing agent are located in different liquid phases and the interaction energy between the metal phase formed and the interface is smaller compared to that at solid electrode substrates. In essence, metal deposition at L/L interfaces is considered to be a useful intermediate case between solution phase metal reduction (relevant to many preparations of metallic particles) and conventional electrodeposition.[5] There are wide-ranging applications of metal particles in various areas, such as electrochemistry,[16] homogeneous and supported

catalysis,[17] solid phase synthesis,[18] bioanalyis[19] and materials science.[20] The electrodeposition of metal particles at L/L interfaces represents an alternative method to traditional chemical and electrochemical methods for preparing and immobilizing metal particles.[8]

Initial research on the formation of metals at L/L interfaces can be traced back to the 19th century when Faraday formed colloidal gold particles at a L/L interface using a carbon disulfide solution of phosphorus to reduce aqueous solutions of $AuCl_4^-$.[21] This method of spontaneous reduction of gold at L/L interfaces, with characterization and control over the deposit size, remains an active area of research. In 2003, Rao et al reported the interfacial reduction of gold at the water/toluene interface and they extended the method to the deposition of gold, silver and copper films at the interface.[11] Earlier, the formation of "liquid-like" films of silver by reduction of aqueous silver nitrate solutions in the presence of certain surfactants was described by Efrima and co-workers.[12]

The demonstration of metal deposition at an externally polarized L/L interface was reported by Guainazzi et al in 1975.[22] In this work, a copper layer was deposited at a water/DCE interface by applying a direct current across the interface between aqueous Cu^{2+} and organic $V(CO)_6^-$. Subsequently, Cheng and Schiffrin used an applied potential to control the rate of gold nanoparticle formation at an electrified L/L interface, due to reduction of organic-phase $AuCl_4^-$ by aqueous $Fe(CN)_6^{4-}$.[3] Polarization measurements at electrified L/L interfaces have been employed to investigate the deposition of palladium, platinum, palladium/platinum and silver particles on macroscopic and

membrane-supported L/L interfaces.[5,6,8-10] To minimize the extent of nucleation at the interface, Guo et al studied the deposition of individual silver particles at polarized micro- and nano-L/L interfaces, which were supported at the ends of tapered glass pipettes.[7]

Scanning electrochemical microscopy (SECM)[23] has become a versatile tool for performing electrochemistry in confined regions and facilitating electrochemical measurements at high spatial resolution.[24,25] SECM has been used for the modification of solid surfaces, such as metal deposition and metal semiconductor etching.[26] Of particular relevance to the studies herein, Mandler et al employed a micropipette as an SECM tip to form μm-size Ag deposits at a gold substrate by a potential assisted ion transfer across a L/L interface.[27] Later, they further developed this method by combining SECM with non-optical shear-force detection to significantly increase the lateral resolution of Ag deposition micropatterning.[28] A similar approach has also been used to study metal deposition at carbon nanotube-patterned surfaces.[29] By comparison, the use of SECM to form nanostructures at L/L interfaces is rather limited.

Although metal particle formation at L/L interfaces has been studied for many years, the mechanism and dynamics of particle formation at the interface are still unclear. In this work, SECM was employed to induce the electrodeposition of Ag particles by the electron transfer reaction between aqueous Ag^+ ions, generated by anodic dissolution of an Ag SECM tip,[30,31] and decamethylferrocene (DMFc) in DCE at a non-polarizable L/L interface. Factors affecting the deposition process, such as the tip-interface separation, the applied potential at the SECM tip, the concentration of the reductant in the DCE phase

and the reaction driving force, which was controlled by the concentration ratio of a common ion (ClO_4^-) in the two phases, were investigated by SECM potential-step chronoamperometry (electrogeneration of Ag^+ ions). A theoretical model was developed to simulate the experimental current-time curves to obtain quantitative information on the deposition process. Proof of Ag electrodeposition was further obtained through confocal microscopy visualization of the L/L interface.

4.2 Experimental Section

Chemicals. DMFc (Sigma-Aldrich, 97 %), silver nitrate ($AgNO_3$, Sigma-Aldrich, ≥ 99 %), lithium perchlorate ($LiClO_4$, Aldrich, 95+ %), tetrabutylammonium perchlorate ($TBAClO_4$, Fluka, ≥ 99 %), potassium nitrate (KNO_3, Fisher, > 99.5 %) and DCE (Sigma-Aldrich, HPLC grade) were used as received. Aqueous solutions were prepared from Milli-Q reagent water (Millipore Corp., resistivity 18.2 MΩ cm at 25 ºC), while the organic solvent was water-saturated DCE.

SECM setup for silver particle nucleation at the water/DCE interface. A schematic representation of the basic idea behind inducing and monitoring Ag particle nucleation at the water/DCE interface is shown in Figure 4-1(a). An Ag ultramicroelectrode (UME), positioned close to the water/DCE interface, is used to "inject" Ag^+ ions in a controllable way. At the interface, these electrogenerated Ag^+ ions react with the DMFc reductant to produce Ag particles. The cylindrical Teflon cell used had a glass body and was fully detachable. It was 4 cm in diameter and had a total volume of about 25 cm^3. The cell was filled with aqueous solution and DCE, as the top and bottom phases,

respectively. For most experiments, the aqueous phase contained 0.1 M $LiClO_4$ and the DCE phase contained 0.03 M DMFc and 0.1 M $TBAClO_4$, except where mentioned otherwise. Electrochemical measurements were made using a two-electrode arrangement. The working electrode was a 25 μm-diameter Ag disk-UME with an *RG* value of 10 (ratio of the overall tip radius to that of the silver disk), while a saturated calomel electrode (SCE) served as the reference electrode. Both electrodes were placed in the top aqueous phase. A model 750A bipotentiostat (CH Instrument, U.S.A.) was employed, controlled by a portable PC, for potentiostatic measurements. The whole setup was shielded by a home-built Faraday cage.

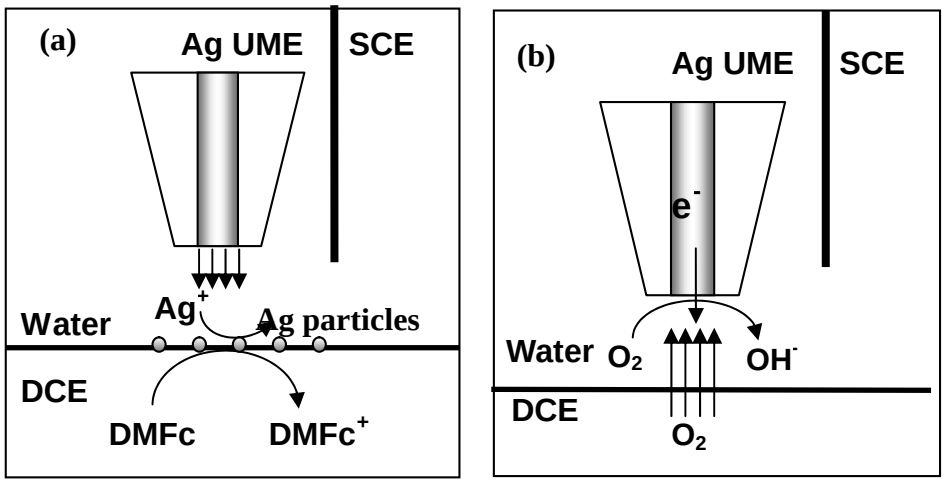

Figure 4-1. Schematic of the SECM setups for (a) Ag particle nucleation at the water/DCE interface and (b) distance setting between the UME and the water/DCE interface.

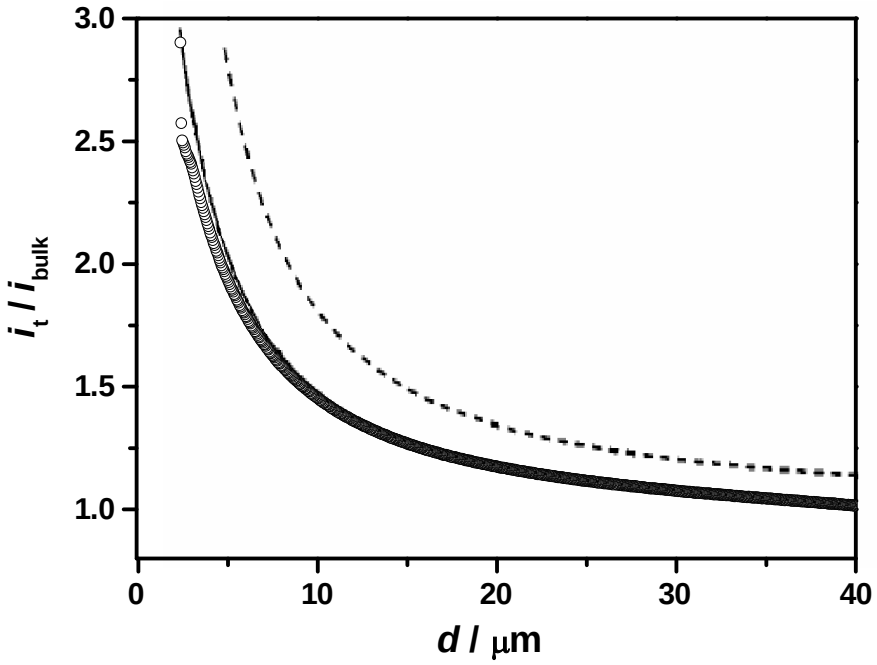

Figure 4-2. Experimental (○) approach curve recorded at a 25 μm-diameter Ag UME in an aqueous solution containing 0.1 M $LiClO_4$, translated towards a DCE solution containing 0.03 M DMFc and 0.1 M $TBAClO_4$. The UME potential was -0.8 V (vs. SCE) to promote the diffusion-limited reduction of oxygen (4-e^- process).[32] The scan speed was 0.5 μm s^{-1}. The solid line corresponds to the theoretical curve for the reduction of oxygen at a tip approaching a water/DCE interface with the parameters defined in the text.[32] The dashed line is the theoretical curve for diffusion-limited infinite-source transfer.[32]

Distance measurements. The SECM protocol for distance setting between the Ag UME and the L/L interface is shown schematically in Figure 4-1(b), in which oxygen was used as the redox mediator. By applying a potential of -0.8 V (vs. SCE) to the Ag UME for the diffusion-controlled reduction of oxygen, it was possible to accurately determine the distance between the UME and the interface by recording a steady-state current, i_t, normalized by the steady-state current in bulk solution, i_{bulk}, as the tip was translated towards the water/DCE interface. As shown in Figure 4-2 induced transfer of oxygen from the DCE phase, which

acted as a source of O_2 to the tip UME, was observed because the concentration and diffusion coefficient of oxygen in the DCE phase ($c_{O_2}^{DCE}$ = 1.39 mM, $D_{O_2}^{DCE}$ = 2.7×10^{-5} cm^2 s^{-1})[32] are higher than those in the aqueous phase ($c_{O_2}^{aq}$ = 0.25 mM, $D_{O_2}^{aq}$ = 2.2×10^{-5} cm^2 s^{-1}).[32] There is a good match between theory[32] and experiment with the parameters defined. Note that although transfer of oxygen from DCE enhances the tip current, the DCE phase does not act as an infinite source and so the approach curve current lies below that for this limiting case (dashed line in Figure 4-2). Experimental approach curves such as this allowed the distance between tip and interface to be determined precisely. For this particular case, which was typical, the distance of closest approach between the tip and interface was 2.2 μm.

Measurements of redox potentials. The redox potentials of $Ag/Ag^+_{(aq)}$ and $DMFc/DMFc^+_{(DCE)}$ needed to estimate driving forces were measured with respect to a common SCE reference electrode (in an aqueous phase). A 25 μm-diameter Ag UME was used for the $Ag/Ag^+_{(aq)}$ measurement and the potential was scanned from 0 to 0.40 V to induce the anodic dissolution of the Ag UME. The one-electron oxidation of DMFc was carried out at a 25 μm-diameter Pt UME in a DCE phase (0.1 M $TBAClO_4$) with two different concentrations of $LiClO_4$ (0.01 and 0.1 M) added to the aqueous phase. The applied potential was scanned from -0.4 to 0.3 V.

Microscopy measurements. Images of Ag particles formed at the water/DCE interface were obtained using a Zeiss LSM 510, Axioplan 2, upright confocal laser scanning microscope (CLSM) with a water immersion objective

lens (Zeiss, Achroplan 20x/50 M) and a 10x tube lens. Images were processed using the LSM Image Browser software (Zeiss).

An all-glass cylindrical cell was specially designed for the CLSM measurements. It comprised a top glass body (diameter: 4 cm, height: 2.5 cm) and a smaller bottom glass window (diameter: 2 cm, height: 0.8 cm). These two compartments were separated by a glass plate containing a 1 mm-diameter hole where the two liquid phases contacted. A glass tube (diameter: 0.5 cm, height: 2.3 cm) was connected to the lower compartment, so that the level of the bottom phase could be adjusted, if necessary, during the experiments.

The CLSM experiments were performed using a helium/neon laser (λ = 543 nm, 100% transmission intensity) and both reflection and transmission modes were employed. The lens of the confocal microscope was dipped into the top phase of the cell to obtain the images of the interface.

All experiments were carried out at ambient temperature (21 ± 1^{o}C) in an air-conditioned room.

4.3 Theory and Simulation

4.3.1 Description of models

Several models have been proposed for metal deposition processes at solid substrates.[4(a),33-38] Herein, the finite element method was used to obtain information on the kinetics of Ag particle formation at the water/DCE interface. We restrict our approach to one phase containing the Ag UME, which is possible because the analysis which follows focuses on conditions where the concentration of DMFc in DCE, c_{DMFc}, was in large excess compared to Ag^{+}

ions, and relatively short times were considered where depletion effects in the second phase would be negligible. The extension to two phases would be straight forward. Two models were involved in the one-domain system: first, the growth of Ag particles was described from a macroscopic point of view and second, a microscopic model was developed to inform the boundary conditions in the macroscopic model.

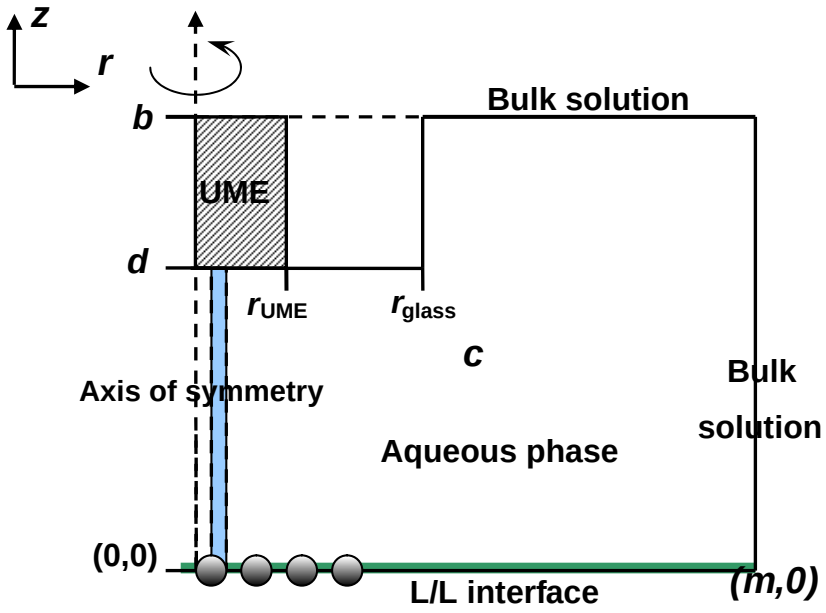

Figure 4-3. Simulation domain and coordinate system for the axisymmetric cylindrical geometry used in the one-domain macroscopic model. Particles are only shown to as a guide and not part of the domain of simulation. Green line represents the domain of simulation for the part of the model concerned with particle size.

4.3.2 Macroscopic model

The macroscopic model is used to describe the concentration of Ag^+ ions in aqueous solution and also the average particle size at the L/L interface. Necessarily, the two parts are coupled through the interfacial flux.

First, the part of the macroscopic model concerned with Ag^+ ion concentration is considered. The geometry of this part of the model is shown in Figure 4-3, using

axisymmetric cylindrical coordinates. The following diffusion equation was solved on the interior of this domain:

$$D\nabla^2 c = \frac{\partial c}{\partial t} \tag{4.1}$$

where D is the diffusion coefficient, and c is the concentration of Ag^+ ions in the aqueous solution, which varies both spatially and temporally.

The tip current for the oxidation of Ag UME is expressed by:

$$i_{\mathrm{UME}} = 2n\pi FD\int_0^{r_{\mathrm{UME}}} \left.\frac{\partial c}{\partial z}\right|_{z=d} r\,dr \tag{4.2}$$

where n is the number of electrons transferred (n = 1 for the anodic dissolution of Ag to form Ag^+ ions), F is the Faraday constant, r and z are the axisymmetric coordinates in the radial and normal directions, respectively, r_{UME} is the radius of the Ag UME and d is the distance between the Ag UME and the L/L interface. In this case, the diffusion coefficient of Ag^+ ions in water, D, was 1.6×10^{-5} cm^2 s^{-1}.[39] The origin (0, 0) is chosen to be the intersection of the axis of symmetry of the UME with the L/L interface.

Initially, no Ag^+ ions are present in solution, therefore:

$$t = 0,\ 0 < r < m,\ 0 < z < d:\ c = 0 \tag{4.3}$$

$$t = 0,\ r_{\mathrm{glass}} < r < m,\ d \le z < b:\ c = 0 \tag{4.4}$$

where m is the radius of the domain of simulation and b is the distance in the z-direction to which back diffusion behind the surface of the UME is considered.

After the potential step ($t > 0$), because the electrogeneration of Ag^+ ions is electrochemically reversible,[30] the boundary condition at the electrode surface is:

$$t > 0,\ 0 \le r \le r_{\mathrm{UME}},\ z = d:\ c = c^{*} \tag{4.5}$$

where c^{*} is the concentration of generated Ag^{+} ions at the electrode surface (governed by the applied potential). The insulating glass around the electrode is inert to Ag^{+} ions, so:

$$t > 0,\ r_{\mathrm{UME}} < r < r_{\mathrm{glass}},\ z = d:\ D\frac{\partial c}{\partial z} = 0 \tag{4.6}$$

$$t > 0,\ r = r_{\mathrm{glass}},\ d \le z < b:\ D\frac{\partial c}{\partial r} = 0 \tag{4.7}$$

where r_{glass} is the radius of the Ag UME plus glass body. At the axis of cylindrical symmetry, the boundary condition is:

$$t > 0,\ r = 0,\ 0 \le z < d:\ D\frac{\partial c}{\partial r} = 0 \tag{4.8}$$

Assuming no Ag^{+} ions would reach the edge of the domain in the bulk solution during the experiment,

$$t > 0,\ r_{\mathrm{glass}} \le r < m,\ z = b:\ c = 0 \tag{4.9}$$

$$t > 0,\ r = m,\ 0 \le z \le b:\ c = 0 \tag{4.10}$$

At the water/DCE interface, where the deposition of Ag particles occurs, the boundary condition can be written as:

$$t > 0,\ 0 < r < m,\ z = 0:\ D\frac{\partial c}{\partial z} = k^{*}(r_{\mathrm{p}})c \tag{4.11}$$

where k^* is the rate function for particle formation, which is derived in Section 4.3.3 from a microscopic model and is dependent on the local particle radius function defined on the interface, r_p, which varies over time as described in Section 4.3.4 and is a function of *r*, though it is not explicitly written as such.

The experimental results outlined below indicate that there is an additional flux at short times, which we treat as an adsorption process. In this instance, the boundary conditions at the interface (equation 4.11) is replaced by equation 4.12 [30].

$$t > 0,\ 0 < r < m,\ z = 0:\ D\frac{\partial c}{\partial z} = k^*(r_p)c + k_{ads}c(1-\theta) \qquad (4.12)$$

where k_{ads} is the kinetic rate constant for the adsorption process and θ is the fraction of adsorption sites occupied with Ag^+ ions at the L/L interface, a function of *r* and *t*. The variation of θ with time is described by:

$$N\frac{\partial \theta}{\partial t} = k_{ads}c(1-\theta) \qquad (4.13)$$

where *N* is the number of adsorption sites per unit area.

In this model, the L/L interface is approximated to be flat. For the simplest case, the UME current-time behaviour depends on the distance between the electrode and the L/L interface, *d*, the kinetic rate constants k^* and k_{ads}, the electrode surface concentration of generated Ag^+ ions, c^*, and the number of adsorption sites per unit area, *N*. The following microscopic model will show how we converted the flux obtained in the microscopic model to a rate constant in the macroscopic simulation.

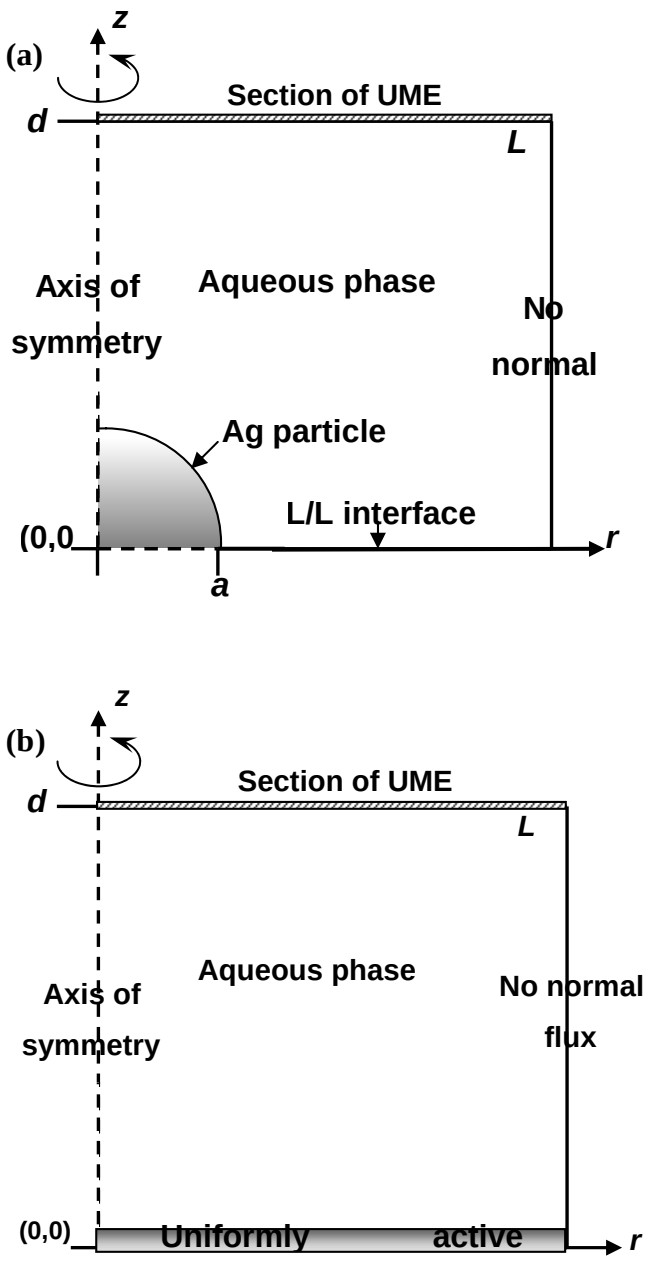

Figure 4-4. (a) Simulation domain and coordinate system for the axisymmetric cylindrical geometry used in the one-domain microscopic model and (b) the domain for a flat interface with a layer of Ag particle formed to which the model is equated.

4.3.3 Microscopic model

The geometry for the microscopic model is shown in Figure 4-4(a), corresponding to the region in the aqueous phase marked with a blue colour in the macroscopic model in Figure 4-3. Instantaneous nucleation is considered,

which is reasonable given that we wish to focus on the initial process and even progressive nucleation collapses to an instantaneous process at sufficiently short times.[40] Furthermore, for externally polarized microscale-L/L interfaces, we have shown that Ag nucleation and growth areas appear to be best described as an instantaneous process.[7] A number of seed particles separated by an average particle-particle spacing of 2*L* are considered at $t > 0$, which are allowed to grow based on the flux to them. Only one cross-section of an Ag particle at the interface is simulated due to the axisymmetric nature of the problem. The steady-state diffusion problem (equation 4.14) was solved in the interior of this domain.

$$D\nabla^2 c = 0 \tag{4.14}$$

The tip current for the oxidation of the Ag UME is similar to equation 4.2, except the domain of integration is restricted only to the portion of UME simulated. The boundary conditions are:

$$a < r < L,\ z = 0:\ D\frac{\partial c}{\partial z} = 0 \tag{4.15}$$

$$r = L,\ 0 \le z \le d:\ D\frac{\partial c}{\partial r} = 0 \tag{4.16}$$

$$0 \le r < L,\ z = d:\ c = c^* \tag{4.17}$$

$$r = 0,\ a < z < d: \tag{4.18}$$

where *a* is the radius of the particle.

The boundary condition on the Ag particle surface is expressed by equation 4.19.

$$0 \le r \le a,\ z = \sqrt{a^2 - r^2}: D\nabla \cdot \mathbf{n} = kc \tag{4.19}$$

where $\mathbf{n}$ is the inward pointing unit normal and k is the rate constant on the surface of the particle.

The flux (as a function of a), calculated for the model illustrated in Figure 4-4(a), was used to determine the rate constants, k^*, (also a function of a) necessary to achieve an equivalent flux on the uniformly active surface illustrated in Figure 4-4(b). The derivation is outlined below. Note, to ease notation, k^* is not explicitly written as a function of a.

First, the relationship between J, the total flux in the model in Figure 4-4(b), and the current density at the Ag UME, j, is given by

$$J = \pi L^2 j \tag{4.20}$$

In this system, j was dependent on the reaction rate constant k^* by:

$$j = D\left(\frac{c^* - c^{\text{inter}}}{d}\right) = k^* c^{\text{inter}} \tag{4.21}$$

where c^{inter} is the concentration of Ag^+ ions at the water/DCE interface. From equation 4.21, k^* can be expressed by

$$k^* = \frac{D}{c^{\text{inter}}}\left(\frac{c^* - c^{\text{inter}}}{d}\right) \tag{4.22}$$

Combining equations 4.20 and 4.21,

$$\frac{J}{\pi L^2} = D\left(\frac{c^* - c^{\text{inter}}}{d}\right) \tag{4.23}$$

Then from equation 4.23, c^{inter} is given by:

$$c^{\text{inter}} = c^* - \frac{Jd}{D\pi L^2} \tag{4.24}$$

Inputting equation 4.24 into equation 4.22, the relationship between k^* and J is written as

$$k^* = \frac{D}{\left(c^* - \frac{Jd}{D\pi L^2}\right)}\left[\frac{c^* - \left(c^* - \frac{Jd}{D\pi L^2}\right)}{d}\right] \qquad (4.25)$$

Equation 4.25 is further simplified to:

$$k^* = \frac{JD}{D\pi L^2 c^* - Jd} \qquad (4.26)$$

Many simulations were preformed using the model illustrated in Figure 4-4(a). The corresponding fluxes were used to determine k^* as a function of a, which was implemented in the macroscopic model using an interpolating function.

4.3.4 Particle growth application mode

As described above, the boundary conditions at the L/L interface are dependent on the particle size. A set of equations are described below which relate the flux at the L/L interface to the average particle size, which is a function of r and time (t). For ease of notation, the dependence on r is dropped.

Both the volume and radius of the Ag particle formed are dependent on time (t):

$$\text{Vol}(t) = \frac{4}{3}\pi a(t)^3 \qquad (4.27)$$

Then, it follows that

$$\frac{d\text{Vol}(t)}{dt} = 4\pi a(t)^2 \frac{da(t)}{dt} \qquad (4.28)$$

So

$$\frac{da(t)}{dt} = \frac{1}{4\pi a(t)^2}\frac{d\text{Vol}(t)}{dt} \qquad (4.29)$$

The rate of volume change is proportional to the flux to the particle, so in our situation

$$\frac{d\mathrm{Vol}(t)}{dt} = \frac{1}{\rho} AD \left.\frac{\partial c}{\partial z}\right|_{z=0} \tag{4.30}$$

where ρ is the Ag molar density, which was calculated from the Ag density[41] as 97.3 mol dm^{-3}, and A is the whole area of a single particle at the interface, which is equal to πL^2. Thus,

$$\frac{da(r,t)}{dt} = \frac{A}{4\pi\, a(r,t)^2\, \rho} D \left.\frac{\partial c(r,z,t)}{\partial z}\right|_{z=0} \tag{4.31}$$

According to equation 4.31, the rate of change of the particle radius can be deduced from the interfacial flux.

The mass transport problem outlined was modelled using a commercial finite element method modelling package (Comsol Multiphysics, Version 3.3a), in conjunction with MATLAB (Version 7.4.0 (R2007a)). This was run on a Dell desktop PC (4 GB RAM and a 2.52 GHz Pentium 4 Processor) running Windows XP. The problem was solved in real space to allow direct analysis of the experimental data. In the model described, the distances into which bulk solution was simulated, i.e., *m* and *b*, were empirically determined by running simulations of increasingly large domain until no change in the tip current was observed. The number and density of mesh elements were again determined heuristically, through successive refinements of the mesh until no change in the current was observed.

4.4 Theoretical results and discussion

As stated above, the anodic tip current response is sensitive to the interaction of Ag^+ ions with the water/DCE interface, notably the rate constant for Ag particle growth at the particle surface, k, the concentration of generated Ag^+ ions at the electrode surface, c^*, the tip-interface separation, d, and the average particle-particle half spacing, L. The aim of this section is to analyze the Ag particle nucleation process based on the theoretical models we developed above and to examine the effects of the above parameters on the tip current response. As discussed above, a relatively short time scale of 1 s was considered to simplify the analysis.

4.4.1 Ag particle growth at the interface with time

Firstly, we consider an example of the current-time characteristics to a series of typical parameters, specifically a large rate constant, k = 10 cm s^{-1}, c^* = 1.0 mM, d = 4 μm and $L = 7\times10^{-5}$ cm. A typical simulated current-time curve is shown in Figure 4-5 and compared to the limiting behaviour for an inert interface. Initially, the behaviour is similar to that for an inert interface, since the electrogenerated Ag^+ ions in the aqueous phase have to diffuse to the interface and nucleate Ag particles, and then grow, consuming an increasing flux of Ag^+ ions with time. At longer times, specifically after 0.03 s, the formation of Ag particles at the L/L interface from the reaction between generated Ag^+ ions and DMFc causes the flux of Ag^+ ions to the interface to increase, resulting in an enhancement of the tip current with time.

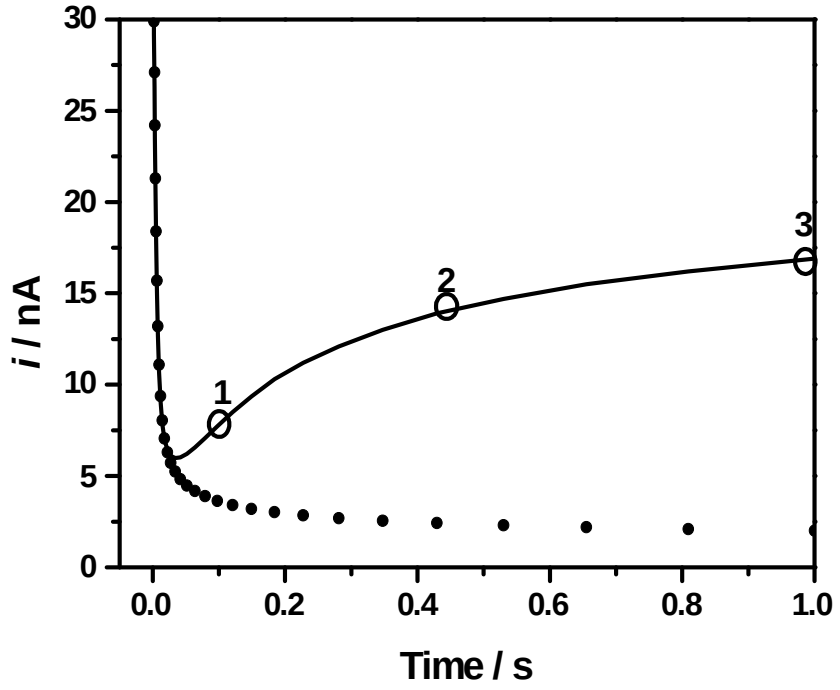

Figure 4-5. Simulated current-time characteristics (solid curve) over a period of 1 s for a nucleation process characterized by k = 10 cm s^{-1}, C^* = 1.0 mM, d = 4 μm and $L = 7\times10^{-5}$ cm. The dotted curve is the theoretical curve corresponding to no nucleation process (k = 0), i.e., an inert interface.

Figure 4-6 shows a sequence of concentration profiles of electrogenerated Ag+ ions in the aqueous solution, c, in a small domain below the electrode (d = 4 μm) for three simulation times, corresponding to the points labelled 1, 2 and 3 in Figure 4-5 (NB: length scales vary on r and z axes). In Figure 4-6(a), corresponding to a short time of 0.1 s, c decreases only slightly from its defined value at the tip surface (C^* = 1.0 mM), to about 0.8 mM at the part of the interface directly under the centre of the tip. There is also some lateral dispersion of Ag+ ions, because of the small interfacial flux of Ag+ ions used to form Ag particles at the L/L interface at this short time. With prolonged simulation time, a

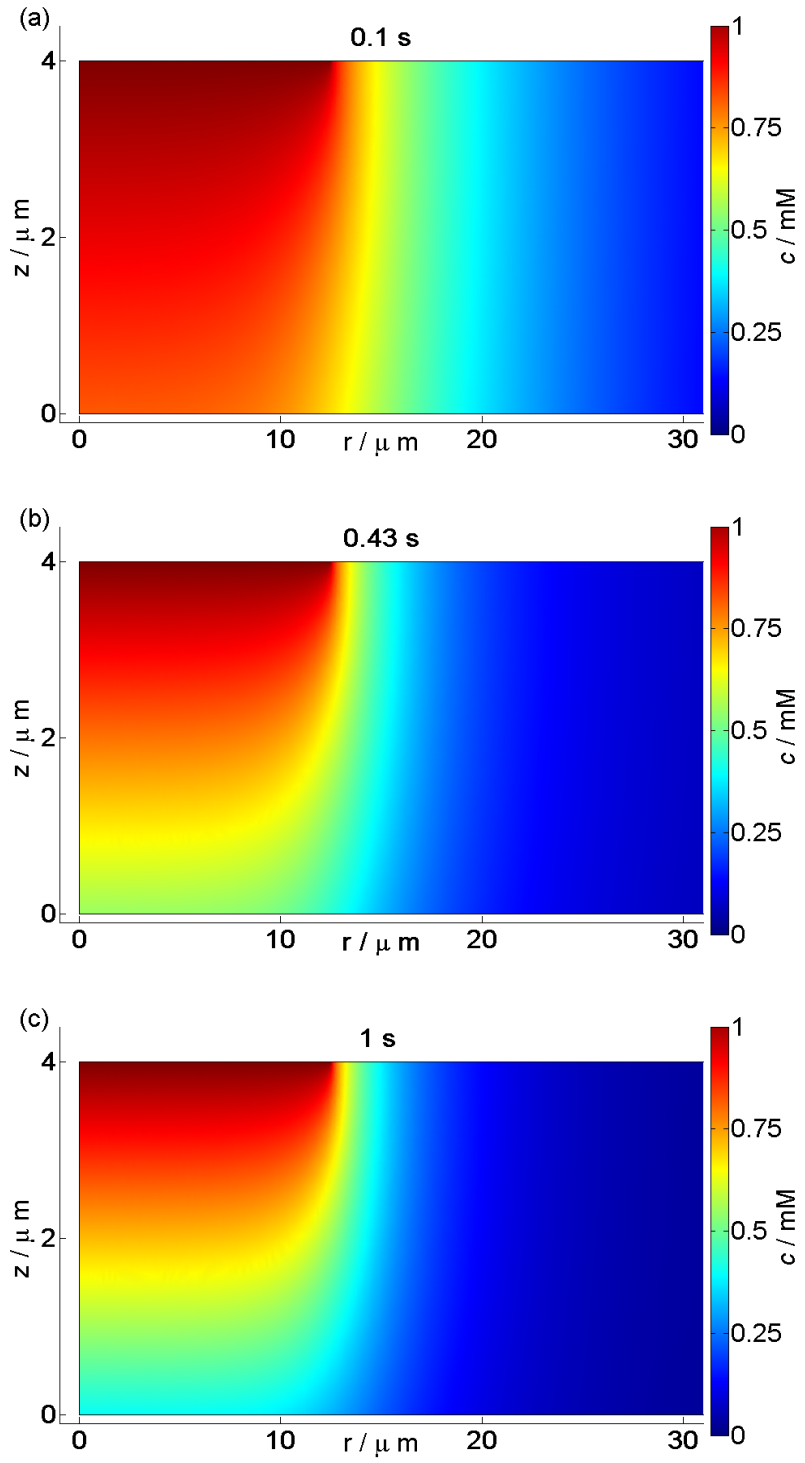

Figure 4-6. Simulated concentration profiles for electrogenerated Ag+ ions, c, in the aqueous phase at time scales of (a) 0.1 s, (b) 0.43 s and (c) 1 s. The parameters used for simulation were the same as for Figure 4-5. NB: Horizontal and vertical length scales are not in proportion.

more extensive decrease of *c* at the L/L interface can be seen in Figure 4-6(b) and (c), with values of *c* at the part of the interface directly below the tip of about 0.5 and 0.4 mM, respectively, for 0.43 and 1 s. The corresponding steepening of the concentration profiles, due to the consumption of Ag^+ ions in the nucleation and growth process, is reflected in the enhanced tip currents at these times. It should be noted that at a time of 1 s, the flux of Ag^+ ions is highly focused towards a portion of the interface that approximates to the UME size. This has implications for the form of experimental transients, at long times, reported later (see Sections 4.5.1 and 4.5.2).

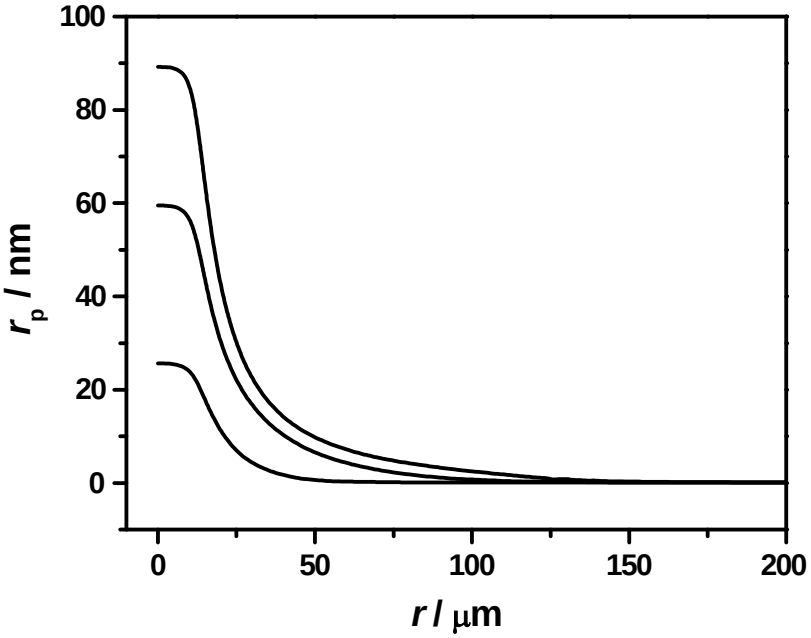

Figure 4-7. Simulated radius of particles formed at the interface, rp, as a function of radial distance, r, for different times. From bottom to top, the simulation times were 0.1, 0.43 and 1 s, respectively. The parameters used for simulation were the same as for Figure 4-5.

The model also provides information on the particle size distribution at the interface with time. Figure 4-7 shows the particle radius, r_p, as a function of radial distance, r, at the interface at several simulation times (0.1 s, 0.43 s and 1 s). For each time, as the radial distance, r, increases, there is a gradual decrease of r_p, which is because particle nucleation and growth occurs most significantly in the region of the L/L interface closest to the location of the UME. With prolonged simulation times, the particle radius becomes greater and particles grow to some extent in a larger portion of the interface. However, in general, the simulation result further confirms that the growth process is largely confined to region of the L/L interface similar in size to the UME.

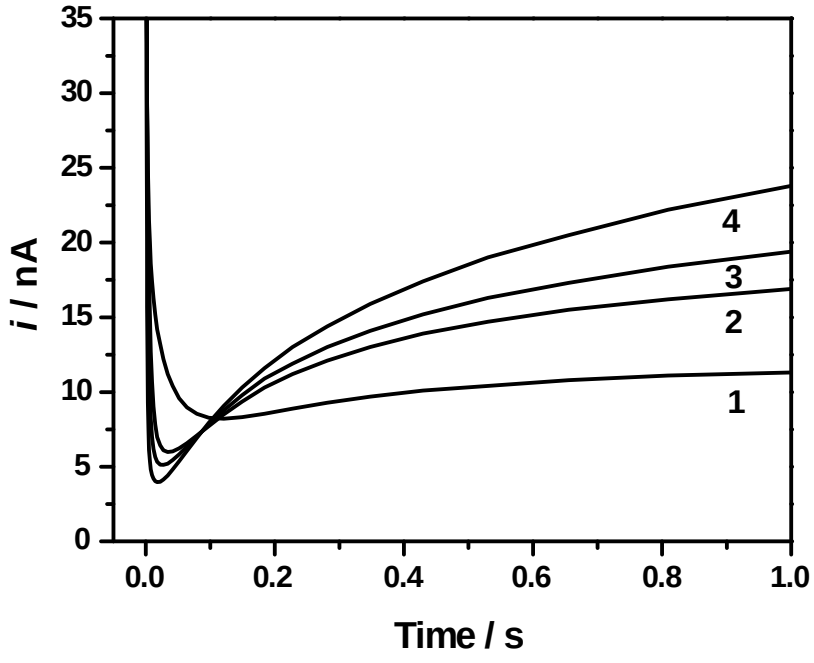

Figure 4-8. Simulated current-time curves over a time period of 1 s for tip-interface separations, *d*, of (1) 10 μm, (2) 4 μm, (3) 3 μm and (4) 2 μm. Other simulation parameters were: k = 10 cm s^{-1}, C^* = 1.0 mM and $L = 7\times 10^{-5}$ cm.

4.4.2 Effect of tip-interface distance

The effect on the tip current-time response of varying the tip-interface distance, *d*, while keeping other parameters constant, is shown in Figure 4-8 for k = 10 cm s^{-1}, c^* = 1.0 mM and $L = 7\times10^{-5}$ cm. The general form of the transients was explained above in the discussion of Figure 4-5. Here, it can be seen that decreasing the tip-interface separation, *d*, causes a larger difference between the extremes of an essentially inert surface at short times and active surface at longer times because the smaller the value of *d*, the higher the mass transport challenge on the interface, as evident in earlier SECM transient studies of interfacial reactivity.[42,43]

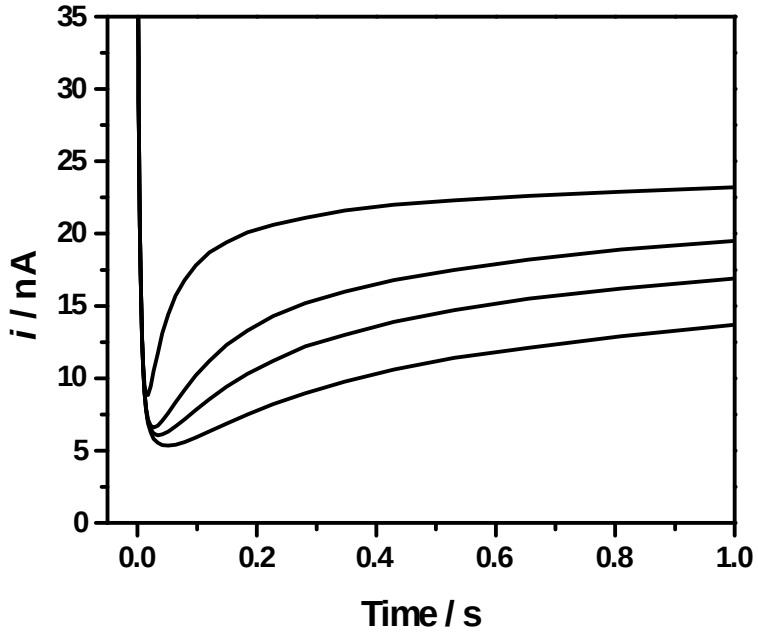

Figure 4-9. Simulated current-time curves over a time period of 1 s for several values of the particle-particle half spacing, L. From bottom to top, the values of L were 1×10^{-4}, 7×10^{-5}, 5×10^{-5} and 2×10^{-5} cm, respectively. Other simulation parameters were: k = 10 cm s^{-1}, C^* = 1.0 mM and d = 4 μm.

4.4.3 Effect of particle-particle half spacing

The particle-particle half spacing, L, is also a very important parameter for this system. A large value of L corresponds to a small density of nucleation sites and this naturally means the net growth process is less extensive, for a given rate constant; certainly at short times. Figure 4-9 shows simulated current-time curves for four different values of L (1×10^{-4}, 7×10^{-5}, 5×10^{-5} and 2×10^{-5} cm). As expected, at any time after the Ag^{+} ion diffusion field intercepts the L/L interface, decreasing L has the effect of increasing the tip current. Furthermore, the smaller the value of L, the more sharply the tip current increases during the growth phase.

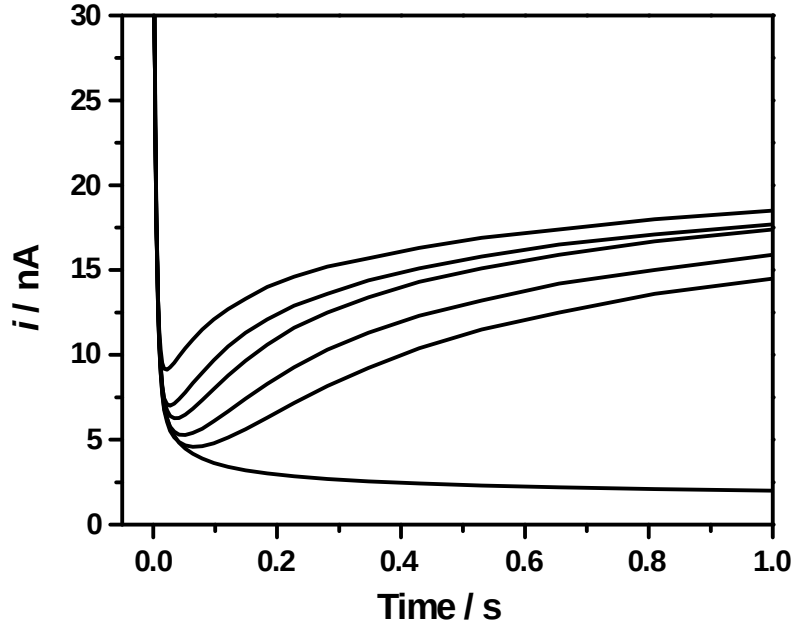

Figure 4-10. Simulated current-time curves over a time period of 1 s for several rate constants, *k*, for Ag particle growth. From bottom to top, the values of *k* were 0, 4, 6, 10, 20 and 1000 cm s^{-1}, respectively. Other parameters were: c^{*} = 1.0 mM, *d* = 4 μm and *L* = 7×10^{-5} cm.

4.4.4 Effect of reaction rate constant

The reaction rate constant for Ag particle growth at the particle surface, *k*, clearly determines the growth rate and thus the form of the tip current transient. This can be seen in Figure 4-10, in which the tip current-time response was simulated for six reaction rate constants including a value close to the limit of most rapid growth (k = 1000 cm s^{-1}) and no growth (k = 0). The tip current increases with *k*, because *k* controls the rate of growth of Ag particles at the water/DCE interface, leading to an enhancement of the flux of generated Ag^+ ions away from the tip electrode. It can be seen that the tip current is rather sensitive to the rate constant over a wide range of values (see captions to Figure 4-10). Significantly, large rate constants can be characterized by this technique because the initial nuclei are so small that the mass transport rate to individual particles is extremely high.

4.4.5 Effect of Ag+ ion adsorption at the interface

In light of the experimental results which follow, the effect of the adsorption of Ag^+ ions at the L/L interface on the tip current response was examined. The treatment which follows is general and could involve electron transfer coupled to adsorption as well as simple adsorption. As stated in Section 4.3.2 two parameters are used to quantify the adsorption process, the adsorption rate constant, k_{ads}, and the adsorption sites per unit area, *N*. It is reasonable to consider an essentially irreversible process because the adsorption process will be driven in that direction by the electrogenerated flux of Ag^+ ions towards the L/L interface. The effect of k_{ads} was studied in this section with $N = 9 \times 10^{-10}$ mol cm^{-2}, which would be consistent with (maximum) monolayer coverage. Typical

current-time curves are shown in Figure 4-11 for an adsorption process with k_{ads} in the range 0.01 cm s^{-1} to 0.1 cm s^{-1}, coupled to nucleation and growth characterized by k = 10 cm s^{-1} and $L = 1.0\times10^{-4}$ cm. The other parameters were $c^* = 1.0$ mM and d = 4 μm. For comparative purposes, data are also shown for $k_{ads} = 0$. It can be seen that adsorption causes the minimum in the i-t curves to be much less pronounced, because adsorption provides an extra sink of the ion flux from the electrode. With a faster adsorption process, there is an increasingly pronounced current enhancement at the shortest times (t < 0.05 s) and the minimum in the i-t curve actually shifts to longer times, compared to the case shown with no adsorption. It is important to note that at long times, the

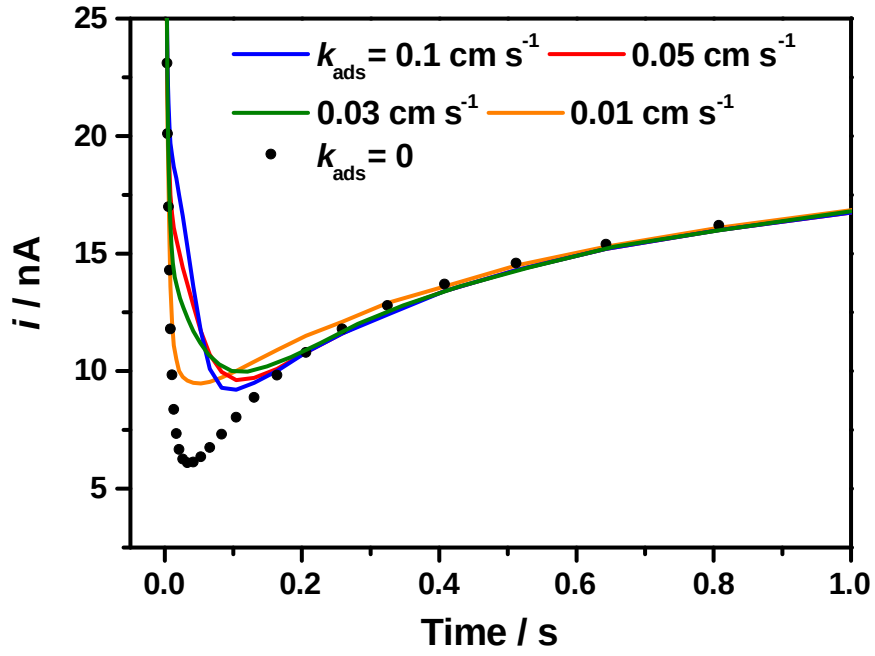

Figure 4-11. Simulated current-time curves over a time period of 1 s for several values of k_{ads} (shown in the figure). Other parameters were: k = 10 cm s^{-1}, c^* = 1.0 mM, d = 4 μm, $L = 1.0\times10^{-4}$ cm and $N = 9\times10^{-10}$ mol cm^{-2}. The limiting case of no adsorption is shown by the dotted curve.

adsorption process is essentially complete and this portion of the *i*-*t* curve ($t > 0.4$ s) is similar for all cases.

4.5 Experimental Results and Discussion

4.5.1 Growth of Ag particles at the water/DCE interface

Metal deposition occurs at L/L interfaces by an interfacial reduction process between a metal precursor located in the aqueous phase and a reducing agent in the organic phase. Given a suitable interfacial potential difference, heterogeneous electron transfer from the organic redox couple to the aqueous metal ion takes place, leading to the electrodeposition of a metal phase at the interface. In this system, the difference of the redox potentials of the aqueous Ag/Ag^+ couple and organic electron donor, $DMFc/DMFc^+$ couple, may drive the interfacial reduction of the aqueous phase silver ion to solid metallic silver at the interface. The net process is:

$$Ag^+_{(aq)} + DMFc_{(o)} \rightarrow Ag_{(s)} + DMFc^+_{(o)} \quad (4.32)$$

The large difference in the standard potentials of the two redox couples suggests that this electron transfer reaction may occur spontaneously when the two phases are brought into contact. This was readily proven: when an aqueous solution containing 1 mM $AgNO_3$ and 0.1 M $LiClO_4$ was shaken with a DCE solution containing 2 mM DMFc and 0.1 M $TBAClO_4$ for about 30 s, a dark layer formed at the interface, evident of Ag formation. The DCE solution changed from yellow to the green after the reaction, which indicates the production of $DMFc^+$ from the yellow-coloured DMFc.

In the SECM experiments, Ag^+ ions in the aqueous phase were provided by applying an appropriate oxidation potential to the UME probe:

$$Ag \rightarrow Ag^+ + e^- \quad (4.33)$$

The flux of electrogenerated Ag^+ ions from the UME surface was controlled by the applied potential at the electrode, since this controlled the surface concentration c^*, based on equation 4.34:

$$E_{Ag/Ag^+} = E^{0'}_{Ag/Ag^+} + \frac{RT}{F}\ln c^* \quad (4.34)$$

where E_{Ag/Ag^+} is the potential applied to the electrode, $E^{0'}_{Ag/Ag^+}$ is the formal potential for the Ag/Ag^+ couple, R and T are the gas constant and temperature, respectively.

Figure 4-12(a) is a linear sweep voltammogram of Ag oxidation at the Ag UME in the aqueous solution. A significant oxidation current flows at potentials more anodic than 0.3 V, which we have shown previously to follow a Nernstian response.[30,44] Figure 4-12(b) is a series of current-time curves, obtained by stepping the potential from a value where no current flowed to various anodic values. In each case, immediately after the potential step, the UME current starts high and rapidly decays to a steady-state potential-dependent value. Again these transients have been shown to have the form of a diffusion-controlled process.[30,44] From these responses, the steady-state limiting currents, recorded at the Ag UME with different applied potentials in the bulk solution (i_{bulk}), could be obtained, from which the corresponding electrode surface concentrations were deduced from equation 4.35:

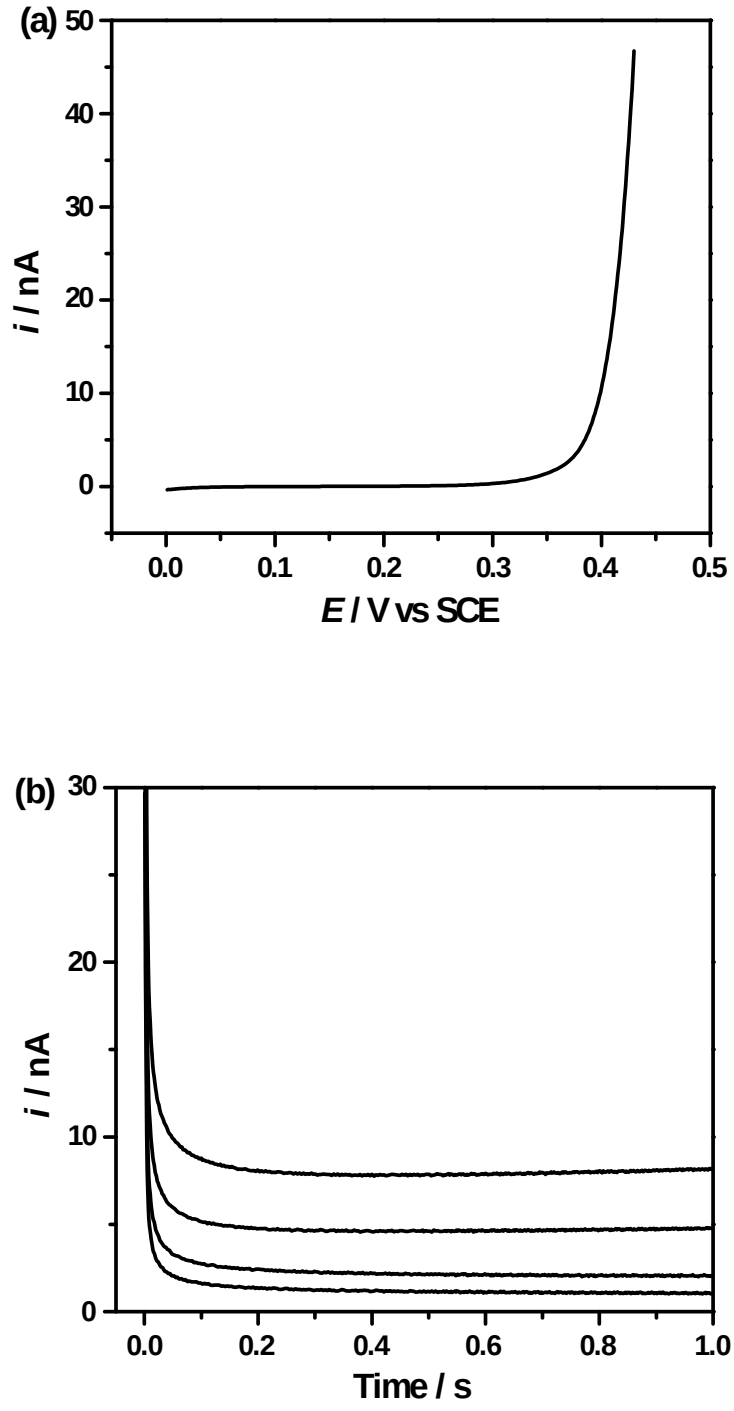

Figure 4-12. (a) Voltammogram of Ag oxidation from a 25 μm-diameter Ag disk-UME in an aqueous solution containing 0.1 M $LiClO_4$. The scan rate was 20 mV s^{-1}. (b) Current-time curves recorded at the Ag UME in bulk solution with different applied potentials of 0.34, 0.36, 0.38 and 0.39 V (vs. SCE) (from bottom to top).

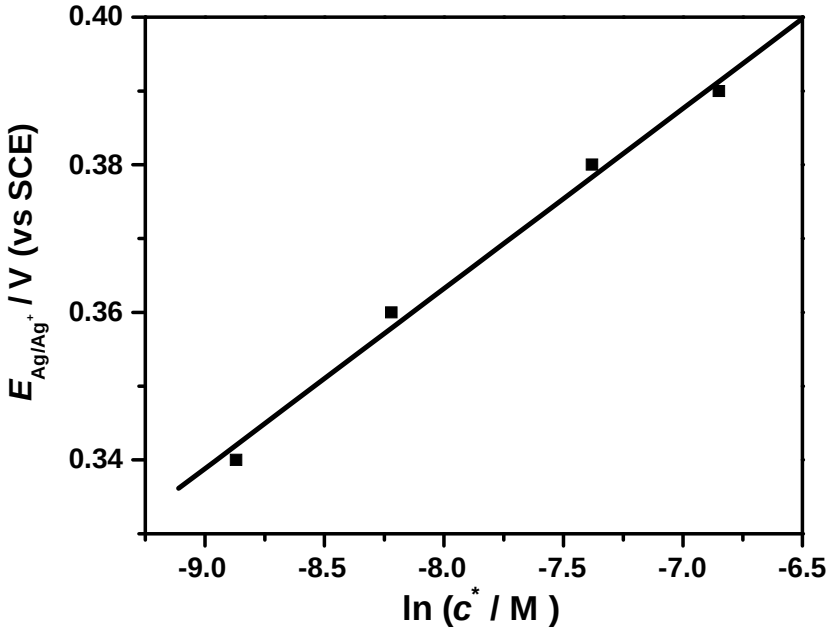

Figure 4-13. Plot of E_{Ag/Ag^+} vs. ln(c^*).

$$i_{bulk} = 4nFDr_{UME}c^* \tag{4.35}$$

The resulting plot of E_{Ag/Ag^+} vs. ln(c^*), shown in Figure 4-13, is linear with a slope of 0.0244 V, close to the value of *RT/F* at 22℃, 0.025 V. This analysis, and our earlier work,[30,44] proves that the Ag/Ag^+ couple is entirely reversible on the SECM scale, essential for the studies which follow.

To minimize the effect of the diffusion of the organic electron donor DMFc on the kinetics of the overall reaction, the concentration of DMFc (c_{DMFc}) in the DCE phase was kept in significant excess over that of Ag^+ ions (c) in the aqueous phase and the quantitative analysis of current-time curves focused on short times, i.e., on the initial nucleation and growth phase, as stated in the theory section. This time region was most compatible with the assumptions and

simplifications of the model, which considered instantaneous nucleation of well-defined spherical particles. The transfer of the common ion of the supporting electrolytes in the two phases, ClO_4^-, across the interface maintained the electroneutrality of the reaction.

After positioning the Ag UME very close to the water/DCE interface (as described in the experimental section), a chronoamperometric measurement of Ag anodic dissolution was made by applying a potential step from 0 V to the desired potential, recorded over a period of 2 s. A typical result is shown in Figure 4-14 (solid curve) alongside the behaviour that would have been expected for a completely inert L/L interface. The experimental current flow reflects the

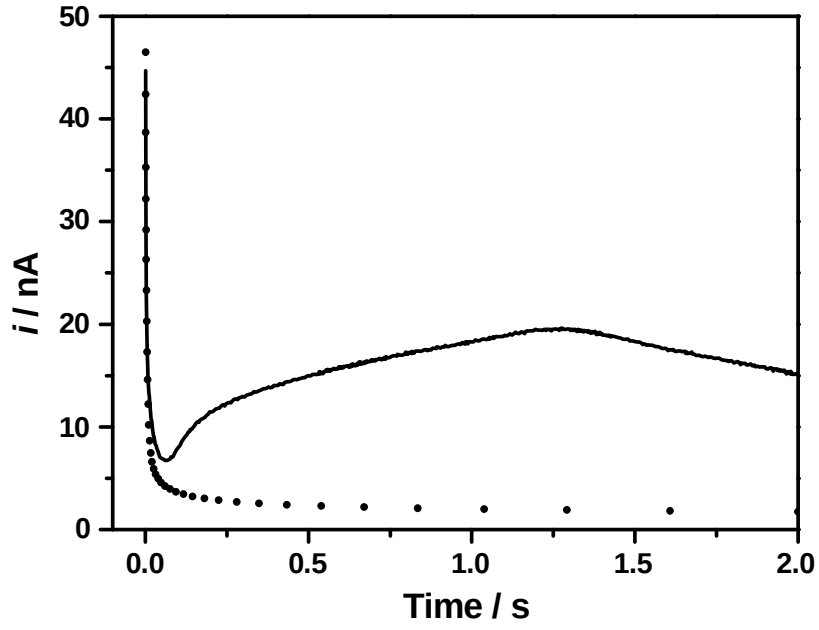

Figure 4-14. A current-time transient (solid curve) recorded at a 25 μm-diameter Ag UME in an aqueous solution with a potential step from 0 to 0.39 V (vs SCE). The aqueous solution contained 0.1 M $LiClO_4$ and the DCE phase contained 0.03 M DMFc and 0.1 M $TBAClO_4$. The distance between the UME and interface was 3.8 μm. The dotted curve is the theoretical behaviour for an inert interface.

rate of diffusion of Ag^+ ions from the electrode and the interaction of Ag^+ ions with the interface, which is linked to the process of Ag particle nucleation at the interface, as discussed earlier. Except at the very shortest times, when the Ag^+ ion flux from the UME has not interacted with the L/L interface, the current response (top solid curve) is always higher than that for an inert interface (bottom dotted curve).

The enhanced current response of the UME probe is indicative of nucleation and growth of Ag particles at the water/DCE interface, due to the interfacial reaction of Ag^+ ions with DMFc. This process leads to an enhancement of the flux of Ag^+ ions away from the UME, which is manifested in the current response shown. In essence, to maintain the concentration of Ag^+ ions at the Ag UME, at a value dictated by the Nernst equation for this reversible couple (eq. 4.34), Ag^+ ions are generated at a greater rate due to their increasing consumption in the growth of Ag particles at the L/L interface. It is interesting to note that at about 1.2 s in Figure 4-14, the current reaches a maximum value and then decreases. We attribute this to the growth process becoming partly limited by the concentration of DMFc in the DCE phase which, even though at high concentration, gradually becomes depleted.

As discussed in Section 4.4.1, Ag deposition occurs at a spot about the size of the electrode. The absolute maximum current that DMFc can sustain is $4nFD_{\mathrm{DMFc}}c_{\mathrm{DMFc}}\gamma$ (where γ is radius of the Ag deposit), which is about 100 nA. In Figure 4-14, the highest tip current recorded for the generation of Ag^+ ions is about 20 nA, which is around 20% of the maximum current that DMFc can

sustain. Thus, the formation of Ag particles at the interface causes the local depletion of DMFc in the DCE phase.

4.5.2 Effects of experimental parameters on the kinetics of Ag particle nucleation at the interface.

Effect of tip-interface distance. To be most sensitive to Ag particle nucleation at the water/DCE interface, the SECM tip should be placed close to the interface,[30] as discussed earlier in the theoretical section. Current-time transients for Ag^+ ions electrogeneration at different tip-interface distances (in

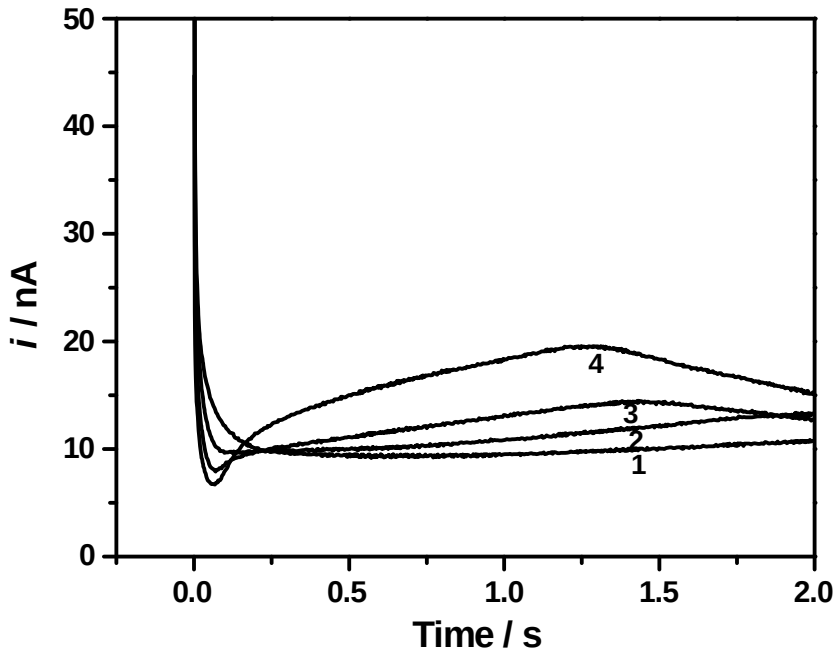

Figure 4-15. Current-time transients recorded at a 25 μm-diameter Ag UME in an aqueous solution as a function of the tip-interface separation. The aqueous phase contained 0.1 M $LiClO_4$ and the DCE phase contained 0.03 M DMFc and 0.1 M $TBAClO_4$. The UME potential was stepped from 0 to 0.39 V (vs SCE). From curve 1 to 4, the tip-interface separations were 9.2, 7.3, 5.8 and 3.8 μm, respectively.

the range of 9.2 to 3.8 μm), depicted in Figure 4-15, confirm this point

experimentally. The data in Figure 4-15 show that the tip current response becomes most sensitive to the interfacial process (most pronounced current minimum at short times; highest current at longer times) as the tip-interface separation decreases. This is entirely consistent with the simulation results presented above.

As discussed in the theory and simulation section, the closer the tip-interface separation, the greater the mass transport challenge provided by the SECM technique and so the lower the current value attained during the period of initial nucleation. Then, as the particles grow, the current increases steeply with time, because the growth flux becomes increasingly strong. By contrast, at greater tip-interface separations, these effects - the minimum and the rise in current - are somewhat washed out, as the lower mass transport (challenge) does not place such demands on the interfacial process. Clearly, the closer the tip-interface separation, the earlier and greater the maximum in the current response before a longer time decline is observed, due to DMFc depletion in the DCE phase which leads to a diminution of the growth flux. It can be seen in Figure 4-15 that the current decrease in this time domain is most significant for the closer tip-interface separations (3.8 and 5.8 μm), whereas it is barely evident for the larger tip-interface separations (7.3 and 9.2 μm).

The data in Figure 4-15 highlight the sensitivity of this method for following interfacial Ag deposition. Based on this experiment, a typical tip-interface separation in the range 3-5 μm was chosen in most of the SECM experiments that follow, to ensure the current response was sufficiently sensitive to the nucleation and growth process.

Effect of the applied UME potential. Figure 4-16(a) shows current-time transients recorded at the Ag UME with different potentials of 0.37, 0.38, 0.39 and 0.4 V applied to the UME. As shown in the figure, the transient current responses show a marked dependence on the applied potential: notably, following the initial minimum, the current increases earlier and more steeply, the greater applied potential. This is because the greater the applied potential, the higher is the flux of Ag^+ ions delivered from the UME probe to the interface. Furthermore, the greater the applied potential, the earlier is the peak current before the long time current decay corresponding to the onset of DMFc depletion in the DCE phase.

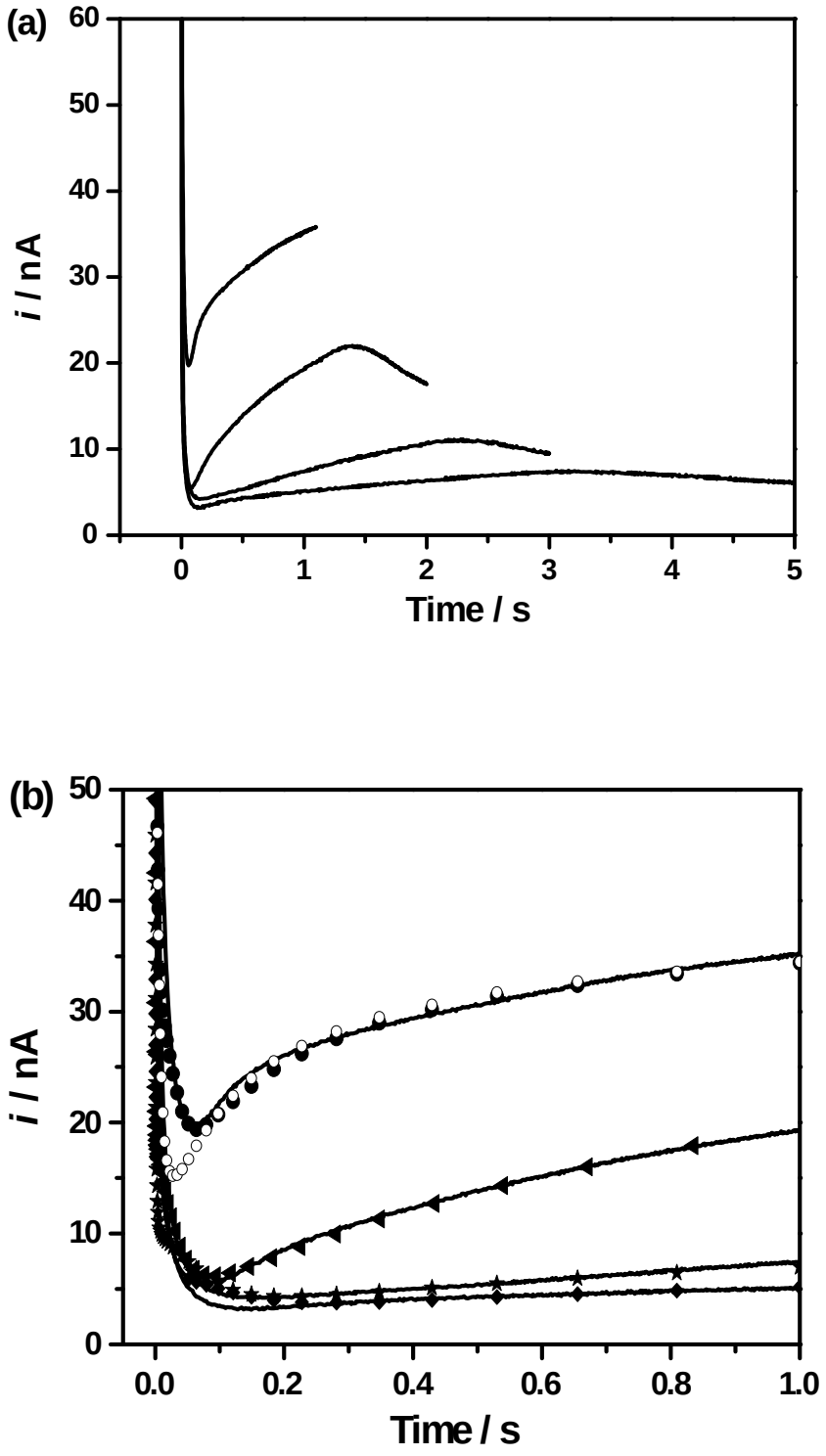

Figure 4-16. (a) Current-time transients recorded at a 25 μm-diameter Ag UME with different applied potentials (vs. SCE) giving c^* values of 0.42, 0.59, 1.0 and 1.95 mM (from bottom to top). The aqueous solution contained

0.1 M $LiClO_4$ and the DCE phase contained 0.03 M DMFc and 0.1 M $TBAClO_4$. From bottom to top, the distances between the UME and interface were 3.5, 3.1, 3.4 and 4.6 μm, respectively. (b) Simulations of the experimental tip currents in (a) over a time scale of 1.0 s (solid symbols). The parameters providing the best fit between the experimental and simulated curves were: ♦ $L = 1.0\times10^{-4}$ cm (d = 3.5 μm); ★ $L = 9.7\times10^{-5}$ cm (d = 3.1 μm); ◄ $L = 8.0\times10^{-5}$ cm (d = 3.4 μm); ● $L = 6.0\times10^{-5}$ cm (d = 4.6 μm). Other parameters used for the simulations were: k = 10 cm s^{-1}, k_{ads} = 0.05 cm s^{-1}, $N = 9\times10^{-10}$ mol cm^{-2} and $D_{Ag^+} = 1.60\times10^{-5}$ cm^2 s^{-1}. The curve comprised of open circles is the simulation for the data at an applied tip potential of 0.40 V, but with k_{ads} and N set to zero.

By fitting the early part of the experimental curves with the one-domain numerical model highlighted in the theory section, the nature of the nucleation process at the L/L interface can be analyzed quantitatively. Simulation results are shown in Figure 4-16(b) alongside the experiment data. The analysis focused on the first 1 s of the transients to ensure that DMFc depletion and Ag aggregate formation would be negligible. The UME-surface concentration of Ag^+ ions was determined from the applied potential according to equation 4.34 and the accurate tip-interface separation used for simulation was determined from the oxygen reduction current, in steady-state approach curve positioning, as described above. In the simulation, the rate constant for Ag particle growth, k, and the particle-particle half spacing, L, were variables in fitting the data. The influence of these two parameters on the current-time behaviour is sufficiently different to allow a unique fit. In Figure 4-16(b), from bottom to top, with increasing potential applied at the Ag UME, the value of k was obtained as a constant, 10 cm s^{-1}, and the value of L decreased slightly from 1.0×10^{-4} cm to

6×10^{-5} cm. Although there is a small variation in *d* (see the caption to Figure 4-16(a)), this trend can be rationalized because the greater the initial Ag^+ ion flux from the UME to the L/L interface, the higher the probability of Ag particle formation, leading to a decrease of spacing between nuclei (*L*) formed at the interface. On the other hand, *k* is related to the rate of Ag^+ ion discharge at a growing particle. Beyond ultra-small particles, this would be expected to be independent of particle size and spacing.

It is important to note that the experiments could not be modelled without considering an initial adsorption of Ag^+ ions at the interface. Take the experimental curve of 0.40 V as an example (the highest curve in Figure 4-16 (b)). Without considering the adsorption process, the theoretical current-time curve (o), matched to long times, is much lower than the experimental curve in the first 0.25 s. To fit the data in this initial period, the adsorption rate constant, k_{ads} (0.05 cm s^{-1}), and the number of adsorption sites per unit area, *N* (9×10^{-10} mol cm^{-2}), were used. The experimental curves clearly indicate that there is an additional flux of Ag^+ ions from the aqueous phase to the interface, which leads to a higher initial tip current. For the different potentials applied at the electrode in Figure 4-16(b), the values of k_{ads} and *N* were all 0.05 cm s^{-1} and 9×10^{-10} mol cm^{-2}, providing confidence about this assignment. SECM experiments of Ag^+ ion electrogeneration to observe solely the adsorption process, without DMFc in the DCE phase, gave *i*-*t* curves which showed no evidence of Ag^+ ion adsorption. The fact that an electron donor is needed in the DCE phase to observe the short time phenomenon seen in the transients in Figure 4-16(b) suggests the initial process may involve some electrodic discharge. Note that if one considered purely a progressive nucleation process, the minimum in the

chronoamperometric curve would be even more pronounced than for the case of instantaneous nucleation shown. The experimental observations can only be accounted for by a high initial flux to the interface, coupled with the nucleation and growth process.

Effect of concentration of organic reductant DMFc. Figure 4-17(a) summarizes current-time transients recorded at the Ag UME with three different concentrations of DMFc in DCE. As the concentration of DMFc decreases, the position of the peak maximum in the current transient appears at longer times and its magnitude becomes smaller. This is perhaps counterintuitive, because one might consider that depletion should occur sooner at lower DMFc concentration. However, the reaction rate depends on particle size and the higher the DMFc concentration, the quicker the particles grow. Thus, the higher the DMFc concentration, the earlier the depletion of DMFc. Figure 4-17(b) shows the best match of theory to experiment for the initial part of the transients. The best fit parameters were k = 5 cm s^{-1} ($L = 7.0\times10^{-5}$ cm), k = 7 cm s^{-1} ($L = 8.0\times10^{-5}$ cm) and k = 10 cm s^{-1} ($L = 8.0\times10^{-5}$ cm) for DMFc concentrations of 0.01, 0.02 and 0.03 M, respectively. Thus the rate constant is strongly dependent on the DMFc concentration.

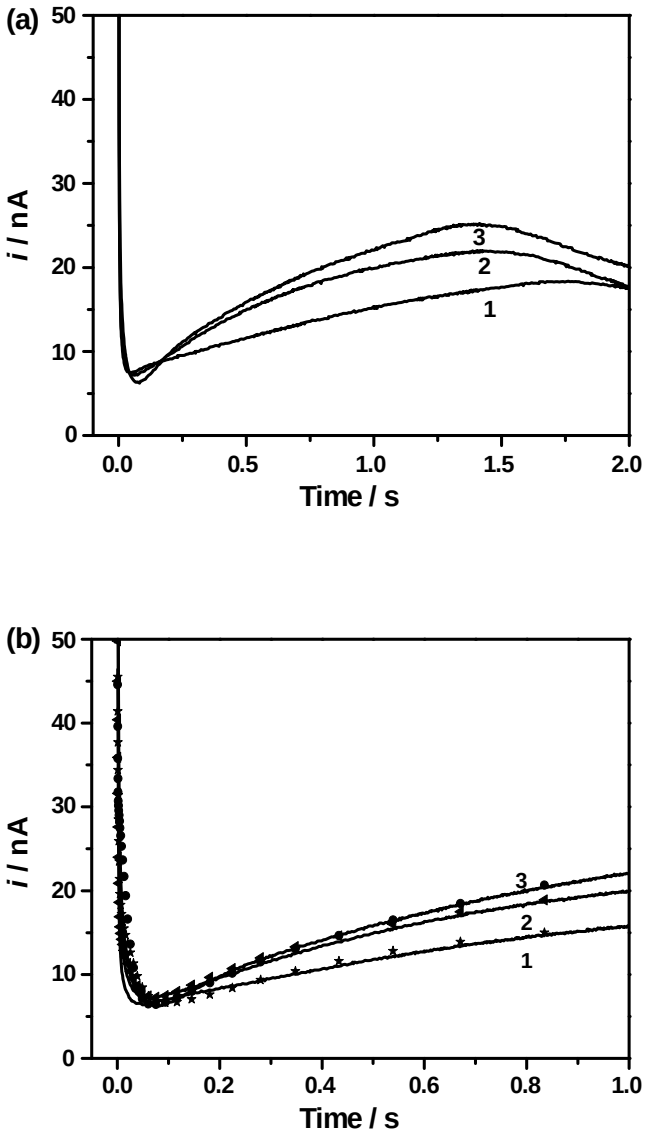

Figure 4-17. (a) Current-time transients recorded at a 25 μm-diameter Ag UME with different concentrations of DMFc in DCE. The aqueous solution contained 0.1 M $LiClO_4$ and the DCE phase contained 0.1 M $TBAClO_4$ and 0.01, 0.02 and 0.03 M DMFc, from curve 1 to 3, respectively. The distances between the UME and L/L interface were 4.0, 2.5 and 3.4 μm, respectively. The UME potential was stepped from 0 to 0.39 V (vs. SCE). (b) Simulations of the experimental tip currents in (a) over a time scale of 1.0 s (solid symbols). The parameters providing the best fit between the experimental and simulated curves were: ★ k = 5 cm s^{-1}, M, $L = 7.0\times10^{-5}$ cm (d = 4.0 μm); ◀ k = 7 cm s^{-1}, $L = 8.0\times10^{-5}$ cm (d = 2.5 μm); ● k = 10 cm s^{-1}, $L = 8.0\times10^{-5}$ cm (d = 3.4 μm). Other parameters used for the simulations were: C^* = 1.0 mM, k_{ads} = 0.05 cm s^{-1}, $N = 9\times10^{-10}$ mol cm^{-2}, and $D_{Ag^+} = 1.60\times10^{-5}$ cm^2 s^{-1}.

Effect of reaction driving force. In this system, the reaction driving force (χ) is determined by the difference in the formal potentials of the Ag/Ag^+ and $DMFc/DMFc^+$ couples ($\Delta E^{0'} = E^{0',w}_{Ag^{0/+}} - E^{0',o}_{DMFc^{0/+}}$) and the Galvani potential drop across the ITIES ($\Delta^w_o\phi$):

$$\chi = \Delta E^{0'} + \Delta^w_o\phi \tag{4.36}$$

In this case, $\Delta^w_o\phi$ was controlled by the partitioning of a single potential-determining ion, ClO_4^-, in the two phases. To consider briefly the effect of driving force across the L/L interface, two different concentrations of the aqueous supporting electrolyte, $LiClO_4$, were studied, while the concentration of the supporting electrolyte in the DCE phase, $TBAClO_4$, was maintained constant.

At standard temperature and pressure, assuming experimental conditions where the activity coefficients of ClO_4^- in water and DCE are constant, within the concentration range of interest, the following equation should hold for $\Delta^w_o\phi$

$$\Delta^w_o\phi = \Delta^w_o\phi^{0'} - 0.059\log\frac{[ClO_4^-]_o}{[ClO_4^-]_w} \tag{4.37}$$

where w and o denote water and organic (DCE) phases, $[ClO_4^-]_w$ and $[ClO_4^-]_o$ are the concentrations of ClO_4^- in water and the DCE phase, respectively, and $\Delta^w_o\phi^{0'}$ is the formal transfer potential for ClO_4^-.[45] Thus, the ratio of the ClO_4^- concentrations in the two phases determines the Galvani potential drop across the L/L interface.

Cyclic voltammograms of the anodic oxidation of Ag in the aqueous solution and DMFc oxidation in the DCE solution with 0.1 and 0.01 M $LiClO_4$ in the aqueous phase, respectively, are shown in

Figure **4-18**. It can be seen that the driving force for the reduction of Ag^+ by DMFc is greater by approximately 60 mV with 0.1 M $LiClO_4$.

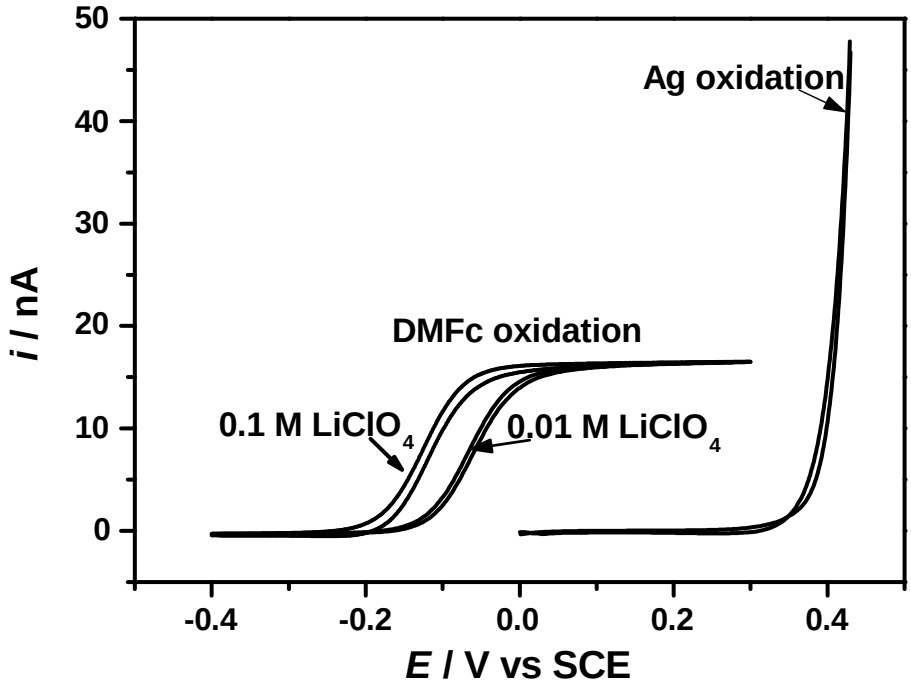

Figure 4-18. Cyclic voltammograms of Ag oxidation recorded at a 25 μm-diameter Ag UME in an aqueous solution containing 0.1 M $LiClO_4$ and DMFc oxidation recorded at a 25 μm-diameter Pt UME in a DCE solution containing 5 mM DMFc and 0.1 M $TBAClO_4$ with either 0.1 M or 0.01 M $LiClO_4$ in the aqueous phase. The scan rate was 20 mV s^{-1}. SCE in the aqueous phase served as the reference electrode.

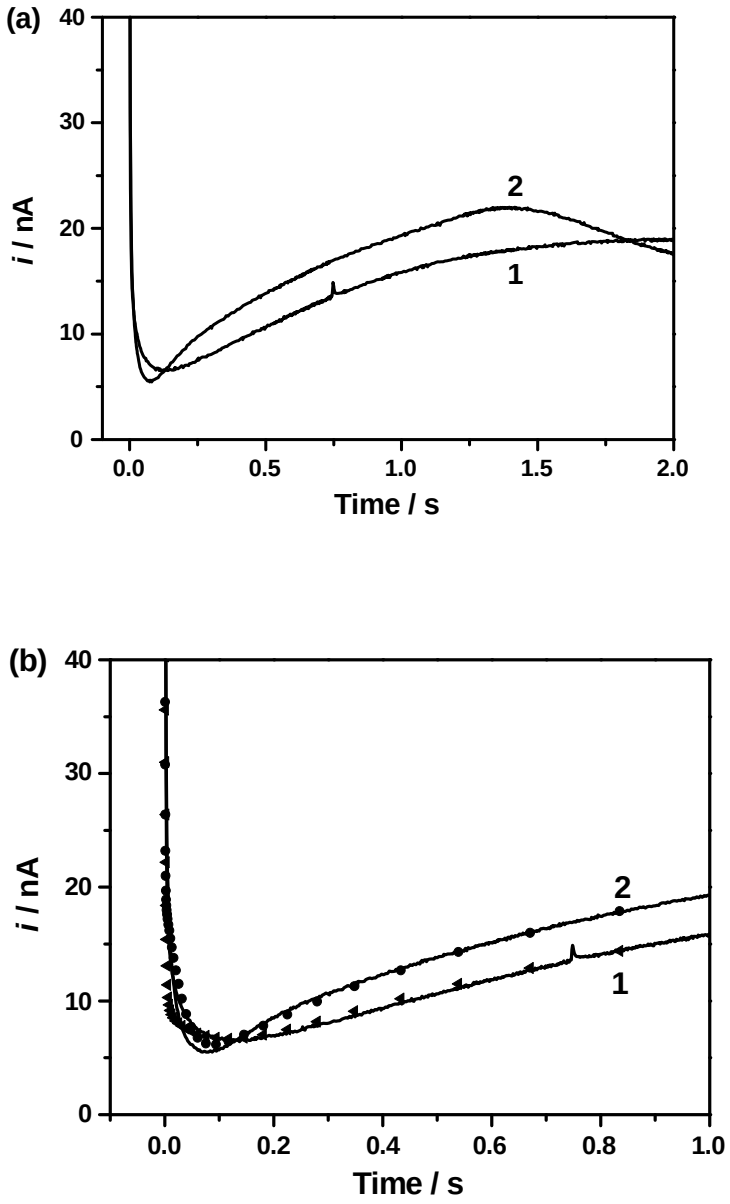

Figure 4-19. (a) Current-time transients recorded at a 25 μm-diameter Ag UME with different concentrations of $LiClO_4$ in the aqueous phase. The aqueous solutions contained 0.01 M $LiClO_4$ and 0.09 M KNO_3 (curve 1) and 0.1 M $LiClO_4$ (curve 2), while the DCE solution contained 0.03 M DMFc and 0.1M $TBAClO_4$ in each case. The tip-interface separations were 3.0 μm (curve 1) and 3.4 μm (curve 2). The UME potential was stepped from 0 to 0.39 V (vs. SCE). (b) Simulations of experimental tip currents (solid symbols) over a time scale of 1.0 s. The parameters providing the best fit between the experimental and simulated curves were: ◂ k = 5 cm s^{-1} (d = 3.0 μm); ● k = 10 cm s^{-1} (d = 3.4 μm). Other parameters used for simulation were: C^* = 1.0 mM, $L = 8.0\times10^{-5}$ cm M, k_{ads} = 0.05 cm s^{-1}, $N = 9\times10^{-10}$ mol cm^{-2} and $D_{Ag^+} = 1.60\times10^{-5}$ cm^2 s^{-1}.

Figure 4-19(a) shows typical current-time curves recorded at the Ag UME with the two different concentrations of $LiClO_4$ in the aqueous phase. The transient with 0.1 M $LiClO_4$ shows a sharper minimum and more steeply rising portion thereafter. The tip current increases more slowly for the case of 0.01 M $LiClO_4$, which is because the reaction driving force is smaller with a lower concentration of ClO_4^- in the aqueous phase. Clearly, the smaller driving force leads to a slower nucleation reaction rate as manifested in a more gradual increase of the tip current with time. By fitting the experimental curves to the numerical simulation (Figure 4-19(b)), the rate constant, *k*, was 5 cm s^{-1} (0.01 M $LiClO_4$) and 10 cm s^{-1} (0.1 M $LiClO_4$). In both cases $L = 8\times10^{-5}$ cm best described the data. These preliminary suggest that the Galvani potential difference has a rather weak effect on the nucleation and growth process. This contrasts with many simpler ET processes at L/L interfaces which show much stronger potential dependent rate constants.[46]

4.5.3 Microscopy of Ag particles formed at the water/DCE interface

CLSM was employed to confirm that particles were formed at the interface. For these experiments, the SECM potential-step experiments lasted for 5 s, the applied potential was 0.39 V and the tip to interface separation was 3.5 μm. This ensured there should be sufficient deposition for optical characterization. After the potential step, the interface formed at the small hole inside the cell was examined by CLSM in both transmission and reflection modes, using a dipping lens. Typical confocal images obtained using the two modes are shown in Figure 4-20. In both modes, Ag deposits were visible as dark/bright particles. The patch of particles is irregular because the cell had to be moved from an

electrochemistry environment to the confocal microscope, which took some minutes and involved the cell being carried some distance. Nonetheless, one can clearly see that an area approximating to the UME size is observed. This is consistent with the simulations presented earlier. Some agglomeration of particles is observed, which again highlights why the quantitative analysis of transients focused on short times where this problem was less likely.

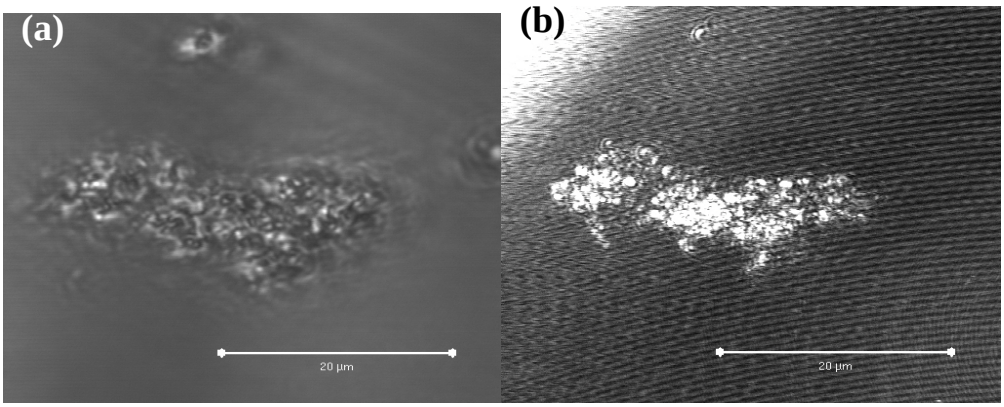

Figure 4-20. Visualization by confocal microscopy in transmission (a) and reflection modes (b) of Ag particles formed at a water/DCE interface. The scale bar is 20 µm. See text for SECM parameters used to form particles.

4.6 Conclusions

The SECM induced deposition of Ag particles at a non-polarizable water/DCE interface by the electron transfer reaction between aqueous electrogenerated Ag^+ ions and DCE-phase DMFc has been demonstrated. Using a two-electrode system, with an Ag UME as the source of Ag^+ ions, factors influencing the interfacial deposition process, such as the tip-interface separation, the potential applied at the tip, the concentration of the reductant in the DCE phase and the interfacial reaction driving force, have been investigated by SECM potential-step chronoamperometry. A theoretical model was developed that

allowed the rate constants for Ag particle growth at the water/DCE interface to be obtained, along with an estimate of the particle density.

This study has demonstrated that SECM is a promising technique to study interfacial metal nucleation and growth processes quantitatively and the methodology could readily be used to study solid/liquid interfaces and extended to other materials and composites. The methodology is particularly sensitive to coupled processes, such as adsorption phenomena, and could prove powerful in the study of phase formation at a wide variety of electrode/electrolyte interfaces. The type of approach described could also be expanded to include the electrogeneration of other metal ions from solid electrodes and amalgams (e.g. mercury) and liquid filled micro- and nanopipettes.

References

(1) Binder, W. H. *Angew. Chem. Int. Ed.* **2005**, *44*, 5172.

(2) Dryfe, R. A. W. *Phys. Chem. Chem. Phys.* **2006**, *8*, 1869.

(3) Cheng, Y. F.; Schiffrin, D. J. *J. Chem. Soc. Farad. Trans.* **1996**, *92*, 3865.

(4) (a) Johans, C. J.; Lahtinen, R.; Kontturi, K.; Schiffrin, D. J. *J. Electroanal. Chem*. **2000**, *488*, 99; (b) Johans, C.; Kontturi, K.; Schiffrin, D. J. *J. Electroanal. Chem.* **2002**, *526*, 29.

(5) (a) Platt, M.; Dryfe, R. A. W.; Robert, E. P. L. *Chem. Comm.* **2002**, 2324; (b) Platt, M.; Dryfe, R. A. W.; Roberts, E. P. L. *Electrochim. Acta* **2003**, *48*, 3037; (c) Platt, M.; Dryfe, R. A. W. Roberts, E. P. L. *Electrochim. Acta* **2004**, *49*, 3937; (d) Platt, M.; Dryfe, R. A. W. *Phys. Chem. Chem. Phys.* **2005**, *7*, 1807; (e) Platt, M.; Dryfe, R. A. W. *J. Electroanal. Chem*. **2007**, *599*, 323.

(6) Dryfe, R. A. W.; Simm, A. O.; Kralj, B. *J. Am. Chem. Soc.* **2003**, *125*, 13014.

(7) Guo, J. D.; Tokimoto, T.; Othman, R.; Unwin, P. R. *Electrochem. Comm.* **2003**, *5*, 1005.

(8) Trojanek, A.; Langmaier, J.; Samec, Z. *Electrochem. Comm.* **2006**, *8*, 475.

(9) Lahtinen, R. M.; Fermin, D. J.; Jensen, H.; Kontturi, K.; Girault, H. H. *Electrochem. Comm.* **2000**, *2*, 230.

(10) (a) Johans, C.; Clohessy, J.; Fantini, S.; Kontturi, K.; Cunnane, V. J. *Electrochem. Comm.* **2002**, *4*, 227; (b) Johans, C.; Liljeroth, P.; Kontturi, K.

Phys. Chem. Chem. Phys. **2002**, *4*, 1067; (c) Scholz, F.; Hasse, U. *Electrochem. Commun.* **2005**, *7*, 541.

(11) (a) Rao, C. N. R.; Kulkarni, G. U.; Thomas, P. J.; Agrawal, V. V.; Saravanan, P. *J. Phys. Chem. B* **2003**, *107*, 7391; (b) Rao, C. N. R.; Kulkarni, G. U.; Agrawal, V. V.; Gautum, U. K.; Ghosh, M.; Tumkurkar, U. *J. Colloid Interface Sci.* **2005**, *289*, 305.

(12) (a) Yogev, D.; Efrima, S. *J. Phys. Chem.* **1988**, *92*, 5754; (b) Yogev, D.; Deutsch, M.; S.; Efrima, S. *J. Phys. Chem.* **1989**, *93*, 4147; (c) Yogev, D.; Shtutina, S.; Efrima, S. *J. Phys. Chem.* **1990**, *94*, 752; (d) Zeiri, L; Younes, O.; Efrima, S.; Deutsch, M. *J. Phys. Chem. B* **1997**, *101*, 9299; (e) Schwartz, H.; Harel, Y.; Efrima, S. *Langmuir* 2**001**, *17*, 3884.

(13) Reincke, F.; Hickey, S. G.; Kegel, W. K.; Vanmaekelbergh, D. V. *Angew. Chem. Int. Ed.* **2004**, *43*, 458.

(14) Sakata, J. K.; Dwoskin, A. D.; Vigorita, J. L.; Spain, E. M. *J. Phys. Chem. B* **2005**, *109*, 138.

(15) Greef, R.; Peat, R.; Peter, L. M.; Pletcher, D.; Robinson, J. *Instrumental methods in Electrochemistry* Ellis Horwood, Chichester, 1985, pp. 283–316.

(16) (a) Crooks, R. M.; Zhao, M. Q.; Sun, L.; Chechik, V.; Yeung, L. K. *Acc. Chem. Res.* **2001**, *4*, 181; (b) Song, Y.; Murray, R.W. *J. Am. Chem. Soc.* **2002**, *124*, 7096; (c) Hicks, J. F.; Miles, D. T.; Murray, R. W. *J. Am. Chem. Soc.* **2002**, *124*, 13322; (d) Peng, Z. Q.; Wang, E. K.; Dong, S. J. *Electrochem. Comm.* **2002**, *4*, 210; (e) Cheng, W. L.; Dong, S. J.; Wang, E.

K. *Electrochem. Comm.* **2002**, *4*, 412; (f) Quinn, B. M.; Liljeroth, P.; Kontturi, K. *J. Am. Chem. Soc.* **2002**, *124*, 12915.

(17) Bonnemann, H.; Richards, R. M. *Eur. J. Inorg. Chem.* **2001**, 2455.

(18) Kanie, O.; Grotenbreg, G.; Wong, C. *Angew. Chem. Int. Ed.* **2000**, *39*, 4545.

(19) Ma, Z.; Sui, S. *Angew. Chem. Int. Ed.* **2002**, *41*, 2176.

(20) Alivisatos, A. P.; Johnson, K. P.; Peng, X.; Wilson, T. E.; Loweth, C. J.; Burchez, M. P.; Schultz, Jr. P. G. *Nature* **1996**, *382*, 609.

(21) Faraday, M. *Philos. Trans. R. Soc. London*, **1857**, *147*, 145.

(22) Guainazzi, G.; Silvestri, G.; Serravalle, G. *J. Chem. Soc., Chem. Comm.* **1975**, 200.

(23) Bard, A. J.; Fan, R. F.; Kwak, J.; Lev, O. *Anal. Chem.* **1989**, *61*, 132.

(24) James, P. I.; Garfias-Mesais, L. F.; Moyer, P. J.; Smyrl, W. H. *J. Electrochem. Soc.* **1998**, *145*, L64.

(25) (a) Gonsalves, M.; Barker, A. L.; Macpherson, J. V.; Unwin, P. R.; O'Hare, D.; Winlove, C. P. *Biophysical. J.* **2000**, *78*, 1578; (b) Gonsalves, M.; Macpherson, J. V.; O'Hare, D.; Winlove, C. P.; Unwin, P. R. *Biochim. Biophys. Acta* **2000**, *66*, 1524; (c) Macpherson, J. V.; Unwin, P. R. *Anal. Chem.* **2000**, *72*, 276; (d) Macpherson, J. V.; Unwin, P. R. *Anal. Chem.* **2001**, *73*, 550; (e) Fonseca, S. M.; Barker, A. L.; Ahmed, S.; Kemp, T. J.; Unwin, P. R. *Chem. Comm.* **2003**, 1002; (f) Fonseca, S. M.; Barker, A. L.;

Ahmed, S.; Kemp, T. J.; Unwin, P. R. *Phys. Chem. Chem. Phys.* **2004**, *6*, 5218.

(26) (a) Craston, D. H.; Lin, C. W.; Bard, A. J. *J. Electrochem. Soc.* **1988**, *135*, 785; (b) Husser, O. E.; Craston, D. H.; Bard, A. J. *J. Electrochem. Soc.* **1989**, *136*, 3222; (c) Bard, A. J.; Denuault, G.; Lee, C.; Mandler, D.; Wipf, D. O. *Acc. Chem. Res.* **1990**, *23*, 357; (d) Mandler, D.; Bard, A. J. *J. Electrochem. Soc.* **1989**, *136*, 3143; (e) Mandler, D.; Bard, A. J. *J. Electrochem. Soc.* **1990**, *137*, 1079; (f) Mandler, D.; Bard, A. J. *J. Electrochem. Soc.* **1990**, *137*, 2468.

(27) Yatziv, Y.; Turyan, I.; Mandler, D. *J. Am. Chem. Soc.* **2002**, *124*, 5618.

(28) Turyan, I.; Etienne, M.; Mandler, D.; Schuhmann, W. *Electroanalysis* **2005**, *17*, 538.

(29) Day, T. M.; Unwin, P. R.; Macpherson, J. V. *Nano Lett.* **2007**, *7*, 51.

(30) Burt, D. P.; Cervera, J.; Mandler, D.; Macpherson, J. V.; Manzanares, J. A.; Unwin, P. R. *Phys. Chem. Chem. Phys.* **2005**, *7*, 2955.

(31) Martin, R. D.; Unwin, P. R. *J. Chem. Soc., Faraday Trans.* **1998**, *94*, 753.

(32) Barker. A. L.; Macpherson, J. V.; Slevin, C. J.; Unwin, P. R. *J. Phys. Chem. B* **1998**, *102*, 1586.

(33) Hills, G. J.; Schiffrin, D. J.; Thompson, J. *Electrochim. Acta* **1974**, *19*, 657.

(34) Scharifker, B.; Hills, G. *Electrochim. Acta* **1983**, *28*, 879.

(35) Sluyters-Rehbach, M.; Wijenberg, J. H. O. J.; Bosco, E.; Sluyters, J. H. *J. Electroanal. Chem.* **1987**, *236*, 1.

(36) Mirkin, M.V.; Nilov, A. P. *J. Electroanal. Chem.* **1990**, *283*, 35.

(37) Heerman, L.; Tarallo, A. *J. Electroanal. Chem.* **1999**, *470*, 70.

(38) Trojánek, A.; Langmaier, J.; Samec, Z. *J. Electroanal. Chem.* **2007**, *599*, 160.

(39) Heyrovsky, J.; Kuta, J. *Instrumental Techniques in Electrochemistry*, Academic Press, New York, 1966.

(40) Johans, C.; Kontturi, K.; Schiffrin, D. J. *J. Electroanal. Chem.* **2002**, *526*, 29.

(41) *CRC Handbook of Chemistry and Physics*, 86th ed.; CRC Press: Boca Raton, FL, 2005.

(42) Unwin, P. R.; Bard, A. J. *J. Phys. Chem.* **1992**, *96*, 5035.

(43) (a) Macpherson, J. V.; Unwin, P. R. *J. Phys. Chem.* **1995**, *99*, 14824; (b) Macpherson, J. V.; Unwin, P. R. *J. Phys. Chem.* **1995**, *99*, 3338; (c) Macpherson, J. V.; Unwin, P. R. *J. Phys. Chem*. **1994**, *98*, 1704 .

(44) Unwin, P. R.; Macpherson, J. V.; Martin, R. D.; McConville, C. F. *Proc. Electrochem. Soc.* **2000**, Vol 99-28, pp 104-121.

(45) Volkov, A. G.; Deamer, D. W. (Eds.) *Liquid-liquid Interfaces: Theory and Methods*, CRC Press, Boca Raton, 1996.

(46) (a) Tsionsky, M.; Bard, A. J.; Mirkin, M. V. *J. Phys. Chem.* **1996**, *100*, 17881; (b) Barker, A. L.; Unwin, P. R.; Amemiya, S.; Zhou, J. F.; Bard, A. J. *J. Phys. Chem. B* **1999**, *103*, 7260; (c) Ding. Z. F.; Quinn, B. M.; Bard, A.

J. *J. Phys. Chem. B* **2001**, *105*, 6367; (d) Zhang, J.; Barker, A. L.; Unwin, P. R. *J. Electroanal. Chem.* **2000**, *483*, 95; (e) Zhang, Z. Q.; Yuan, Y.; Sun, P.; Su, B.; Guo, J. D.; Shao, Y. H.; Girault, H. H. *J. Phys. Chem. B* **2002**, *106*, 6713; (f) Barker, A. L.; Unwin. P. R.; Zhang, J. *Electrochem. Comm.* **2001**, *3*, 372.

Chapter 5: Towards a Quantitative Understanding of Tip Position Modulation-Scanning Electrochemical Microscopy (TPM-SECM)

5.1 Introduction

Scanning electrochemical microscopy[1-3] (SECM) has proven effective for imaging activity on a local scale in a multitude of varied situations. These include many biological and industrially relevant processes, e.g. enzyme activity,[4-9] corrosion[10-13], permeability in biological tissues[14, 15] and probing transfer across[16-22], and laterally within membranes[23-27].

For flat substrates e.g. when studying the corrosion of metal surfaces[10, 11], or examining electrode activity(e.g. boron doped diamond (BDD) electrodes[28-30]), one can obtain a map of activity from current measurements via straightforward calculations. More usually samples will have topographic variation as well, and to resolve these two factors several approaches have been used. First, one can perform experiments with two mediators, one active, one inert, with respect to the activity being probed on the surface. This allows one to gain purely topographical information on an initial scan with the inert mediator. As the distance from the surface is known calculations of activity are possible from

measurements in the second scan. This approach has been used to probe permeability of methyl viologen and oxygen in cartilage.[14, 15]

The combination of an electrode with the sharp probe of an atomic force microscope[31-33] (AFM) in so called SECM-AFM[34-39] allows the simultaneous measurement of topography, through flexion of the AFM cantilever, and activity, through the electrode-response. This approach has been used to image the activity and topography of glucose oxidase supported in a soft polymer matrix, electrodeposited on a micropatterned substrate[37], to probe the diffusion field of a microelectrode[38], and to image transport through single nanoscale pores in membranes[40].

A further method of assessing topography is through shear-force modulation[41-43]. The electrode is 'dithered', via a small oscillation in the plane of the surface. As the electrode is brought close to a surface, the oscillation is damped, to a degree depending on the tip-substrate separation[44]. Images are usually acquired at a constant damping amplitude, analogous to constant distance imaging.

Alpuche-Aviles and Wipf demonstrated that one can determine the tip-surface separation through the measurement of electrical impedance[45]. Impedance is calculated by measuring the response to a low amplitude high frequency AC voltage superimposed upon a much large DC component. Through judicious design of circuitry, the two components can be separated, allowing one to use the impedance component as a measure of tip-surface separation. A more complete investigation was performed by Gabrielli et al.[46] Feedback based upon impedance has been shown to be successful for imaging in biological situations[47, 48].

Tip position modulation (TPM) is an interesting candidate to the problem of resolving activity and topography, an avenue which we pursue in this work. In the TPM mode of SECM operation, the position of the tip is oscillated sinusoidally perpendicular to the surface, a small amount about a fixed height. The tip current (usually at a diffusion-limited value) then oscillates, with a frequency equal to that of the positional oscillation[49]. The amplitude and phase - relative to the position - of the oscillating current should enable one to deconvolute the activity and topography of the surface[50]. The diffusion model currently available only matches data in the case of a conducting substrate, being off by around an order of magnitude in the case of an inert surface[49]. We aim to take the technique forward, developing a model to describe the expected current response. We also explore the use of this modulation technique to probe the permeability of samples.

5.2 Theory

Borrowing, and expanding upon, the notation used by Wipf and Bard[49] we let the frequency of modulation be f_m, the amplitude of modulation be δ (maximum to minimum), the midpoint distance of the oscillations be d. The distance from the tip to the surface at time t is thus completely described by:

$$d - \delta/2 \cos(2\pi f_m t) \tag{5.1}$$

The tip current, i, can be decomposed into the sum of two elements, a direct current component, i_{DC}, and an oscillating component being of an amplitude i_{AC}, and of the same period as the oscillation of the tip. We define the current i_{lim} to be the current achieved when the tip is held at an infinite distance from a surface and allowed to achieve a maximum steady-state value for the diffusion-limited amperometric detection of a species in solution. The radius of the electrode will

be called *a* and the ratio to the radius of the glass sheath surrounding the electrode is denoted *RG*.

Throughout this chapter it will be assumed that the electrode is held at such a potential that the current flowing is limited by transport (diffusive and/or convective) and not by electrode kinetics. The expected current when an ultramicroelectrode (UME) is approached to a surface, at a slow enough speed to allow steady-state diffusion to be achieved, is well understood and characterized[2, 51]. Experiments are observed to tally closely to these theoretical approach curves. It is from these curves that the theoretical response of an electrode undergoing TPM was originally developed[49].

Under suitably small oscillations it is assumed that the AC component of the current, i_{AC} will be sinusoidal, with an amplitude proportional to the absolute value of the derivative of the approach curve – this is equivalent to expecting the current to be that achieved at a steady-state throughout the oscillation. Furthermore, it is assumed that the phase of the AC signal can be used to determine the activity of the surface. The current magnitude decreases on approach to an inert surface, giving an AC voltage in phase with the tip-surface separation. Conversely, approaching an active surface (where redox feedback[52] or induced transfer occurs[53]) gives an increase in the magnitude of the current compared to the inert case. In the limit of a highly active surface, the AC response would be out of phase with the tip-surface separation. It has been shown that the AC response in approaching an electrode to an active electrode surface with positive feedback fits closely to this theory, and that the phase response is indeed indicative of the activity[49, 54]. However, it was noted by Wipf and Bard[49]

that this theory did not give predictions matching experimental approaches to an inert surface.

We aim to develop a theoretical framework describing the current response during TPM over both inert and permeable surfaces; the extension of this model to other situations of active surfaces should become apparent and be easy to implement. Prior to this we briefly introduce the theory of SECM induced transfer (SECMIT), developed previously by Barker et al,[53] describing the approach to interfaces of phases with arbitrary partition coefficients, diffusion coefficients, and interfacial kinetics. Through numerous numerical simulations current-time transients for a UME at various distances from interfaces of varying permeabilities were computed. It is shown that the steady-state current measured with the UME a fixed distance from the surface is dependent on the product of the ratio of the diffusion coefficients γ, with the partition coefficient K_e[53].

5.2.1 Model 1

Our first model will describe the current of an oscillating UME in close proximity to an inert surface. The axisymmetric nature of the problem allows us to model it in only the radial, *r*, and axial, *z*, directions. Due to the small magnitude of the oscillations in TPM we model the geometry of the problem by fixing the UME at the midpoint of its oscillation, *d*. We consider the fluid flow in the gap between the UME and the surface. If we consider the flow through any cylinder, from surface to UME, centred on the electrode axis, radius *R*, then we know through conservation of mass and the relative incompressibility of water that the total flow must be equal to the rate of change of volume of the cylinder.

Differentiating this equation we get the tip velocity:

$$\pi f_m \delta \sin(2\pi f_m t) \tag{5.2}$$

Multiplying by the area of the end of the cylinder (πR^2) gives us the volume flow rate into the cylinder:

$$\frac{\mathrm{dVol}_R}{\mathrm{d}t} = (\pi R)^2 f_m \delta \sin(2\pi f_m t) \tag{5.3}$$

Due to the differing magnitudes of the axial and radial components of the velocity we can make the simplifying assumption that the velocity of the fluid only has a non-zero component in the radial direction. Knowing the flow between two parallel plates to assume a parabolic profile, with zero velocity on either plate, we let the radial component of the velocity be represented by a function of the form:

$$v_{t,f_m,\delta,R}(z,d) = v^*_{t,f_m,\delta,R} z(d-z) \tag{5.4}$$

where $v^*_{t,f_m,R}$ is a constant, with respect to *d* and *z*, chosen such that total fluid flow through the cylinder, radius *R*, is as described in equation 5.3. Integrating equation 5.4 over the surface of the cylinder radius *R* and we get the flow into the cylinder:

$$\frac{\mathrm{dVol}_R}{\mathrm{d}t} = -\tfrac{1}{3}\pi R v^*_{t,f_m,\delta,R} d^3 \tag{5.5}$$

Equating equations 5.3 and 5.5 and rearranging gives us:

$$v^*_{t,f_m,\delta,R} = -3/d^3 \delta f_m R\pi \sin(2\pi f_m t) \tag{5.6}$$

Finally substituting the value of $v^*_{t,f_m,\delta,R}$ from equation 5.6 into equation 5.4 we arrive at an expression, for the radial velocity of the fluid:

$$v_{d,f_m,\delta}(t,r,z) = -3/d^3 \delta f_m r\pi \sin(2\pi f_m t) z(d-z) \tag{5.7}$$

It is with the above derived expression for fluid flow within the domain below the sheath of the electrode that we proceed to define our model:

$$\frac{\partial c}{\partial t} = D\nabla^2 c - \underline{v}_{d,f_m,\delta} \cdot \nabla c \tag{5.8}$$

$$\left.\begin{array}{l} r = 0, 0 < z < d \\ 0 \le r \le RG \times a, z = 0 \\ a < r < RG \times a, z = d \end{array}\right\} \frac{\partial c}{\partial t} \cdot \underline{n} = 0 \qquad (5.9a, b, c)$$

$$0 \le r \le a, z = d \quad c = 0 \qquad (5.10)$$

$$r = RG \times a, 0 < z < d \quad c = c_b \qquad (5.11)$$

where equation 5.8 is the convection-diffusion equation, with c representing concentration of the species of interest, c_b the concentration of this species in bulk solution and D its diffusion coefficient; $\underline{n}$ represents the unit normal to the boundary, and $\underline{v}_{d,f_m,\delta} = (v_{d,f_m,\delta}(t,r,z),0)$ is the velocity as described in equation 5.7. Equations 5.9a, b and c define the boundary condition of no flux on the axis of symmetry, the inert substrate, and the inert sheath of the electrode, respectively. Equation 5.10 states that the concentration on the electrode is zero because the potential being is set at a value where current is limited by transport, and not kinetics at the electrode. Figure 5-1a illustrates the geometry and boundary conditions of the model.

It is possible to show through coordinate transforms that if c(r, z, t) is a solution to equation 5.8 then for an electrode radius a^*, with the same RG, diffusion coefficient D^*, the function $c^*(R, Z, T) = c(\frac{a}{a^*}R, \frac{a}{a^*}Z, \left(\frac{a}{a^*}\right)^2 \frac{D}{D^*}T)$ will satisfy the reaction-diffusion equation (equation 5.8) for amplitude $\delta^* = \frac{a}{a^*}\delta$, frequency $f_m^* = \left(\frac{a}{a}\right)^2 \frac{D}{D^*} f_m$ and tip-substrate separation $d^* = \frac{a}{a^*}d$. Furthermore, under normalization, by i_{Lim} and δ/a, both systems will give equivalent i_{AC} vs. d/a responses.

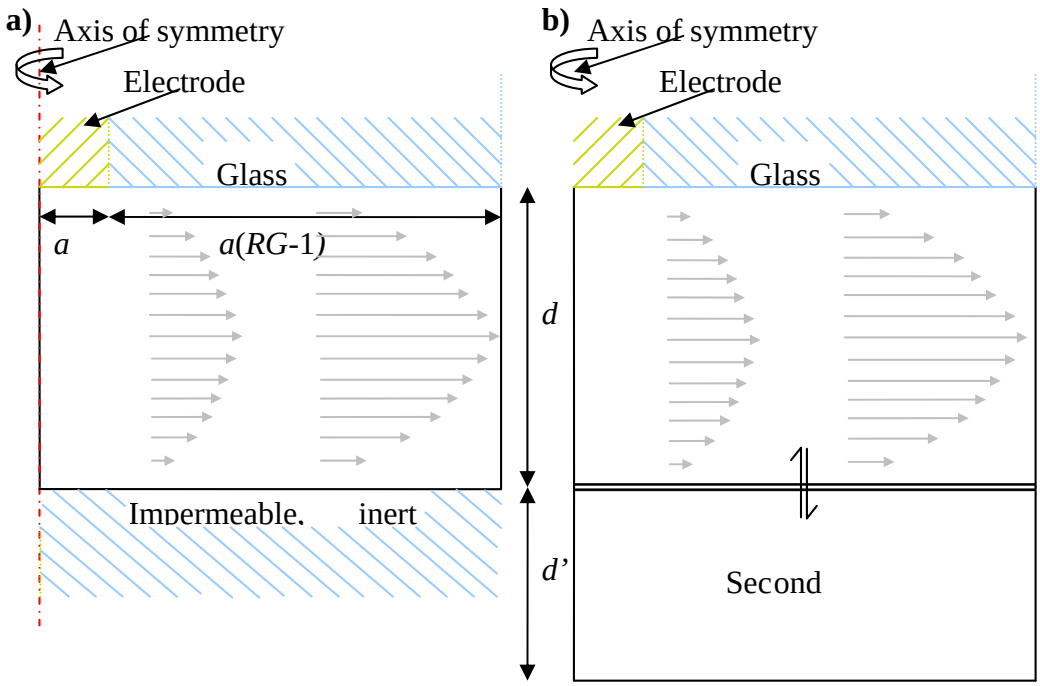

Figure 5-1: Schematic of the geometries for models 1 (a) and 2(b). Equations were solved only within the solution phase (unshaded area); the electrode, glass and surface are depicted only to aid understanding. Grey arrows are representative of the fluid velocity when the tip is moving towards the interface, their magnitude is not exact.

5.2.2 Model 2

The second model introduces a second domain below the interface (second phase, Figure 5-1b) representing a permeable substrate. Within this domain, the concentration will obey:

$$\frac{\partial c}{\partial t} = D' \nabla^2 c \qquad (5.12)$$

the diffusion equation, where D' represents the diffusion coefficient in the second phase. The boundary conditions in the fluid domain (domain 1) are as described in equations 5.9, 5.10 and 5.11, with the exception that equation 5.9b is replaced by equation 5.13, representing continuity between the concentrations in the two domains. This condition is appropriate to the case where interfacial

transfer kinetics between the two phases occurs on a much faster time scale than diffusion.

$$0 \le r \le RG \times a, z = 0 \quad c\big|_{Domain\ 1} = c\big|_{Domain\ 2} \tag{5.13}$$

The depth to which the second domain was simulated is denoted by d'. The remaining boundary conditions are summarised in equations5.14, 5.15 and 5.16, with quantities as previously defined.

$$r = 0, 0 > z > -d' \quad \tfrac{\partial c}{\partial t} \cdot \underline{n} = 0 \tag{5.14}$$

$$r = RG \times a, 0 > z > -d' \quad \tfrac{\partial c}{\partial t} \cdot \underline{n} = 0 \tag{5.15}$$

$$0 \le r \le RG \times a, z = -d' \quad c = c_b \tag{5.16}$$

To calculate the current we integrate the flux into the electrode and multiply by the charge on a mole of singly charged species (F=96485 C/mol) before multiplying by the number of electrons transferred in the electrode reaction, *n*. As the model is formulated in cylindrical axisymmetric coordinates the integral is formed as the integral of a surface of revolution. Thus:

$$Current = 2\pi nF \int_0^a r \tfrac{\partial c}{\partial z} dr \tag{5.17}$$

All currents reported are normalized by the limiting current at a long distance from the surface with the UME held still, i_{Lim}.

5.3 Experimental

Electrodes. The ultramicroelectrodes (UMEs) used were constructed from 10 and 25 μm Pt wires (Goodfellow Metals, Ltd., Cambridge, UK) sheathed in glass. The electrode was polished to give a disk geometry, and the ratio of the radius of glass insulator to the radius of the metal, *RG*, varied from 4 to ≈100 and is quoted within the results. The fabrication process has previously been

described in detail.[55, 56] A Ag/AgCl reference electrode was used for the two electrode voltammetric-amperometric setup employed.

Instrumentation. The probe electrode was mounted perpendicularly to the surface, with coarse positioning achieved by manual manipulator screws (Newport, 461-XYZ-M). Fine positioning was achieved by piezo actuators fitted with strain gauge sensors (Nanocube P-611.3S, Physik Instrumente, Germany) controlled by a amplifier/servo (E-664 LVPZT, Physik Instrumente), operated in open loop on the axis perpendicular to the surface, and closed loop on the two axes parallel to the surface. This, in turn, was controlled by signals from digital to analogue converter (DAC) card (Model no. NI-6731, National Instruments). Data were acquired using a data acquisition (DAQ) card (Model No. NI PCI-6143, National Instruments.). Both cards were controlled by a PC running LabView 7.1 software (National Instruments). All experimentation was performed within a Faraday cage. Tip currents were converted to voltages using a home built current to voltage converter prior to data acquisition.

In tip position modulation (TPM) experiments, the tip oscillation was driven by a home built wave generator. The signals from the wave generator and DAQ card were combined using a home built instrumentation amplifier.

All data were acquired through self-written LabVIEW modules, designed in a flexible and user-friendly style. For tip position modulation experiments, phase and amplitude information were extracted using self-written software for a lock-in amplifier written also in LabVIEW. Phase was chosen to be the value maximising the mean product of the reference and current signals. The software also recorded the mean current. The software controlled the piezo amplifier

based upon a best fit to the expansion calibration curve. A calibration of the set-up for TPM-SECM experiments is given in Figure 5-2.

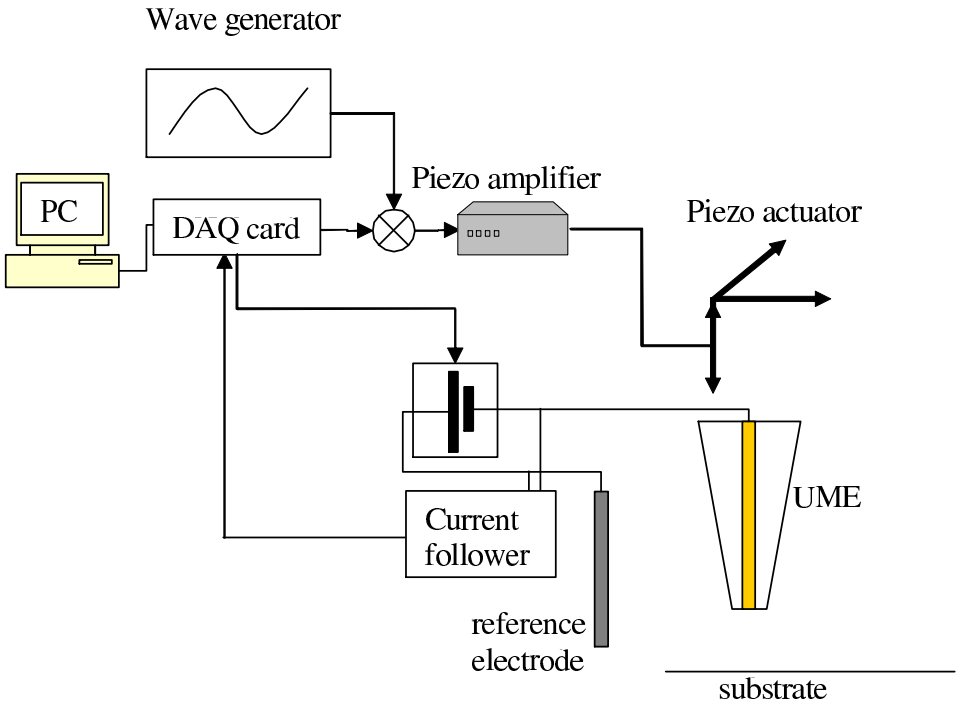

Figure 5-2: Schematic of the experimental set-up for a tip position modulation scanning electrochemical microscopy (TPM-SECM) experiment.

Solutions. Solutions were prepared using analytical-grade chemicals, Hexaaminеruthenium (III) chloride with KNO_3 (all Fisher Scientific), water was used was doubly distilled Milli-Q 18 MΩ reagent water (Millipore Corp.)

All SECM experiments were performed under similar experimental procedures, the only variations being the substrate, the electrolyte, and the protocol for movement of tip and application of the potential. The passage below describes the typical experimental setup for the approach of an UME tip to a glass surface, with the tip undergoing TPM. Substrates were prepared by cleaning with distilled water. For permeability studies the substrate was a hydrogel, prepared as described previously[57]. The hydrogel was soaked for at least 72 hours in distilled water (Milli-Q 18 MΩ cm at 25 °C), with several (at

least 5) changes of water in order to remove any residual acid contaminant from the synthesis process. Prior to experiments, the hydrogel was allowed to equilibrate with solution of same composition as the electrolyte.

Experiments were performed in a solution of either 2 mM $K_4Fe(CN)_6$ with a background electrolyte comprising 0.1 M KCl or 10 mM Hexaammineruthenium (III) chloride with a background electrolyte of 0.2 M KNO_3 (all Fisher Scientific).

For approach curve measurement and imaging experiments, a constant potential, of such a size that the current was diffusion-limited for the analyte of interest, was applied to the tip. For TPM experiments, frequencies approaching that of mains current and its harmonics were avoided.

Simulations. The model was discretised and solved using the finite element method, implemented in COMSOL multiphysics 3.2b, on a Dell PC, under Windows XP, with a Pentium 4 (2.5 GHz) and 1.5 GB of RAM.

The simulations used $D=8.8x10^{-6}$ cm^2 / s (characteristic of $[Ru(NH_3)_6]^{3+/2+}$).[15] The depth of the second domain in model 2, *d'* was chosen such that any further increase in it did not influence the current response.

Initially, a steady-state concentration profile ($\frac{\partial c}{\partial t} = 0$), with the velocity set to zero, was calculated. This was used as the initial condition for a time-dependent simulation with the velocities as described in equation 7. A sufficient number of cycles was simulated such that the current became periodic (600 cycles was found to be sufficient). The final cycle was taken as the result of the simulation for subsequent analysis.

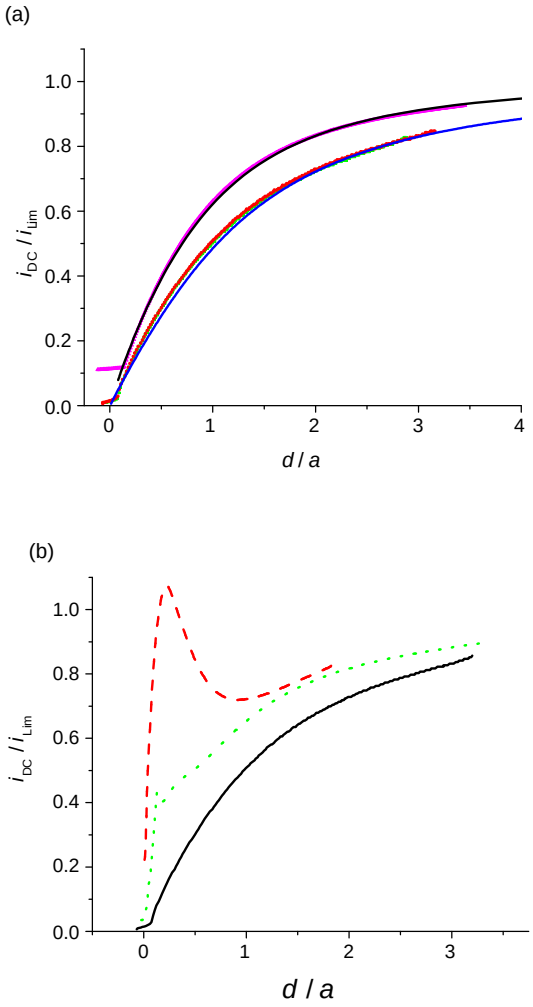

Figure 5-3. Plots of the mean current, $i_{DC,}$ of an oscillating 25 μm diameter UME as it is approached to an inert surface (glass). Curves in part (a) represent the theoretical response of a non-oscillating probe according to the theory presented by Amphlett et al.[51] for a UME with *RG*=10 (blue) and *RG*=4 (black). Points represent experimentally recorded data for *RG*=10, δ = 475 nm, f_m = 69 Hz (green); *RG* = 4, δ = 60 nm, f_m= 70 Hz (magenta); and for a non-oscillating *RG*=10 UME (red). Curves in (b) represent experimental tip approaches for an *RG*=10 UME, with the black curve representing a non-oscillating UME and the red and green curves representing oscillations of f_m = 120 Hz, δ ≈ 700 nm and f_m = 230 Hz, δ ≈ 50 nm. In all experiments $[Ru(NH_3)_6]^{3+}$ was reduced at a diffusion-controlled rate at the electrode and the solution was 5 mM $[Ru(NH_3)_6]^{3+}$ in 0.1 M KNO_3.

5.4 Results

5.4.1 TPM at an inert surface

Figure 5-3 shows the mean current, i_{DC}, normalized by the limiting current far from the surface, i_{Lim}, for a 25 μm-diameter UME approached to an inert surface, while it was oscillated in a direction normal to the sample. The electrode was poised at a potential such that diffusion-limited reduction of $[Ru(NH_3)_6]^{3+}$ occurred. The oscillation amplitudes and frequencies, were (part (a): RG = 10, δ = 475 nm, f_m= 69 Hz, green; RG = 4, δ = 60 nm, f_m= 70 Hz, magenta; RG = 10, δ = 0 nm, red; part (b): RG = 10, δ ≈ 700 nm, f_m= 120 Hz, red, RG = 10, δ ≈ 50 nm, f_m= 230 Hz, green). Also shown are the experimental (red) and theoretical[51] (blue) current response for the UME approaching the surface without any oscillation (δ = 0). There is clearly excellent overlap between the curves, indicating that the average mass transport to the electrode through-out the period of oscillation shows no change. This is in stark contrast to Figure 5-3b, which also shows i_{DC} as a UME was approached to an inert surface while oscillating normally to the surface. On this occasion the amplitude/frequency of oscillation (f_m=120 Hz, δ≈700 nm, red curve; f_m=230 Hz, δ≈50 nm, green curve) was considerably greater than in part (a). It can be seen that there is a marked deviation from the response of a non-oscillating UME (black curve), with an increase in i_{DC} compared to this response, particularly as the UME encounters the surface (d / a < 1). In the case of oscillating at f_m=120 Hz, δ≈700 nm i_{DC} increases to a value greater than i_{Lim} (the steady-state diffusion-limited current to a stationary electrode situated in bulk solution). The enhanced mass transport to the UME is due to convective transport, with the oscillating gap between the tip and the surface acting as a miniature “pump”. This increased mass transport may

have applications in competition modes of SECM[58] where there may be "dead-zones" with little analyte in the tip substrate gap, it was chosen to concentrate on the response in the steady-state regime as seen in Figure 5-3a, where understanding the current response was likely to be an easier task. Henceforth, the frequencies and amplitudes of oscillation were chosen to be in this regime.

From observing the point of inflection, close to the origin, in experimentally recorded i_{DC} curves (e.g. Figure 5-3 and Figure 5-4a) it is possible to infer the probe coming into contact with the surface. This point of contact occurs a small distance from the point where the i_{DC} curve would extrapolate to $i_{DC} = 0$, which can be due to small deviations from perpendicularity between the UME and the surface. Ordinarily in SECM, as is done in Figure 5-3 and Figure 5-4a, the zero point is chosen based on extrapolation of the current-distance curve. When working with an oscillating UME there are other choices of where to define d=0 in an approach curve. The correct choice, to allow fair comparison between i_{AC} measured in different systems, should use the contact with the surface as a defining point. This is demonstrated Figure 5-4, which shows current response for two experiments where a UME was approached to an inert surface while oscillating normal to it at the same amplitude and frequency (δ =34 nm, f_m=34 Hz), but where the alignments between the electrode was slightly different in each case; as can be seen by differing heights of the contact point in Figure 5-4a. The zero point in the plots has been set to either the extrapolation from the extrapolation of i_{DC} values ((a) and (b)), or as the inflection (contact) point of the i_{DC} curve (c). It is clear that agreement in i_{AC} arises only when the inflection point is chosen and this was observed in all experiments. All data will below be

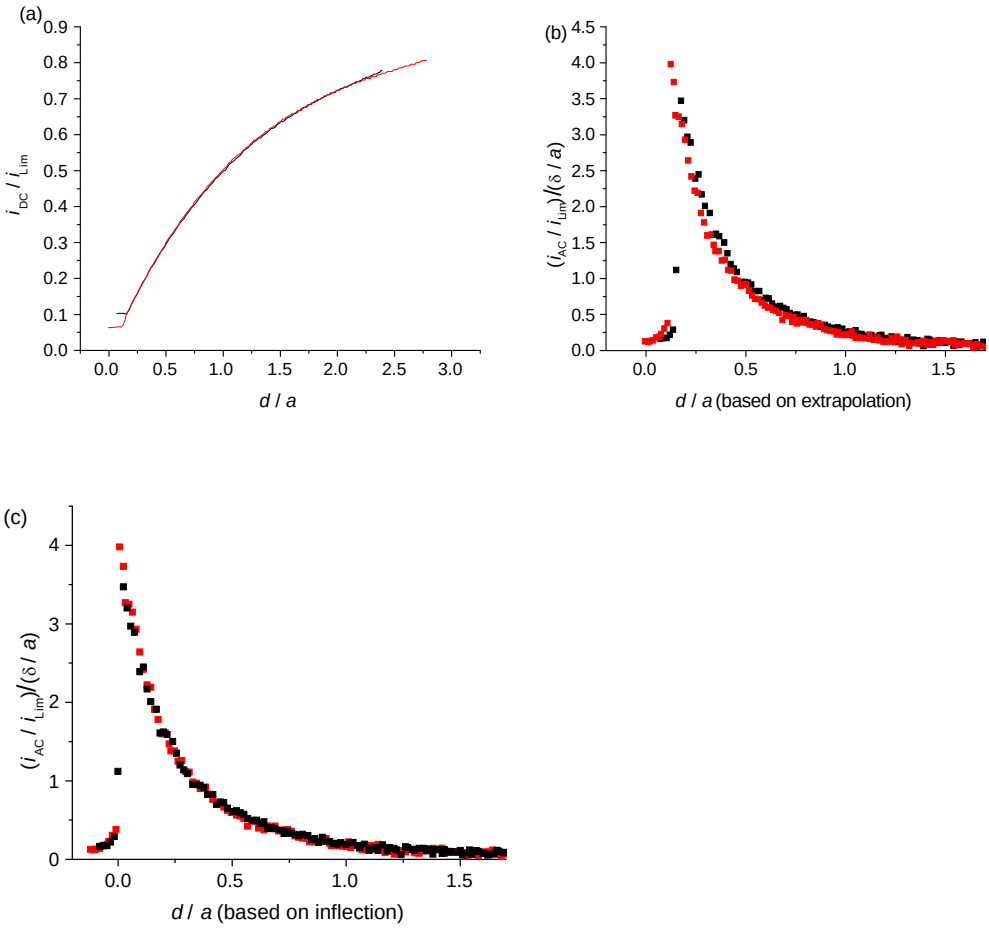

Figure 5-4. Plots of the mean, i_{DC}, and oscillating, i_{AC}, components of the current ((a) and (b,c), respectively) as a UME was moved towards a glass surface while oscillating in a direction normal to surface (*RG*=10, *a*=12.5 μm, δ = 34 nm, f_m = 34 Hz). The two sets of points on each plot represent experiments performed on different days, where the degree of perpendicularity between the electrode and surface was slightly different; colours are used consistently to denote each experiment. In parts (a) and (b) the *d*=0 distance was assigned such that extrapolation of the experimentally current-distance relationship gave a current of i_{DC}=0 at *d*=0 based on an SECM inert substrate model[52]. The distance *d*=0 in part (c) was taken to be the point of inflection in the measured value of the mean current, i_{DC}, which in part (a) occur at approximately *d*=0.1*a* (red) and *d*=0.15*a* (black). In both experiments $[Ru(NH_3)_6]^{3+}$ was reduced at a diffusion-controlled rate at the electrode and the solution was 5 mM $[Ru(NH_3)_6]^{3+}$ in 0.1 M KNO_3.

therefore presented with *d*=0 taken as the inflection point. The effect of tip-substrate separation on fluid flow and the strong influence of this on i_{AC} (*vide infra*) is the reason for choosing this measure of distance for TPM (i_{AC}) measurements. If alignment of the UME perpendicular to the surface of interest

is perfect, then there is equivalence between using the inflection point and extrapolation of the approach curve as methods to set the point d=0. As such, this is something that one should strive for in TPM experiments. With the simulations presented, the perpendicularity can be defined trivially and thus the two choices of distance measure are always equivalent.

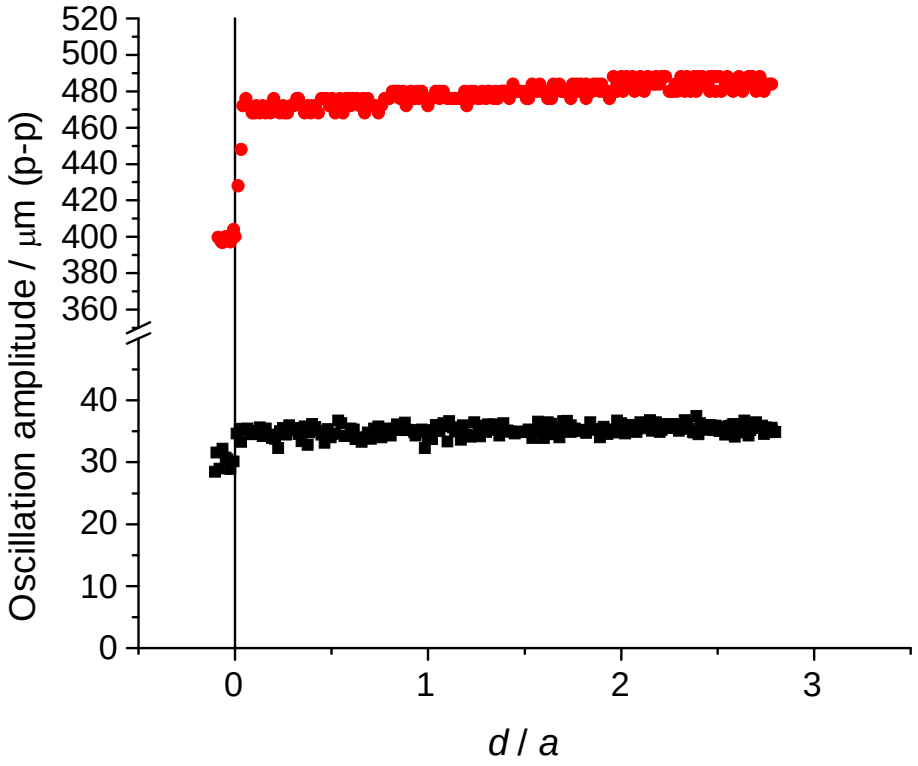

Figure 5-5. Plot of the amplitude of oscillation of a piezo actuator, controlling the oscillating approach of a 25 µm-diameter, *RG*=10, UME to a glass surface; both the direction of driving and the physical oscillations was normal to the surface. The amplitude of piezo oscillation was measured by an integral strain gauge sensor. Note: the break in the vertical axis, to allow different amplitudes of oscillation (35 nm at 34 Hz, black and 475 nm, 69 Hz, red) to be displayed.

The tip-surface interaction can be seen by other measurements. Figure 5-5 shows the oscillation amplitude of the z-piezoelectric positioner, as recorded by a strain gauge sensor, while an oscillating UME (*RG*=10, a=12.5 µm and δ=35 nm, f_m=34 Hz (black) or δ=475 nm, f_m=69 Hz (red)) is approached to a glass surface.

A step change in amplitude of circa 15 % is clearly visible at d/a=0 and is indicative of the damping of the piezo oscillation upon contacting the surface. Damping of lateral oscillations is used to detect proximity to the surface in the shear-force mode of SECM operation[59-61], but this involves a non-contact (shear) force. There is a possibility to use the damped oscillation as a distance sensing mechanism for imaging with SECM. However, further experiments would certainly necessary to verify this. The slight decrease in amplitude over the duration of the entire approach visible in the curve for δ=475 nm and f_m=69 Hz, this is due to the piezos having a slightly non-linear expansion.

Figure 5-6 shows the i_{AC} response as a UME undergoing TPM is brought towards a glass surface. The value of i_{AC} has been twice normalized; firstly, by the limiting current far from the surface, i_{Lim}, and secondly, by the normalized oscillation amplitude, δ / a. The 25 μm diameter UME was characterised by RG = 10. There is excellent overlap between approaches made at the same frequency (19 Hz, red and blue; 69 Hz, green and black) despite the different amplitudes, thus, within the range of parameters investigated (f_m=69 Hz, δ=475 nm and 20 nm, green and black curves respectively; f_m=19 Hz, δ=637 nm and 29 nm**,** red and blue curves respectively), i_{AC} is proportional to the oscillation amplitude, as was shown by Wipf and Bard[49]. All i_{AC} will be presented with this normalization to allow simple comparison. Agreement between the normalized curves only breaks down when the electrode is very close to the surface <0.1a, because at this distance the fluid flow becomes more complex as a large fraction of the gap between tip and surface is equivalent to the distance travelled by the tip in a single oscillation cycle. Moreover, variations from ideal perpendicularity will be further accentuated within this region. No attempt is made in this work to

accurately describe or understand this part of the current-distance response because of these complications. In practice one is unlikely to operate TPM at such close distances.

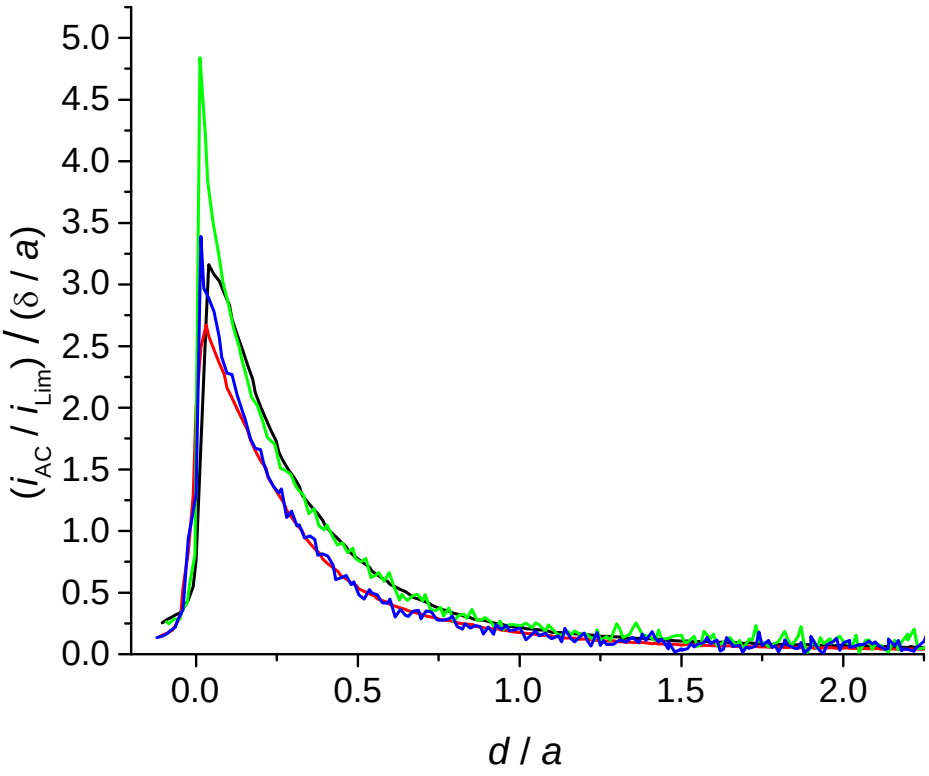

Figure 5-6. Plot of the normalized first harmonic amplitude of the current oscillation, i_{AC}, for an oscillating 25 μm diameter, *RG*=10, UME moved towards a glass surface. Normalization occurs through dividing by the limiting current with the UME far from the surface, i_{Lim}, and also dividing by the oscillation amplitude, δ, which is itself normalized by the electrode radius, *a*. Green and black curves are both for a frequency of oscillation of f_m=69 Hz, with amplitudes of 475 nm and 20 nm, respectively; while red and blue are both for f_m=19 Hz, with δ=637 nm and δ=29 nm, respectively. In all experiments $[Ru(NH_3)_6]^{3+}$ was reduced at a diffusion-controlled rate at the electrode and the solution was 5 mM $[Ru(NH_3)_6]^{3+}$ in 0.1 M KNO_3.

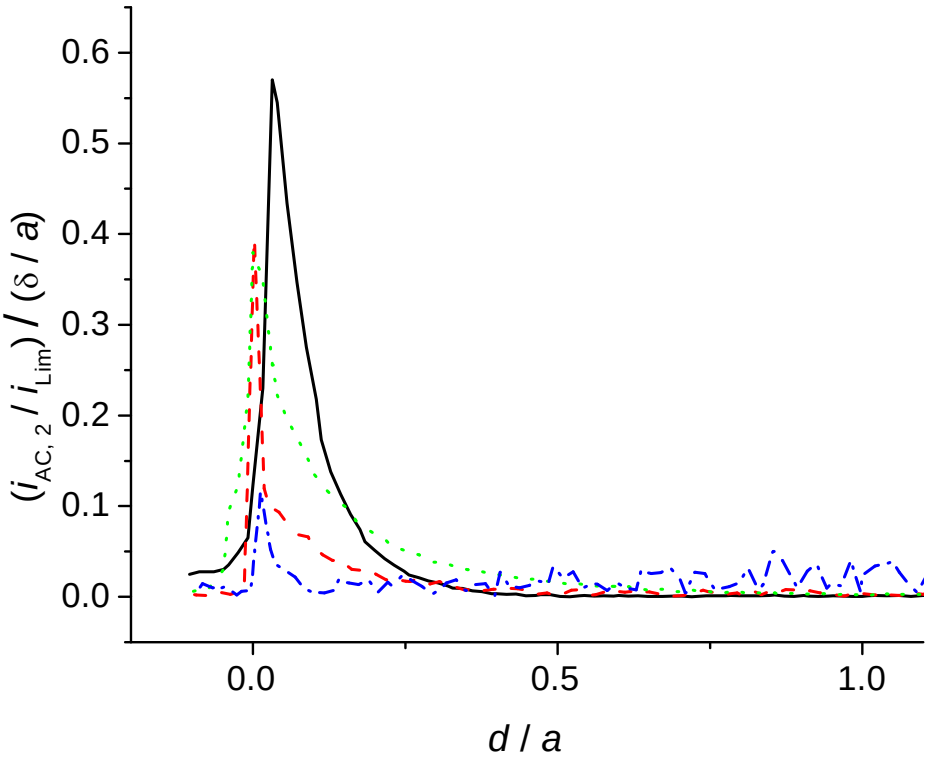

Figure 5-7 Plot of the normalized second harmonic of the current, $i_{AC,2}$, for the approach of an oscillating 25 μm diameter UME (*RG*=10) to a glass surface, for various frequencies and amplitudes of oscillation (δ =475 nm, f_m=69 Hz, black solid line; δ =106 nm, f_m=34 Hz, red dashed line; δ =637 nm, f_m=19 Hz, green dotted line; δ =20 nm, f_m=69 Hz, blue dash-dotted line). In all cases $[Ru(NH_3)_6]^{3+}$ was reduced at a diffusion-controlled rate at the electrode and the solution was 5 mM $[Ru(NH_3)_6]^{3+}$ in 0.1 M KNO_3

The complexity of the mass transport when close to a surface can be observed in Figure 5-7, which shows plots of the second harmonic of the current oscillation as an oscillating 25 μm diameter, *RG*=10, UME is approached to an inert (glass) surface. Frequencies and amplitudes of oscillation were: δ =475 nm, f_m=69 Hz, black solid line; δ =106 nm, f_m=34 Hz, red dashed line; δ =637 nm, f_m=19 Hz, green dotted line; δ =20 nm, f_m=69 Hz, blue dash-dotted line. We see correlation between the amplitude and frequency of the second harmonic of the current and the oscillation amplitude, with larger amplitude/higher frequency oscillations giving rise to large second harmonic components, which are noticeable at greater distance from the surface. However, the interplay between frequency and amplitude appears to be complex, as is indicated by the intersecting curves. The

apparently larger noise for the low amplitude oscillation, δ=20 nm, is an artefact of the normalization. Referring back to Figure 5-6, it is apparent that only for the highest frequency/amplitude combinations (δ =475 nm, f_m=69 Hz) is the 2nd harmonic a noticeable fraction of the 1st harmonic. For δ =475 nm, f_m=69 Hz this amounts to a maximum of around 15 %, representing a relatively small proportion of the current. Furthermore, this component is only observed in a region very close to the surface. This behaviour contrasts markedly with the approach curves that deviated from standard i_{DC} theory (Figure 5-3b), where the 2nd harmonic component (not shown) was found to exceed the 1st harmonic in magnitude.

Proportionality of the 1st harmonic, i_{AC}, with oscillation amplitude, observed experimentally (Figure 5-6), was also seen in the simulated current responses as exemplified by Figure 5-8 which shows i_{AC} versus distance as simulated using model 1 (D = 8.8x10^{-6} cm^2 s^{-1}, a = 12.5 μm, RG = 10). There is perfect agreement of the blue curve (δ = 10 nm) and points (δ=100 nm); for both simulations for the frequency of oscillation was f_m=70 Hz. The proportionality observed is not necessarily an expected property of the model, but is clearly applicable for parameters (D, a, δ, f_m) in the range we have investigated. It is however the case that the simulated response of i_{AC} on approach to the surface is a function of frequency (frequencies shown in Figure 5-8: f_m=20, 37, 53 and 70 Hz), however the difference is only noticeable in close proximity to the surface, i.e. d / a<1, with a trend of higher frequencies showing higher values of i_{AC} close to the surface. Note that at the closest distances, the simulated values of i_{AC} are unlikely to represent the true physical situation as will be discussed later.

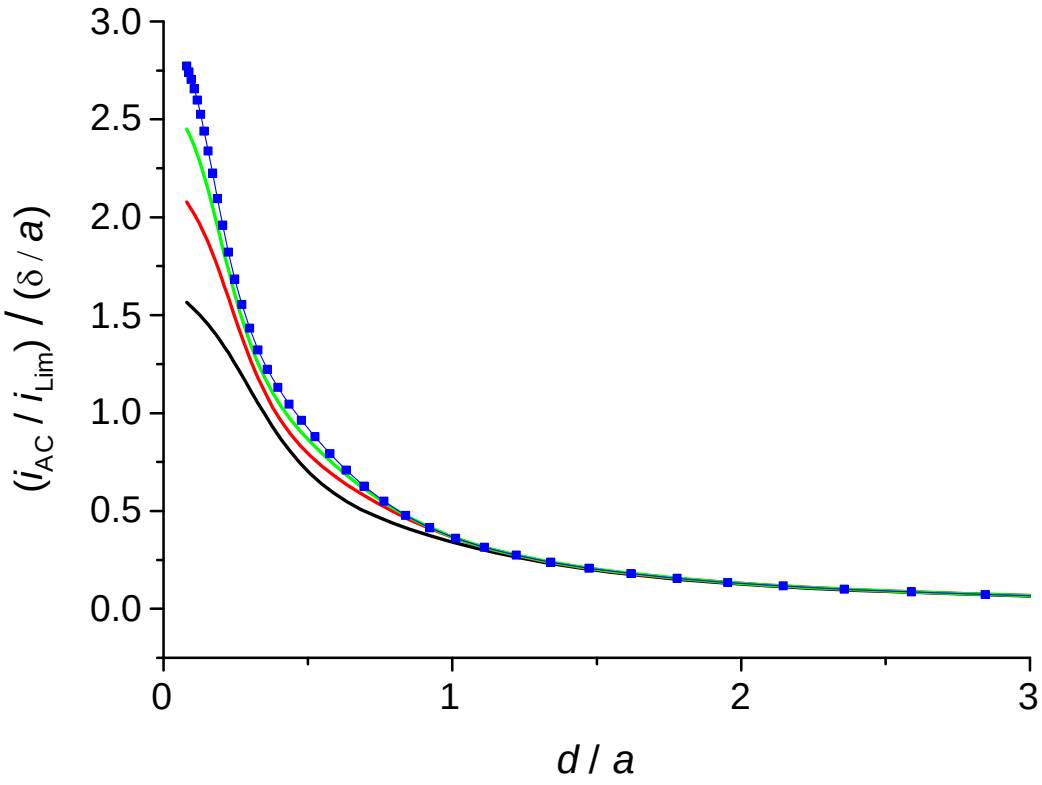

Figure 5-8: Plot of simulated i_{AC} for a 25 μm diameter, *RG*=10, UME as it was approached to an inert glass surface. The tip was oscillated at various frequencies (f_m=20 Hz, black; fm=37 Hz, red, f_m=53 Hz green; f_m=70 Hz, blue). All simulations performed using D = 8.8 x 10^{-6} cm^2 s^{-1}. Oscillation amplitudes were δ = 58 nm for the 20, 37 and 53 Hz oscillations; blue points are for δ=100 nm, blue line for δ=10 nm.

Figure 5-9 compares theory with experiment, showing plots of simulated (points) and experimentally measured (lines) i_{AC} as a UME (*RG*=10, a=12.5 μm) is brought towards an inert (glass) substrate, while the tip was oscillated at f_m=19 Hz, δ=637 nm (red curve) or f_m=69 Hz, δ=475 nm (black curve). There is fair agreement between the experimental and simulated curves and a clear improvement over using the earlier derivative-based theory (green curve)[49] to predict the i_{AC} response.

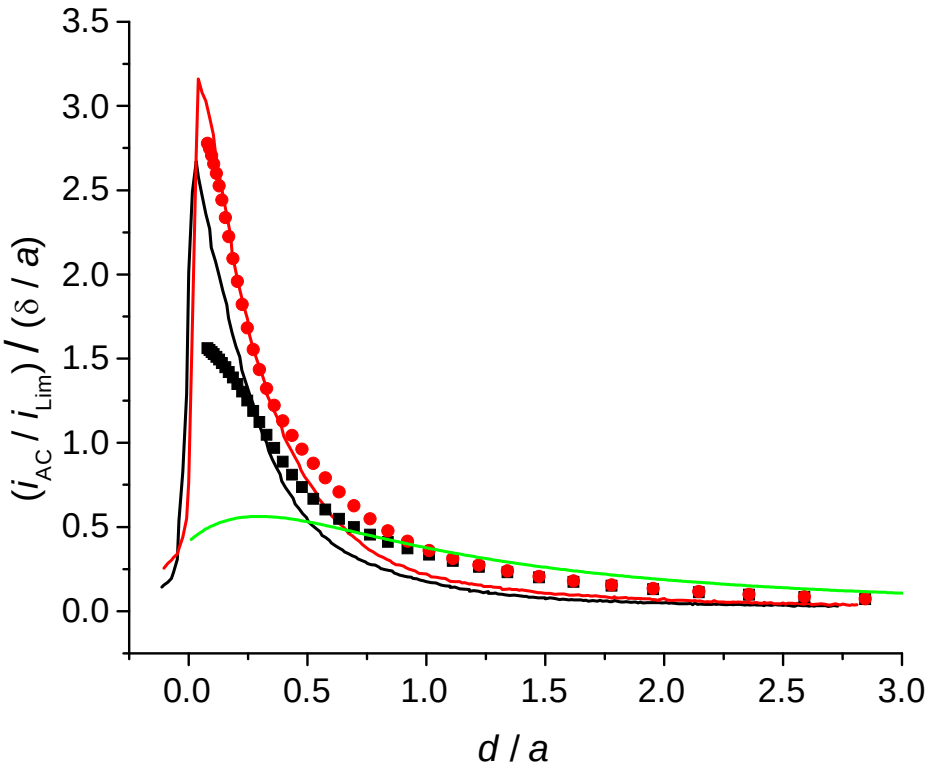

Figure 5-9. Experimental and simulated response of i_{AC} as a 25 μm diameter, *RG*=10 UME was approached to an inert (glass) surface, while it was oscillated normally to the surface. Black lines and points represent the experimental and simulated response, respectively, for δ=637 nm, f_m=19 Hz; red lines and points represent the experimental and simulated response, respectively, for δ=475 nm, f_m=69 Hz. Green line represents the result of the derivative based theory as introduced, and concluded previously to be unsatisfactory for the approach to an insulator, in Wipf and Bard.[49]). In all experiments $[Ru(NH_3)_6]^{3+}$ was reduced at a diffusion-controlled rate at the electrode and the solution was 5 mM $[Ru(NH_3)_6]^{3+}$ in 0.1 M KNO_3. For the simulations a value of the diffusion coefficient, D=8.8x10^{-6} cm^2 s^{-1},[15] was used.

Because we have identified convective effects to be strong in the approach of an oscillating tip to an inert surface, we carried out some experiments to explore the influence of *RG* on the response. Clearly the larger the *RG* value the stronger the effect, as can be seen by the radial dependence of velocity (equation 5.7).

Figure 5-10 demonstrates the influence of the ratio of total tip width (electrode and surrounding glass sheath) to electrode width, *RG*, on the i_{AC}

response. The experimental i_{AC} curve for an *RG*=4, 25 μm UME approached to a surface (δ=60 nm, f_m=70 Hz, red curve) is around half that of the response for an *RG*=10, 25 μm UME (δ=475 nm, f_m=69 Hz, green curve) and is further from the simulated curve for the same parameters (*RG*=4, *a*=12.5 μm, δ=60 nm, f_m=70 Hz, black curve).

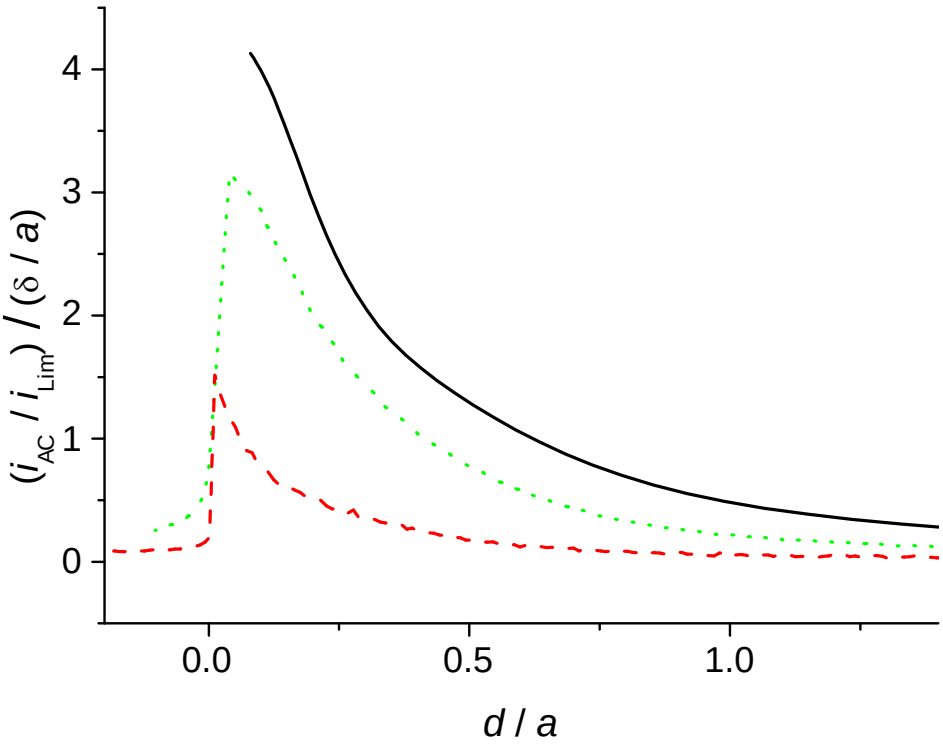

Figure 5-10. Plot of normalized i_{AC} for an oscillating 25 μm diameter UME brought towards an inert (glass) substrate. Red curve is for an electrode with *RG*=4, oscillating with δ=60 nm, f_m=70 Hz. A simulation with the same parameters is plotted as the black curve. The Green curve represents the response of an *RG*=10 electrode (δ=475 nm, f_m=69 Hz).

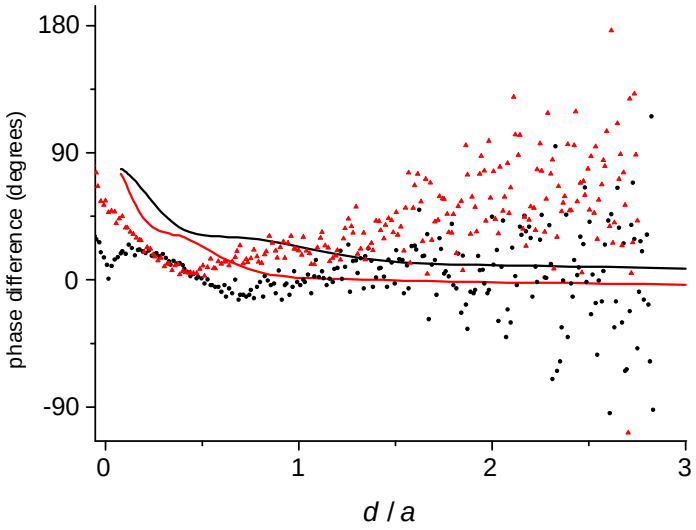

Figure 5-11 : Experimental and theoretical responses of the phase difference between tip-surface separation and the current oscillations as a 25 μm, *RG*=10, UME was approached to an inert (glass) substrate while the tip was oscillated at f_m = 19 Hz δ = 58 nm (black); or f_m = 70 Hz, δ = 37 nm (red) in a direction normal to the sample. The current has been treated as positive, so that a phase difference of zero indicates coincidence of current and tip-substrate maxima. The order of the differencing calculation is such that a value greater than zero indicates that the current maximum occurs prior to the maximum in the tip-substrate separation. In all experiments $[Ru(NH_3)_6]^{3+}$ was reduced at a diffusion-controlled rate at the electrode and the solution was 5 mM $[Ru(NH_3)_6]^{3+}$ in 0.1 M KNO_3. For the simulations a value of the diffusion coefficient, D=8.8x10^{-6} cm^2 s^{-1}, was used. [15]

There is also good agreement between theory and experiment for the phase of the oscillating current, relative to the physical oscillation of the UME, for the approach of a 25 μm diameter, *RG*=10, UME to an inert surface, as shown in Figure 5-11. When the UME is far from the interface the maximum current amplitude (taking measured current to be positive) is observed at the point during the tip oscillation cycle when the UME is furthest from the interface, as is indicated by a phase of zero. As the mean tip-substrate separation, *d*, is decreased the phase difference shifts to a value greater than zero, indicating

that the maximum in current occurs at a point in the tip oscillation cycle prior to the tip-substrate separation reaching its maximum value during the cycle.

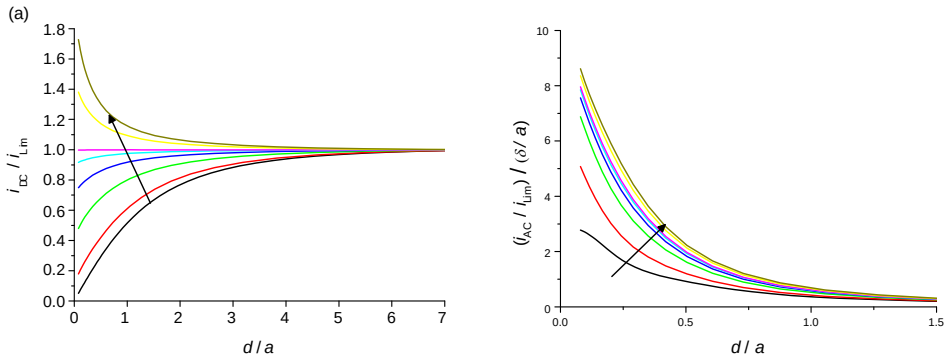

Figure 5-12: Simulated mean current, i_{DC}, (a) and 1st harmonic, i_{AC}, (b) for a 25 μm, *RG*=10, UME as it was approached through a first (aqueous) phase to the interface with a second (gel) phase of differing permeability. During the approach the UME was oscillated 36 nm at 70 Hz in a direction normal to the sample while detecting an electroactive species, present in both phases, at a diffusion-limited rate. The permeability was altered by varying diffusion coefficient of the second phase. Lines represent permeabilities of: *D'/D* = 0, 0.1, 0.4, 0.7, 0.9, 1, 1.5, 2.0 (*D* = 8.8 x 10^{-6} cm^2 s^{-1}); the arrow indicates the direction of increasing permeability

5.4.2 TPM with induced transfer at a permeable substrate

Figure 5-12 plots the simulated current response of an oscillating electrode moved through a first (aqueous) phase towards the interface with a second (gel) phase of differing permeability (varying from *D'/D*=0 to 2), as calculated using model 2. Simulation parameters: *a*= 12.5 x 10^{-6} m, f_m = 70 Hz, δ = 36 nm, *RG* = 10, *D* = 8.8 x 10^{-6} cm^2 s^{-1}. Part (a) shows i_{DC}, which demonstrates behaviour previously described for SECMIT [53], indicating that the average mass transport to the electrode over the period of an oscillation is not altered. Part (b) shows that in this situation the i_{AC} response is strongly dependent on the permeability of the second phase, with an increase in the i_{AC} response occurring with increasing

D'/D ratio. For *D'/D*=2 it attains a value more than twice that for an inert surface. It is also evident that the AC response is sensitive to *D'*.

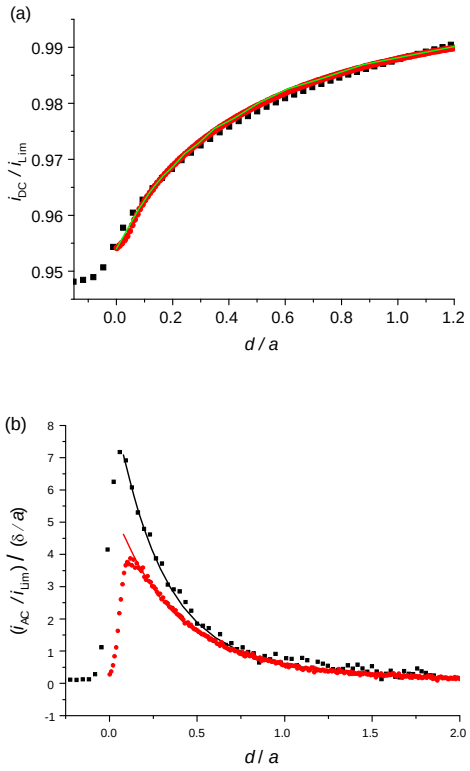

Figure 5-13: Simulated (curves) and experimental (points) data for the approach of a UME through a first (aqueous) phase to the interface with a second (gel) phase of differing permeability with respect to the electroactive species $[Ru(NH_3)]^{3+}$ detected at the tip at a diffusion-limited rate. In the experiments the second phase was 1% agar. During the approach, the UME was oscillated at: f_m = 60 Hz, δ = 65 nm, black; f_m = 32 Hz, δ = 110 nm, red. Part (a) is a plot of the mean current, i_{DC}, and (b) is of the 1st harmonic, i_{AC}. The green curve in part (a) is the simulated i_{DC} response, which is independent of frequency. The mediator for the experiments was 10 mM $[Ru(NH_3)_6]^{3+}$ in 0.1 M KNO_3. Simulations were performed with D=8.8x10^{-6} cm^2 s^{-1} and D'=0.945 D.

To confirm the simulation results, SECM-TPM experiments were carried out to prove the permeability of $Ru(NH_3)_6^{3+}$ in an 1 % agar gel. The tip was held at a potential to detect $Ru(NH_3)_6^{3+}$ by reduction at a transport-limited rate while approaching the sample. Figure 5-13 demonstrates the excellent agreement between simulated (lines) and experimental (points) current responses for an

oscillating UME approaching the sample. The i_{DC} response in (a) allows accurate determination of the substrate permeability ($D'/D \approx 0.95$). The i_{AC} response demonstrates frequency dependence, with higher frequencies (f_m=60 Hz vs. f_m=32 Hz) yielding a larger response in both experiment and theory. As with the approach to an inert substrate both the experimental and theoretical i_{AC} responses were proportional to δ and this was removed through normalization. Compared to the DC response, this is a massive change in the AC signal. It is satisfying that the AC and DC responses yield the same values of D' giving confidence that the TPM method could be valuable for future applications to permeability measurements.

5.5 Discussion

Despite the simplicity of the models presented here they offer a greatly improved understanding of the processes involved SECM-TPM. It is clear that fluid flow, and consequent convective mass transport, is a major factor affecting the oscillating component of the current. This is perhaps most clear in the experimental approach to a surface with permeability $D'/D \approx 1$ (Figure 5-13) where derivative theory would give i_{AC}=0. The strong signal in i_{AC} when an oscillating UME is approached to a permeable substrate with permeability close to 1, is in contrast to the i_{DC} response, highlighting the possibility to use TPM as a mode for monitoring the distance of the UME from an interface which would be invisible to most standard modes of SECM operation.

It is important to comment on the applicability of the model developed. By restricting the domain of simulation to the volume directly under the tip, the transport of species laterally out from the tip is only described approximately. When the surface is inert species only move to and from the electrode in the thin

gap between the tip and surface, whereas when the substrate is permeable there is additional transport from the second phase underneath the electrode, which is accurately described by model 2. A consequence of this is that the model provides a better description of induced transfer with a permeable sample than the limiting case of mass transport above an inert impermeable surface. This may account for the poorer fit or simulated to experimental i_{AC} for an inert substrate than a permeable one.

Describing mass-transport beyond the UME radius would improve the theoretical model; however, there are other limitations that need to be pointed out. The fluid velocity is described as having a zero axial component and a parabolic radial velocity profile, which is a simplification. However, if the frame of reference is taken to move with the electrode then it should be a reasonable assumption close to the electrode surface and when the relative magnitudes of the axial and radial components is large, but not when the UME is far from the surface. Also, the oscillating tip changes the dimensions of the gap between tip and substrate and when the UME is close to the surface this deviation would be a much larger fraction, leading to further inaccuracies. A more accurate model, which would address these issues would couple the explicit solution of the fluid dynamics profile with a moving geometry.

Various non-idealities in terms of the experimental geometry and tip-substrate alignment will affect whether the simulations accurately reproduce the experimental results. It has already been highlighted that the perpendicularity between tip and substrate is an issue in many SECM experiments, but also the flatness of the sample and its rigidity under fluid forces could cause significant differences for soft samples.

The permeability model used in this paper arises from a simple steady-state result of SECMIT theory[53], which found that under certain conditions the permeability can be viewed in terms of the product of the partition coefficient between the two phases and the ratio of diffusion coefficients between the phases. A more complicated model could be invoked when this does not hold and/or kinetics at the interface need to be taken in to account. This would easily be incorporated into model 2, but with the predominantly aqueous structure of agar, used for the experimental demonstration, it was not deemed necessary to introduce kinetics.

While the time-dependent simulation of TPM, as performed in this work, can provide the results necessary for understanding TPM, it may be prudent to formulate the problem as a 3-dimensional steady-state problem, where, in addition to the radial and axial coordinates a third coordinate is introduced for time. This coordinate would be periodic with the period of oscillation. A solution could be reached significantly faster than having to perform many, highly accurate, iterations in a 2D simulation.

5.6 Conclusion

This work demonstrates that including fluid effects is necessary to quantitatively understand SECM-TPM. A model has been presented that delivers the current response in agreement with experimental TPM approach curves to both inert and permeable substrates (under SECMIT conditions). Avenues for refinement of the model have been discussed. The extension of the current model to further modes of SECM operation is would be straightforward.

References

(1) Bard, A. J.; Fan, F.-R. F.; Kwak, J.; Lev, O. *Anal. Chem.* **1989**, *61*, 132.
(2) Kwak, J.; Bard, A. J. *Anal. Chem.* **1989**, *61*, 1221.
(3) Bard, A. J.; Mirkin, M. V., Eds. *Scanning Electrochemical Microscopy*; Marcel Dekker: New York, 2001.
(4) Pierce, D. T.; Unwin, P. R.; Bard, A. J. *Anal Chem* **1992**, *64*, 1795-1804.
(5) Bard, A. J.; Fan, F.-R. F.; Pierce, D. T.; Unwin, P. R.; Wipf, D. O.; Zhou, F. *Science* **1991**, *254*, 68.
(6) Pierce, D. T.; Bard, A. J. *Anal. Chem.* **1993**, *65*, 3598.
(7) Shiku, H.; Takeda, T.; Yamada, H.; Matsue, T.; Uchida, I. *Anal. Chem.* **1995**, *67*, 312.
(8) Shiku, H.; Matsue, T.; Uchida, I. *Anal. Chem.* **1996**, *68*, 1276.
(9) Shiku, H.; Hara, Y.; Takeda, T.; Matsue, T.; Uchida, I. In *Solid-Liquid Electrochemical Interfaces*; Jerkiewicz, G., Soriaga, M. P., Uosaka, K., Wieckowski, A., Eds.; American Chemical Society: Washington, DC, 1997, pp 202.
(10) Wipf, D. O. *Colloids and Surfaces, A* **1994**, *93*, 251-261.
(11) Lister, T. E.; Pinhero, P. J.; Trowbridge, T. L.; Mizia, R. E. *Journal of Electroanalytical Chemistry* **2005**, *579*, 291–298.
(12) Macpherson, J. V.; Unwin, P. R. *J. Phys. Chem.* **1995**, *99*, 3338.
(13) Basame, S. B.; White, H. S. *Anal. Chem.* **1999**, *71*, 3166-3170.
(14) Gonsalves, M.; Macpherson, J. V.; O'Hare, D.; Winlove, C. P.; Unwin, P. R. *Biochim. Biophys. Acta.* **2000**, *1524*, 66.
(15) Macpherson, J. V.; O'Hare, D.; Unwin, P. R.; Winlove, C. P. *Biophys. J.* **1997**, *73*, 2771.
(16) Zhang, J.; Unwin, P. R. *Langmuir* **2002**, *18*, 1218-1224.
(17) Pu, G.; Longo, M. L.; Borden, M. A. *J. Am. Chem. Soc.* **2005**, *127*, 6524-6525.
(18) Ciani, I.; Burt, D. P.; Daniele, S.; Unwin, P. R. *J. Phys. Chem. B* **2004**, *108*, 3801-3809.
(19) Cannan, S.; Zhang, J.; Grunfeld, F.; Unwin, P. R. *Langmuir* **2004**, *20*, 701-707.
(20) Borden, M. A.; Longo, M. L. *J. Phys. Chem. B* **2004**, *108*, 6009-6016.
(21) Yamada, H.; Matsue, T.; Uchida, I. *Biochem. Biophys. Res. Comm.* **1991**, *180*, 1330-1334.
(22) Pohl, P.; Rokitskaya, T.; Pohl, E. E.; Saparov, S. M. *Biochim. Biophys. Acta* **1997**, *1323*, 163-172.
(23) Zhang, J.; Unwin, P. R. *J. Am. Chem. Soc.* **2000**, *122*, 2597.
(24) Zhang, J.; Unwin, P. R. *Langmuir* **2002**, *18*, 1218.
(25) Slevin, C. J.; Unwin., P. R. *J. Am. Chem. Soc.* **2000**, *122*, 2597.
(26) Yamada, H.; Matsue, T.; Uchida, I. *Biochem. Biophys. Res. Comm.* **1991**, *180*, 1330.
(27) Matsue, T.; Shiku, H.; Yamada, H.; Uchida, I. *J. Phys. Chem.* **1994**, *98*, 11001.
(28) Holt, K. B.; Bard, A. J.; Show, Y.; Swain, G. M. *Journal of Physical Chemistry B* **2004**, *108*, 15117-15127.

(29) Fortin, E.; Chane-Tune, J.; Delabouglise, D.; Bouvier, P.; Livache, T.; Mailley, P.; Marcus, B.; Mermoux, M.; Petit, J.-P.; Szunerits, S.; Vieil, E. *Electroanalysis* **2005**, *17*, 517-526.
(30) Colley, A. L.; Williams, C. G.; D'HaenensJohansson, U.; Newton, M. E.; Unwin, P. R.; Wilson, N. R.; Macpherson, J. V. *Anal. Chem.* **2006**, *78*, 2539-2548.
(31) Binnig, G.; Quate, C. F.; Gerber, C. *Phys. Rev. Lett.* **1986**, *56*, 930.
(32) Rugar, D.; Hansma, P. K. *Phys. Today* **1990**, *43*, 23.
(33) Wiesendanger, R. *Scanning Probe Microscopy, Spectroscopy*; Cambridge University Press: Cambridge, UK, 1994.
(34) Macpherson, J. V.; Unwin, P. R. *Anal. Chem.* **2000**, *72*, 276.
(35) Gardner, C. E.; Macpherson, J. V. *Anal Chem* **2002**, *74*, 576A.
(36) Kranz, C.; Friedbacher, G.; Mizaikoff, B.; Lugstein, A.; Smoliner, J.; Bertagnolli, E. *Anal. Chem.* **2001**, *73*, 2491.
(37) Keung, A.; Kranz, C.; Lugstein, A.; Bertagnolli, E.; Mizaikoff, B. *Angew. Chem. Int. Ed.* **2003**, *42*, 3238.
(38) Burt, D. P.; Wilson, N. R.; Weaver, J.; Dobson, P. S.; Macpherson, J. V. *Nanoletters* **2005**, *5*, 639.
(39) Dobson, P. S.; Weaver, J. M. R.; Holder, M. N.; Unwin, P. R.; Macpherson, J. V. *Anal Chem* **2005**, *77*, 424.
(40) Jones, C. E.; Unwin, P. R.; Macpherson, J. V. *ChemPhysChem* **2003**, *4*, 139-146.
(41) Buchler, M.; Kelley, S. C.; Smyrl, W. H. *Electrochemical and Solid-State Letters* **2000**, *3*, 35-38.
(42) Katemann, B. B.; Schulte, A.; Schuhmann, W. *Chemistry* **2003**, *9*, 2025-2033.
(43) Oyamatsu, D.; Hirano, Y.; Kanaya, N.; Mase, Y.; Nishizawa, M.; Matsue, T. *Bioelectrochem.* **2003**, *60*, 115-121.
(44) Ludwig, M.; Kranz, C.; Schuhmann, W.; Gaub, H. E. *Rev. Sci. Instrum.* **1995**, *66*, 2857.
(45) Alpuche-Aviles, M. A.; Wipf, D. O. *Anal Chem* **2001**, *73*, 4873-4881.
(46) Gabrielli, C.; Huet, F.; Keddam, M.; Rousseau, P.; Vivier, V. *J. Phys. Chem. B* **2004**, *108*, 11620-11626.
(47) Osbourn, D. M.; Sanger, R. H.; Smith, P. J. S. *Anal Chem* **2005**, *77*, 6999-7004.
(48) Kurulugama, R. T.; Wipf, D. O.; Takacs, S. A.; Pongmayteegul, S.; Garris, P. A.; Baur, J. E. *Anal Chem* **2005**, *77*, 1111-1117.
(49) Wipf, D. O.; Bard, A. J. *Anal. Chem.* **1992**, *64*, 1362-1367.
(50) Wipf, D. O.; Bard, A. J. *Anal. Chem.* **1993**, *65*, 1373-1377.
(51) Amphlett, J. L.; Denault, G. *J. Phys. Chem. B* **1998**, *102*, 9946-9951.
(52) Kwak, J.; Bard, A. J. *Anal. Chem.* **1989**, *61*, 1221-1227.
(53) Barker, A. L.; Macpherson, J. V.; Slevin, C. J.; Unwin, P. R. *J. Phys. Chem. B* **1998**, *102*, 1586.
(54) Wipf, D. O.; Bard, A. J. *Anal. Chem.* **1993**, *65*, 1373-1377.
(55) Wightman, R. M.; Wipf, D. O. In *Electroanalytical Chemistry, Vol. 15*; Bard, A. J., Ed.; Marcel Dekker: New York, 1989, pp 267.
(56) Bard, A. J.; Fan, F.-R.; Kwak, J.; Lev, O. *Anal. Chem.* **1989**, *61*, 132-138.
(57) Barker, A. L.; Macpherson, J. V.; Slevin, C. J.; Unwin, P. R. *J. Phys. Chem. B* **1998**, *102*, 1586.

(58) Eckhard, K.; Chen, X.; Turcu, F.; Schuhmann, W. *Phys. Chem. Chem. Phys.* **2006**, *8*, 5359.
(59) Katemann, B. B.; Schulte, A.; Schuhmann, W. *Chem Eur J* **2003**, *9*, 2025-2033.
(60) Hengstenberg, A.; Kranz, C.; Schuhmann, W. *Chem Eur J* **2000**, *6*, 1547-1554.
(61) Buchler, M.; Kelley, S. C.; Smyrl, W. H. *Electrochem Solid-State Lett* **2000**, *3*, 35-38.

Chapter 6: Scanning Micropipette Contact Method (SMCM) for High Resolution Imaging of Electrode Surface Redox Activity

6.1 Introduction

High resolution chemically-sensitive microscopy techniques have proven powerful in elucidating the properties and reactivity of a wide variety of interfaces and interfacial processes, particularly in probing the spatially heterogeneous activity of electrode surfaces.[1-9] This type of experimental technique has led to an understanding of how characteristic active sites on electrode surfaces may dominate the overall electrochemical response,[4-9] providing insights that cannot be obtained by classical voltammetric methods alone.

Among electrochemical mapping techniques, scanning electrochemical microscopy (SECM)[5-11] is particularly popular and now well-established for imaging both surface topography[10, 12] and the reactivity of electrode substrates.[5-9, 13-23] SECM utilizes an ultramicroelectrode (UME) as a mobile tip, the response of which provides information on the physicochemical properties of an underlying substrate. There is a growing family of SECM operation modes,[5, 6, 9,

[24, 25] among which the feedback mode[8, 12, 26] and generation/collection[27, 28] modes are used most in the investigation of electrode surfaces and related interfaces. In the feedback mode, the tip is used to generate a redox species from a precursor in solution, which may be regenerated at the substrate, thereby enhancing the tip current. In the generation-collection modes, one working electrode (tip or substrate) generates a species which is then collected by the second electrode (substrate or tip).

The spatial region probed by SECM is greater than the dimensions of the active part of the UME probe,[29] and is sensitive to the tip-substrate separation, the surface kinetics and the detection mode employed.[29] While probe electrodes with characteristic dimensions of less than 1 μm have been fabricated,[30-33] they have proved generally difficult to reproduce, characterize and deploy as imaging probes, as evidenced by a relatively sparse number of reports and limited applications.[34-37] Furthermore, edge diffusion to the tip electrode in all SECM modes and the overlap of diffusion fields of neighbouring active sites on the substrate, for tip collection measurements, results in a loss of lateral resolution.

Microcapillary-based techniques have previously been employed to probe the electrochemistry of small areas of macroscopic electrode surfaces. [38-42] This approach has been used to examine the electrochemical properties of defined areas on metal surfaces. For example, the technique has been used to study pit initiation on stainless steels[38, 39]. Tip diameters between 1 and 1000 μm were employed, with a solution-filled capillary attached to the lens of a microscope, to allow easy positioning over the site of interest. The substrate generally served as a working electrode and the reference electrode was connected externally to a

microcapillary via an electrolytic bridge. This technique was subsequently adapted[43] to incorporate a flow-through capillary system to allow use in applications with large current densities (> 100 A/cm^2).

Initially, the microcapillary technique only allowed individual measurements to be made at specific surface locations, but was subsequently developed[44] to facilitate surface imaging. To date, these experiments have tended to focus on surface electrochemical processes intrinsic to corrosion and passivation,[40, 41] but there is clearly scope for investigating electrochemical processes involving solution redox couples, which is the focus of the studies herein. Such applications require a detailed description of mass transport within the micropipette and this aspect is addressed in this chapter. For completeness, it should also be mentioned that micropipettes have been used as the imaging probes in both scanning ion conductance microscopy (SICM)[45-54] and SECM.[55-57] In these cases the tip does not usually make intimate contact with the surface, although SICM has been used in this format to carry out nanowriting on surfaces.[58, 59]

In this chapter we report the use of a scanning micropipette contact method (SMCM) to allow electrochemical reactions of solution species to be carried out on an electrode surface in a highly localized manner, exemplified by two systems. First, we consider carbon electrodes, where localized electroactivity measurements are especially topical in the light of recent reports which have suggested that specific sites (e.g. step edges or defects) appear to play a significant role in the electrochemistry of highly ordered pyrolytic graphite (HOPG) and carbon nanotube electrodes.[60] In particular, it has been suggested

that the electron transfer (ET) rate at basal plane HOPG is vanishingly small[61, 62] and that a sparse density of step edges dictates the overall response of conventional voltammetric studies. It has recently been proposed that the standard rate constant for ferrocyanide oxidation at basal plane HOPG is less than 10^{-9} cm s^{-1}.[60, 63] Much of the previous work on HOPG[60, 64-70] has focused on conventional cyclic voltammetric (CV) studies, but this represents the response of the entire surface. In contrast the micropipette method offers the opportunity to focus measurements on a small area of an electrode surface, which in the case of HOPG is smaller than the typical inter-step spacing on the basal plane.

As a second case, we have considered studies of the electroactivity of aluminium alloys. Aluminium is relatively chemically stable due to the oxide barrier that naturally forms on the surface.[71] However, metals - such as copper and magnesium - can be incorporated, to form alloys with improved mechanical strength,[72] and other elements, such as silicon and iron, may be naturally present as impurities.[73] These intermetallics within the aluminium matrix, whether naturally present or deliberately added, may be more susceptible to corrosion.[74] Clearly, an understanding of the local redox activity of these different sites would be valuable in understanding corrosion processes. The two alloys that were examined in the experiments described herein were a 5% Cu – 95% Al alloy, and AA1050, a material containing at least 99 % aluminium.

6.2 Experimental Section

Materials. All aqueous solutions were prepared using Milli-Q reagent grade water with a resistivity *ca.* 18.2 MΩ cm at 25 °C. Solutions contained either 0.1 M NaCl (Aldrich, AR grade) or 0.1 M KNO_3 as the supporting electrolyte.

NaCl (AR grade), potassium ferrocyanide ($Fe(CN)_6^{4-}$) trihydrate (99%) and potassium ferricyanide ($Fe(CN)_6^{3-}$) (99%+) were purchased from Sigma-Aldrich, and used as received. Trimethylammoniomethylferrocene hexafluorophosphate, ($FA^+PF_6^-$), was obtained by metathesis of trimethylammonioferrocene iodide (FA^+I^-) with $AgPF_6$ following a procedure reported elsewhere.[75] HOPG was the highest grade commercially available (ZYA grade) 12 mm x 12 mm x 2 mm (SPI Supplies, West Chester, PA, USA).

Preparation of Aluminium Alloys. Aluminium samples (AA1050 and 95 % Al – 5 % Cu) kindly supplied by Dr. Andreas Afseth (Novelis). The surfaces were initially ground using increasingly fine grades of SiC paper; 240, 600, 1500 and 4000 (Buehler, Coventry) to remove any deformed material. The surface was then polished with 3 μm, 1 μm and finally ¼ μm abrasive diamond suspension polishes (Kemet). The samples were cleaned in Teepol (Harvey Washington, Kent, UK), then rinsed in ethanol between each polish. Finally, the surface was polished with a 0.05 μm alumina slurry and sonicated in ethanol to remove any alumina that remained on the surface.

The sample was covered in a photoresist microposit S1818 (Shipley) and a small area of the alloy exposed using the argon laser (λ = 488 nm) of a Zeiss LSM 510, Axioplan 2 confocal microscope. Tapping mode atomic force microscopy (Veeco MultiMode AFM equipped with NanoScope IIIa controller) indicated that this procedure left a clean surface. Preparing the sample in this way allowed ready identification of the area imaged with the micropipette for subsequent surface analysis. The sample was finally attached to a conducting puck using silver dag (Agar Scientific), with a tinned copper wire connected to

the puck, again using silver dag, providing an electrical connection to the sample. The alloys were imaged using either optical microscopy (Olympus BH2) for the 95% Al – 5% Cu alloy or field-emission scanning electron microscopy (FE-SEM; Zeiss Supra 55VP), employing a backscattered detector, for the AA1050 alloy. This allowed the regions imaged using SMCM to be correlated with the surface features.

Electrical Contact to HOPG. HOPG was adhered onto a square section of printed circuit board (PCB), with an underlying electrical contact, using double-sided adhesive tape (Agar Scientific). Silver dag was gently applied to the edge of the HOPG and the PCB so that a continuous electrical connection was made. Tinned copper wire was soldered to the PCB in order to make an external electrical contact. Before undertaking each experiment, a freshly prepared HOPG surface was obtained by cleaving using adhesive tape.[76] Several surfaces were imaged using tapping mode AFM to reveal typical surface topography and inter-step spacing.

Electrochemical Setup. Micropipettes with internal diameters of 300 nm - 1 μm were pulled from standard borosilicate capillaries (Harvard Apparatus, UK) of dimensions (o.d. x i.d.) 1.0 x 0.58 mm, using a laser puller (P-2000, Sutter Instruments, USA). Voltammetric measurements were carried out using a two-electrode set-up with the substrate of interest serving as the working electrode. For HOPG experiments, a potential was applied with respect to a Ag/AgCl (0.1 M NaCl) reference electrode present within the micropipette. For experiments involving the aluminium alloys, a Ag quasi-reference electrode (AgQRE) was employed, as the presence of chloride is highly detrimental to the

alloys.[77, 78] The Ag/AgCl reference electrode (comprising a AgCl-coated wire in contact with 0.1 M NaCl) was found to have the almost the same potential as a saturated calomel electrode (SCE) (+33 mV vs. SCE), all potentials are quoted vs the Ag/AgCl electrode defined, but may be considered analogous to that of SCE. The micropipette acted as a vessel for the redox mediator in each electrochemical experiment, with the electrochemical processes occurring when the meniscus came into contact with the surface, as shown in the schematic in Figure 6-1.

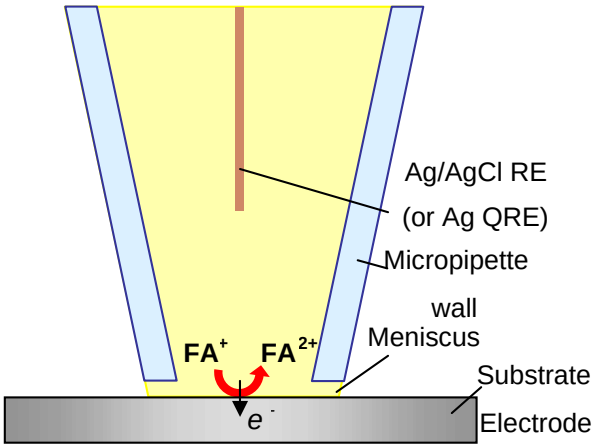

Figure 6-1: **Schematic of the set up for SMCM experiments, showing an example of the oxidation of FA^{+}, to FA^{2+} confined to a small region of a substrate electrode by the micropipette contact method.**

A purpose-built instrument, also capable of SECM and SICM imaging, was used for the measurements described herein. The position of the micropipette tip with respect to the substrate was controlled using a Nanocube piezo block (Physik Instrumente, Germany), allowing movement of the tip in the *x*, *y* and *z* directions over 100 µm with 1 nm resolution. Initial coarse tip movements were made using a micrometer (Newport, NJ, USA). A camera (PixeLINK, Edmund optics) was utilized to monitor the proximity of tip and substrate. A typical image of a micropipette positioned close to an HOPG surface is shown in Figure 6-2, which gives an idea of the scale of the measurements. Software, written in-house using

Figure 6-2. Optical image of a 300 nm (i.d.) micropipette approaching an HOPG surface. Scale bar 500 μm.

LabVIEW (National Instruments), facilitated the approach of the tip to the substrate in the *z* direction, typically with a 1 nm step size. A potential of 1 V was typically applied to the HOPG substrate in order that an easily distinguishable current would be generated upon meniscus contact with the surface (due to the oxidation of either FA^+ or $Fe(CN)_6^{4-}$). For the aluminium sample, where $Fe(CN)_6^{3-}$ was the redox species, the bias potential was -0.5 V. On fulfilment of this condition, the *z* approach program automatically paused, holding the meniscus in contact with the surface and allowing further electrochemical measurements to be carried out. CVs were run using additional LabVIEW software, also written in-house.

For electrochemical imaging experiments on HOPG and the aluminium alloys, which involved scanning the micropipette over the sample, a further LabVIEW program was used. This ensured that the tip was not pulled across the sample whilst in contact; rather it approached the surface, paused on contact whilst either the steady-state current generated at that point, or current-voltage curve, was recorded. The tip then retracted back from the surface a defined distance in the *z* direction (typically 5 μm) before moving in the *x* and/or *y* direction and repeating the process. Tips of internal diameter (i.d.) ~ 580 nm were employed for experiments on HOPG, i.d. ~ 300 nm for experiments on AA1050 aluminium alloy and i.d. ~ 1 μm for measurements on the 95% Al - 5% Cu alloy.

Finite element modelling. All numerical simulations were performed on a Viglen Intel Core 2 Duo 2.4 GHz computer equipped with 4 GB of RAM and running Windows XP 64 bit edition. Modelling was performed using the commercial finite element modelling package Comsol Multiphysics 3.3a (Comsol AB, Sweden), using the Matlab interface (Release 2006b) (The MathWorks, Cambridge, UK). Simulations were typically carried out with 15000 triangular mesh elements. Mesh resolution was defined to be greatest in regions where the concentration gradients were steepest. Simulations with finer meshes were carried out (not shown) to confirm the mesh was sufficiently fine to ensure the accuracy of the solution.

Table 6-1: Boundary conditions for the simulation of the voltammetric response of a micropipette in the contact method

Boundary Description	**Number in** Figure 6-3	**Coordinates**	**Equation**
Solution/electrode interface (uniform surface)	5	z=0, $0 \le r \le a$	$c = \frac{c^*}{1+\theta}$ (case 1) $\frac{\partial c}{\partial z} D = k_f c - k_b (c^* - c)$ (case 2)
Solution/electrode interface (basal plane)	5a = basal plane	z=0, $0 \le r \le r_{in}$ AND $r_{out} \le r \le a$	$0 = \nabla c \cdot \underline{n}$
Solution/electrode interface (defect)	5b = defect	z=0, $r_{in} \le r \le r_{out}$	(case 1) and (case 2) as for boundary number 5
Meniscus/air interface	4	$0 < z < h$ $r = \left(\frac{r_p - a}{h} \right) z + a$	$0 = \nabla c \cdot \underline{n}$
Capillary wall	3	$r = z \tan(\gamma) + r_p$ $h \le z \le l$	$0 = \nabla c \cdot \underline{n}$
Bulk solution	2	$0 < r < l \tan(\gamma) + r_p$ $z = l + h$	$c = c^*$
Axis of symmetry	1	$r = 0$, $0 < z \le l + h$	$0 = \nabla c \cdot \underline{n}$

6.3 Simulations

The finite element method[79] was used to simulate cyclic voltammograms generated using SMCM. We outline the method for the reduction $FA^{+} + e^{-} \underset{k_b}{\overset{k_f}{\rightleftharpoons}} FA^{2+}$, setting it for the other redox species is trivial. The boundary conditions are listed in Table 6-1.

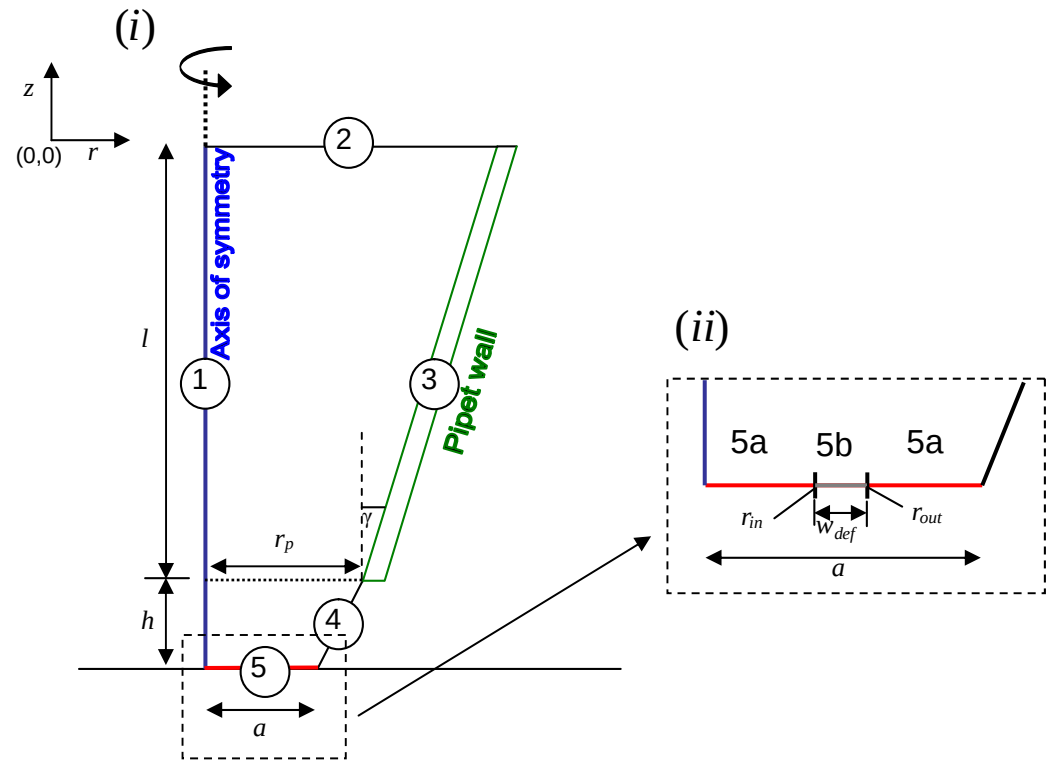

Figure 6-3: **Simulation domain for the axisymmetric cylindrical geometry used to model the micropipette system: (i) the full geometry for a uniformly active surface; and (ii) the modification when the substrate is partially active.**

The equation solved on the interior of the domain illustrated in Figure 6-3 is the time-dependent diffusion equation cast in axisymmetric coordinates (equation 6.1).

$$\frac{\partial c}{\partial t} = D\left(\frac{\partial^2 c}{\partial z^2} + \frac{1}{r}\frac{\partial c}{\partial r} + \frac{\partial^2 c}{\partial r^2}\right) \tag{6.1}$$

where z and r are the axial and radial coordinates respectively. We take the diffusion coefficient of both forms of the redox couple, D, to be identical in order to reduce the problem to the consideration of one species. The concentration of FA^+ is represented by c. Table 1 shows the boundary conditions for the simulation of the voltammetric response of a micropipette in the contact method. In Table 1, the geometric quantities r_p, a, l, and h represent the pipette radius, the contact radius with the substrate, the length of the pipette considered in order to obtain a good solution and the height of the meniscus, respectively (as depicted in Figure 6-3). The pipette semi-angle is denoted by γ, $\underline{n}$ represents the inward pointing unit normal vector and c^* represents the bulk concentration of FA^+. At the solution/electrode interface, there are two possible cases: Nernstian ET (case 1),[80] where

$$c = \frac{c^*}{1+\theta} \qquad \text{where} \qquad \theta = \exp\left(-\eta \cdot \frac{nF}{RT}\right) \tag{6.2}$$

and η is the overpotential, defined as $E–E^{0'}$, where $E^{0'}$ is the formal electrode potential; or Butler-Volmer kinetics (case 2),[81] where

$$k_f = k_0 \exp(-\alpha F\eta / RT) \tag{6.3}$$

and

$$k_b = k_0 \exp((1-\alpha) F\eta / RT) \tag{6.4}$$

where k_f and k_b are the rate constants for electon transfer (reduction, k_f; oxidation, k_b) and a typical value of the transfer coefficient, $\alpha = 0.5$, has been used.

The cases outlined above are for the situation where the portion of the substrate investigated is uniformly active. Figure 6-3(*ii*) shows the simulation domain at the solution/electrode interface when the presence of a defect is taken into consideration. Here, r_{in} and r_{out} represent the inner and outer radii, respectively, of the defect, and w_{def} represents the width of the defect, where

$$w_{def} = r_{out} - r_{in} \tag{6.5}$$

For simplicity and to maintain the axisymmetric geometry, we are thus considering a ring-shaped defect but we have chosen parameters such that the equivalent length of step encapsulated by the capillary is above the maximum we might expect to find on a surface, for the case of HOPG.

It is difficult to predict the shape that the meniscus takes on contact with the surface as it depends on factors such as the hydrophilicity/hydrophobicity of the substrate electrode surface and the volume of solution contacting the electrode. However, preliminary simulations demonstrated that the meniscus shape had little effect on the steady-state current, as shown in Figure 6-4.

Simulations were carried out for a micropipette with $r_p = 1$ μm, $l = 400$ μm, and a solution of concentration 2 mM with $D = 6 \times 10^{-6}$ cm^2 s^{-1} to investigate the effect of varying the value of a (the contact radius) on the current, as shown in Figure 6-4(a). In this plot, which is for a meniscus height, $h = 100$ nm, the currents have been normalized by the current when the contact radius is the same as the pipette, to give a normalized steady-state current, i_{ss}. It can be seen that as

the radius, *a*, decreases from 1.0 μm (equivalent to the internal radius of the pipette) to 0.5 μm, there is essentially no change in the current. This is because the steady-state current is largely dominated by diffusion through the capillary.

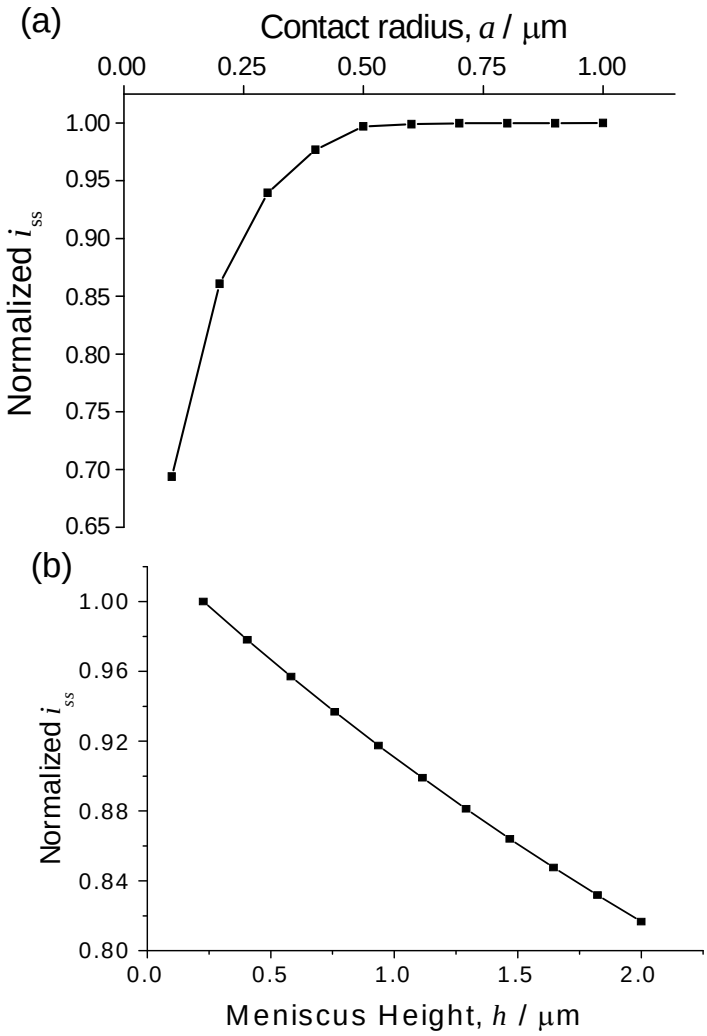

Figure 6-4: **Plot of simulated data demonstrating how the steady state diffusion-limited current (normalized as described in the text) at a 1 μm radius micropipette (*l* = 400 μm, γ=7.5°, *c**=2 mM, *D* = 6 ×10^{-6} cm^2 s^{-1}) is affected by: (a) the meniscus radius, *a*, (h=100 nm); and (b) meniscus height, *h* (a=1 μm).**

Only at smaller contact radii does the current fall, as the size of the electrode contact becomes more important. For subsequent simulations (unless explicitly

mentioned), including the analysis of experimental data, a was given a value of r_p, which was considered to be reasonable.

Figure 6-4(b) shows the results of simulations to investigate the effect of varying the height of the meniscus. The simulation was again for a 1 μm radius micropipette (contact radius, a = 1 μm). For values of h between 0.2 μm (to which all steady-state currents, i_{ss}, have been normalized) and 2 μm there was a decrease in current of only 18%. The micropipette semiangle of 7.5° used in these simulations was estimated from FE-SEM images and is typical of the probes employed in practice.

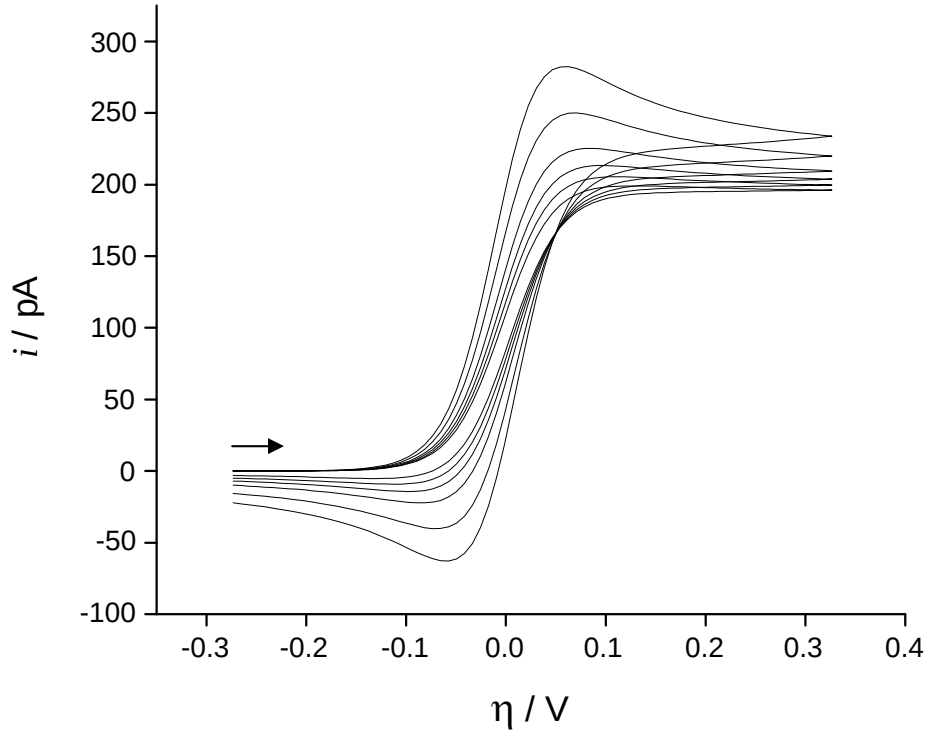

Figure 6-5: **Simulated cyclic voltammograms at scan rates of 20, 50, 100, 200, 500 and 1000 mV s^{-1} for Nernstian ET at a 1 μm radius micropipette (a=800 nm, c*=5 mM, h=200 nm, γ=7.5°). The arrow indicates the direction of the scan.**

Figure 6-5 shows simulated CVs obtained for a variety of scan rates, ranging from 20 mV s^{-1} to 1 V s^{-1}, for a micropipette with r_p = 1 μm, semiangle 7.5°, and meniscus with a = 800 nm and h = 200 nm. The diffusion coefficient used was 1 x 10^{-5} cm^2 s^{-1} and c^* = 5 mM. The CVs demonstrate that, for the Nernstian case shown, a quasi-steady current is ultimately attained on the timescales studied herein. The current shows a slight scan rate dependence over this range because the height of the concentration boundary that develops is relatively large compared to the dimensions of the electrochemically active area and a true steady-state is not attained on the voltammetric timescale.

Figure 6-6 shows a typical steady-state concentration profile within a 1 μm radius micropipette (r_p=a=1 μm), having a semiangle of 7.5°, where an electroactive species is consumed at the substrate electrode at a diffusion-limited rate. This demonstrates that the concentration change occurs over *ca.* 100 μm (assuming that 95% bulk concentration approximates to the bulk). A steady-state can be achieved because the pipette allows some non-linear diffusion, although clearly not to the extent that would be observed at an inlaid disk electrode. Nonetheless, this is an important feature of the micropipette method and the relatively high mass transport rates that result are attractive for the measurement of fast kinetics.

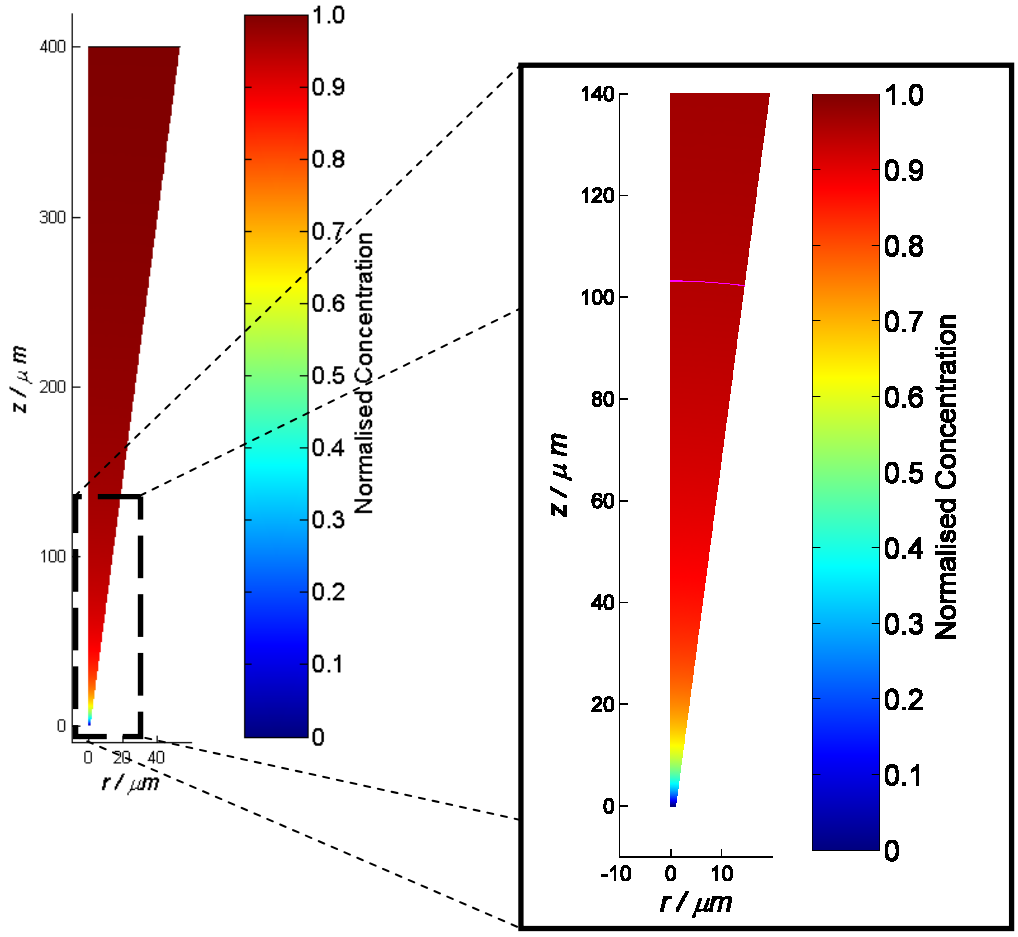

Figure 6-6: **Simulated steady-state diffusion-limited concentration profile within a micropipette, where $r_p = a = 1$ µm, $h = 200$ nm, and $l = 400$ µm. Contour line on magnified image shows 95% concentration.**

Figure 6-7 highlights the influence of kinetics on the voltammetric response for a uniformly active surface. The pipette parameters were as defined for Figure 6-5, with a scan rate of 0.1 V s^{-1}. It is clear that the transition from the Nernstian case to Butler-Volmer conditions induces a significant change in the shape and position of the voltammograms. Even for a standard rate constant of 0.1 cm s^{-1}, there is a measurable change in the voltammetric waveshape that could be determined experimentally, and as k_0 decreases to 0.01 cm s^{-1} and 0.001 cm s^{-1} the shift in half-wave potential is sizeable and easily measurable. Clearly,

standard rate constants quoted for basal plane HOPG[60, 63] of 10^{-9} cm s^{-1} would result in barely any current over the voltammetric range shown, so allowing the activity of electrode surfaces to be elucidated with high confidence using this technique.

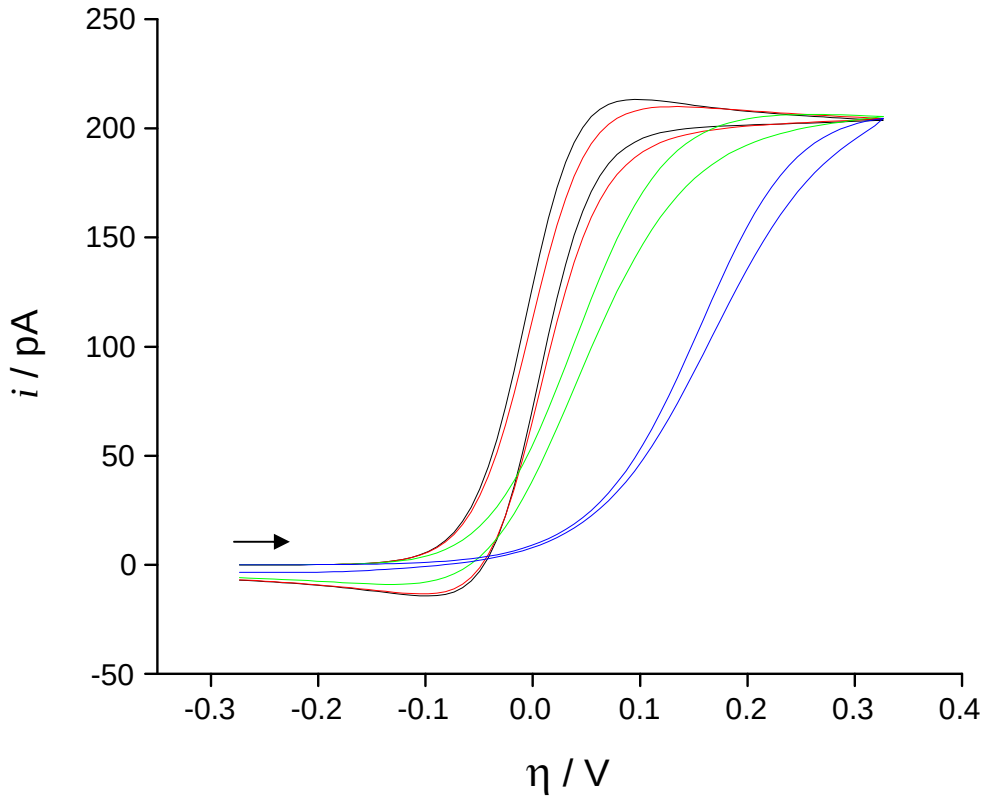

Figure 6-7: **Simulations showing the effect of kinetics on the shape of cyclic voltammograms. Black: Nernstian response. Red: k_0 = 0.1 cm s^{-1}. Green: k_0 = 0.01 cm s^{-1}. Blue: k_0 = 0.001 cm s^{-1}. Scan rate 100 mV s^{-1}. The concentration of electroactive species was 5 mM, with r_p = 1µm, a = 800 nm, h = 200 nm, and l = 400 µm. The arrow indicates the direction of the scan.**

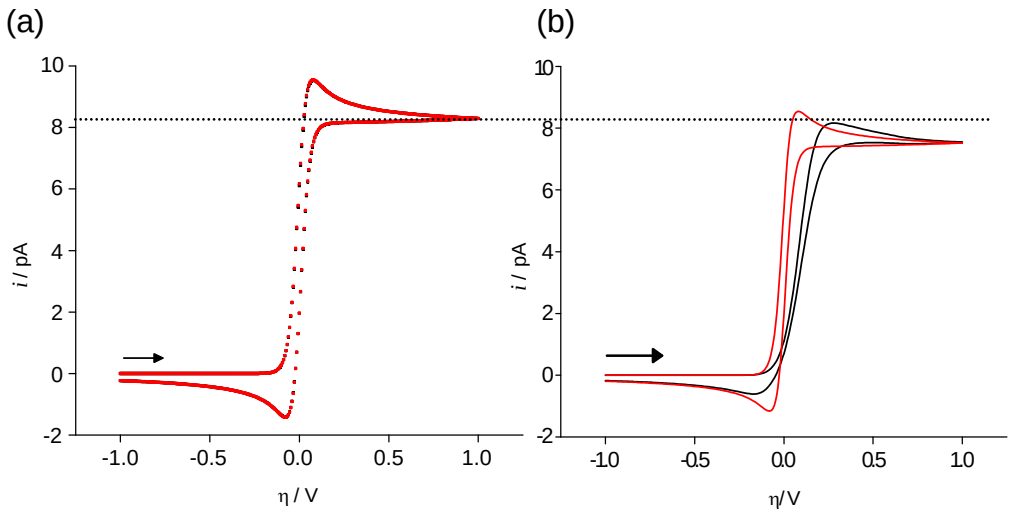

Figure 6-8: **Simulations showing the voltammetric responses of (a) a uniform surface with Nernstian response (red) and Butler-Volmer (black) kinetics with k_0 = 0.5 cm s^{-1}; compared with (b) a surface containing a 1 nm width step defect (see Figure 6-3 for geometry). In this latter situation the data are for Nernstian ET (red) and Butler-Volmer kinetics (black) with k_0 = 0.5 cm s^{-1} inert basal plane. A 580 nm diameter micropipette containing 2 mM redox active species (D = 6 × 10^{-6} cm^2 s^{-1}) was simulated. The arrows indicate the direction of the scans. Horizontal line to aid comparison.**

Figure 6-8 compares the response of a uniformly active surface with one where there is a 1 nm wide active step edge set in an inert (basal) plane, with r_p = a = 250 nm, h = 20 nm, l = 400 µm, and a solution of concentration 5 mM, with D = 6 × 10^{-6} cm^2 s^{-1}. Simulated CVs for a uniformly active surface are shown in Figure 6-8(a) for Nernstian ET (red line) and Butler-Volmer kinetics (black line) with k_0 = 0.5 cm s^{-1}. The two voltammetric waveshapes in this case are very similar; and the half-wave potentials are essentially coincident. Conversely, for rapid Butler-Volmer kinetics (k_0 = 0.5 cm s^{-1}) when only the defect is active there is a large deviation in the half-wave potential from Nernstian behaviour on the step edge, as exhibited in Figure 6-8(b). Notably, the limiting steady-state current is independent of the kinetics, as would be expected. However, there is a small

difference in the voltammetric behaviour for the case of the uniformly active surface and step edge active surface (compare the red curves in Figure 6-8(a) and (b)). However, the small difference seen in the simulations would be difficult to elucidate in practice. In summary, the analysis of the simulations indicates that for a uniformly active surface one can measure quite rapid kinetics with the SMCM technique. For the case where only a small step-like portion of the surface is active, even very fast kinetics (k_0 > 0.5 cm s^{-1}) can be distinguished due to the high mass transport rate to the step.

6.4 Results and Discussion

6.4.1 Electrochemical interrogation of HOPG redox activity

The micropipette contact method was first used to record CVs on HOPG (ZYA grade basal plane). This material exhibits the optimal HOPG order of any material currently available commercially [82] and as such offers the widest step spacing on freshly cleaved surfaces

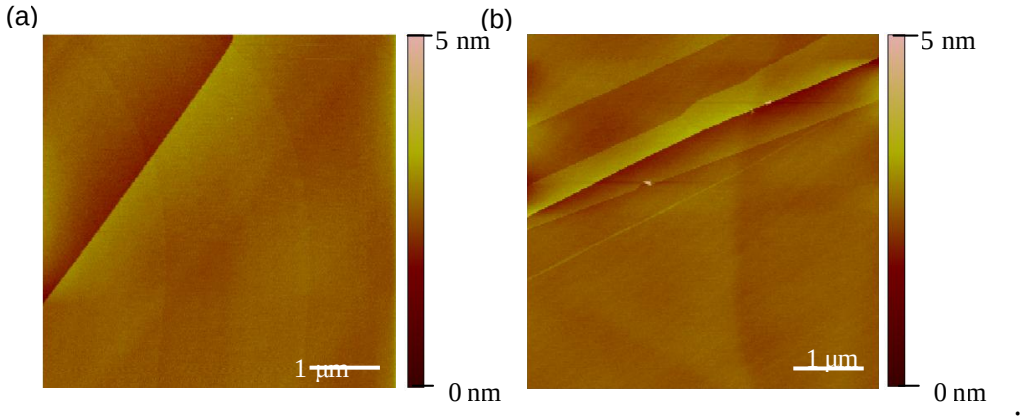

Figure 6-9: Typical tapping mode atomic force microscopy (AFM) images of ZYA grade HOPG. Scale bar 1 µm, height range 0 - 5 nm. (a) shows a region with a step density of 0.2 µm/µm²; (b) shows a region with a step density of 0.7 µm/µm².

Exhaustive atomic force microscopy (AFM) studies have been undertaken to estimate the step spacing distribution in ZYA grade HOPG.[83] The images, shown in Figure 6-9, illustrate typical surface morphologies. Expressed as length of step per unit area,[84] the step density was found to vary between 0.2 and 0.7 μm μm^{-2} with a mean of 0.5 ± 0.1 μm μm^{-2}. This suggested a typical characteristic step spacing of 2 μm between parallel steps, as evident in the images. The micropipettes used in the SMCM studies on HOPG had a diameter of 580 nm and thus it would be expected that they would rarely encounter a step on a surface and, at most, only cross a maximum of one step edge.

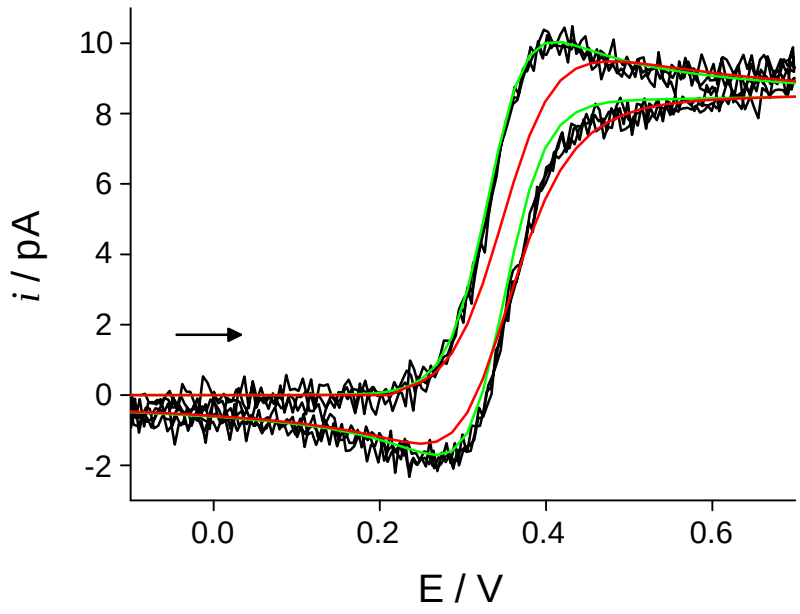

Figure 6-10: Experimental (black) and simulated (Nernstian, green and k_0 = 0.01 cm s^{-1}, red) cyclic voltammograms for a micropipette with r_p = 290 nm. The solution was FA^+ (2 mM) with 0.1 M NaCl. The arrow indicates the direction of the scan. A clear fit to a Nernstian response is seen.

Figure 6-10 shows a typical CV recorded for the oxidation of FA^+ at 100 mV s^{-1} plotted in tandem with simulated CVs (r_p = a = 290 nm; h = 100 nm, l = 400 μm, solution of concentration 2 mM with D = 6 × 10^{-6} cm^2 s^{-1}). On comparing

the experimental voltammogram to the simulations, there is a clear fit to Nernstian ET (green line). The simulation for Butler-Volmer kinetics with k_0 = 0.01 cm s^{-1} (red line) (uniformly active surface) gives a broader wave which is quite different to the experimental response. Thus, the electrochemical process appears entirely reversible on a typical voltammetric timescale. Evidence from the simulations reported earlier suggests that even if the tip had encountered a step, and this was the only active area of the surface, k_0 at the step edge would have to be considerably in excess of 0.5 cm s^{-1} to provide a reasonable fit to the experimental data, far greater than typically considered for the step edges of HOPG.[63]

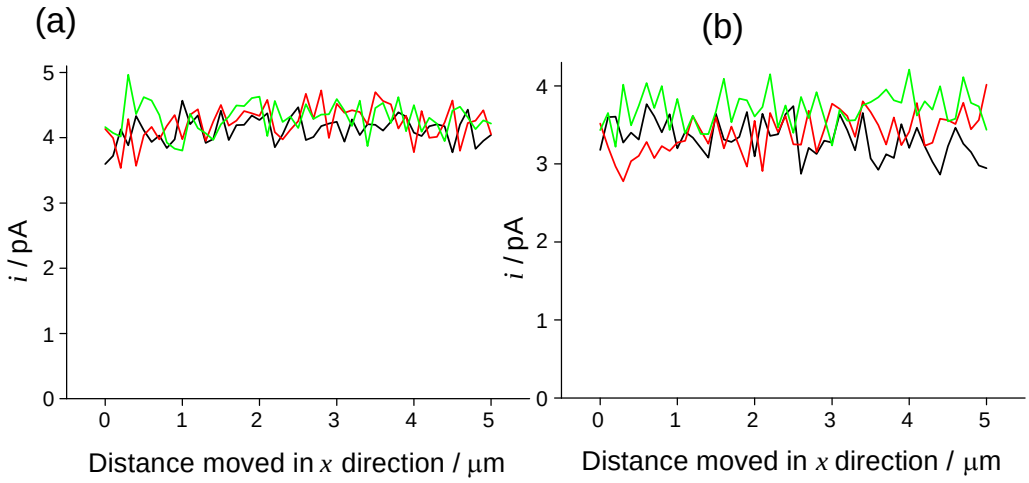

Figure 6-11: Line scans showing the current generated when the reversible half-wave potential was applied to an HOPG surface, for a series of line scans using (a) FA^+ or (b) $Fe(CN)_6^{4-}$ as the redox species. Black, red and green lines represent sequential lines recorded as described in the text.

The scanning aspect of the technique was first introduced as a short series of lines cans across the sample. Figure 6-11 shows a series of three line scans carried out with a 580 nm i.d. micropipette using the oxidation of two redox

species, (*a*) FA^+ and (*b*) $Fe(CN)_6^{4-}$, at concentrations of 2 mM in each case. Rather than apply a potential corresponding to the limiting current, the reversible half-wave potential deduced from full voltammetric analyses at Pt disc UMEs was applied so that the current would reveal information on any variations in electrode activity across the surface. Several line scans (5 μm long) were acquired with a 100 nm separation between points and between each line. The small spacing was to ensure that a tiny region of approximately 780 nm × 5580 nm, oriented with the long axis approximately perpendicular to the step direction, was covered thoroughly.[64] No significant variations in current across the scan were evident and the current was as expected for the half-wave potential. This suggests that the basal surface of HOPG shows no apparent variation in activity on the length scale considered in these studies. With measurements made over this range, in further experiments, CVs were also recorded at twelve points across the HOPG surface using a 580 nm tip containing 2 mM FA^+, as shown in Figure 6-12.

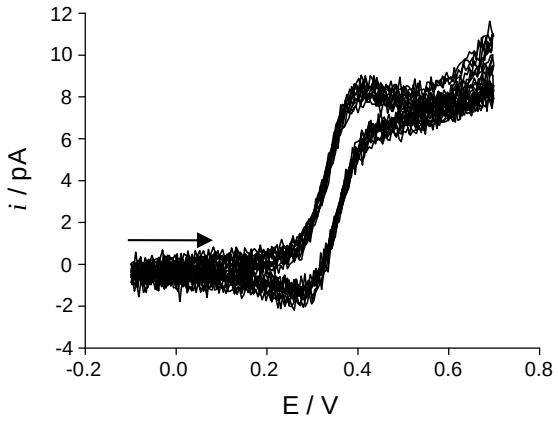

Figure 6-12: **A series of 12 CVs recorded at consecutive points on an HOPG surface with a 580 nm diameter micropipette for the oxidation of FA^+. The scan rate was 150 mV s^{-1}. The arrow indicates the direction of the scan.**

These again indicate that the surface exhibits fundamentally uniform electroactivity, as the quasi-peak current and voltammetric waveshape is similar across the series of CVs.

These studies highlight that basal plane HOPG is highly active towards redox reactions of iron complexes, as evident from studies of $Fe(CN_6)^{4-/3-}$ and $FA^{+/2+}$. The size of the micropipettes used in these studies compared to the inter-step spacing suggests a high probability that measurements were made without the influence of steps. The fact that steps have little effect on the overall activity is further confirmed by the scanning measurements where one would expect to encounter some steps during a scan, yet there were no observable changes in current at the reversible half-wave potential. It is important to highlight, of course, that the basal plane itself contains point defects,[85] and so there may be variations in electroactivity on the basal plane on a length scale that cannot yet be accessed by SMCM or other electrochemical techniques. On the length scale considered in this investigation, *i.e.* hundreds of nanometres, the basal plane appears to be active and is not inactive as suggested recently.[38, 39, 63]

6.4.2 Investigation of Heterogeneities in the Electroactivity of Al Alloys

Figure 6-13 shows (*a*) an optical image of the 95% Al - 5% Cu alloy; and (*b*) a SMCM image of the alloy, obtained using a 1.0 μm diameter micropipette containing 2 mM $Fe(CN_6)^{3-}$ and 0.1 M KNO_3 in the region highlighted by the yellow box in Figure 6-13(a). To facilitate identification of the area, the micropipette was touched onto the region in which the scan had been carried out after the end of the experiment in order to deposit some of the electrolyte solution on the aluminium sample.

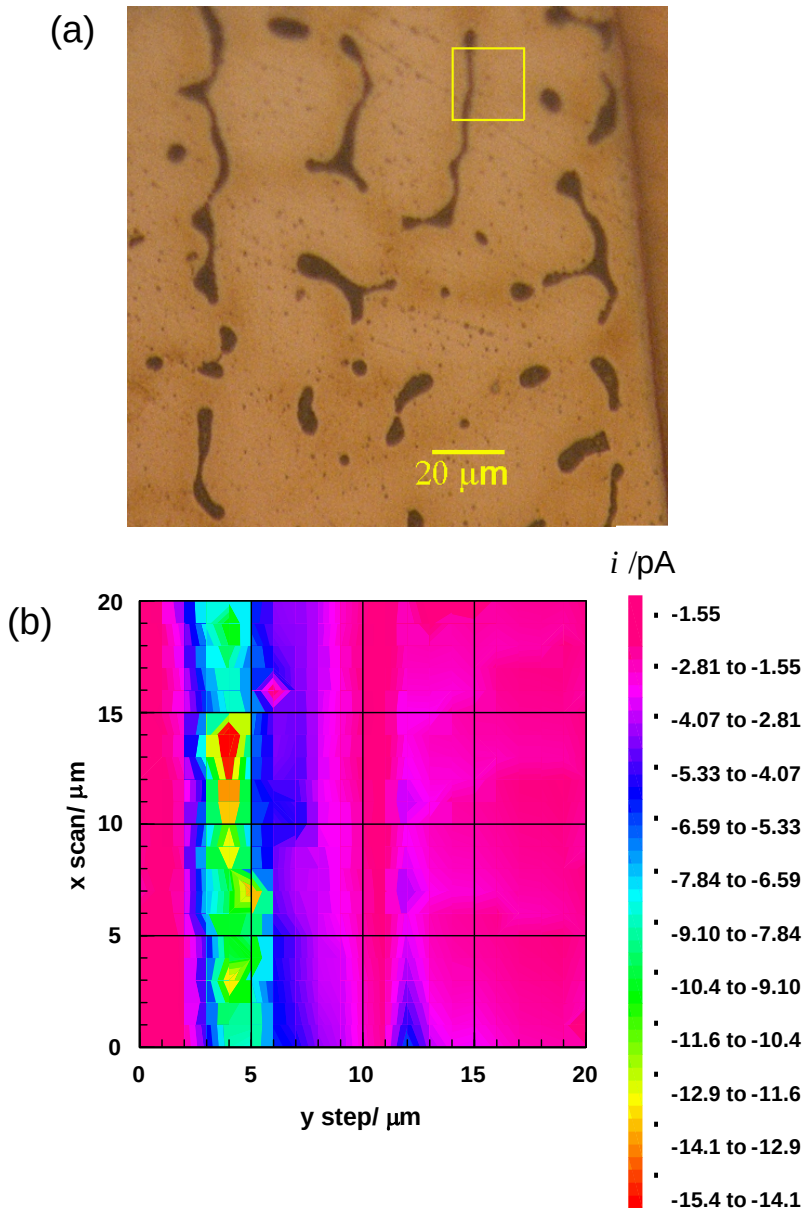

Figure 6-13: **(a) Optical microscope image of a 95% - 5% Al-Cu alloy; and (b) a SMCM image of a region of the alloy (marked by small square in (a)), obtained using a 1 μm diameter micropipette containing 2 mM $Fe(CN_6)^{3-}$ and 0.1 M KNO_3. The alloy was held at a potential of -0.10 V versus AgQRE, corresponding approximately to the half-wave potential for the reduction of $Fe(CN)_6^{3-}$ at noble metal electrodes.**

For the imaging experiment, the alloy was held at a potential of -0.10 V versus AgQRE, corresponding approximately to the half-wave potential for the

reduction of $Fe(CN)_6^{3-}$ at noble metal electrodes. A 20 μm × 20 μm imaging scan was carried out with a 1 μm separation between points. An approximately rectangular region may clearly be seen in Figure 6-13(b) where there was a significant enhancement in cathodic current, 3 μm into the *y* scan and running the length of the *x* scan. The current magnitude increases from -1.55 pA over what can be assumed to be the stable oxide-protected aluminium to more than -13.0 pA. This current is as expected, for the half-wave potential, for this size micropipette and $Fe(CN_6)^{3-}$ concentration and clearly indicates that a portion of the surface shows high cathodic activity. Comparison of the SMCM image in Figure 6-13(b) with the optical image in Figure 6-13(a) indicates that the electroactivity is confined to the copper inclusions in the alloy. The optical image revealed the dimensions of the imaged copper intermetallic to be ~2.5 μm in width and over 40 μm in length. The electrochemical image correlates well with this finding, demonstrating the exceptional spatial resolution achievable using the SMCM technique. A defined boundary is observed at the edge of the intermetallic region in the electrochemical image in Figure 6-13 (b), highlighting again the good spatial resolution of SMCM. The excellent correlation between the optical and electrochemical image highlights that the solution is confined to the capillary in these measurements.

The AA1050 material is much purer than the above alloy and therefore any intermetallic features within it are small, typically between 0.1-3 μm in length. The intermetallics are randomly spaced with gaps in the range 2 to 15 μm between individual particles, as shown in Figure 6-14(a), which presents an FE-SEM image of the alloy used in the experiment. Figure 6-14 (b) shows a 2 μm x

3 μm SMCM scan, with a 100 nm separation between points, of the AA1050 alloy recorded using a 300 nm diameter micropipette containing 2 mM $Fe(CN_6)^{3-}$

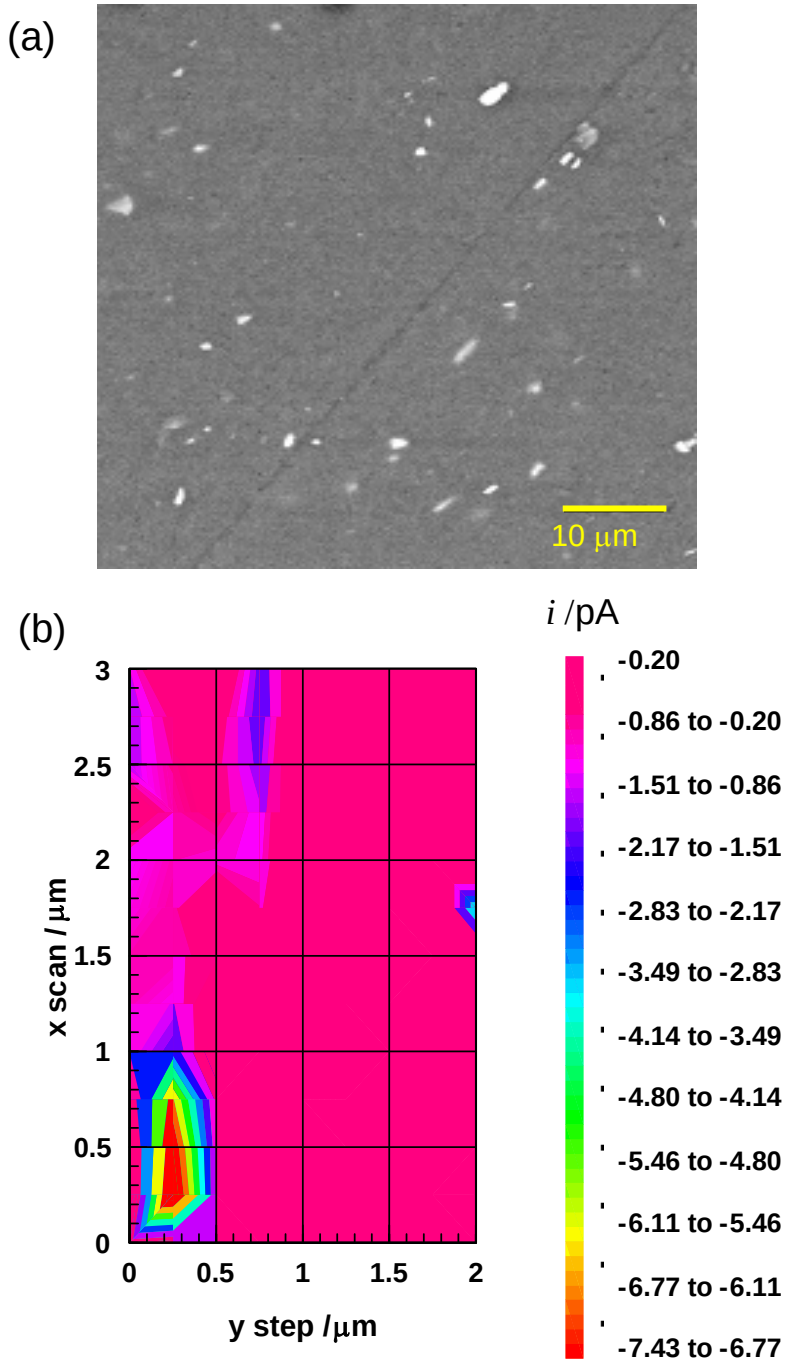

Figure 6-14: (a) FE-SEM image of an AA1050 alloy surface; and (b) SMCM image of the alloy, obtained using a 300 nm diameter micropipette containing 2 mM $Fe(CN_6)^{3-}$ and 0.1 M KNO_3. The substrate potential was held at a value to effect the diffusion-limited reduction of ferricyanide.

and 0.1 M KNO_3. The substrate potential was held at a value to promote the diffusion-limited reduction of $Fe(CN_6)^{3-}$. In the region x = 0.5 μm, y = 0.2 μm, a small oval shaped area of 0.5 μm x 1 μm with an enhancement in current of approximately an order of magnitude was seen. The size of the region will be broadened slightly due to the finite tip shape, but is, nonetheless within the size range of the individual intermetallic regions and single particles. The typical spacing of the intermetallics, identified from FE-SEM, suggests that only one particle would be imaged in a 2 μm x 3 μm scan, which supports the results obtained electrochemically.

6.5 Conclusions

SMCM has proven a valuable tool for probing the localized electroactivity of heterogeneous electrode surfaces. The small dimensions of the micropipette probe allow voltammetric measurements to be made in microscopic regions of an electroactive surface. In SMCM, the tip converges on the surface and so there are no issues related to tip-substrate separation, which can sometimes occur in SECM. Furthermore, the resolution is simply governed by the dimensions of the pipette, opening up the possibility of readily confining a measurement to a single active site or region, as shown herein. Since micropipettes can be pulled readily with high reproducibility and their geometry characterized with high precision, a key feature of the technique is that experimental measurements can be supported by detailed simulations.

The measurements on basal plane HOPG reveal essentially uniform electroactivity across the surface. The electroactivity of the basal plane is far greater than recently reported,[60, 63] based on macroscopic CV measurements. We

shall report elsewhere the critical importance of electrode history in determining the response of basal plane HOPG.[83] Here, we point out that for SMCM measurements the solution is only in contact with the region of the surface of interest for a brief time during which a CV measurement is made and that this is critically important.

The redox activity of individual intermetallic particles in aluminium alloys has been determined using the SMCM technique. Again, an attractive feature of SMCM is that each portion of the surface imaged is only in contact with solution for a brief period so that the possibility for side reactions, such as corrosion, is greatly reduced.

Heterogeneity in electrode surface activity, as considered herein, is common in the field of electrochemistry. The SMCM technique represents a facile mean of examining the local redox activity of electrode materials. We have shown SMCM to be highly quantitative (e.g. very well defined mass transport) and we expect it to find widespread application.

References

(1) Bowyer, W. J.; Xie, J.; Engstrom, R. C. *Anal. Chem.* **1996**, *68*, 2005 - 2009.

(2) Kranz, C.; Friedbacher, G.; Mizaikoff, B.; Lugstein, A.; Smoliner, J.; Bertagnolli, E. *Anal. Chem.* **2001**, *73*, 2491.

(3) Macpherson, J. V.; Unwin, P. R. *Anal. Chem.* **2000**, *72*, 276.

(4) Rudd, N. C.; Cannan, S.; Bitziou, E.; Ciani, I.; Whitworth, A. L.; Unwin, P. R. *Anal. Chem.* **2005**, *77*, 6205-6217.

(5) Amemiya, S.; Bard, A. J.; Fan, F. R.-F.; Mirkin, M. V.; Unwin, P. R. *Annu. Rev. Anal. Chem.* **2008**, *1*, 95–131.

(6) Bard, A. J.; Mirkin, M. V., Eds. *Scanning Electrochemical Microscopy*; Marcel Dekker: New York, 2001.

(7) Bard, A. J.; Fan, F.-R. F.; Pierce, D. T.; Unwin, P. R.; Wipf, D. O.; Zhou, F. *Science* **1991**, *254*, 68-74.

(8) Sun, P.; Laforge, F. O.; Mirkin, M. V. *Phys. Chem. Chem. Phys.* **2007**, *9*, 802-823.

(9) Wittstock, G.; Burchardt, M.; Pust, S. E.; Shen, Y.; Zhao, C. *Angew. Chem. Int. Ed.* **2007**, *46*, 1584.

(10) Kwak, J.; Bard, A. J. *Anal. Chem.* **1989**, *61*, 1794.

(11) Engstrom, R. C.; M.Weber; Wunder, D. J.; Burgess, R.; Winquist, S. *Anal. Chem.* **1986**, *58*, 844.

(12) Kwak, J.; Bard, A. J. *Anal. Chem.* **1989**, *61*, 1221-1227.

(13) Basame, S. B.; White, H. S. *J. Phys. Chem.* **1995**, *99*, 16430.

(14) Wipf, D. O.; Bard, A. J. *J. Electrochem. Soc.* **1991**, *138*, L4-L6.

(15) Wipf, D. O.; Bard, A. J. *Anal. Chem.* **1992**, *64*, 1362-1367.

(16) Etienne, M.; Schulte, A.; Schuhmann, W. *Electrochemistry Communications* **2004**, *6*, 288-293.

(17) Eckhard, K.; Schuhmann, W. *Electrochimica Acta* **2007**, *53*, 1164-1169.

(18) Díaz-Ballote, L.; Alpuche-Aviles, M.; Wipf, D. O. *Journal of Electroanalytical Chemistry* **2007**, *604*, 17-25.

(19) Wilson, N. R.; Clewes, S. L.; Newton, M. E.; Unwin, P. R.; Macpherson, J. V. *J. Phys. Chem. B* **2006**, *110*, 5639-5646.

(20) Holt, K. B.; Bard, A. J.; Show, Y.; Swain, G. M. *J. Phys. Chem. B* **2004**, *108*, 15117-15127.

(21) Basame, S. B.; White, H. S. *Anal. Chem.* **1999**, *71*, 3166.

(22) Basame, S. B.; White, H. S. *Langmuir* **1999**, *15*, 819.

(23) Serebrennikova, I.; Lee, S.; White, H. S. *Faraday Discuss.* **2002**, *121*, 199.

(24) Bard, A. J.; Fan, F.-R. F.; Kwak, J.; Lev, O. *Anal. Chem.* **1989**, *61*, 132.

(25) Edwards, M. A.; Martin, S.; Whitworth, A. L.; Macpherson, J. V.; Unwin, P. R. *Physiol. Meas.* **2006**, *27*, R63.

(26) Unwin, P. R.; Bard, A. J. *J. Phys. Chem.* **1992**, *96*, 5035-5045.

(27) Martin, R. D.; Unwin, P. R. *J. Chem. Soc., Faraday Trans.* **1998**, *94*, 753-759.

(28) Demaille, C.; Unwin, P. R.; Bard, A. J. *J. Phys. Chem.* **1996**, *100*, 14137-14143.

(29) Bard, A. J.; Mirkin, M. V.; Unwin, P. R.; Wipf, D. O. *J. Phys. Chem.* **1992**, *96*, 1861-1868.
(30) Gray, N. J.; Unwin, P. R. *Analyst* **2000**, *125*, 889.
(31) Mirkin, M.; Fan, F.-R. F.; Bard, A. J. *J. Electroanal. Chem.* **1992**, *328*, 47.
(32) Kateman, B. B.; Schuhmann, W. *Electroanalysis* **2002**, *14*, 22.
(33) Shao, Y.; Mirkin, M. V.; Fish, G.; Kokotov, S.; Palanker, D.; Lewis, A. *Anal. Chem.* **1997**, *69*, 1627.
(34) Sun, P.; Mirkin, M. V. *Anal. Chem.* **2006**, *78*, 6526.
(35) Sun, P.; Laforge, F. O.; Abeyweera, T. P.; Rotenberg, S. A.; Carpino, J.; Mirkin, M. V. *Proc. Nat. Acad. Sci.* **2008**, *105*, 443.
(36) Tel-Vered, R.; Walsh, D. A.; Mehrgardi, M. A.; Bard, A. J. *Anal. Chem.* **2006**, *78*, 6959.
(37) Etienne, M.; Anderson, E. C.; Evans, S. R.; Schuhmann, W.; Fritsch, I. *Anal. Chem.* **2006**, *78*, 7317.
(38) Suter, T.; Böhni, H. *Electrochim. Acta* **1997**, *42*, 3275.
(39) Suter, T.; Böhni, H. *Electrochim. Acta* **1998**, *43*, 2843.
(40) Assi, F.; H.Böhni *Wear* **1999**, *233*, 505.
(41) Böhni, H.; Suter, T.; Assi, F. *Surface and Coatings Technology* **2000**, *130*, 807.
(42) Hassel, A.; Lohrengel, M. *Electrochim. Acta* **1997**, *42*, 3327.
(43) Lohrengel, M.; Rosenkranz, C.; Kluppel, I.; Moehring, A.; Betteremann, H.; Bossche, B. V. d.; Deconinck, J. *Electrochimica Acta* **2004**, *49*, 2863.
(44) Eng, L.; Wirth, E.; Suter, T.; Bohni, H. *Electrochim. Acta* **1998**, *43*, 3029.
(45) Hansma, P. K.; Drake, B.; Marti, O.; Gould, S. A. C.; Prater, C. B. *Science* **1989**, *243*, 641-643.
(46) Prater, C. B.; Hansma, P. K.; Tortonese, M.; Quate, C. F. *Rev. Sci. Instrum.* **1991**, *62*, 2634-2638.
(47) Korchev, Y. E.; Milovanovic, M.; Bashford, C. L.; Bennett, D. C.; Sviderskaya, E. V.; Vodyanoy, I.; Lab, M. J. *J Microsc-Oxford* **1997**, *188*, 17-23.
(48) Korchev, Y. E.; Bashford, C. L.; Milovanovic, M.; Vodyanoy, I.; Lab, M. J. *Biophys J* **1997**, *73*, 653-658.
(49) Korchev, Y. E.; J.Gorelik; Lab, M. J.; Sviderskaya, E. V.; Johnston, C. L.; Coombes, C. R.; Vodyanoy, I.; Edwards, C. R. W. *Biophys J* **2000**, *78*, 451-457.
(50) Pastre, D.; Iwamoto, H.; Liu, J.; Szabo, G.; Shao, Z. F. *Ultramicroscopy* **2001**, *90*, 13-19.
(51) Shevchuk, A. I.; Gorelik, J.; Harding, S. E.; Lab, M. J.; Klenerman, D.; Korchev, Y. E. *Biophys J* **2001**, *81*, 1759-1764.
(52) Gorelik, J.; Zhang, Y. J.; Shevchuk, A. I.; Frolenkov, G. I.; Sanchez, D.; Lab, M. J.; Vodyanoy, I.; Edwards, C. R. W.; Klenerman, D.; Korchev, Y. E. *Mol Cell Endocrinol* **2004**, *217*, 101-108.
(53) Ying, L. M.; White, S. S.; Bruckbauer, A.; Meadows, L.; Korchev, Y. E.; Klenerman, D. *Biophys J* **2004**, *86*, 1018-1027.
(54) Shin, W.; Gillis, K. D. *Biophys J* **2006**, *91*, L63-L65.
(55) Ervin, E. N.; White, H. S.; Baker, L. A.; Martin, C. R. *Anal. Chem.* **2006**, *78*, 6535.
(56) Walsh, D. A.; Fernández, J. L.; Mauzeroll, J.; Bard, A. J. *Anal. Chem.* **2005**, *77*, 5182.

(57) Hengstenberg, A.; Kranz, C.; Schuhmann, W. *Chem. Eur. J.* **2000**, *6*, 1547.
(58) Ying, L. M.; Bruckbauer, A.; Zhou, D. J.; Gorelik, J.; Shevchuk, A.; Lab, M.; Korchev, Y.; Klenerman, D. *Phys Chem Chem Phys* **2005**, *7*, 2859-2866.
(59) Rodolfa, K. T.; Bruckbauer, A.; Zhou, D. J.; Korchev, Y. E.; Klenerman, D. *Angew Chem Int Edit* **2005**, *44*, 6854-6859.
(60) Banks, C. E.; Davies, T. J.; Wildgoose, G. G.; Compton, R. G. *Chem. Comm.* **2005**, *7*, 829.
(61) McDermott, M. T.; Kneten, K.; McCreery, R. L. *J. Phys. Chem. B* **1992**, *96*, 3124.
(62) Kneten, K. R.; McCreery, R. L. *Anal. Chem.* **1992**, *64*, 2518.
(63) Davies, T. J.; Hyde, M. E.; Compton, R. G. *Angew. Chem.* **2005**, *117*, 5251.
(64) Cline, K. K.; McDermott, M. T.; McCreery, R. L. *J. Phys. Chem.* **1994**, *98*, 5314-5319.
(65) Banks, C. E.; Moore, R. R.; Davies, T. J.; Compton, R. G. *Chem. Comm.* **2004**, *16*, 1804.
(66) Banks, C. E.; Compton, R. G. *Anal. Sci.* **2005**, *21*, 1263.
(67) Liu, Y.; Freund, M. S. *Langmuir* **2000**, *16*, 283.
(68) Fleming, B. D.; Bell, S. G.; Wong, L.-L.; Bond, A. M. *J. Electroanal. Chem.* **2007**, *611*, 149.
(69) Bowling, R. J.; Packard, R. T.; McCreery, R. L. *J. Am. Chem. Soc.*, **1989**, *111*, 1217-1223.
(70) Robinson, R. S.; Sternitzke, K.; McDermott, M. T.; McCreery, R. L. *J. Electrochem. Soc.* **1991**, *138*, 2412.
(71) Kolics, A.; Besing, A.; Baralai, P.; Haasch, R.; Wieckowski, A. *J. Electrochem. Soc.* **2001**, *148*, B251.
(72) Yasakau, K.; Zheludkevich, M. *Electrochim. Acta* **2007**, *52*, 7651.
(73) Bringas, J. E. *CASTI Metals Red Book-Nonferrous Data (Fourth Edition)*; CASH Publishing Inc., 2003.
(74) Aballe, A.; Bethencourt, M.; Botana, F. J.; Cano, M. J.; Marcos, M. *Corr. Sci.* **2003**, *45*, 161.
(75) Szentirmay, M. N.; Martin, C. R. *Anal. Chem.* **1984**, *56*, 1898.
(76) Chang, H.; Bard, A. J. *Langmuir* **1991**, *7*, 1143.
(77) Böhni, H.; Uhlig, H. H. *J. Electrochem. Soc.* **1969**, *116*, 906.
(78) Leblanc, P.; Frankel, G. S. *J. Electrochem. Soc.* **2002**, *149*, B239.
(79) Burnett, D. S. *Finite Element Analysis*; Addison-Wesley: USA, 1987.
(80) Bard, A. J.; Faulkner, L. R. In *Electrochemical Methods: Fundamentals and Applications*, 2nd ed.; Wiley: New York, 2001, pp 152.
(81) Brett, C. M. A.; Brett, A. M. O. In *Electrochemistry: Principles, Methods and Applications*; Oxford University Press: Oxford, 2000, pp 74.
(82) http://www.2spi.com/catalog/new/hopgsub.shtml (accessed on 18th August, 2008)
(83) Guille, M., et al *in preparation*.
(84) Wilson, N. R.; Guille, M.; Dumitrescu, I.; Fernandez, V. R.; Rudd, N. C.; Williams, C. G.; Unwin, P. R.; Macpherson, J. V. *Anal. Chem.* **2006**, *78*, 7006.
(85) Amara, H.; Latil, S.; Meunier, V.; Lambin, P.; Charlier, J.-C. *Phys. Rev. B* **2007**, *76*, 115423.

Chapter 7: Slow Diffusion Reveals the Intrinsic Electrochemical Activity of Basal Plane Highly Oriented Pyrolytic Graphite (HOPG) Electrodes

7.1 Introduction

A large number of reports have appeared over several decades focusing on the electrochemical properties and applications of carbon-based materials.[1-13] Because of their widespread use in electroanalysis, there has been particular interest in understanding the factors influencing electron transfer (ET) kinetics at such electrodes.[1, 9-11, 14-17] Many fundamental studies have considered basal plane highly oriented pyrolytic graphite (HOPG) because of the possibility of forming well-defined surfaces over extended length scales. It has generally been established that basal plane HOPG appears to have rather slow ET kinetics for a wide range of redox couples, in contrast to edge plane HOPG[9, 11, 15, 16, 18-20], although it is also recognised that the activity of basal planes HOPG is dependent of the redox couple and electrode history.[1] More recently, and on the basis of CV measurements, it has been reported that the ET rate constant for the ferro/ferricyanide couple at basal plane HOPG is essentially zero, and that step

edges are responsible for the voltammetric response.[12, 13, 21-23] This interpretation has also been extended to different classes of carbon-based materials, such as carbon nanotubes (CNTs).[12, 13, 24] For example, it has been suggested that the electrocatalytic activity of multi-walled carbon nanotubes (MWNTs) resides in ET from the ends of nanotubes and at step edges[12, 13], while in some work the electrochemical response of single-walled carbon nanotubes (SWNTs) has been attributed to the metal nanoparticles from which they are grown. This observation contrasts with other work on well-defined SWNTs samples which indicate that the basal sidewalls have considerable activity.[25-30] Attempts to examine the effects of defects on the electrochemistry of HOPG surfaces have included laser activation[19] and electrochemical pretreatment[20], to deliberately induce defects.

A complication in the interpretation of the ET activity of heterogeneously active electrodes is diffusional overlap between sites of different activity on the characteristic voltammetric timescale. The proposition in this chapter is that if one slows down diffusion so that sites are spatially decoupled, one can obtain new insights into the reactivity. In this chapter we demonstrate this idea and show how *slow diffusion* reveals the ET activity intrinsic to basal plane HOPG. To slow diffusion to HOPG, we use a Nafion coating. Nafion is a perfluorinated ionomer widely used in electroanalysis because of its excellent ion-exchange and permselectivity properties.[31] Nafion is characterized by a multi-phase structure consisting of fluorocarbon hydrophobic phases, hydrophilic sulphonated ionic clusters and interfacial regions[21-23, 32], which can be loaded with cationic redox species. [31, 33-39] We envisage that anion-selective coatings may be used in a similar way to examine ET activity of anionic redox species. Bertoncello et al

have recently reported on the electrochemical properties of redox mediators loaded in ultra-thin Nafion Langmuir-Schaefer (LS) films[33, 34] deposited on indium tin oxide electrodes, as well as a novel procedure to incorporate redox mediators directly during the Langmuir monolayer formation.[35, 36] The distribution of redox species in such films has recently been shown to be homogeneous.[40] The compactness of the Nafion LS films significantly decreases the apparent diffusion coefficient values of the loaded redox mediators.[33, 36] In this study, the encapsulation of the outer-sphere redox species, tris(2-2'-bipyridyl)(ruthenium(II), ($Ru(bpy)_3^{2+/3+}$) and $Ru[(NH_3)_6]^{3+/2+}$, allows us to examine the intrinsic electrochemical activity of the basal plane of HOPG towards these couples. In essence, slow diffusion, electron hopping in the Nafion film limits the extent of diffusional overlap of neighbouring edge plane sites on the voltammetric time scale.

$Ru(bpy)_3^{2+/3+}$ and $Ru[(NH_3)_6]^{3+/2+}$ display quasi-reversible kinetics at basal plane HOPG on the cyclic voltammetric timescale;[1] since both couples have high standard (formal) rate constants on a range of electrode materials, one might explain this behaviour using a model similar to that proposed for ferro/ferricyanide in which only adventitious step edges are highly active and the basal plane is essentially inactive.[12, 13, 24] The results of the cyclic voltammetry (CV) experiments reported herein, supported by finite element method simulations, provide unequivocal evidence that a significant portion of the electrochemical activity of HOPG electrodes must be attributed to the basal plane itself.

7.2 Experimental Section

Materials. Nafion 117 solution (5% w/v mixture of low molecular weight alcohols), sodium chloride and tris(2-2'-bipyridyl)ruthenium(II), ($Ru(bpy)_3^{2+}$) dichloride salt, were purchased from Sigma-Aldrich. Hexaamminoruthenium(III) trichloride was purchased from Strem Chemicals. All other chemicals were of reagent grade quality and used as received.

HOPG (SPI-1 grade), 10 mm x 10 mm x 2 mm was purchased from SPI Supplies, West Chester, PA, USA, was used for electrochemical experiments. This was used for the present studies for direct comparison with recent solution phase work.[12, 13] Freshly prepared HOPG surfaces were obtained by cleaving using adhesive tape. Tapping mode AFM topographical analysis revealed well defined basal plane surfaces with parallel steps with characteristic spacing typically in the range 0.5 – 1.0 μm. Occasionally, step spacing of 0.2 μm were observed. All aqueous solutions were prepared from Milli-Q reagent water (Millipore Corp.); resistivity ≥ 18.2 MΩ cm at 25 °C.

Fabrication of Nafion Langmuir-Schaefer films. Ultra-thin (50 monolayers thick) Nafion LS film containing either $Ru(bpy)_3^{2+}$ or $[Ru(NH_3)_6]^{3+}$ were deposited onto HOPG electrodes using a well established procedure reported by Bertoncello et al.[35, 36] A Langmuir trough (total volume 1 L, from Nima Instruments, Coventry, UK) was used, in which the surface pressure was measured by means of a Wilhemy balance with an accuracy of ± 0.1 mN m^{-1}. The volume of Nafion-$Ru(bpy)_3^{2+}$ and Nafion-$[Ru(NH_3)_6]^{3+}$ added to the subphase (initial area 489 cm^2) was, in all cases, 200 μL. A two minute period was allowed to elapse before compression of the floating films. Based on the

reports of Bertoncello et al,[35, 36] the conditions used for the fabrication of Nafion-$Ru(bpy)_3^{2+}$ and Nafion-$[Ru(NH_3)_6]^{3+}$ films were surface pressure of 20 mN m^{-1} and 0.1 M of NaCl as the subphase.

Electrochemistry. Cyclic voltammetry (CV) curves were recorded using an electrochemical analyzer (CH Instruments, model CHI730A). Multilayers of Nafion were deposited onto HOPG by using the Langmuir-Schaefer method[35, 36]. For the CV experiments we used a setup recently described for the electrochemical investigation of single-walled carbon nanotubes,[30] in which a droplet of electrolyte solution (10 μL) was deposited on the sample. There were no issues with evaporation on the timescale of the measurements. A three electrode configuration was used, where the working electrode was a modified basal plane HOPG, a platinum gauze was used as a counter electrode and a Ag wire served as a quasi-reference electrode (AgQRE). The area of the surface covered by the solution was typically between 0.15 cm^2 and was measured accurately. All voltammetric data are presented as current density, with the current normalised by the geometric area of the electrode.

Finite element modelling. Numerical simulations were performed on a Viglen Intel Core 2 Duo 2.4 GHz computer equipped with 4 GB of RAM and running Windows XP 64 bit edition. Modelling was performed using the commercial finite element modelling package Comsol Multiphysics 3.3a (Comsol AB, Sweden), using the Matlab interface (Release 2006b) (MathWorks™ Inc., Cambridge, UK). Simulations were carried out with >30000 triangular mesh elements. Mesh resolution was defined to be greatest around the step edge on the surface (see below). Simulations with finer meshes were completed (not

reported), to confirm the mesh so fine as to not adversely affect the accuracy of the solution.

It is assumed that no transfer of electroactive species takes place at the film-solution interface. This assumption is valid on the timescale of the measurements performed, and was verified by the reproducibility of sequential voltammetric measurements on the same film.

7.3 Theory and Simulations.

The following system is considered: an ultra-thin Nafion film containing a redox mediator, ($Ru(bpy)_3^{2+}$ or $[Ru(NH_3)_6]^{3+}$), deposited on an HOPG electrode. We define the model for the reduction of $[Ru(NH_3)_6]^{3+}$, however recasting for the oxidation is trivial. We seek a description of the concentration of $[Ru(NH_3)_6]^{3+}$ within Nafion LS films and the current response as a function of applied potential: this is achieved through the solution of the time-dependent version of the diffusion equation (Eq. 7.1).

$$\frac{\partial c}{\partial t} = D_{app} \nabla^2 c \tag{7.1}$$

where c represents the concentration of the $[Ru(NH_3)_6]^{3+}$, D_{app} represents its apparent diffusion coefficient, which may include some contribution from electron hopping.[31, 41-43] The apparent diffusion coefficient values of the oxidised and reduced forms of the redox couple were assumed to be equal; hence, the concentration of $[Ru(NH_3)_6]^{2+}$ can be represented by $(c_b - c)$, where c_b represents

the initial concentration of $[Ru(NH_3)_6]^{3+}$. The model makes the assumption that the HOPG step edges run parallel to each other and are equally sized and spaced. We use *l* and *a* to represent the step height and distance between the steps of HOPG respectively. For the simulations presented in this paper we use values of *l* = 2 nm, and *a* = 200 nm based on the largest and smallest values, respectively, reported in the work of McCreery and coworkers.[9] The use of values away from these extrema are discussed. Note that these values serve as a 'best case scenario' in terms of maximising the contribution from edge plane sites, and thus provide the most stringent test of the proposition that step edges are responsible for the electrochemical activity of basal plane HOPG.

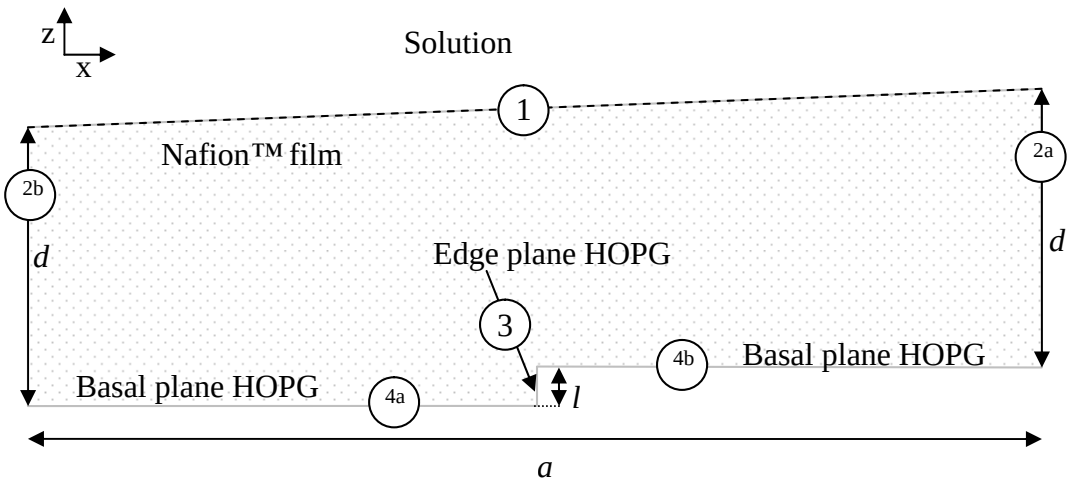

Figure 7-1. **Schematic of the geometry used for the simulation. The size of step edge are exaggerated for clarity. Circled numbers are indicative of the boundary conditions.**

The surface under consideration is composed of two separate domains (basal plane and edge plane sites). The repeat unit periodic two-dimensional domain is illustrated in Figure 7-1, with the boundary conditions as follow. At the basal plane sites (Figure 7-1, edges 4a and 4b) we describe the flux of $[Ru(NH_3)_6]^{3+}$ normal to the surface by:

$$D_{app}\frac{\partial c}{\partial z} = k_f c - k_b (c_b - c) \text{ for } z = 0,\ 0 \le x \le a/2 \text{ and } z = l,\ a/2 \le x \le a \qquad (7.2)$$

where k_b and k_f are the back and forward rate constants respectively, for the reaction $\left[\mathrm{Ru(NH_3)_6}\right]^{3+} + e^- \underset{k_b}{\overset{k_f}{\rightleftharpoons}} \left[\mathrm{Ru(NH_3)_6}\right]^{2+}$, defined as:

$$k_b = k_0 \exp((1-\alpha)F\eta / RT) \qquad (7.3)$$

$$k_f = k_0 \exp(-\alpha F\eta / RT) \qquad (7.4)$$

where k_0 is the standard rate constant, $\alpha = 0.5$ the electron transfer coefficient of the couple, F = 96485 C mol^{-1}, R = 8.31447 J K^{-1} mol^{-1}, and T = 298 K, are, respectively, the Faraday constant, the molar gas constant and the temperature. $\eta(t) = \eta_0(t) - E^{0\prime}$ is the overpotential at time, t, where $E^{0\prime}$ is the formal electrode potential and $\eta_0(t)$ is the applied potential defined as:

$$\eta_0(t) = \begin{cases} E_{\text{upper}} - \nu t & 0 \le t \le t_1 \\ E_{\text{lower}} + \nu(t - t_1) & t_1 < t \le 2t_1 \end{cases} \qquad (7.5)$$

with ν defined as the scan rate; E_{lower} and E_{upper} are the lower and upper limits of the potential range and $t_1 = (E_{\text{upper}} - E_{\text{lower}})/\nu$.

At the edge plane sites (Figure 7-1, edge 3) we ascribe reversible kinetics by setting the concentration:

$$c = \frac{c_b}{1+\theta} \text{ for } x = a/2,\ 0 < z < l \tag{7.6}$$

with:

$$\theta(t) = \exp(-\eta(t)F/RT) \tag{7.7}$$

Thus, the reaction is considered to proceed as fast as possible on these sites, again representing a 'best case scenario' in terms of maximising the contribution of edge sites to the overall current response.

On the periodic boundaries (Figure 7-1, edges 2a and 2b) we set:

$$c(x = 0, z, t) = c(x = a, z + l, t) \text{ for } 0 < z < d \tag{7.8}$$

At the film-solution interface (Figure 7-1, edge 1) we define:

$$\underline{n} \cdot \frac{\partial c}{\partial z} = 0 \text{ for } 0 \le x \le a,\ z = d + l \times x/a \tag{7.9}$$

where $\underline{n}$ represents the inward pointing unit normal vector.

The concentration at time $t = 0$, is taken to be the equilibrium concentration at $\eta(0)$, that is:

$$c\big|_{t=0} = \frac{c_b}{1+\theta(0)} \tag{7.10}$$

We calculate the current density by integrating the flux over the HOPG surface (edges 3, 4a and 4b in Figure 7-1) divided by the size of the domain simulated:

$$j = \frac{1}{a} F D_{app} \int \underline{n} \cdot \nabla c \tag{7.11}$$

7.4 Results and Discussion

The surface coverage of redox species, concentration of redox mediators within the film, film thickness and apparent diffusion coefficients were extracted from cyclic voltammetric data. The surface coverage, Γ, was determined by

integration of the anodic ($Ru(bpy)_3^{2+}$ oxidation to $Ru(bpy)_3^{3+}$ or cathodic currents $Ru[(NH_3)_6]^{3+}$ reduction to $Ru[(NH_3)_6]^{2+}$) for these responses which displayed thin layer, exhaustive electrolysis, characteristics (typically at v = 10 mV s^{-1}).[44] The concentration of the redox species within the film, C_p, was estimated by dividing the values of the surface coverage (Γ, mol cm^{-2}) by the thickness of the film evaluated using AFM in dry conditions. Our previous work has shown swelling of Nafion LS films in solution to be negligible.[35] The AFM results were found to be in agreement with the values of thickness of Nafion LS films deposited on indium tin oxide (ITO) electrodes (data not shown).[35] We used values per LS layer of 1.8 and 1.6 nm for Nafion-$(Ru(bpy)_3^{2+}$ and Nafion-$Ru[(NH_3)_6]^{3+}$, respectively.[35] The D_{app} values reported in Table 1 are for 50-layer Nafion LS films and were determined in a similar manner to Nafion LS films deposited on ITO electrodes, as previously reported by us.[35] The values of Γ, C_p and D_{app} are close to the values estimated for Nafion LS films deposited onto ITO electrodes.[35, 36]

Table 1. Summary of the values of physical parameters used in the finite element simulation of CVs of 50-layer Nafion functionalised LS films.

Redox couple	surface coverage (Γ)/10^{-10} mol cm^{-2}	D_{app}/10^{-11} cm^2 s^{-1}	C_p/ mol dm^{-3}
$Ru[(NH_3)_6]^{3+/2+}$	33	12.0	0.41
$Ru(bpy)_3^{2+/3+}$	46	4.7	0.51

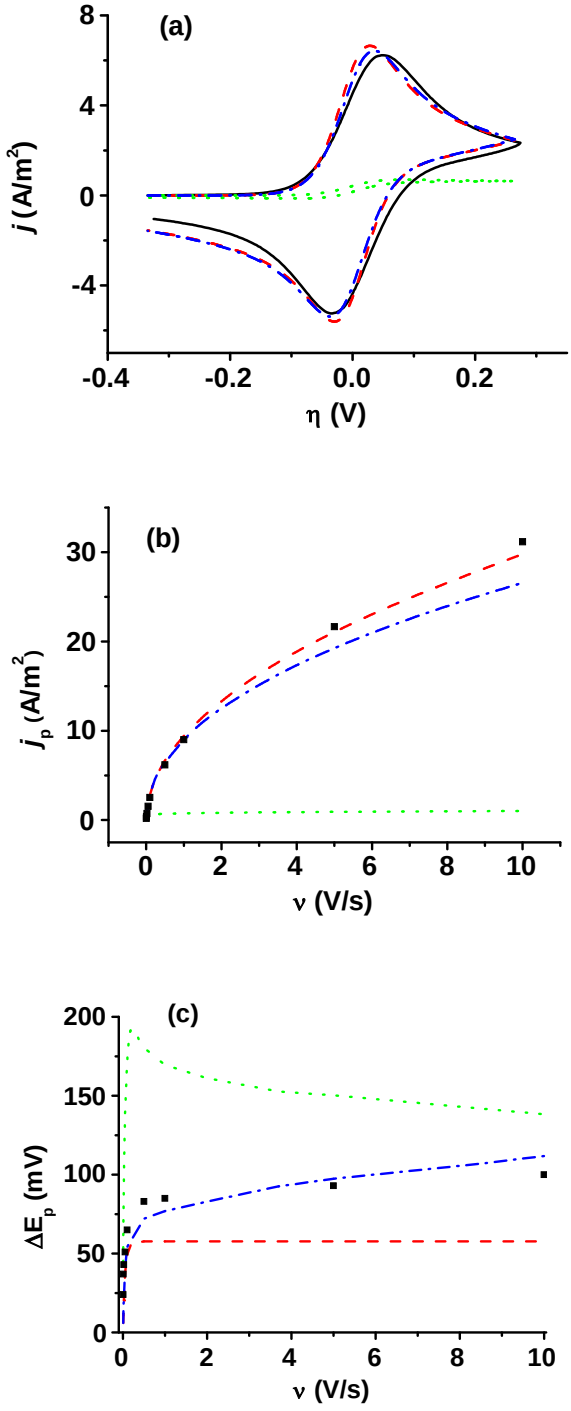

Figure 7-2. (a) CV of a 50-layer Nafion-Ru(bpy)$_3^{2+}$ film, at a scan rate of 0.5 V s^{-1}. Black line: experimental data. Finite element simulations with basal plane kinetics either reversible (red line), inert (k_0= 0 cm s^{-1}, green line), or active with a rate constant of (k_0= 1x10^{-4} cm s^{-1}, blue line). (b) Peak current density of the forward potential sweep versus scan rate. Squares indicate experimentally recorded data. Lines are from simulated CVs; colours as in part (a). (c) Difference in potential between the forward and reverse sweeps (ΔE_P). Lines and points as in part (b).

Figure 7-2(a) reports a typical experimental CV (scan rate 0.5 V s^{-1}) together with simulated CVs where the basal plane kinetics are taken as either k_0 = 0, k_0 = 1x10^{-4} cm s^{-1} or a fully reversible process. It is clear that the simulated current density with an inert basal plane (step edge only active) is much too low and that a large proportion of the activity observed experimentally must be attributed to ET at the basal plane. Figure 7-2 (b) further illustrates that this assertion holds true over a wide dynamic range, showing the peak current density for the forward sweep as a function of scan rate. Clearly, the peak current density values are very close to those obtained with k_0 = 1x10^{-4} cm s^{-1} which is also close to a reversible process on the basal plane for the timescale of these measurements. The case with the inert basal plane (k_0 = 0 cm s^{-1}) predicts current densities which are much too low. This effect is most evident at shortest timescales, i.e. higher scan rates (v > 1 V s^{-1}), where the cases of active and inactive basal plane became most clearly differentiated. For v = 10 V s^{-1} the peak current density calculated assuming an inert basal plane is more than 30 times lower than that which was experimentally observed. Furthermore, as noted above, the simulations with the step-only active have considered the maximum step density possible. In practice, the step density may be lower and if only the steps were active one might expect to observe an even lower current response than shown for the inert basal plane case. Figure 7-2 (c) illustrates how the peak separation between the forward and reverse sweeps varies with sweep rate. It is apparent that the experimentally observed peak separation is significantly less than one would expect with an inert basal plane, but instead matches closely to that of an active basal plane. The fit appears closest to the k_0 =1x10^{-4} cm s^{-1}, rather than entirely reversible, but resistance may influence these experiments,

given the high concentrations of redox-active species in a rather compact film. The important point is that all the data in Figure 7-2, and particularly the peak current data, highlight that the basal plane of HOPG is active.

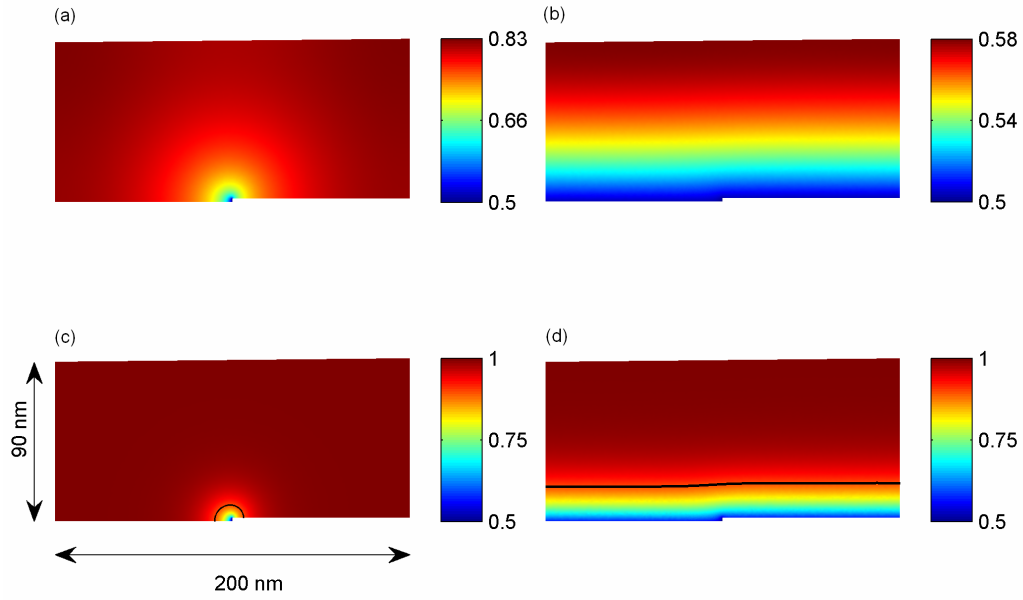

Figure 7-3. Plots of normalised concentration of reactant at the half wave potential of a cyclic voltammogram calculated by finite element simulations for a 50-layer Nafion $Ru(bpy)_3^{2+}$ film, scan rate (a, b) 10 mV s^{-1}, (c, d) 1 V s^{-1}. Basal plane activity is taken to be k_0= 0 cm s^{-1} (a, c) and k_0= 1x10^{-4} cm s^{-1} (b, d). The contours plotted in (c and d) are isoconcentration lines for c= 0.9. Note: concentration scales differ between the images.

Figure 7-3 shows simulated normalized concentrations of the redox active species reactant at the half wave potential on the forward sweep for the situation when the basal plane is inert (Figure 7-3 (a,c)) and when it is considered as active (k_0 = 1x10^{-4} cm s^{-1}) (Figure 7-3 (b, d)) at two different scan rates, 10 mV s^{-1} (a, b) and 1 V s^{-1} (c, d). The other simulation parameters used were those already defined for $Ru(bpy)_3^{2+}$(see Table 1). In the case of an inactive basal plane, the mass transport to the step edge is only sufficient to deplete the redox active species in a small zone about the step edge; this is in contrast to the

active basal plane case where a large portion of the film, across almost the entire film thickness at low scan rate, is depleted. As the rate of depletion is proportional to the current it is clear why the methodology described is so revealing of the extent of basal plane activity. At faster scan rates the difference in depletion is accentuated further, which explains the fact that higher scan rates offer more discrimination between the extreme cases in which the basal plane is considered to be either electrochemically active or inactive.

In a similar way to the Nafion-$Ru(bpy)_3^{2+}$ films described above, we considered a second system based on Nafion-$[Ru(NH_3)_6]^{3+}$ LS films (Figure 7-4). A typical experimental CV shown in Figure 7-4 (a) (scan rate 0.5 V s^{-1}) again indicates that the basal plane of HOPG has considerable activity. The simulation of the case in which step edges alone are active predicts current density magnitudes which are much too low. This is more evident by examining the forward peak current density over the full range of scan rates (Figure 7-4 (b)).

The peak-peak separation (ΔE_P) is less diagnostic of basal plane activity, but nonetheless provides convincing evidence which supports the peak current analysis. At low scan rates, the peak-peak separation is consistent with reversible ET, but at high scan rates there is an increase in ΔE_P which matches $k_0 = 4.5 \times 10^{-5}$ cm s^{-1} most closely.

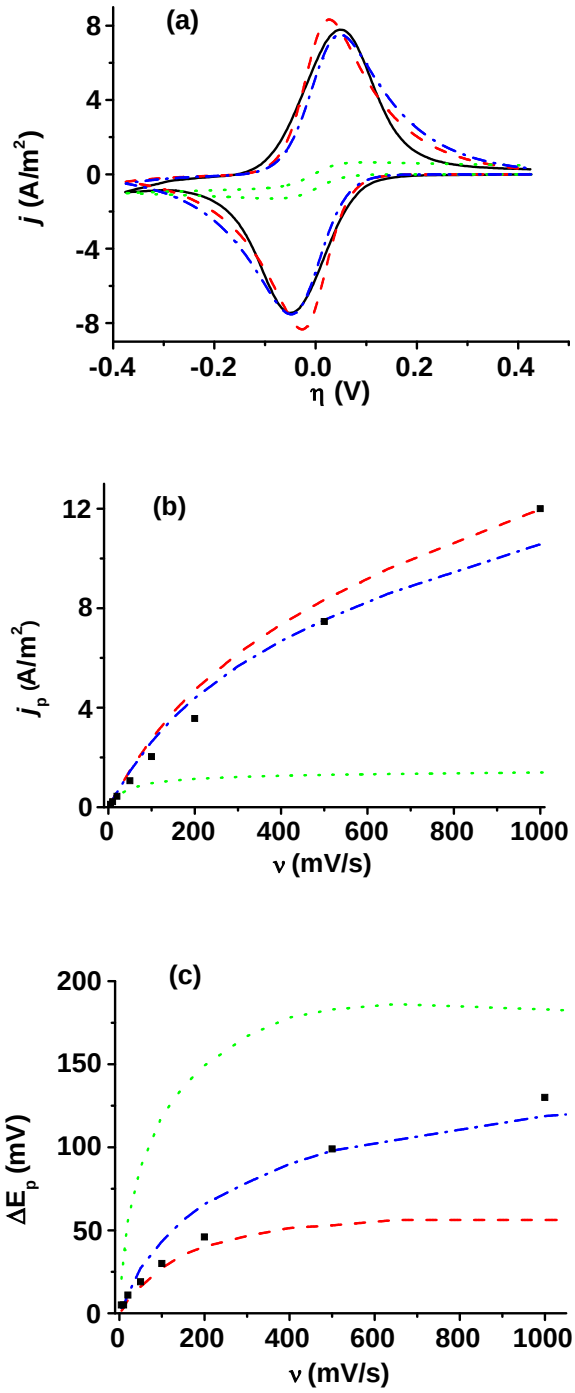

Figure 7-4. (a) CV of a 50-layer Nafion $Ru[(NH_3)_6]^{3+}$ film, at a scan rate of 0.5 V s^{-1}. Black line: experimental data. Finite element simulations with basal plane kinetics either reversible (red line), inert (k_0= 0 cm s^{-1}, green line), or active with a rate constant of k_0= 4.5x10^{-5} cm s^{-1}, (blue line). (b) Plot of peak current density of the forward potential sweep versus scan rate. Squares indicate experimentally recorded currents. Lines are from simulated CVs, colours as in part (a). (c) Plot of the difference in potential between the forward and reverse sweeps (ΔE_P). Lines and points as in part (b).

It is important to comment on the rate constants extracted from this analysis. Various factors not included explicitly in the model, but may have some effect on the peak positions, for example, resistance effects, migration, mixed physical diffusion/electron hopping contributions to the apparent diffusion coefficient. Furthermore, at the highest scan rates the diffusion layer becomes so thin that heterogeneities in films structure and the interaction of the film with the electrode may become important. These issues will probably lead to some uncertainty in the k_0 values quoted, but do not impact the main conclusion that the basal plane of HOPG is very active and the response closely approximates to reversible ET, certainly at scan rates of 200 mV s^{-1} or lower.

As briefly highlighted, further evidence supporting the deduction that basal plane activity contribute significantly to the overall current response of HOPG electrode surfaces is provided by noting that the step height and spacing used in the simulations were taken to be upper and lower limits respectively (2 nm and 200nm) of those reported, and by the fact that kinetics on the step edge were taken to be reversible, thus maximizing their current contribution. Thus, it is evident that the basal plane must contribute substantially to the net current measured. Further simulations were performed with lower activity on the step edge, a smaller step height, and wider step spacing, (data not shown). These parameters did not significantly alter the CVs where the basal plane was taken to be active, but significantly lowered the simulated current density in the case of the basal plane being inert. As the step edges did not significantly alter the CVs for the case where the basal plane is active, we can conclude that the HOPG basal plane dominates the response seen in our experiments.

7.5 Conclusions

The use of ultrathin films of Nafion-encapsulated redox species has allowed ultra-slow diffusional timescales to be accessed, which allow the ET activity of basal plane HOPG to be elucidated unequivocally. Our results show that simple redox couples, such as $Ru(bpy)_3^{2+}$ and $Ru[(NH_3)_6]^{3+}$, undergo close to reversible ET at basal plane HOPG on the timescales considered. Had only the step edges been active, then currents would have been at least an order of magnitude smaller than observed experimentally. It is important to note that if there are variations in activity across the basal plane itself (e.g. point defects) this would have to be on a very small length scale to account for the CV observations.

To simplify modelling, mass transport in the film was described solely by diffusion (equation 7.1) with the apparent diffusion coefficient taken as uniform throughout the film. Migration and electron hopping were not explicitly taken into account. The experimentally determined values for D_{app} will encompass these processes in some sense. However, mass transport in the layer closest to the electrode may differ from that further away due to the influence of the HOPG surface on the film interface. This may explain some of the variation seen in the voltammetric analysis at high scan rates, but does not impact our most important conclusion about the activity of basal plane HOPG.

We are developing complementary methods to provide further insight into the activity of HOPG and other carbon-based materials and the results of these studies will be presented in due course.

References

1. McCreery, R.L. *Chem. Rev.* **2008**, 108, 2646 and references therein.

2. Uslu, B.; Ozkan, S.A. *Anal. Lett.* **2007**, 40, 817.

3. Lee, J.; Kim, J.; Hyeon, T. *Adv. Mat.* **2007**, 18, 2073.

4. Guldi, D.M.; Rahman, G.M.A.; Sgobba, V.; Ehli, C. *Chem. Rev.* **2006**, 35, 471.

5. Gong, K.; Yan, Y.; Zhang, M.; Su, L.; Xiong, S.; Mao, L. *Anal. Sci.* **2005**, 21, 1383.

6. Wang, J. *Electroanalysis* **2005**, 17, 7.

7. Svancara, I.; Vytras, K.; Barek, J.; Zima, J. *Crit. Rev. Anal. Chem.* **2001**, 31, 311.

8. Flandrois, S.; Simon, B. *Carbon* **1999**, 37, 2.

9. Robinson, R.S.; Sternitzke, K.D.; McDermott, M.T.; McCreery, R.L. *J. Electrochem. Soc.* **1991**, 138, 2412.

10. McDermott, C.A.; Kneten, K.; McCreery, R.L. *J. Electrochem. Soc.* **1993**, 140, 2593.

11. Bowling, R.J.; Packard, R.T.; McCreery, R.L. *J. Am. Chem. Soc.* **1989**, 111, 1217.

12. Banks, C.E.; Moore, R.R.; Davies, T.J.; Compton, R.G. *Chem. Comm.* **2004**, 1804.

13. Banks, C.E.; Davies, T.J.; Wildgoose, G.G.; Compton, R.G. *Chem. Comm.* **2005**, 829.

14. Rice, R.J.; McCreery, R.L. *Anal. Chem.* **1989**, 61, 1637.

15. Kneten, K.R.; McCreery, R.L. *Anal. Chem.* **1992**, 64, 2518.

16. Kneten, K.R.; McDermott, M.T.; McCreery, R.L. *J. Phys. Chem.* **1994**, 98, 5314

17. Liu, G.; Freund, M.S. *Langmuir* **2000**, 16, 283.

18. Bowling, R.; Packard, R.T.; McCreery, R.L. *Langmuir* **1989**, 5, 683.

19. Rice, R.J.; Pontikos, N.M.; McCreery, R.L. *J. Am. Chem. Soc.* **1990**, 112, 4617.

20. McCreery, R.L. In Electroanalytical Chemistry, Bard, A.J., Ed., Marcel Dekker, New York, 1991; vol. 17, p. 221.

21. Sternitzke, K.D.; McCreery, R.L. *Anal. Chem.* **1990**, 62, 1339.

22. Chen, P.; Fryling, M.A.; McCreery, R.L. *Anal. Chem.* **1995**, 67, 3115.

23. Ranganathan, S.; McCreery, R.L. *Anal. Chem.* **2001**, 73, 893.

24. Banks, C.E.; Compton, R.G. *Anal. Sci.* **2005**, 21, 1263.

25. Day, T.M.; Unwin, P.R.; Wilson, N.R.; Macpherson, J.V. *J. Am. Chem. Soc.* **2005**, 127, 10639.

26. Dumitrescu, I.; Unwin, P.R.; Wilson, N.R.; Macpherson, J.V. *Anal. Chem.* **2008**, 80, 3598.

27. Gong, K.; Chakrabarti, S.; Dai, L. *Angew. Chem. Int. Ed.* **2008**, 47, 5446.

28. Heller, I.; Kong, J.; Heering, H.A.; Williams, K.A.; Lemay, S.G.; Dekker, C. *Nano Lett.* **2005**, 5, 137.

29. Quinn, B.M.; Dekker, C.; Lemay, S.G. *J. Am. Chem. Soc.* **2005**, 127, 6146.

30. Bertoncello, P.; Edgeworth, J.P.; Macpherson, J.V.; Unwin, P.R. *J. Am. Chem. Soc.* **2007**, 129, 10982.

31. White, H.S.; Leddy, J.; Bard, A.J. *J. Am. Chem. Soc.* **1982**, 104, 4811

32. Mauritz, K.A.; Moore, R.B. *Chem. Rev.* **2004**, 104, 4535.

33. Bertoncello, P.; Ciani, I.; Li, F.; Unwin, P.R. *Langmuir* **2006**, 22, 10380.

34. Bertoncello, P.; Ciani, I.; Marenduzzo, D.; Unwin, P.R. *J. Phys. Chem. C* **2007**, 111, 294.

35. Bertoncello, P.; Wilson, N.R.; Unwin, P.R. *Soft Matter* **2007**, 3, 1300.

36. Bertoncello, P.; Dennany, L.; Forster, R.J.; Unwin, P.R. *Anal. Chem.* **2007**, 79, 7549.

37. Ugo, P.; Bertoncello, P.; Vezza', F. *Electrochim. Acta* **2004**, 49, 3785.

38. Bertoncello, P.; Ugo, P. *J. Braz. Chem. Soc.* **2003**, 14, 517.

39. Bertoncello, P.; Ram, M.K.; Notargiacomo, A.; Ugo, P.; Nicolini, C. *Phys.Chem.Chem.Phys.* **2002**, 4, 4036.

40. Moretto, L.M.; Kohls, T.; Chovin, A.; Sojic, N.; Ugo, P. *Langmuir* **2008**, 24, 6367.

41. Martin, C.R.; Rubinstein, I.; Bard, A.J. J. Am. Chem. Soc. 1982, 104, 4817.

42. Lee, C.; Anson, F.C. Anal. Chem. 1992, 64, 528.

43. Anson, F.C.; Blauch, D.N.; Saveant, J.M.; Shu, C.-F. J. Am. Chem. Soc. 1991, 113, 1922.

44. Bard, A.J. and Faulkner L.R. *Electrochemical Methods: Fundamentals and Applications*, 2nd ed.; Wiley: New York, 2001: chapter 6, p.226.

Chapter 8: Conclusions

This thesis has presented developments in electrochemical scanned probe microscopies, including the development of new members of this family, which have been shown to have considerable potential. Theoretical methods have been developed and results of these presented, which support the interpretation of data obtained from these techniques.

An account of the building of a multi-technique, software driven, electrochemical scanned probe microscope is provided in chapter 2. The instrument, which has been rolled out at Warwick in three versions, provides capabilities in scanning ion conductance microscopy (SICM), scanning electrochemical microscopy (SECM), including tip position modulation (TPM) variants and the scanning microcapillary method (SMCM). The instrumentation and software could be further developed with relative ease.

As outlined in the thesis, SICM is attracting considerable attention for imaging in the life sciences, yet the spatial resolution of the technique has not been addressed. This situation has been remedied through theoretical investigations (chapter 3). Experimental evidence of tip-convolution, as suggested by theoretical predictions, has been reported through several experimental systems. The model provides a foundation for further studies, including investigations of charge effects on the probe and other issues.

Theoretical and experimental investigations of the tip position modulation (TPM) mode of SECM are presented. As discussed in the thesis, this technique was developed in the early 1990's as a possible means of separating topographical and activity effects in the SECM response, but a theory for the baseline case of an inactive interface was not available, precluding the further use of this method. In this thesis, clear evidence has been given for the role of convective effects in the tip-current response and a simple, effective model has been developed.

Demonstration has made of the amenability of this technique to the measurement of permeability of electroactive species, where it has been shown that the AC current in TPM provides greater sensitivity to permeability, compared to DC measurements. The use of this technique in the life sciences (e.g. for probing the permeability of living cells) is envisaged.

Experimental measurements are reported on systems ranging from particle growth at liquid/liquid interfaces (chapter 4) to heterogeneous carbon electrodes (chapters 6 and 7). Notably, rate constants have been determined for the growth of silver particles at a liquid/liquid interface using SECM and the dependence of this rate on various parameters is reported. A key application has been to explore the activity of basal plane highly ordered pyrolytic graphite (HOPG), which is currently a matter of considerable debate and controversy. Studies using the new SMCM technique and a new method to spatially decouple sites in cyclic voltammetry measurements, has demonstrated that basal plane HOPG has far greater activity than previously believed. Since carbon electrodes are used extensively for electroanalysis in the life science (due to biocompatibility), and given the significant interest in related materials such as carbon nanotubes, the new insights obtained are of considerable importance.